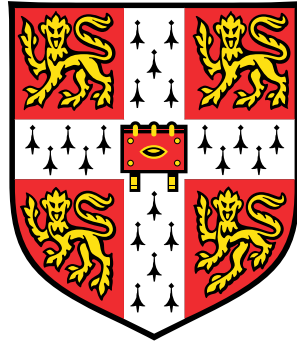


The impact of tropical sea surface  
temperature perturbations on  
atmospheric circulation over north  
Canada and Greenland



Michelle Roisin McCrystall

British Antarctic Survey

Department of Chemistry, University of Cambridge

This dissertation is submitted for the degree of

*Doctor of Philosophy*

St Edmunds College

September 2017



To everyone who helped me along the way



## **Declaration**

I hereby declare that except where specific reference is made to the work of others, the contents of this dissertation are original and have not been submitted in whole or in part for consideration for any other degree or qualification in this, or any other university. This dissertation is my own work and contains nothing which is the outcome of work done in collaboration with others, except as specified in the text and Acknowledgements. This dissertation contains fewer than 60,000 words including appendices, bibliography, footnotes, tables and equations.

Michelle Roisin McCrystall

September 2017



## Acknowledgements

I would like to thank my supervisors, Dr Scott Hosking, Dr Amanda Maycock and Prof John Pyle for all their help and guidance me throughout this PhD, particularly Scott, who was my primary supervisor. I cannot thank him enough everything that he has done to help me and my project over the last three and a half years, I just hope his first experience as a PhD supervisor wont be his last.

Secondly I want to thank everyone in the Atmosphere, Ice and Climate team, namely the Polar Climate and Predication team at the British Antarctic Survey and the Centre for Atmospheric Science team at the Department of Chemistry. Every person on both teams were amazingly supportive and always willing to help with every question, concern and frustrating error I had.

To all the PhD students at BAS and in Chemistry, thank you for being there to help me through all of this, your support and encouragement, was amazing. In particular I want to thank Ian White, I am indebted to him for all of his help throughout, he never tired of my endless questions and was always there to help and encourage me when I needed it most. Secondly to all students from my year at BAS and especially my office mates in 154 you all made this journey fun. I particularly want to thank Jenny Turton whose endless support and encouragement definitely helped me make it through this PhD.

To everyone at Eddies, you are an amazing bunch of people. I could not have got through the last few months without you, your constant encouragement was the only thing that helped me through. To everyone from the Cambridge Parnells GAC club,

particularly Aoife McCann who was so thoughtful and generous throughout my PhD, I am so thankful for your friendship and support. To all my friends who have been with me in this over the last three and a half years, I am so thankful for your friendship and your constant and unwavering support and encouragement

To my family, thank you so much for bearing with me these last three years and especially final few months. To my mum, dad and godmother, Margaret, Pat and Briege, I cannot thank you all enough for everything you have done for me both throughout this PhD and throughout my academic life so far. I would not have made it here without your support, I am forever indebted to you all. To my brothers and sisters, Brenda, Edel, Conor, and Paul and in-laws, Ruairi, Micheal and Lisa, I thank you all for being a massive stable in my life. You have helped and supported me in ways that you probably are not aware of. I couldn't imagine having a better family. To my wonderful nephews and niece, Padraic, Cara, Eoghan, Odhran and Cadhan, thank you for being the amazing kids you are, you always brighten my day.

Finally, to Neeshie Mc Crystall and Francis Toner, who passed away over the last three years, I still feel your loss, particularly as I wasn't there to say goodbye.

## Abstract

Identifying the drivers of Arctic climate variability is essential for understanding the recent rapid changes in local climate and determining the mechanisms that cause them. Remote tropical sea surface temperatures (SST) have been identified in previous studies as having contributed to the recent positive trends in surface temperature and geopotential height at 200 hPa over north Canada and Greenland (1979-2012) through poleward propagating Rossby waves. However, the source and direction of wave propagation on to north Canada and Greenland (NCG) differs across climate datasets indicating that there are still uncertainties surrounding the mechanisms for how the tropics influence the NCG climate. This thesis aims to further investigate the robustness of the trends over NCG and understand how circulation in this region responds to imposed tropical SST perturbations.

The eddy 200 hPa geopotential height (Z200) trends over NCG are assessed in a number of different datasets and compared to the response of eddy Z200 over NCG to imposed tropical SST perturbations in a number of sensitivity studies using the HadGEM3 atmosphere-only model. These model experiments are forced with observed differences in SSTs from the beginning and end of the satellite record (1979-1988 and 2003-2012), with spatial perturbations for [i] the entire tropics, [ii] global SSTs, [iii] the tropical Pacific only, [iv] the tropical Atlantic SST only, [v] the tropical Indian Ocean only.

The positive spatial trends of eddy Z200 over NCG from ERA-Interim reanalysis is largely captured in ensemble means of two available climate datasets, UPSCALE and

AMIP, indicating that this is a robust climate pattern, however, these trends appear to be stronger in the latter part of the record specifically over the UPSCALE period (1985 to 2011).

The model sensitivity studies show that a negative eddy Z200 anomaly over NCG was found in response to all imposed tropical SST perturbations (2003-2012) relative to a background state (1979-1988). This was due a stationary trough over the region that was able to intensify in response to a lack of a strong anomalous wave forcing from changes in mid-tropospheric temperature and zonal winds. The forcing from the tropical Atlantic, relative to the other tropical ocean basins, resulted in the largest eddy Z200 response over NCG, indicating its dominance in forcing the large scale tropical signal. The influence of extratropical SST perturbations relative to tropical SST perturbations were also investigated and it was demonstrated that this negative anomaly is largely driven by the change in tropical sea surface temperatures.

# Table of contents

List of figures	xv
List of tables	xxix
Acronyms	xxxix
<b>1 Introduction</b>	<b>1</b>
1.1 The structure and general circulation of the atmosphere . . . . .	1
1.1.1 General circulation of the troposphere . . . . .	2
1.2 Wave teleconnections and their implications on high latitudes . . . . .	5
1.3 Waves in the atmosphere . . . . .	17
1.3.1 Rossby wave source . . . . .	18
1.3.2 Wave propagation . . . . .	22
1.3.3 Calculating waves in the atmosphere . . . . .	25

---

1.4	Arctic and north Canada and Greenland . . . . .	25
1.5	Arctic climate . . . . .	27
1.5.1	Local and remote drivers of climate . . . . .	28
1.6	Motivations and Aims . . . . .	33
<b>2</b>	<b>Data, Model and Methods</b>	<b>35</b>
2.1	Existing climate and model records . . . . .	36
2.1.1	ERA-Interim Reanalysis . . . . .	36
2.1.2	UPSCALE . . . . .	37
2.1.3	CMIP5/AMIP . . . . .	38
2.2	Model set-up, design and experiments . . . . .	39
2.2.1	The UM dynamical Core . . . . .	39
2.2.2	Parametrisation schemes . . . . .	42
2.3	HadISST . . . . .	43
2.4	Model Experiments . . . . .	43
2.4.1	Control model run . . . . .	45
2.4.2	Perturbed model runs . . . . .	45
2.4.2.1	OneSST model experiment . . . . .	45
2.4.2.2	TropSST model experiment . . . . .	49

---

2.4.2.3	PacSST, AtISST and IndSST model experiments . . . . .	50
2.4.2.4	GloSST model experiment . . . . .	54
2.5	Methods used in analysis . . . . .	55
2.5.1	Wave Activity Flux . . . . .	55
2.6	Statistical analysis . . . . .	57
2.7	Thermal wind . . . . .	58
2.8	Model Validation . . . . .	60
<b>3</b>	<b>The North Canada-Greenland pattern</b>	<b>71</b>
3.1	Observed changes to the north Canada and Greenland climate . . . . .	71
3.2	The characteristics of the NCG pattern . . . . .	73
3.3	Quantification of temporal variability of NCG anomaly . . . . .	77
3.4	Inter-ensemble member variability of NCG trends . . . . .	80
3.5	Concluding remarks . . . . .	102
<b>4</b>	<b>The tropical influence on NCG</b>	<b>105</b>
4.1	The role of the tropics in high latitudes . . . . .	105
4.2	Tropically induced wave trends in observational data . . . . .	107
4.3	The NCG response to a modelled tropical forcing . . . . .	109
4.3.1	Rossby wave source and propagation . . . . .	115

4.4	Extratropical influence on NCG . . . . .	125
4.5	Concluding remarks . . . . .	130
<b>5</b>	<b>Influence of the three major tropical ocean basins on north Canada and Greenland</b>	<b>133</b>
5.1	The importance of tropical ocean basins in generating teleconnections . . . . .	133
5.2	Response from ocean basin forcings . . . . .	134
5.3	Mechanisms of the tropical forcing on large scale climate and the effect of this on NCG . . . . .	141
5.4	Concluding remarks . . . . .	156
<b>6</b>	<b>Conclusions</b>	<b>159</b>
6.1	Future work . . . . .	167
	<b>References</b>	<b>171</b>

# List of figures

- 1.1 Vertical temperature structure of the atmosphere in K . . . . . 2
  
- 1.2 General circulation of the troposphere, highlighting the Hadley cells as meridional overturning circulations around the equator, Ferrel cells at the mid-latitudes and polar cell in northern high-latitudes. The direction of meridional flow due to Coriolis deflection is also shown in the arrows indicating the direction of the trade winds. This figure is taken from <http://climate.ncsu.edu/edu/k12/.atmosphercirculation> . . . . . 3
  
- 1.3 Observed northward eddy heat flux ( $^{\circ}\text{C m s}^{-1}$ ) for the Northern Hemisphere winter as shown in (Holton and Hakim, 2013) . . . . . 4
  
- 1.4 Anomalous SSTs in shading with red representing the warmest anomalies and blue, cool anomalies, the depth of thermoclines in dark blue, strength of trade winds and locations of greatest convection associated with the La Niña, El Niño and normal conditions between  $120^{\circ}\text{E}$  and  $80^{\circ}\text{W}$ . Largest differences are in the thermocline which is shallower in La Nina compared to normal and El Nino conditions and the warm pool in the west Pacific shifted closer to  $120^{\circ}\text{E}$  compared to normal and El Nino conditions. Taken from ([http://www.eorc.jaxa.jp/TRMM/about/result/earth/el\\_ninoe.htm](http://www.eorc.jaxa.jp/TRMM/about/result/earth/el_ninoe.htm)) . . . . . 6

- 
- 1.5 Signifies the climatic impacts of the El Niño globally for [a] DJF and [b] JJA, with types of climate changes highlighted in colourbar. Taken from <https://www.pmel.noaa.gov/elnino/impacts-of-el-nino> . . . . . 8
- 1.6 Outlines the global climate impacts of the La Niña on climate around for [a] DJF and [b] JJA. Taken from <https://www.pmel.noaa.gov/elnino/impacts-of-el-nino> . . . . . 9
- 1.7 Highlights the warm phase (in the left hand panel) and cold phase (in the right hand panel) of the PDO with temperatures on ° Celsius and wind vectors plotted on top. Taken from <http://research.jisao.washington.edu/pdo/> 10
- 1.8 The PNA mode based on a one point correlation map showing correlation coefficients of 500 hPa heights between 20°N and 160°W which results in correlated lower pressure anomaly over the north east Pacific, higher pressure anomaly over the north west of North America and low pressure anomaly in south east North America. Taken from figure 16 of Wallace and Gutzler (1981) . . . . . 13
- 1.9 The first EOF of the DJFM mean sea level pressure for the northern hemisphere, with contour intervals every 0.5 hPa, and dashed contours representing negative SLP and solid contours, positive SLP. Taken from Ambaum et al (2001). . . . . 14
- 1.10 The first empirical orthogonal function (EOF in the northern Atlantic sector of MSLP for 1899-2006 indicating the NAO, with dashed lines highlighting negative values and solid lines represent positive values. Countour intervals at every 0.5 hPa. Adapted from Hurrell and Deser (2010). . . . 16

1.11	Convection in atmosphere, with [1] convergent winds into the region of the heat source, as depicted by the red circle, [2] large cumulonimbus clouds above the region of warming to depict deep convection and area of greatest precipitation, [3] divergent winds aloft and [4] subsidence of air at either side of the largest region of convection along the equator. . . . .	19
1.12	Climatological Rossby wave source between 1979-2007 for DJF. The light shaded area represents positive values and the dark shaded areas represents the negative values. Taken from Shimizu and de Albuquerque Cavalcanti (2010) . . . . .	21
1.13	Schematic of westward propagating waves . . . . .	22
1.14	Adapted from figure 10 of Scaife et al. (2017). Shows Rossby wave propagation from two arbitrary locations at 200 hPa with smaller wave numbers propagating poleward and larger wave numbers propagating within equatorial region due to wave refraction of higher wave numbers. . . . .	24
1.15	Trends from October to January 1989-2009 for [a] for Surface air temperature in $^{\circ}\text{C decade}^{-1}$ from observations, [b] sea ice concentration ( $\% \text{ decade}^{-1}$ ) from ERA-Interim, [c] surface turbulent fluxes (sensible plus latent) ( $\text{W m}^{-2}$ ), [d] surface sensible heat flux ( $\text{W m}^{-2}$ ), [e] surface latent heat flux ( $\text{W m}^{-2}$ ) and [f] net surface outgoing long wave radiation. Adapted from Screen and Simmonds (2010a). . . . .	30
2.1	Examples of all Arakawa staggered grids showing where difference variables are derived. Taken from <a href="https://www.gfdl.noaa.gov/vb/gridstd/gridstdse2.html">https://www.gfdl.noaa.gov/vb/gridstd/gridstdse2.html</a> . . . . .	40
2.2	Vertical staggered grids of [a] Lorenz and [b] Charney-Phillips (Collins et al. 2013 of <i>Climate Change and Regions/Local responses</i> edited by Zhang and Ray 2013 . . . . .	41
2.3	Annual, globally meaned OLR timeseries for the control model experiment . . . . .	44

2.4	Smoothing function applied between 30°N(°S) and 20°N(°S) between perturbed state in tropics and background state elsewhere . . . . .	46
2.5	Anomalous forcing in the OneSST model experiment relative to the background climatology SST . . . . .	47
2.6	Index of Southern Oscillation index strength from 1965 to 2017 with green rectangular box indicating the ENSO index between 1979-1988 with black rectangular box highlighting the ENSO index between 2003-2012. Taken from ( <a href="https://www.ncdc.noaa.gov/teleconnections/enso/indicators/soi/">https://www.ncdc.noaa.gov/teleconnections/enso/indicators/soi/</a> )	48
2.7	Index of PDO strength from 1900 to 2017 with green rectangular box indicating the positive PDO index between 1979-1988 with black rectangular box highlighting the PDO index between 2003-2012 which tends to be negative in this period. Taken from National Oceanic and Atmospheric Administration (NOAA) National Centres from Environmental Information page ( <a href="https://www.ndc.noaa.gov/teleconnections/pdo/">https://www.ndc.noaa.gov/teleconnections/pdo/</a> ) . . .	48
2.8	Anomalous forcing of TropSST model relative to the background climatology SST . . . . .	50
2.9	Smoothing function applied to the SST perturbations both in latitude and longitude for the [a] PacSST, [b] AtlSST and [c] IndSST model experiments.	52
2.10	Difference in SST forcing between the [a] PacSST model experiment, [b] AtlSST model experiment, [c] IndSST model experiment and the control model experiment . . . . .	53
2.11	Difference between the SST forcing of GloSST minus TropSST to show anomalous forcing in the extratropics . . . . .	55

- 
- 2.12 Eddy Z200 climatology for [a] ERAI for 1979-1988 [b] Control model experiment over all model data and [c] the absolute difference between the Control model experiment and ERAI to indicate bias in model. Areas of purple in [c] highlight where model simulates larger anomalies than in ERAI and green shading indicates where the model simulates weaker anomalies than in ERAI . . . . . 62
- 2.13 Difference in eddy Z200 between the control model experiment and ERAI highlighting model bias, with purple showing where the model simulates larger anomalies than ERAI and green shading as weaker anomalies in model than ERAI for [a] DJF, [b] MAM, [c] JJA, [d] SON . . . . . 63
- 2.14 Surface temperature climatology for [a] ERAI for 1979-1988 at 2m, [b] Control model experiment at 1.5m and [c] the difference between the control and ERAI with purple shading indicating areas of where the model temperatures are higher than in ERAI and green shading, where the model is relatively colder. . . . . 65
- 2.15 As is figure 2.14 c, but showing the differences in surface temperature between the model and ERAI for [a] DJF, [b] MAM, [c] JJA, [d] SON . . . . . 66
- 2.16 200 hPa U wind climatology for [a] ERAI for 1979-1988, [b] Control model experiment, [c] the difference between control and ERAI with purple indicating model bias with purple representing model overestimation and green model underestimation . . . . . 67
- 2.17 Seasonal difference of U wind at 200 hPa between the control model experiment and ERAI to represent bias in model with purple indicating model overestimation and green indicating underestimation for [a] DJF, [b] MAM, [c] JJA, [d] SON . . . . . 68

- 
- 3.1 Annual trend in geopotential height at 200hPa from 1979-2012 in ERA-Interim. Stippling denotes statistical significance at  $p < 0.05$ . . . . . 72
- 3.2 Annual trend in eddy geopotential height at 200hPa from 1979-2012 in ERA-Interim. Stippling denotes statistical significance at  $p < 0.05$ . . . . . 73
- 3.3 Eddy Z200 annual mean trends for [a] ERAI from 1985 to 2011 and [b] UPSCALE ensemble mean for 1985-2011. . . . . 75
- 3.4 Eddy Z200 annual mean trends in [a] ERAI for 1979-2005 (following AMIP record) [b] AMIP multi model mean for 1979 to 2005. Stippling denotes statistical significance ( $p < 0.05$ ) and green dashed box denotes area of interest north Canada and Greenland (NCG) . . . . . 76
- 3.5 Timeseries of eddy Z200 over NCG for ERAI from 1979-2012 (in blue), UPSCALE ensemble mean from 1985-2011 (in green) and AMIP multi-model mean from 1979-2005 (in red). Faded lines represent the actual timeseries each dataset, with bold lines represented the smoothed timeseries using lower pass five year filtering. . . . . 79
- 3.6 Eddy Z200 trends for ERAI from 1979-2012 for [a] December-February, [b] March-May, [c] June-August, [d] September-November. Stippling denotes statistical significance ( $p < 0.05$ ), and green dashed box highlights the region of interest. . . . . 79
- 3.7 Timeseries of eddy Z200 for ERAI from 1979-2012 (in blue), UPSCALE ensemble mean from 1985-2011 (in green) and AMIP multi-model mean from 1979-2005 (in red) for [a] DJF, [b] MAM, [c] JJA, [d] SON. The faded lines in background represent the actual timeseries whereas the bold lines in front are the smoothed timeseries, using Kernel low-pass five year filtering 81

- 
- 3.8 Box and whisker plots representing the spread of all UPSCALE ensemble members for [a] annual trends in eddy Z200 over NCG and [b] DJF trends for NCG eddy Z200 from 1985-2011. Red and green solid lines in each represents the mean and median for the annual and DJF ensemble respectively. The solid and dashed lines highlight the annual and DJF ERAI trend over the same time period . . . . . 82
- 3.9 Box and whisker plot of all AMIP model members for [a] annual and [b] DJF trends of eddy Z200 over NCG for 1979-2005. Red and green solid lines represent multi-model mean and median respectively. The solid and blue lines denote the annual and DJF trends in ERAI of eddy Z200 over NCG for 1979-2005. . . . . 84
- 3.10 Annual trends in eddy Z200 for all 13 UPSCALE ensemble members from 1985-2011 of [a-e] N96 resolution (130 km), [f-h] N216 resolution (60 km), [i-m] N512 resolution (25 km). The stippling denotes statistical significance ( $p < 0.05$ ) . . . . . 86
- 3.11 DJF trend in eddy Z200 for all 13 UPSCALE ensemble members from 1985-2011 for [a-e] N96 resolution (130 km), [f-h] N216 resolution (60 km) and [i-m] N512 resolution (25 km). NCG is denoted by green dashed box 87
- 3.12 Annual trends in eddy Z200 of UPSCALE ensemble means for [a] 5 models at N96 resolution, [b] 3 models at N216 resolution and [c] 5 models at N512 resolution. Stippling indicates statistical significance at  $p < 0.05$  . . . 88
- 3.13 Annual trend (1979-2005) of all AMIP models whose trend of eddy Z200 over NCG was greater than the ERAI mean over the same area (AMIP-GTE). NCG domain is outlined by green dashed box . . . . . 90
- 3.14 The DJF trend in eddy Z200 of AMIP models whose model mean trend of eddy Z200 over NCG was greater than ERAI (AMIP-GTE) with NCG region highlighted by green dashed box . . . . . 91

3.15 Annual trend (1979-2005) of all AMIP models whose trend of eddy Z200 over NCG was greater than the ERAI mean over the same area (AMIP-GTE). NCG domain is outlined by green dashed box . . . . .	92
3.16 The DJF trend in eddy Z200 of AMIP models whose model mean trend of eddy Z200 over NCG was greater than ERAI (AMIP-GTE) with NCG region highlighted by green dashed box . . . . .	93
3.17 Annual trend (1979-2005) of all AMIP models whose trend of eddy Z200 over NCG was less than the ERAI mean over the same area (AMIP-LTE). NCG region is outlined by green dashed box . . . . .	95
3.18 The DJF trend in eddy Z200 of AMIP models whose model mean trend of eddy Z200 over NCG was less than ERAI (AMIP-LTE) with NCG region highlighted by green dashed box . . . . .	96
3.19 Scatter plots of all AMIP models showing annual eddy Z200 data over NCG compared to ERAI annual eddy Z200 data from 1979-2005. Red line depicts regression line. Root mean square error of each model is highlighted in bottom right hand corner . . . . .	97
3.20 Scatter plots of all UPSCALE members showing the annual eddy Z200 data over NCG compared to ERAI from 1985-2011 with red line depicting the linear regression line. Root mean square error of each model in highlighted in bottom right hand corner of each plot . . . . .	98
3.21 Scatter plot of the AMIP multi-model mean annual eddy Z200 data over NCG with red line highlighting the linear regression line. Root mean square error for the multi-model mean is noted in the bottom right hand corner . . . . .	99

3.22	Scatter plot of the UPSCALE ensemble mean annual eddy Z200 data over NCG with red line highlighting the linear regression line. Root mean square error for the UPSCALE ensemble mean is noted in the bottom right hand corner . . . . .	100
4.1	Annual spatial trends of eddy Z200 in metres per year in coloured contours and WAF trends in black vectors for [a] ERAI from 1979-2012, [b] UPSCALE ensemble means from 1985-2011 and [c] AMIP multi-model means from 1979-2005. Vector scaling differs for each dataset and subsequent vector scaling can be found immediately below each figure. . . . .	108
4.2	Response of Z200 in metres of TropSST model experiment relative to control model experiment for boreal winter. Black stipling highlights statistical significance ( $p < 0.05$ ). . . . .	110
4.3	Eddy Z200 in metres for boreal winter for [a] Control model experiment, [b] TropSST model experiment and [c] the difference between TropSST and control model experiments, relating to the response of tropical forcing. Black stipling in [c] highlights statistical significance at $p < 0.05$ . . . . .	111
4.4	[a] Eddy Z at 500 hPa response in the TropSST forcing and [b] The response of MSLP from TropSST forcing for boreal winter averaged over all 58 years of model simulations. Black stipling indicates statistical significance at $p < 0.05$ . . . . .	112
4.5	Wave activity flux (WAF) at 200 hPa for boreal winter in black vectors superimposed over eddy Z200 climatological fields for boreal winter for [a] Control model experiment and [b] TropSST model experiment . . . . .	114

4.6	Response in eddy Z200 (coloured contours) and WAF (black vectors) at 200 hPa from the TropSST model experiment forcing relative to the control model experiment. The statistical significance of these anomalies are shown previously in figure 4.3 . . . . .	114
4.7	DJF mean of Rossby wave source for [a] ERA-Interim Reanalysis, [b] Control model experiment and [c] TropSST model experiment . . . . .	116
4.8	Response of [a] Rossby wave source, [b] absolute vorticity and [c] divergence from the TropSST model experiment forcing, as an average over 58 year model simulation for DJF. Stippling indicates statistical significance at $p < 0.05$ . . . . .	118
4.9	Response of [a] Precipitation and [b] Outgoing Longwave Radiation from the TropSST model experiment forcing. Stippling indicates regions of statistical significance at $p < 0.05$ . . . . .	119
4.10	Response in WAF from TropSST model experiment relative to control model experiment in blue vectors for boreal winter with climatological DJF winds for control model experiment in unfilled contours, at contour level of $10 \text{ m s}^{-2}$ and for response of zonal U winds from TropSST model experiment forcing in shading. Stippling indicates regions of statistical significance ( $p < 0.05$ ). . . . .	121
4.11	Difference in mid tropospheric (300-800hPa) air temperature in $^{\circ}\text{C}$ between the TropSST model and control model experiments in DJF. Stippling indicates statistical significance at $p < 0.05$ . . . . .	122
4.12	DJF mid tropospheric (300-800hPa) air temperature in $^{\circ}\text{C}$ from control model experiment . . . . .	122
4.13	Difference in eddy Z200 and wind vectors in DJF between the TropSST model and control model experiments . . . . .	123

- 
- 4.14 Response of eddy Z200 anomaly from GloSST model experiment relative to control in coloured contours for DJF. Black hatching represents statistical significance at  $p < 0.05$  . . . . . 126
- 4.15 Response of eddy Z200 anomaly from extratropical SSTs, where the GloSST model experiment is differenced with respect to the TropSST model experiment for DJF. Statistical significance where  $p < 0.05$  is depicted by black hatching . . . . . 127
- 4.16 Eddy Z200 and WAF response from GloSST model experiment relative to control model experiment in coloured contours and black vectors respectively for boreal winter . . . . . 128
- 4.17 WAF (shown by black vectors) and eddy Z200 (in coloured contours) response from extratropical SSTs through differencing of GloSST model experiment and TropSST model experiment for boreal winter . . . . . 129
- 4.18 Response of Rossby wave source, highlighted by coloured contours, zonal wind and WAF to an extratropical SST forcing (found through differencing the GloSST and TropSST model experiments) for boreal winter, averaged over 58 years of HadGEM3-A model output . . . . . 130
- 5.1 Boreal winter response of eddy Z200 to anomalous forcing from [a] PacSST model experiment, [b] AtlSST model experiment, [c] IndSST model experiment. Hatching denotes statistical significance at  $p < 0.05$  . . . . . 135
- 5.2 The response of eddy Z200 from the [a] PacSST model relative, [b] AtlSST model experiment, [c] IndSST model experiment relative to the control model experiment in shading as in figure 5.1. Climatological eddy Z200 from control model experiment in contours with contour interval at 40m. Solid contours indicate positive eddies and dashed contours show negative contours. . . . . 137

5.3	[a] The response of eddy Z200 from the TropSST model relative to the control model experiment, [b] the sum of the response of eddy Z200 from the PacSST, AtlSST and IndSST model experiments, [c] the difference between ([a]-[b]) to test linearity of model . . . . .	139
5.4	Response of DJF precipitation rate for [a] PacSST model experiment, [b] AtlSST model experiment, [c] IndSST model experiment. Stippling indicates statistical significance at $p < 0.05$ . . . . .	141
5.5	Response of outgoing longwave radiation in DJF for [a] PacSST model experiment, [b] AtlSST model experiment, [c] IndSST model experiment. Stippling indicates statistical significance at $p < 0.05$ . . . . .	143
5.6	Response of horizontal wind divergence in DJF for [a] PacSST model experiment, [b] AtlSST model experiment, [c] IndSST model experiment. Stippling indicates statistical significance at $p < 0.05$ . . . . .	145
5.7	Response of Rossby wave source in DJF from [a] PacSST model experiment, [b] AtlSST model experiment, [c] IndSST model experiment relative to control model experiment. Stippling indicates statistical significance at $p < 0.05$ . . . . .	146
5.8	Response of WAF (black vectors) and eddy Z200 (shading) in DJF for [a] PacSST model experiment, [b] AtlSST model experiment and [c] IndSST model experiment . . . . .	148
5.9	DJF response of wave activity flux (blue vectors) and zonal wind (shading) in the [a] PacSST model experiment and [b] AtlSST model experiment. Superimposed in unfilled contours in the zonal wind from the control model experiment. . . . .	149

---

5.10	Response of mid tropospheric air temperature taken across 350-800 hPa for [a] PacSST model experiment, [b] AtISST model experiment. Stippling indicates statistical significance at $p < 0.05$ . . . . .	151
5.11	Response of zonal wind at 200 hPa, calculating through the thermal wind equations for [a] PacSST model experiment and [b] AtISST model experiment. . . . .	152
5.12	DJF eddy Z200 response from [a] PacSST model experiment and [b] AtISST model experiment relative to the control model experiment with wind vectors superimposed . . . . .	154
5.13	[a] DJF WAF and U wind at Z200 response from TropSST model experiment relative to the control model experiment, [b] sum of response of DJF WAF and U wind at 200 hPa from the PacSST and AtISST model experiment . . . . .	155



# List of tables

3.1 List of all AMIP models and identification of which are in AMIP-LTE and  
in AMIP-GTE . . . . . 101



# Acronyms

## Acronyms / Abbreviations

*AGCM* Atmospheric Global Climate Models

*AMIP* Atmospheric Model Intercomparison Model

*AMIP – GTE* AMIP models which are greater than the ERAI mean for eddy Z200 means

*AMIP – LTE* AMIP models which are less than the ERAI mean for eddy Z200 trends

*AVHRR* Advanced Very High-Resolution Radiometer

*CAPE* Convectively Available Potential Energy

*CMIP5* Coupled Model Intercomparison

*ECMWF* European Centre for Medium Range Weather Forecasts

*ENDGame* Even Newer Dynamics for General atmospheric modelling of the environment

*ERA-Interim* ERA-Interim Reanalysis Data

*GCM* Global Climate Model

*GL3* Global Land 3

*HadGEM3* Hadley Centre Global Environmental Model 3

*HadISST* Hadley Centre Sea Ice and Sea Surface Temperature

*JULES* Joint UK Land Environmental Simulator

*MDB* Marine Data Bank

*NAM* Northern Annular Mode

*NAO* North Atlantic Oscillation

*NCG* north Canada and Greenland

*ND* New Dynamics

*OLR* Outgoing Longwave Radiation

*OLR* Outgoing Longwave Radiation

*OSTIA* Operational Sea Surface Temperature and Sea Ice Analysis

*PC2* Prognostic Cloud Prognostic Condensate

*PSO* Pacific Decadal Oscillation

*QG* Quasi-Geostrophic

*RMSE* Root mean square error

*RWS* Rossby wave source

*SLP* Sea-level Pressure

*SST* Sea Surface Temperature

*UM* Unified Model

*UPSCALE* UK on Prace: Weather-resolving Simulations of Climate for globAL Environmental risk

*WAF* Wave Activity Flux

*Z200* Geopotential height at 200 hPa

# Chapter 1

## Introduction

### 1.1 The structure and general circulation of the atmosphere

The earth's atmosphere is divided into a number of layers due to the variation of thermal structure in the vertical direction. The troposphere is the lowermost part of the atmosphere which extends from the surface to, on average, 10 km in height, although the height of the tropopause varies in height between the equator (approximately 16 km) and the poles (8 km). The troposphere is characterised by generally decreasing temperatures with height (Fig. 1.1) with a lapse rate of approximately  $-6.5^{\circ}\text{C km}^{-1}$  (Wallace and Hobbs, 2006a). It also contains around 80% of atmospheric mass which is relatively well mixed and is comprised of nitrogen (78% of total dry air), oxygen (21%) and argon (1%) along with other trace gases such as carbon dioxide and water vapour.

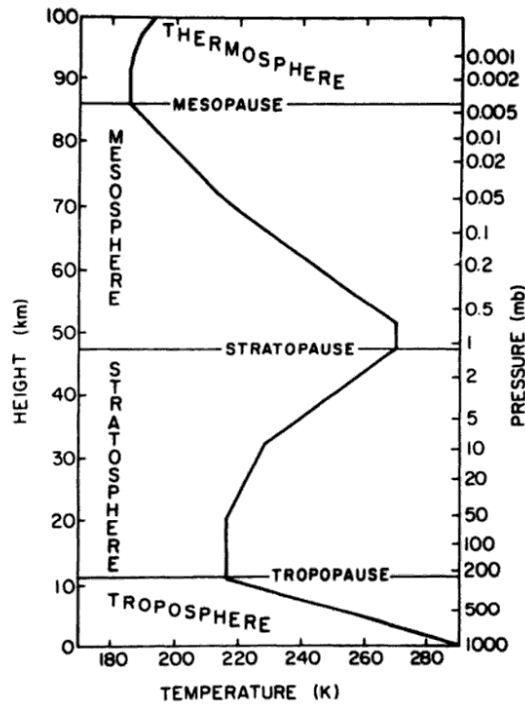


Fig. 1.1 Vertical temperature structure of the atmosphere in K

The stratosphere by comparison, is essentially the antithesis of the troposphere. It has a larger vertical extent, extending from 10 to 50 km and it is much more stably stratified than the troposphere. This is due to the large increase in temperature from around 20km upwards (Fig. 1.1) which peaks at 50 km due to the absorption of ultraviolet (UV) radiation as a result of the ozone layer and thus acts to inhibit vertical motion and mixing. Therefore, the mixing timescales in the stratosphere are typically much longer than in the troposphere with long residence times of different constituents such as ozone or for example pollutants from volcanic eruptions which can circle the entire planet and impact surface climate (Wallace and Hobbs, 2006a).

### 1.1.1 General circulation of the troposphere

Circulation within the troposphere is fundamentally driven by differential radiative heating between the equator and poles. A large gradient of heat and energy is found

between these regions whereby there is energy surplus at the equator, due to the greater absorption of short wave radiation, and energy deficiency at the pole due to more long wave radiation to space (Salby and Garcia, 1987). To ensure energy is balanced the circulation in the atmosphere and ocean must balance the differential heating through poleward transfers of heat (Liu and Alexander, 2007; Salby, 2012). This therefore drives large-scale meridional overturning circulation cells which are associated with the planetary scale transfer of heat and momentum (Andrews et al., 1987; Holton and Hakim, 2013; Salby, 2012).

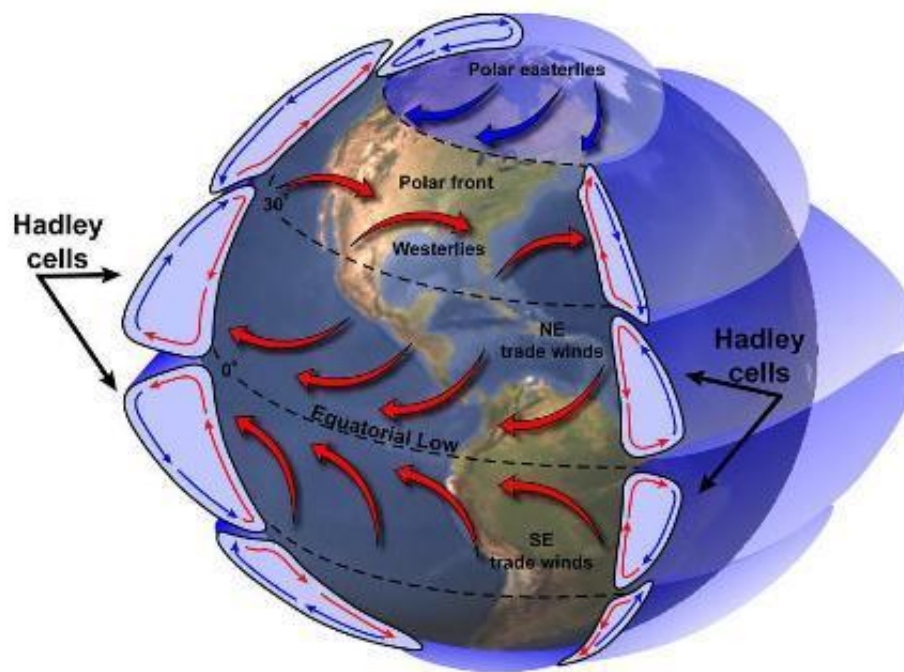


Fig. 1.2 General circulation of the troposphere, highlighting the Hadley cells as meridional overturning circulations around the equator, Ferrel cells at the mid-latitudes and polar cell in northern high-latitudes. The direction of meridional flow due to Coriolis deflection is also shown in the arrows indicating the direction of the trade winds. This figure is taken from <http://climate.ncsu.edu/edu/k12/atmospherecirculation>

Circulation associated with the Hadley cell features rising air rising near the equator due to convection and latent heat release which drives strong vertical motion which moves polewards once the air reaches the tropopause and becomes neutrally buoyant.

This circulation cells extends to approximately  $30^{\circ}\text{N}$  and  $30^{\circ}\text{S}$ , where through adiabatic cooling, descends and flows back to the equator at the surface.

The meridional flow within the Hadley cell at both upper and lower levels, however, is deflected by the Coriolis effect as a result of the Earth's rotation. This results in upper-level westerlies and surface easterlies in both the northern and southern hemisphere.

These winds converge at the equator (Fig. 1.2) leading to the generation of the inter-tropical convergence zone (ITCZ), which is the upward branch of the Hadley circulation (Fig. 1.2) (Andrews, 1987; Salby, 2012).

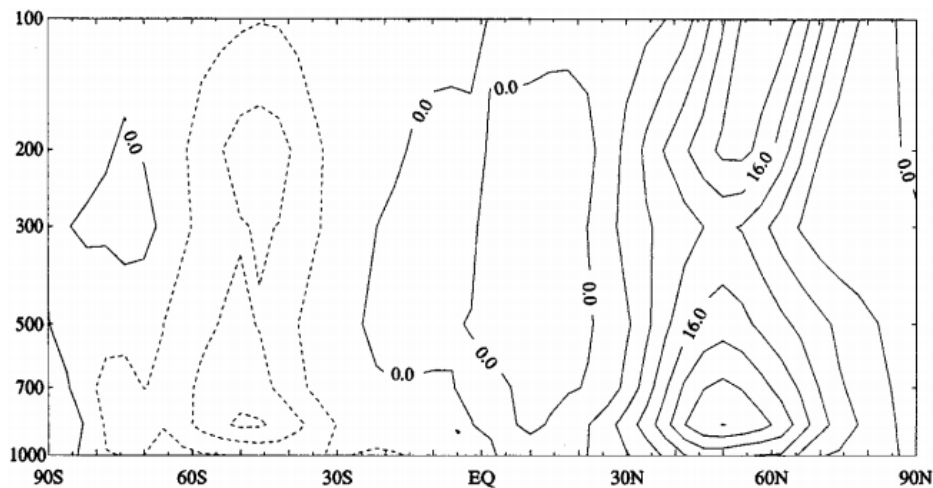


Fig. 1.3 Observed northward eddy heat flux ( $^{\circ}\text{C m s}^{-1}$ ) for the Northern Hemisphere winter as shown in (Holton and Hakim, 2013)

A second, thermally indirect meridional circulation cell occurs at the mid-latitudes roughly between  $30^{\circ}\text{N}$  ( $30^{\circ}\text{S}$ ) and  $60^{\circ}\text{N}$  ( $60^{\circ}\text{S}$ ) known as the Ferrel cell (Fig 1.2) (Holton and Hakim, 2013; Liu and Alexander, 2007). This circulation cell is mainly the result of mid-latitude eddy heat and momentum fluxes. This occurs through transient eddies, which are perturbations from the mean background flow, and stationary planetary waves, where the zonally asymmetric wave phase remains constant. Holton and Hakim (2013) found that the eddy heat flux ( $\overline{v'T'}$ ) reached peak amplitude at around  $50^{\circ}\text{N}$  (Fig.1.3) causing eddy convergence to the north and divergence to the south of this peak. This

results in a vertical motion with adiabatic warming and descent of air over the regions of eddy heat divergence at warmer, lower latitudes balanced by adiabatic cooling and ascent of air where eddy convergence takes place at relatively colder, higher latitudes, to generate a mid-latitude meridional overturning circulation cell (Holton and Hakim, 2013).

## 1.2 Wave teleconnections and their implications on high latitudes

The processes that drive the large-scale general circulation of the atmosphere can also result in climatological phenomena known as teleconnections (Liu and Alexander, 2007). Teleconnections can account for more regional changes in climate and describe the relationship in low frequency variability of atmospheric circulation and temperature anomalies between one location and another, usually over very large distances (Barnston and Livezey, 1987; Branstator, 2002; Ding and Wang, 2005; Liu and Alexander, 2007; Wallace and Gutzler, 1981). They can occur on a number of different timescales ranging from short timescales of around 2.5-6 days, 10-30 days on intermediate timescales and longer timescales of over 30 days, such as seasonal or interannual timescales (Blackmon et al., 1984; Liu and Alexander, 2007).

Teleconnection patterns are generated through both internal atmospheric processes and forced by anomalous diabatic heating such as from anomalous sea surface temperatures (SST) generally within the tropical regions. Either one, or a combination of both these processes can generate large scale teleconnections such as the El Nino Southern Oscillation (ENSO), the Pacific Decadal Oscillation (PDO), Pacific-North American pattern (PNA) Arctic Oscillation (AO) and North Atlantic Oscillation (NAO).

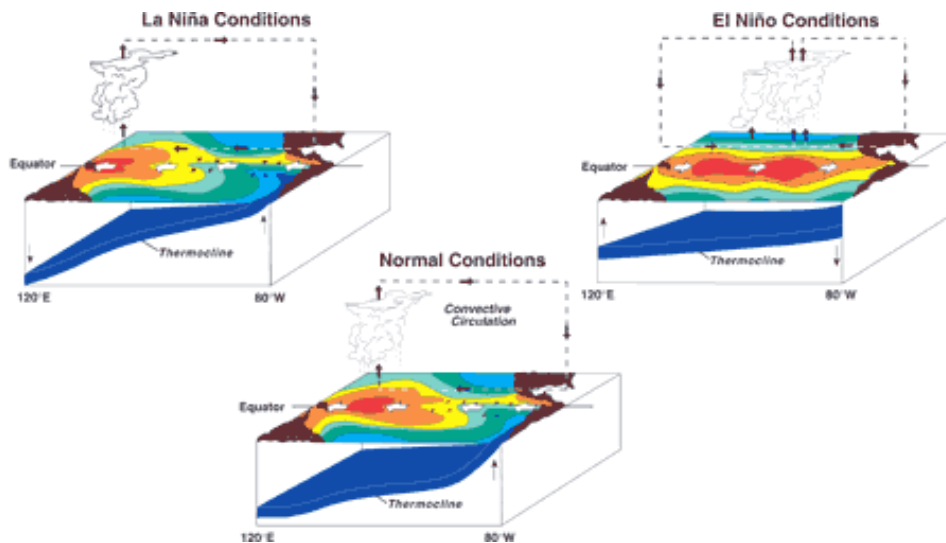


Fig. 1.4 Anomalous SSTs in shading with red representing the warmest anomalies and blue, cool anomalies, the depth of thermoclines in dark blue, strength of trade winds and locations of greatest convection associated with the La Niña, El Niño and normal conditions between  $120^{\circ}\text{E}$  and  $80^{\circ}\text{W}$ . Largest differences are in the thermocline which is shallower in La Nina compared to normal and El Nino conditions and the warm pool in the west Pacific shifted closer to  $120^{\circ}\text{E}$  compared to normal and El Nino conditions. Taken from (<http://www.eorc.jaxa.jp/TRMM/about/result/earth/elniño.htm>)

ENSO is a coupled atmosphere-ocean phenomena where, during the warm phase El Niño, large-scale warming of the Pacific ocean occurs and large scale cooling in the east Pacific in the cool phase, La Niña, that are coupled to changes in atmospheric circulation, known as the Southern Oscillation, which is characterised by an interannual see-saw in sea-level pressure (SLP) between the east and west Pacific (Rasmusson and Wallace, 1983; Wang et al., 2012a). More specifically as highlighted by the schematic in figure 1.4, the positive/warm phase of ENSO, the El Niño (Fig. 1.4 b) is characterised by excessively warm water off the coast of Peru and in the east Pacific along the western coastline of South America. Anomalously colder waters are also found within the west Pacific, along with weaker trade winds and reduced upwelling of the equatorial Pacific thermocline (Wyrtki, 1975). In the negative/cool La Niña phase (Fig 1.4 a), SSTs are anomalously colder in the east Pacific which expand westwards, strengthening the trade winds and result in greater upwelling of the thermocline in the east Pacific even in comparison to normal conditions presented in figure 1.4. The El Niño is strongest in boreal winter and

displays an oscillatory behaviour between these two phases of with preferred time scales roughly between two to five years (Suarez and Schopf, 1988; Wang et al., 2012a; Wyrтки, 1975; Zebiak and Cane, 1987).

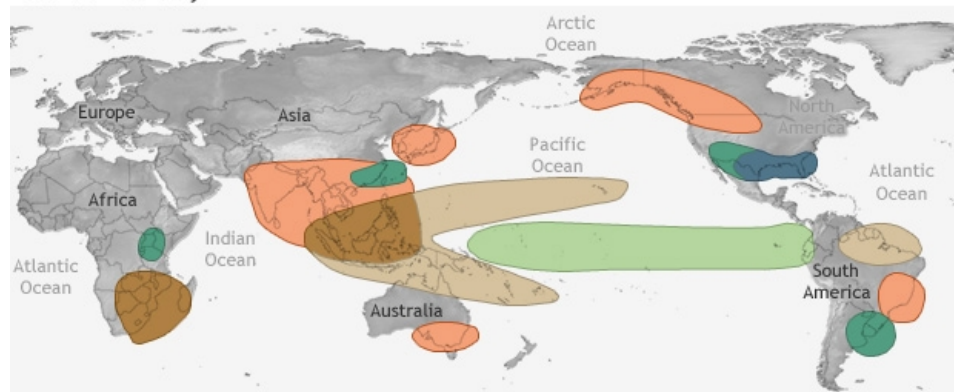
The ENSO occurs through the coupled interactions of the ocean and atmosphere and is initiated with a positive SST anomaly over the east Pacific associated with a depression of the thermocline. This then results in a change in the strength of the Walker circulation and thus weaker trade winds. The thermocline, as a result, deepens even further, reinforcing and enhancing the SST anomaly. A negative feedback is then required to break this cycle (Wang et al., 2012a), however the exact mechanism for this negative feedback and thus decay of the El Niño is not fully understood yet. A number of different mechanisms have been proposed, one of which outlines how a relaxation of east Pacific trade winds, which results in warm water propagation in to this region, are eventually eroded through colder SSTs from the west Pacific (Wang et al., 2012a; Wyrтки, 1975). Another proposed mechanism outlines how the reflection of Rossby and Kelvin waves can either reverse SSTs in the east Pacific or act to push the warm pool from the east to the west Pacific back to its climatological position (Picaut et al., 1997; Suarez and Schopf, 1988).

Although the full mechanisms behind the oscillatory nature of the ENSO are still not fully understood, its general pattern and impacts are generally well known. Locally both phases of ENSO affect the large-scale motion of the tropical atmosphere, namely the Intertropical Convergence Zone (ITCZ) and South Pacific Convergence Zone (SPCZ), which are areas of low level convergence, enhanced convection and precipitation. These are shifted equatorward and poleward and the convergence zones are displaced eastward and westwards during El Niño and La Niña years, respectively, resulting in anomalous precipitation and sea level pressure between the east and west Pacific (Philander, 1985). On larger scales, as depicted in figures 1.5 and 1.6 La Niña and El Niño exert contrasting impacts on the seasonally averaged climate. In boreal winter, December to February (DJF), the El Niño results in a warming of the west coast of North America along with most of south Asia and south Australia. Southern countries of Africa become warmer and drier and the most northerly point of the eastern South American coastline

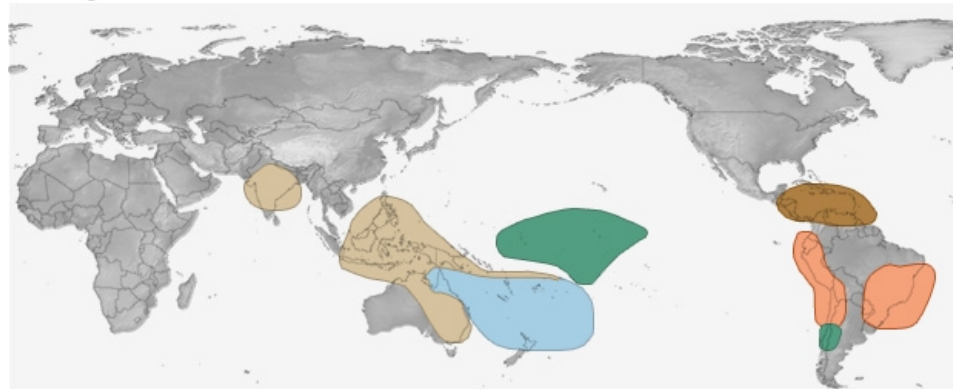
is wetter. The La Niña results in approximately the opposite of this with cooler and wetter average conditions along the western coastline of North America and east coast of South America. Boreal summer, June to August (JJA), impacts differ also, most of the southern hemisphere regions become warmer and drier aside from central south Pacific which becomes wetter during El Niño years. In La Niña years most of southern Asia, western coastline of South America become cooler and western south Pacific becomes warmer and drier.

## EL NIÑO CLIMATE IMPACTS

December-February



June-August



NOAA Climate.gov

Fig. 1.5 Signifies the climatic impacts of the El Niño globally for [a] DJF and [b] JJA, with types of climate changes highlighted in colourbar. Taken from <https://www.pmel.noaa.gov/elnino/impacts-of-el-nino>

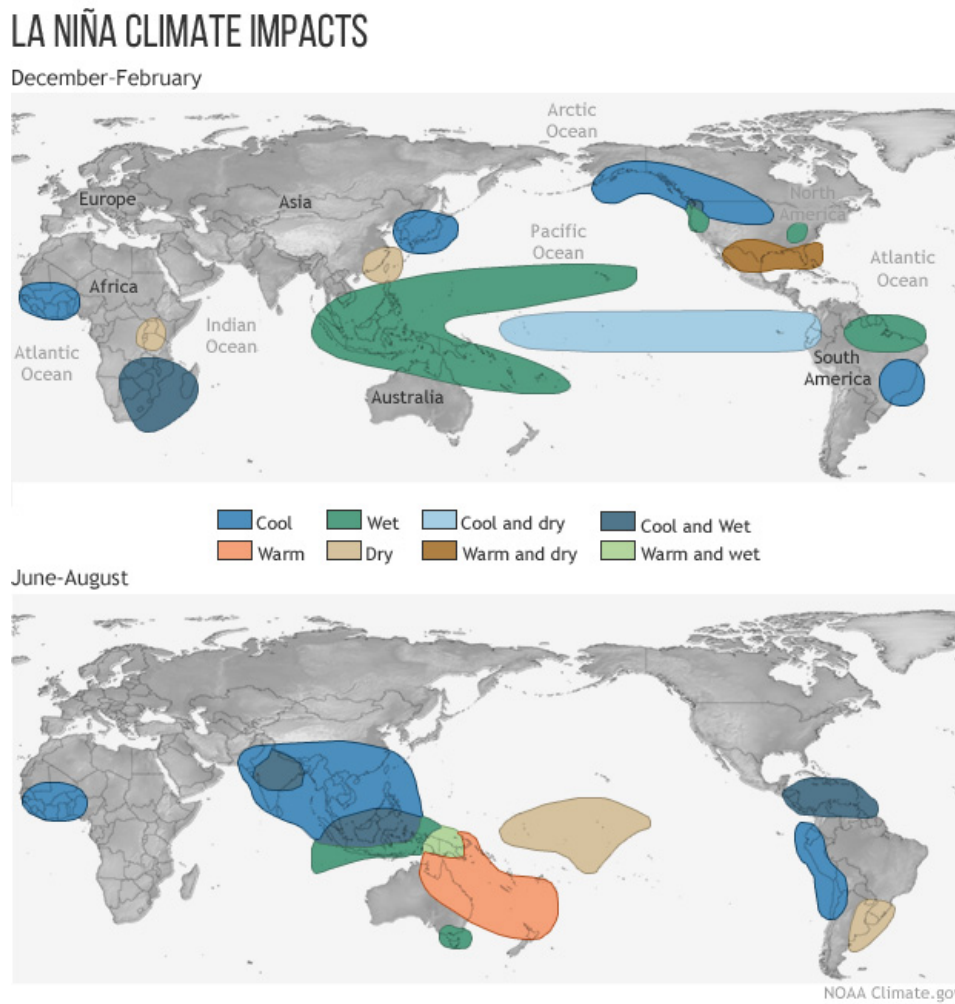


Fig. 1.6 Outlines the global climate impacts of the La Niña on climate around for [a] DJF and [b] JJA. Taken from <https://www.pmel.noaa.gov/elnino/impacts-of-el-nino>

Recent studies of ENSO have found that there are two types of El Niño located across the equatorial Pacific. They can be divided into the east Pacific El Niño (EP) and central Pacific El Niño (CP) and characterised through differences in anomalous SSTs. The EP El Niño anomalously warm SSTs extend from central to east Pacific, similar to the conventional ENSO and CP El Niño largest anomalous SSTs are within the central Pacific (Kao and Yu, 2009; Kug et al., 2009). These differences in anomalous SSTs also result in different responses in atmospheric circulation with stronger westerlies and greater precipitation in EP El Niño relative to CP El Niño.

In addition to year to year SST variability, Pacific SST anomalies also fluctuate on decadal or interdecadal timescales such as through the Pacific Decadal Oscillation (PDO). The PDO, often described as a long lived El Niño, is a dominant, year round pattern of north Pacific ( $20^{\circ}$ - $70^{\circ}$ N) SST monthly average anomalies (Mantua and Hare, 2002; Newman et al., 2016). It varies on decadal time scales, roughly 20-30 years (Schneider and Cornuelle, 2005) with its greatest amplitude from November to June and minima in late summer-early fall (Newman et al., 2016). In its warm phase (Fig. 1.7 a), spatially, the anomalous SSTs resemble a horseshoe-like pattern with SSTs in central north and west Pacific anomalously cool and anomalously warm along the west coast of North and South America and into the central Pacific (Schneider and Cornuelle, 2005). It also results in anomalously high sea-level pressure (SLP) over the north subtropical Pacific, which extend throughout the depth of the troposphere, resulting in enhanced cyclonic winds (Mantua and Hare, 2002). SST anomalies in the negative phase of the PDO, exhibit the same horseshoe-like shape (Fig. 1.7 b) but are anomalously cool in the east Pacific, stretching along the west coast North and South America, and anomalously warm in the west Pacific.

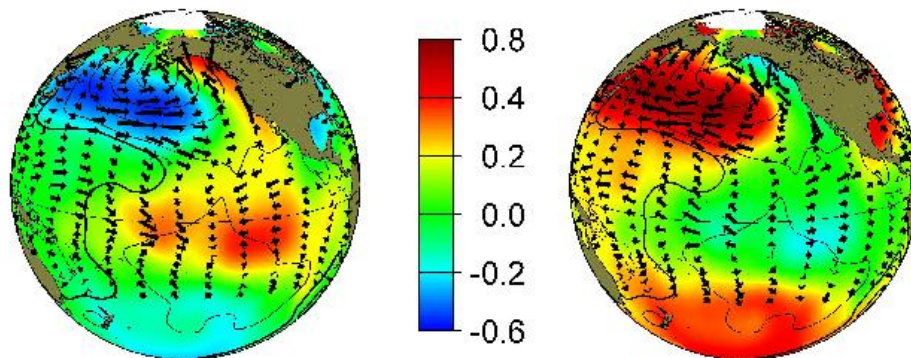


Fig. 1.7 Highlights the warm phase (in the left hand panel) and cold phase (in the right hand panel) of the PDO with temperatures on  $^{\circ}$  Celsius and wind vectors plotted on top. Taken from <http://research.jisao.washington.edu/pdo/>

Recent consensus, resulting from over 15 years of research, shows that the spatial and temporal variability of the PDO is not the result of a single phenomenon but rather a combination of processes (Newman et al., 2016; Wang et al., 2012b). These processes include fluctuations in the strength of the Aleutian low, caused by local variable

weather and remote forcing, resulting in changes to ocean surface heat fluxes and Ekman transport. They also include ocean memory and ‘re-emergence’ of temperature anomalies that, initially formed in the surface, mix downward through the deep winter mixed layer. They remain under the summer seasonal thermocline, insulated from the surface fluxes and ‘re-emerge’ when the mixed layer deepens again (Newman et al., 2016). Climatologically, a warm PDO phase results in dry periods over eastern Australia, Korea, Japan, the far east of Russia, interior of Alaska, central America, and northern South America. The coastal Gulf of Mexico, southwest US and Mexico, southeast Brazil and western Australia also experience wetter conditions in response to a warm PDO phase. It also results in warmer temperatures over northwest of North America, north of South America and northwest Australia and cooler temperatures in China, Korea, Japan and south east North America (Mantua and Hare, 2002). Other studies have suggested a link between the negative phase of the PDO and Arctic amplification, a phenomenon which describes the amplified warming of the Arctic region relative to the global average (Cohen et al., 2014b), with greater sea ice loss in negative PDO years which reduces the poleward gradient of tropospheric thickness leading to pronounced upper-level westerly reductions (Screen and Francis, 2016).

The Pacific-North American pattern has been found to be both a mode of internal variability (Straus and Shukla, 2002) and a large scale wave train that is excited by tropical SST anomalies (Dai et al., 2017), that some authors found was correlated to PDO and ENSO-related SST anomalies (Garfinkel and Hartmann, 2008; Hsieh et al., 2006; Mo et al., 1998), although some authors dispute this (Straus and Shukla, 2002).

The PNA is a mode of low frequency variability, emerging in both rotated and non-rotated empirical orthogonal function (REOF and EOF) analysis (Dai et al., 2017; Feldstein, 2002) and in teleconnection calculations through monthly and seasonally averaged data (Straus and Shukla, 2002; Wallace and Gutzler, 1981), found in mid-to upper tropospheric geopotential height and streamfunction fields (Feldstein, 2002; Straus and Shukla, 2002; Wallace and Gutzler, 1981) in Northern Hemisphere winter. It is a quadrupole pattern that is made up of four centres of action beginning around

Hawaii and moving poleward, following a great circle pathway ending up within the Gulf of Mexico as highlighted in the one point correlation map from Wallace and Gutzler 1981 in figure 1.8 (Palmer, 1988; Wallace and Gutzler, 1981). It is strongest in winter, specifically in February when it attains maximum amplitude (Barnston and Livezey, 1987). The positive PNA is characterised by a deepening of the Aleutian low, which is a region of negative height anomalies in the northeast Pacific, and in its negative phase when the Aleutian low is anomalously weak (Wallace and Gutzler, 1981). It varies on both interannual and interdecadal timescales (Wallace and Gutzler, 1981) although its temporal evolution was found to be around 10 days based on the use of different models, such as a linear-stochastic model and power spectra model, for either geopotential height or streamfunction in the upper troposphere (Cash and Lee, 2001; Feldstein, 2000; Franzke et al., 2011). The growth and maintenance of the PNA has been attributed to a number of different processes; The first is through a Rossby wave train excited through tropical heating in the equatorial Pacific (Hoskins and Karoly, 1981; Sardeshmukh and Hoskins, 1988; Simmons, 1982). The second process finds that the PNA can be triggered through barotropic energy conversion, derived from zonally asymmetric flow (Feldstein, 2002) or by stationary eddy advection that occurs due to a dominant subtropical jet in the north Pacific (Dai et al., 2017; Franzke and Feldstein, 2005). Dai et al. (2017) finds that the growth of the PNA is aided by barotropic amplification due to wave activity fluxes associated with a Eurasian wave train which extends across Europe and Southeast Asia to the central subtropical Pacific, where PNA growth is favoured.

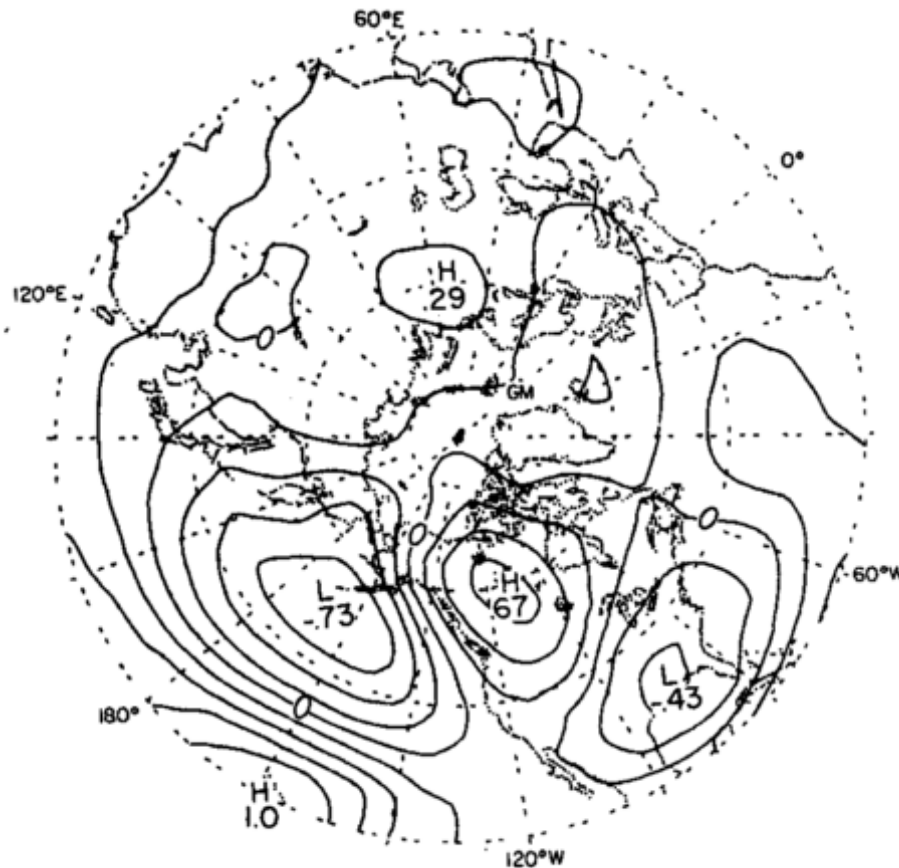


Fig. 1.8 The PNA mode based on a one point correlation map showing correlation coefficients of 500 hPa heights between 20°N and 160°W which results in correlated lower pressure anomaly over the north east Pacific, higher pressure anomaly over the north west of North America and low pressure anomaly in south east North America. Taken from figure 16 of Wallace and Gutzler (1981)

Internally driven teleconnection patterns in the northern hemisphere, particularly in winter, predominately found through empirical orthogonal function (EOF) analysis over a certain domain, display large-scale annular modes of variability (Liu and Alexander, 2007). The largest of these in the northern hemisphere is the Arctic Oscillation (AO) also known as the Northern Annular mode (NAM) (Baldwin and Dunkerton, 1999; Gong et al., 2003; Thompson and Wallace, 2000a,b).

The AO is defined as the leading mode of high latitude sea-level pressure (SLP) variability poleward of 20°N (Fyfe et al., 1999; Thompson and Wallace, 1998). It is a

meridional see-saw or standing oscillation of atmospheric pressure and mass between the central Arctic and mid-latitudes, whereby in the positive phase there is a decreased SLP over the Arctic and increased over the mid-latitudes (Baldwin and Dunkerton, 1999; Holland, 2003). This feature is robust throughout the troposphere as found in geopotential height from 1000 hPa to 30 hPa, which when most active between January to March actually amplifies with height (Thompson and Wallace, 2000a). It dominates intraseasonal and interannual winter SLP variability, and accounts for between 22-25% of temperature variability poleward of 20°N (Ambaum and Hoskins, 2002; Hurrell and Deser, 2010). Thompson and Wallace 1998 found that the 50 hPa and SLP were both strongly correlated, sharing remarkably similar features in surface temperature.

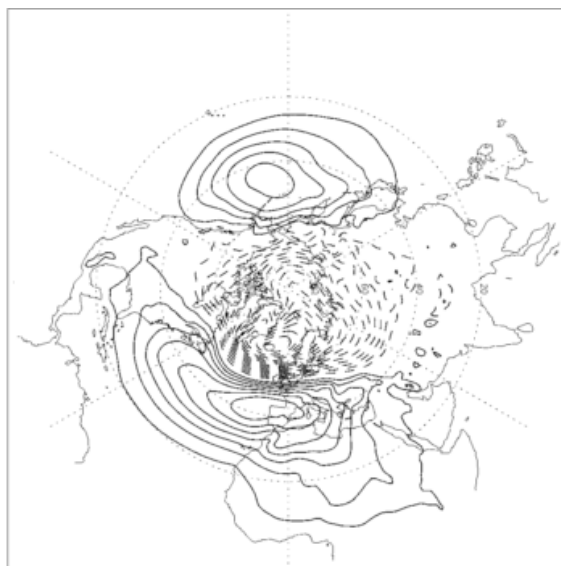


Fig. 1.9 The first EOF of the DJFM mean sea level pressure for the northern hemisphere, with contour intervals every 0.5 hPa, and dashed contours representing negative SLP and solid contours, positive SLP. Taken from Ambaum et al (2001).

During a positive AO phase there are stronger mid-latitude westerlies poleward of around 45°N, of equivalent barotropic structure that amplify with height from the surface to the lower stratosphere, low geopotential heights and temperatures over the polar cap region and anomalously warm mid-latitudes (Thompson and Wallace, 2000a,b, 2001). In its negative phase, the mid-latitude westerlies are anomalously weak and

cold temperatures are still evident with an increase of blocking and cold anticyclonic conditions over central Canada and Russia (Thompson and Wallace, 2001).

The North Atlantic Oscillation (NAO) is a pattern that is similar to the AO with debate ongoing on whether or not the NAO is a regional expression of the larger annual AO pattern (Hurrell and Deser, 2010). Deser (2000), Hurrell and Deser (2010) and Holland (2003) argue that they reflect the same mode of variability, as the AO timeseries is indistinguishable from the NAO. However, Thompson and Wallace (1998) find that the NAO only resembles the AO, while Ambaum et al. (2001) suggest that they are different as, for example, the NAO reflects correlations between surface pressure variability at all centres of action, whereas the AO does not. In spite of this uncertainty of association to the AO, the NAO pattern is a dominant feature of variability over the north Atlantic sector and can be defined as a redistribution of mass between the Arctic and Atlantic, with out of phase height anomalies between the mid- and high-latitudes (Hurrell and Deser, 2010). It accounts for one third or around 35% of the SLP variation over the north Atlantic (Hurrell and Deser, 2010; Moore et al., 2013) with the positive phase being associated with higher than normal surface pressures south of  $55^{\circ}\text{N}$  and anomalous low surface pressure across the Arctic. An index for the NAO measures the SLP difference between the Azores high and Icelandic low (Moore et al., 2013; Osborn, 2011). It is evident all year round (Barnston and Livezey, 1987; Hurrell and Deser, 2010) but the winter NAO index is stronger as a result of a more dynamically active atmosphere that results in peak amplitudes of anomalies. Summer, however, has the weakest NAO index with the centres of action shifted north and eastward relative to winter.

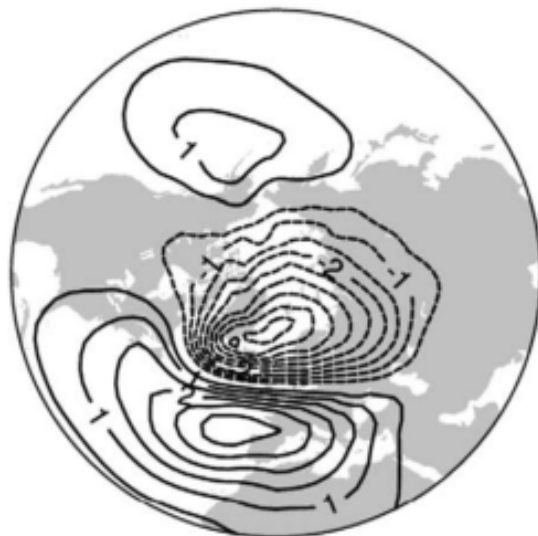


Fig. 1.10 The first empirical orthogonal function (EOF) in the northern Atlantic sector of MSLP for 1899-2006 indicating the NAO, with dashed lines highlighting negative values and solid lines represent positive values. Countour intervals at every 0.5 hPa. Adapted from Hurrell and Deser (2010).

The NAO plays an important role in wintertime temperature in the Northern Hemisphere affecting surface air temperatures in the mid-latitudes and Arctic (Hurrell and Deser, 2010). It affects the strength of the westerly winds and north Atlantic storm intensity and frequency most prominently in Newfoundland and Europe (Hurrell, 1995, 1996; Hurrell and Deser, 2010; Moore et al., 2013). Higher sea level pressures (SLP) over the southern centre of action and lower SLPs over the northern centre of action are found (Moore et al., 2013), resulting in anomalous southerly flow over eastern United States of America and anomalous northerly flow over west Greenland and Canadian Arctic. This results in more precipitation over Europe and north Africa and greater evaporation, relative to precipitation rates over Greenland and Canada (Hurrell, 1995; Hurrell and Deser, 2010; Moore et al., 2013). Furthermore the positive phase of the NAO also affects sea ice within the Arctic in both extent and transport. The meridional extent of sea ice between the Labrador and Greenland seas changes depending on phase such that in the positive NAO phase the Labrador sea has a greater meridional extent of sea ice compared to sea ice extent in the Greenland sea, and vice versa for the negative phase (Hurrell and Deser, 2010). The transport of sea ice out of the Arctic is also affected by

the NAO, mainly in the positive phase, where there was more transport, specifically after 1987, out of the Fram strait due to an anomalous meridional wind component forced due to an eastward position of the NAO centre (Hilmer and Jung, 2000).

As well as the defined teleconnection patterns highlighted above, e.g. the NAO and AO, anomalous large scale waves, usually wave 1 and 2, driven primarily by remote forcing such as anomalous tropical SSTs, have the ability to propagate and impose climate anomalies at high latitudes. Focusing first on the southern high-latitudes, a number of different studies identified teleconnections to this region. Ding et al. (2011) and Schneider et al. (2011) both found teleconnections between the Pacific ocean and warming over West Antarctica in observations due Rossby waves generated from the central Pacific in winter driven by anomalous SSTs which instigated anomalous circulation and warm air advection in to the region. Teleconnections to southern high-latitudes from anomalous Atlantic SSTs have also been found to result in West Antarctic warming. Simpkins et al. (2014), using the NCAR Community Atmosphere Model version 3 (CAM3), found that anomalous SSTs over the Atlantic, specifically in the Caribbean sea, perturbed the zonal Walker circulation resulting which resulted in upper level divergence and induced a poleward flow. This led to an intensification of the Hadley cell branch in the southern hemisphere, which in its descending branch led to convergence and created a rossby wave source in that region. The intensification of this source over time resulted in Rossby wave propagation eastward and promote warming in the West Antarctic.

Arctic teleconnections, borne out of Rossby wave initiation have also been found, however these will be discussed within the Arctic section 1.6.1.

## 1.3 Waves in the atmosphere

Teleconnections patterns, as alluded to above, are generally the result of waves generated in the atmosphere. Waves are quasi-periodic disturbances in time and space that via wave trains, can disperse energy and transfer information downstream, over large distances,

through the oscillation of fluid parcels (Ambrizzi et al., 1995; Holton and Hakim, 2013). Due to a restorative force, which is essential to their existence, they generate sinusoidal like motions. This is wave-dependent, with buoyancy acting as the restorative force for gravity waves and the  $\beta$  effect, which is the variation of the Coriolis force with latitude on a sphere, the restorative force for planetary or Rossby waves (Andrews, 1987, 2010; Holton and Hakim, 2013). Rossby waves, specifically, link seemingly unrelated climate anomalies across large distances and are key components in generating atmospheric teleconnection patterns (Barnston and Livezey, 1987; Ding and Wang, 2005; Liu and Alexander, 2007; Wallace and Gutzler, 1981). These waves are excited through inhomogeneities in the atmosphere which are either driven through a mechanical forcing such as over orography, via flow over regions of thermal contrast (e.g. land/sea contrast), or via anomalous heating of tropical regions which generates tropical convections to excite planetary waves (Ko and Hsu, 2010; Lau, 1979; Simmons, 1982). This thesis focuses on stationary Rossby waves resulting from diabatic heating and therefore the following review of literature will discuss these kinds of waves only.

### 1.3.1 Rossby wave source

Stationary planetary waves are excited through large sustained regions of thermal forcing such as from anomalous seas surface temperatures (SSTs) (Hoskins and Karoly, 1981; Liu and Alexander, 2007; Sardeshmukh and Hoskins, 1985). This anomalous heating source drives convergence at the surface and the adiabatic ascent of air parcels, which forces air to rise. This results in a saturation of the atmospheric column as water vapour condenses, which releases latent heat. Over tropical ocean waters, this process is sustained due to large area of warm SSTs and this constant heat source ultimately drives these processes to generate large-scale convection in the atmospheric column. This process is associated with convective outflow and upper level divergence at the top of the column as can be seen in figure 1.11 (Hoskins and Karoly, 1981; Ko and Hsu, 2010; Liu and Alexander, 2007; Sardeshmukh and Hoskins, 1985). This process will continue until the heating rate can be balanced by the rate of adiabatic cooling as air rises, expands and cools in

the vertical therefore acting as a negative feedback on itself (Sardeshmukh and Hoskins, 1985). Rossby wave sources (RWS) tend to be found poleward of these regions due to the need for a strong meridional gradient of absolute vorticity, in order for there to be an effective source, which does not exist around equatorial regions (Sardeshmukh and Hoskins, 1988; Shimizu and de Albuquerque Cavalcanti, 2010).

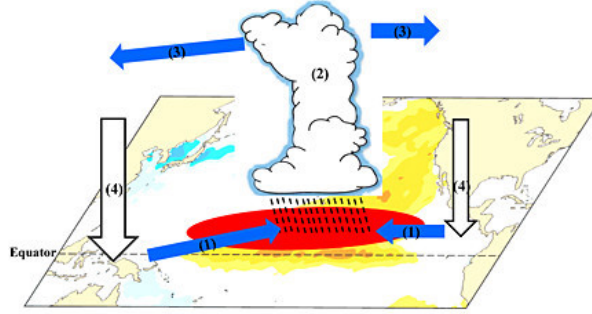


Fig. 1.11 Convection in atmosphere, with [1] convergent winds into the region of the heat source, as depicted by the red circle, [2] large cumulonimbus clouds above the region of warming to depict deep convection and area of greatest precipitation, [3] divergent winds aloft and [4] subsidence of air at either side of the largest region of convection along the equator.

RWSs can be inferred from the barotropic vorticity equation,

$$\frac{\partial \zeta}{\partial t} + \mathbf{v}_\psi \cdot \nabla \zeta = -\zeta D - \mathbf{v}_\chi \cdot \nabla \zeta \quad (1.1)$$

where  $\zeta$  is the absolute vorticity, which is the sum of relative vorticity, more specifically the local vorticity of fluid parcel and planetary vorticity, or Coriolis,  $D$  is the horizontal wind divergence ( $\partial u/\partial x + \partial v/\partial y$ ) and  $\mathbf{v}_\psi$  is the rotational component and  $\mathbf{v}_\chi$  is the divergent component of the horizontal wind velocity  $\mathbf{v}$ . This highlights that Rossby waves will be generated in regions where divergence, divergent outflow of wind, absolute vorticity, and a large gradient of absolute vorticity are found such as that that can be seen over the west Pacific and east Asia (Fig.1.12) (Shimizu and de Albuquerque Cavalcanti, 2010). These variables constitute the Rossby wave source,

$$S = -\mathbf{v}_\chi \cdot \nabla \zeta - \zeta D = -\nabla \cdot (\mathbf{v}_\chi \zeta) \quad (1.2)$$

which demonstrates that diabatic heating, represented by divergence (as diabatic heating results in divergence) (Shimizu and de Albuquerque Cavalcanti, 2010), forces Rossby waves despite the fact the absolute vorticity is small near the region of heating (James, 1994; Shimizu and de Albuquerque Cavalcanti, 2010). This is because absolute vorticity is expelled away from the regions of largest heating due to the divergent component of flow generating a large gradient of absolute vorticity in the subtropics. This means that  $S$  is larger further away from the equator (James, 1994; Sardeshmukh and Hoskins, 1988). Figure 1.12 highlights that RWSs for boreal winter (DJF), using National Centres for Environmental Prediction/National Centre for Atmospheric Research (NCEP/NCAR) reanalysis, are strongest at the subtropics, around  $20^\circ\text{N}$  and  $20^\circ\text{S}$ . The gradient of absolute vorticity is therefore more important than the divergence anomaly in generating Rossby wave sources, as divergence above heating does not necessarily result in a Rossby wave source (Cai and Huang, 2012; Sardeshmukh and Hoskins, 1988; Shimizu and de Albuquerque Cavalcanti, 2010). The contribution of the terms in 1.2 are often divided and analysed separately in order to understand which term contributes most to the overall RWS, with term 1 ( $-\zeta D$ ) representing the vortex stretching term, or generation of vorticity by divergence and term 2 ( $-\mathbf{v}_\chi \cdot \nabla \zeta$ ) is the advection of absolute vorticity by divergent flow (Freitas et al., 2016; Qin and Robinson, 1993; Shimizu and de Albuquerque Cavalcanti, 2010). Qin and Robinson 1993 found that the contribution of the term 1 is more effective at generating extratropical waves than term 2 and Shimizu and de Albuquerque Cavalcanti demonstrated that the contribution of terms to 1.2 changed by seasons over East Asia with term 1 changing signal from positive to negative from DJF (December-February) to JJA (June-August) resulting in a Rossby wave sink in this region in JJA.

The two terms of the Rossby wave source explain it as the rate of change of vorticity due to vortex stretching  $-\zeta D$  and the advection of absolute vorticity  $\mathbf{v}_\chi \cdot \nabla \zeta$  (Scaife et al.,

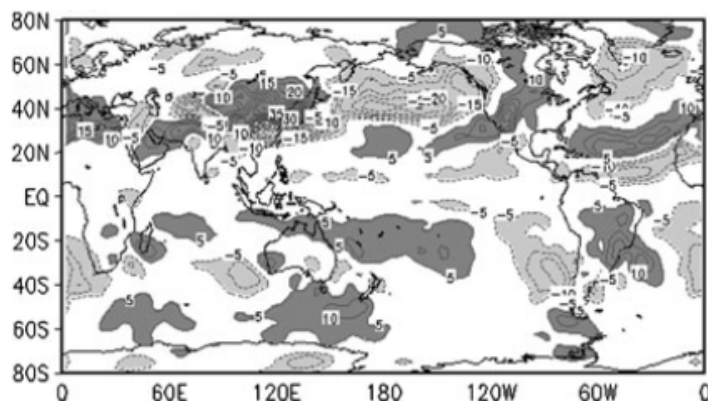


Fig. 1.12 Climatological Rossby wave source between 1979-2007 for DJF. The light shaded area represents positive values and the dark shaded areas represents the negative values. Taken from Shimizu and de Albuquerque Cavalcanti (2010)

2017; Shimizu and de Albuquerque Cavalcanti, 2010). Absolute vorticity is balanced differently between the tropics and extratropics, with the source term in the tropics dominated by the advection of absolute vorticity from divergent flow while a source of Rossby waves in the extratropics is due to vortex stretching (Qin and Robinson, 1993). Seasonally, the contribution of each term can vary, for example, over east Asia the vortex stretching term changes sign from positive in DJF to negative in boreal summer (JJA). This results in a Rossby wave sink in JJA due to the dominance of the advection of absolute vorticity term over the vortex stretching term. Nonetheless, the location and timing of the source is important for regional climate (Freitas et al., 2016) specifically in the ability to generate large stationary planetary waves.

### 1.3.2 Wave propagation

The main signature of Rossby waves are their westward phase propagation, as can be found through its phase speed which is unique from other waves such as acoustic waves which are able to propagate in any direction (Hoskins and James, 2014)

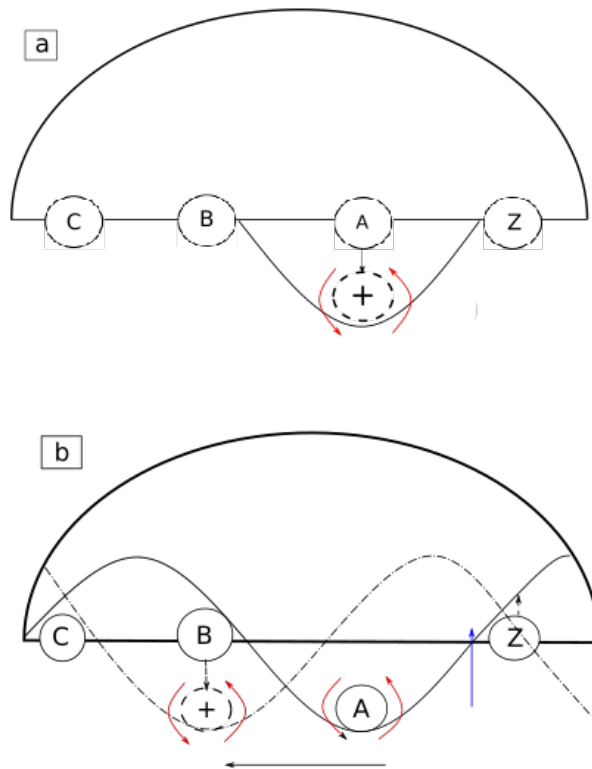


Fig. 1.13 Schematic of westward propagating waves

To explain this, imagine a chain of fluid parcels stretched around a latitude circle in the northern hemisphere (Fig. 1.13 a) with higher absolute vorticity on the poleward side and lower on the equatorward side. This is because absolute vorticity is the sum of relative (local) and planetary vorticity (Coriolis) which is zero at the equator but becomes larger moving polewards. A fluid parcel (A) is displaced equatorward to a region of negative vorticity relative to its equilibrium latitude (Fig. 1.13 b). To conserve absolute vorticity, relative vorticity increases (due to decrease in planetary vorticity) resulting in a cyclonic spin up (anticlockwise flow) of the fluid parcel. This induces a

meridional velocity, which encourages fluid parcel B to move southward, and thus advects the fluid parcel to the west of the vorticity maximum. Subsequently, northward motion is induced ahead of fluid parcel A, which deflects the parcel poleward, across its line of equilibrium latitude, causing it to flow anticyclonically. This results in fluid parcels oscillating back and forth across equilibrium latitude, with a westward phase speed. The gradient of planetary vorticity, the vorticity generated by the rotation of the earth, acts as the restoring forcing for this wave motion and thus provides the mechanism for Rossby waves (Andrews, 2010; Holton and Hakim, 2013; Hoskins and James, 2014; Salby, 2012).

While phase speed of Rossby waves gives westward phase propagation of the wave relative to the background flow, the group velocity, which determines the rate at which information is carried from one part of the fluid to another, of waves of sufficiently long wave lengths is actually carried eastward with the background flow (Hoskins and James, 2014). These quasi-stationary Rossby waves therefore tend to propagate in westerlies and specifically in regions of the strong westerly jet streams such as the Asian and north America waveguides (Ambrizzi et al., 1995; Branstator, 1983; Hoskins and Ambrizzi, 1993). These jets are favourable for propagation due to their zonal wind curvature which gives rise to maximum absolute vorticity making them effective waveguides (Branstator, 1983; Hoskins and Ambrizzi, 1993). Wave propagation in easterlies, however, can occur but only for small scale Rossby waves such as transient or short waves which are reflected to the equator (Branstator, 1983; Lau and Lim, 1984). These waves are therefore trapped at the equator, in other words cannot propagate to higher latitudes, as the jets tend to filter out smaller waves in favour of large waves resulting in their propagation in a poleward direction (Branstator, 1983; Lau and Lim, 1984; Lau, 1979; Qin and Robinson, 1993; Simmons, 1982). Branstator (1983) and Scaife et al. (2017) found that this resulted in an energy split generating two Rossby wave trains, with shorter waves refracted more strongly in the equatorial region and the other that propagated polewards as seen in Rossby ray tracing by Scaife et al. (2017) in figure 1.14.

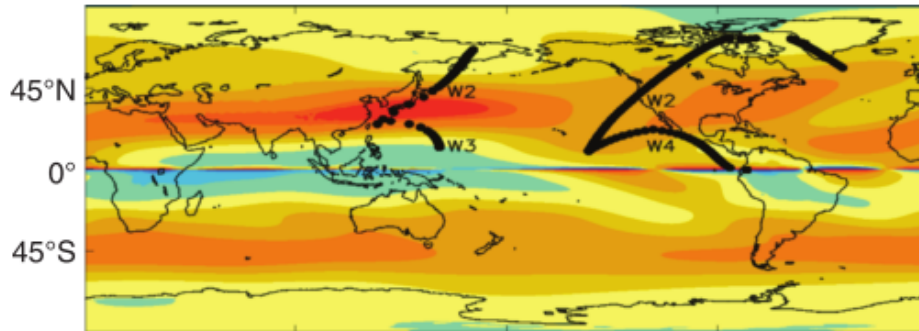


Fig. 1.14 Adapted from figure 10 of Scaife et al. (2017). Shows Rossby wave propagation from two arbitrary locations at 200 hPa with smaller wave numbers propagating poleward and larger wave numbers propagating within equatorial region due to wave refraction of higher wave numbers.

These small scale, equatorially trapped Rossby waves are due to easterlies and weak westerlies which act to damp and decay waves (Branstator, 1983; Lau and Lim, 1984). Wave propagation is also affected by other factors mainly through wave reflection, absorption and refraction. Wave reflection is important as not only does it determine the pathway and resonance of waves, without it mid-latitude waves would either be absorbed by easterlies, generally present around the equator, or propagate between hemispheres (Branstator, 1983). Small and even negative absolute vorticity gradients such as those found on the flanks of a jet act to reflect waves. Critical lines, where the mean zonal wind ( $\bar{U}$ ) tends to zero, also reflect waves (Ambrizzi et al., 1995; Branstator, 1983; Hoskins and Ambrizzi, 1993), although some authors argue that it can also, or solely result in absorption (Lau and Lim, 1984; Matsuno, 1970). These critical lines have been shown to act as a barrier to wave propagation forming between easterlies or weak westerlies as shown by Branstator (1983); Hoskins and Karoly (1981); Lau and Lim (1984). They show that when a wave train propagates towards a critical line, this train would elongate in the east-west direction, become meridional and finally dampen the wave train as the group velocity decreases. Refraction, such as that around the equator or the jets can also affect the flow. A refractive index can indicate if waves are propagating or evanescent, with the latter occurring when the angular velocity is large such as around the jets or for large zonal wave numbers and can damp waves in a dissipative state around weak westerlies, such as near the equator (Branstator, 1983).

### 1.3.3 Calculating waves in the atmosphere

Plumb (1985) derived a measure of wave activity flux (WAF) for linear quasi-geostrophic disturbances on a background flow to understand and describe the flux of stationary planetary wave activity in three-dimensions. It identifies the direction of wave propagation as it is parallel to the group velocity and highlights areas of convergence and divergence indicating a concentration or export of wave activity (McIntosh and Hendon, 2017). Used in Karoly et al. (1989), they highlighted its usefulness as a diagnostic for the horizontal propagation of stationary waves forced by a thermal anomaly. When used to examine northern hemisphere stationary wave patterns they identified a zonal wave over the north Pacific ocean with an equatorward flux over North America which appears to agree with the height anomalies of the PNA pattern and the position of Pacific jet and storm track. In general, they find that the direction of flux agrees well with Rossby wave propagation based on Hoskins and Karoly (1981).

## 1.4 Arctic and north Canada and Greenland

As this research concerns Rossby wave-induced teleconnections to the Arctic, this following section will discuss the climate of the Arctic, detailing the key drivers of Arctic as well as recent changes in Arctic climate.

The Arctic has been defined as the region north of around 66°N (Screen et al., 2012; Serreze and Barry, 2005) and is made up by the Arctic Ocean surrounded by the Eurasian and North American continents. The Arctic ocean covers about 14 million km<sup>2</sup> with landforms in the Arctic region varying between uplands, plains and plateaus and folded mountains such as Canadian Rockies (Huntington et al., 2005). It is dominated by cryospheric processes with sea ice extent that fluctuates annually with its peak in March of  $16 \times 10^6$  km<sup>2</sup> and minima in September of approximately  $7 \times 10^6$  km<sup>2</sup> (Serreze et al., 2007), the Greenland ice sheet which spans approximately 1.7 million square kilometers (National Snow and Ice Data Centre (NSIDC), 2017) and other glaciers and permafrost

which span the region (Serreze and Barry, 2005). It is the interactions between these bodies of ice, landforms, ocean and atmosphere which are fundamental in driving the climate of the region (McBean et al., 2005; Serreze and Barry, 2005).

The main area of interest in this study is over north Canada and Greenland, roughly between 60-88°N and 50-10°E. This region specifically was highlighted by Ding et al. (2014) as having the largest trend in surface temperature from 1979-2012 relative to the rest of the Arctic. Changes in the climate of this region are particularly significant as they are located directly over the Canadian Archipelago and Greenland which has the largest concentration of multi-year ice and the second largest ice sheet on the planet. Previous studies on the Greenland ice sheet have shown how changes of climate have affected the mass balance of the ice sheet (van Angelen et al., 2014). From 2007-2012 compared to 1960-1990, warm air advection from the continental Canada over the ice sheet has resulted in a 2 K warming. This resulted in a decrease of albedo due to the increase in bare ice which is darker than wet snow and surface runoff leading to a decrease in surface mass balance. Climate change is expected to further exacerbate the instability of the ice sheet particularly through changes in supraglacial lakes which are expected to move further inland based on climate change simulations using representative concentration pathways (RCP) 8.5. This is important because if they drain through the ice sheet, they can result in basal melting, from the relatively warm water, add lubrication to the underside of the ice sheet and increase the potential for ice sheet flow from further inland (Leeson et al., 2015). Therefore it is paramount to understand drivers of the climate of the Arctic and how they affect the climate of Arctic. The following section addresses the main drivers of climate, including some of the most recent rapid changes that have occurred in the Arctic putting further importance on the need to understand the key Arctic drivers.

## 1.5 Arctic climate

Arctic climate is marked by large spatiotemporal variability due to the spatial distribution of different landforms and seas across the Arctic. It is also seasonally varying through changes of incoming solar radiation that varies between 24 hours daylight in summer to no daylight in boreal winter. Temperature fluctuates quite extensively over space and time within the Arctic. January temperatures can range between  $-40^{\circ}\text{C}$  in parts of Siberia to between  $-25^{\circ}\text{C}$  to  $-32^{\circ}\text{C}$  over the central Arctic, due to the modulation of heat flux from lead and polyna formation, and even reaching freezing point around Iceland due to warm water and heat transports from the north Atlantic. Mid-summer Arctic temperatures can range between  $0$  to  $20^{\circ}\text{C}$ , with freezing point temperatures expected in the central Arctic ocean, as a result of melting, and higher temperatures expected over snow-free land surfaces (Serreze and Barry, 2005). Spatially, precipitation in the Arctic is also highly variable where, based on rain-gauge data, precipitation minima occurs in April and maximum in July, although with bias corrected precipitation this has been found to be September (Yang, 1999). Spatially, precipitation can vary between 200 mm over the Canadian Archipelago to over 1000 mm in the Atlantic sector. However, there are problems in finding accurate measurements of precipitation primarily due to the lack of observing stations over the Arctic and also inaccuracies in satellite data (Serreze and Barry, 2005).

Internal modes of variability such as the NAO and AO, as mentioned previously, also contribute to the variability of the climate over the Arctic. A negative NAO index is associated with a positive mean sea level pressure and anticyclonic circulation over the central Arctic with the opposite effect for a positive NAO index (Venegas and Mysak, 2000). It also dominates winter time temperature over much of the Northern Hemisphere where, a positive NAO index results in warm and wet conditions over north Europe and cold conditions over the western Atlantic (Bader et al., 2011). A positive AO index results in, on average, warmer conditions over central Canada, Europe and throughout the Barents and Kara Seas with a negative AO index results in more cold outbreaks over Russia, North America and parts of Europe (Thompson and Wallace, 2001).

### 1.5.1 Local and remote drivers of climate

The Arctic climate is driven by local processes such as through interactions between ocean-cryosphere-atmosphere or from remote regions. Changes in these parameters, specifically in sea-ice, can and have resulted in large changes in Arctic climate, namely at the surface. The Arctic has been warming twice as fast as the global average (Cohen et al., 2014b; Screen and Simmonds, 2010b; Serreze and Francis, 2006) with linear trends of surface air temperature from 1979-2014 over the Arctic ( $70^{\circ}$  -  $80^{\circ}$ N) at  $0.86^{\circ}\text{C}$  per decade compared to  $0.3^{\circ}\text{C}$  per decade over lower latitudes ( $30^{\circ}$  -  $40^{\circ}$ N) (Screen, 2014) (Screen and Simmonds, 2010b; Serreze et al., 2009; Serreze and Francis, 2006). This ratio of greater Arctic warming relative to the global mean is known as Arctic Amplification (Haine and Martin, 2017; Screen, 2014). It is apparent in all months over the last 21 years (Screen and Simmonds, 2010a; Serreze and Francis, 2006), but is most prevalent in autumn and early winter particularly at the surface, (Deser et al., 2010; Screen et al., 2012; Screen and Simmonds, 2010a,b; Serreze et al., 2009; Serreze and Francis, 2006), consistent with changes in reduced sea ice cover (Screen and Simmonds, 2010a,c; Serreze et al., 2009). It is therefore found that changes in sea ice are thought of as the main contributor of surface warming in autumn and winter. These changes in Arctic sea ice are viewed to be as the direct result of increased greenhouse warming (Screen et al., 2015; Stroeve et al., 2012) and thus an anthropogenic climate change impact. Sea ice trends over the Arctic, specifically in summer and early autumn months have been rapidly declining at rate of approximately  $13.3\%$  decade<sup>-1</sup> relative to the 1981-2010 period which equates to ice loss trends of approximately  $86,000\text{ km}^{-2}\text{ yr}^{-1}$  (Serreze and Stroeve, 2015). This trend has increased in the the last number of decades whereby seven of the lowest sea ice years occurred in the last ten years with 2012 and 2007 the lowest and second lowest years of sea ice extent at  $3.4 \times 10^6\text{ km}^2$  and  $4.1 \times 10^6\text{ km}^2$ , respectively (Comiso et al., 2008; Parkinson and Comiso, 2013). Most of this sea ice loss is found to be within the Kara, Barents, Chukchi, Beaufort and Laptev seas (Devasthale et al., 2013; Liu et al., 2004; Stroeve et al., 2014). Sea ice has also been found to be thinning as multi-year ice extent and area in winters between 1979-2011 declined at a greater rate of  $-15.1\%$  decade<sup>-1</sup> and  $-17.2\%$  decade<sup>-1</sup> compared to perennial, single year sea ice extent and area

which declined at a rate of  $-12.2\%$  decade<sup>-1</sup> and  $-13.5\%$  decade<sup>-1</sup> respectively. This is important as it indicates that as the average thickness of sea ice declines, which can also be indicative of ice volume, it is more susceptible to melting each summer and returning as perennial sea ice only which is thinner than multi-year ice (Comiso, 2012). Furthermore, the melt season is also lengthening by approximately five days decade<sup>-1</sup> from 1979 to 2013, dominated especially by the later autumn freezeup of the Kara, Laptev, Beaufort and Chukchi seas by between 6 and 11 days decade<sup>-1</sup> (Stroeve et al., 2014).

The loss of this sea ice affects the Arctic temperature through two mechanisms. The first, identified by Screen and Simmonds (2010a), named the insulation mechanism. This shows that surface warming is due in part to the removal of winter sea ice which acts as an insulator between relatively warm water in the upper regions of the ocean and the cold surface air temperature. As sea ice begins to melt this results in a transfer of heat to the atmosphere. The second mechanism, much more widely discussed by different authors is based on the ice-albedo feedback and is found to be the largest contributor of surface warming in the Arctic in autumn and winter (Chung and Räisänen, 2011; Screen and Simmonds, 2010a,b; Serreze and Francis, 2006). This mechanism is due to a reduced sea ice extent in summer and early autumn months. This results in a strong atmosphere to ocean heat flux and warming of the upper ocean which can lead to a warming of approximately  $0.5\text{-}1.5^{\circ}\text{C}$  as the result of an energy flux of approximately  $752\text{ MJm}^{-2}$  (Stroeve et al., 2014). This will lead to further sea ice melt, approximately between 0.97 and 1.3 m based on Stroeve et al. (2014), allowing for more solar absorption of the oceans thus reducing albedo even further (Screen et al., 2012; Screen and Simmonds, 2010b; Serreze and Francis, 2006). During autumn and early winter, this excess heat in the ocean will be released to the atmosphere which may contribute to the delayed refreezing and therefore longer melt season as found by Stroeve et al. (2014).

This flux between the ocean and atmosphere is found to be the main mechanism by which the Arctic surface warms (Deser et al., 2010). As shown in figure 2 in Screen and Simmonds (2010a) and here also in figure 1.15, regions of largest surface turbulent heat flux (1.15 c), derived through sensible (1.15 d) and latent (1.15 e) heat flux in the Kara, Barents, Chukchi and Beaufort seas appear spatially collocated with the regions

of greatest sea ice loss in figure 1.15 b, where darker blue contours highlight sea ice loss. Compared to surface air temperature (Fig. 1.15 a) these regions also show the greatest trends in warming of approximately  $1.1 \text{ K decade}^{-1}$  for the Barents and Kara seas and  $0.9 \text{ K decade}^{-1}$  for Chukchi and Beaufort seas (Liu et al., 2009), thus highlighting that sea ice loss and subsequent turbulent heat flux between the ocean and atmosphere is the main driver of surface Arctic warming.

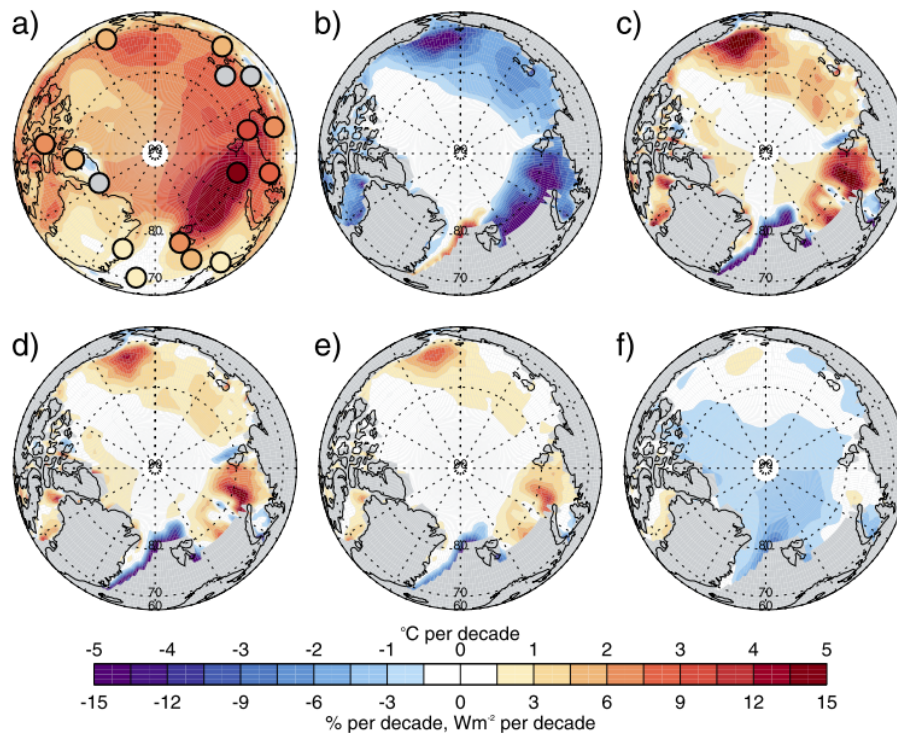


Fig. 1.15 Trends from October to January 1989-2009 for [a] for Surface air temperature in  $^{\circ}\text{C decade}^{-1}$  from observations, [b] sea ice concentration ( $\% \text{ decade}^{-1}$ ) from ERA-Interim, [c] surface turbulent fluxes (sensible plus latent) ( $\text{W m}^{-2}$ ), [d] surface sensible heat flux ( $\text{W m}^{-2}$ ), [e] surface latent heat flux ( $\text{W m}^{-2}$ ) and [f] net surface outgoing long wave radiation. Adapted from Screen and Simmonds (2010a).

Alongside affecting surface temperature, Arctic sea ice loss has also been found to play a role in current and future circulation changes over the Arctic. Higgins and Cassano (2009) found that geopotential height at 1000 hPa was reduced over the Arctic due to increased cyclones in to the region. Deser et al. (2010) found that in response to sea ice loss for the period 2080-2099, sea level pressure (SLP) anomalies over the Arctic, Bering

Sea and northeast Canada were negative in early winter and became negligible in mid winter over the Arctic.

Cloud cover has also been attributed as contributing to the large trend of surface air temperatures over the Arctic. Liu et al. (2009) found that the cloud cover accounted for the  $0.55\text{K decade}^{-1}$  out of the  $1.0\text{ K decade}^{-1}$  of spring warming. Screen and Simmonds (2010b), conversely, found that clouds had very little effect of surface temperature trends. The influences of clouds on Arctic climate, however, are difficult to completely obtain as Screen et al. (2012) found that cloud trends were very noisy and thus a clear signal was hard to obtain.

Part of the surface and mid-tropospheric warming have also been attributed to poleward heat transports from more remote regions. Poleward heat transports have been found to result in warming and moistening of the Arctic troposphere such as in response to a uniform and tropical radiative forcing of  $4\text{ Wm}^{-2}$ , the equivalent of  $2\times\text{CO}_2$  over an aqua-planet (Alexeev et al., 2005). Graversen (2006) found that these large net energy transports across  $60^\circ\text{N}$  result in Arctic warming five days later with conversely small net energy transports across  $60^\circ\text{N}$  followed by cooling five days later. Graversen later found (2009) that most of this warming is concentrated in the mid-troposphere, well above the surface, however, the details of this study are somewhat disputed as the results are based on European Centre for Medium Range Forecasts (ECMWF) ERA-40 reanalysis dataset. Other studies have shown how ERA-40 has a warm bias in the upper troposphere in the Arctic and thus results based on this such as Graversen (2009) have an exaggerated warming and therefore potentially skewed results (Screen and Simmonds, 2010a,b, 2011).

Remote sea surface temperatures have been found to be a main driver of upper atmosphere warming with a specific peak at 500-600 hPa and can also contribute to some surface warming (Screen et al., 2012). Through running a series of model experiments, Screen et al. (2012) found that remote SSTs resulted in nearly all of the warming found in the upper troposphere, as well as approximately one quarter of the simulated and one fifth of the observed Arctic surface warming. The influences of remote sources and specifically SST changes are further investigated by Lee (2012 and 2014) and the

Tropically Excited Arctic warming Mechanism (TEAM). In these studies, she explains how tropical conditions which result in a small concentrated warm pool, such as during a La-Niña, lead to greater tropical convection, exciting large-scale Rossby waves which propagate polewards and result in a warming over the Kara and Barents sea regions and central Arctic while conversely the El-Niño results in a cooling within these regions.

This mechanism of tropical convection driving large poleward propagating waves, are identified by Trenberth et al. (2014) and Ding et al. (2014). Trenberth et al (2014) found that tropical SSTs over the central and west Pacific resulted in Rossby waves in NDJFM that followed a great circle route, as identified in wave theory, altering storm tracks and meridional heat and momentum fluxes. Ding et al. (2014) found a similar pattern of wave trends in observations where waves emanating from the central tropical Pacific followed a great circle path and propagated over north Canada and Greenland. This resulted in anomalous positive annual trends in geopotential height at 200 hPa (Z200) and surface and mid-troposphere warming. They also found similar results in an ensemble model sensitivity study, based on climate model ECHAM4.6 forced with observed transient tropical SSTs from 1979-2012 between 30°N and 30°S, with extratropical SSTs coupled to a slab ocean and a thermodynamic sea ice component. Calculating wave trends based on the wave activity flux derived by Plumb (1985), they found that this was also due to a wave train that emanated from the east Pacific and propagated over North America and on to north Canada and Greenland. This wave train differed from the observations but they attributed this difference to be the result of the different physical set up of the model compared to that of the ECMWF ERA-Interim reanalysis dataset.

## 1.6 Motivations and Aims

This thesis aims to assess and quantify circulation trends over north Canada and Greenland (NCG) and to understand how circulation over this region changes in response to tropical SST forcing.

This study was motivated by a paper published by Ding et al. (2014) who, using ERA-Interim reanalysis data, found that positive trends of surface and mid-troposphere temperature and geopotential height over north Canada and Greenland, between 1979 and 2012, were the result of tropically excited Rossby waves generated from the tropical Pacific. Similar trends were found in a number of model ensemble experiments conducted using ECHAM 4.6, forced with observed transient tropical SSTs between 30°N and 30°S, a thermodynamic sea ice component and extratropical atmosphere coupled to a slab ocean. While Ding et al., (2014) also attributed these modelled trends to a wave train from the tropical Pacific, it, however, did not share much resemblance to the wave train generated by the ERA-Interim reanalysis data.

This indicates that current understanding and knowledge of the tropical influences on climate over north Canada and Greenland are still not well understood, or well represented in models. Furthermore, the model set up used by Ding et al., (2014) may have allowed for the influences of more remote influences such as sea ice or extratropical SSTs, which were not prescribed, to have potentially played a role in the positive trends over north Canada and Greenland.

This study, therefore, aims to address this lack of knowledge and understanding on how the tropics influence the circulation patterns over north Canada and Greenland and to propose a mechanism for this influence. This will be conducted using a number of model experiments using HadGEM3-A and based on an imposed tropical SST perturbation only, with all other variables such as sea ice or CO<sub>2</sub> fixed.

To direct the research, a number of questions were proposed to aid the understanding of how the tropical regions can affect the circulation over north Canada and Greenland

1. How robust are the strength of the trends over NCG?

This will assess whether the positive circulation trends over north Canada and Greenland are found in other climate records and determine the variability of trends within this region.

2. Can the tropical regions influence atmospheric circulation over NCG and how has the circulation of NCG responded to imposed SST perturbations in the tropics?

This will assess whether observed circulation trends are influenced by tropical SST perturbations and how and why circulation changes in response to a tropical forcing.

3. What are the relative contributions of each of the tropical ocean basins: the Pacific, Atlantic and Indian; on the circulation over the NCG region?

To assess if the response was due to only one ocean basin or if it was due to a combination of all or if there were some non-linearities in the model to generate the circulation response.

4. Do extratropical SSTs have an important different effect on the NCG circulation pattern?

This is to assess if extratropical SSTs play a more important or any role in generating circulation changes in the NCG region similar to the observations, relative to the tropical only forcing.

# Chapter 2

## Data, Model and Methods

Assessing circulation trends over the north Canada and Greenland region (NCG) and their sensitivity to tropical sea surface temperature (SST) perturbations requires analysis of both observation based climate records and atmospheric general circulation models (AGCMs). For this study, ERA-Interim Reanalysis is used and GCM performance in capturing these conditions is evaluated using UPSCALE and AMIP models. Additionally a suite of model sensitivity experiments are performed based on the Unified Model (UM) developed by the UK Met Office to test the sensitivity of the circulation over the NCG region response to different tropical SST perturbations. This chapter describes these datasets in detail along with the model set up and experiment design. It also details some analytical tools used in this study and also validates the model, to check for any biases and ensure it represents the large scale circulation in a comparable way to ERA-Interim Reanalysis.

## 2.1 Existing climate and model records

### 2.1.1 ERA-Interim Reanalysis

ERA-Interim reanalysis (ERA-Interim) is the most recent reanalysis dataset produced by the European Centre for Medium Range Weather Forecasts (ECMWF). Produced through the fully coupled atmosphere, ocean and land ECMWF forecasting system, it spans from 1979 to present day producing 3- and 6-hourly surface and atmospheric parameters for both the troposphere and stratosphere (Dee et al., 2011; Simmons et al., 2014). It has a horizontal grid resolution of around 80km and 60 vertical levels ranging from around 10m to 0.1 hPa. Using an assimilating model at a higher resolution (T255 to T159) and 12-hourly four-dimensional variation assimilation (4D-Var), ERA-Interim is an improvement from ERA-40, its predecessor, as it results in a better representation of the hydrological cycle, stratospheric circulation and bias correction of satellite radiance data (Dee et al., 2011; Simmons and Poli, 2014; Simmons et al., 2014, 2010). It has also been shown to have improved fits to Arctic radiosonde data, relative to ERA-40 (Simmons and Poli, 2014) and can better account for biases that change in time as a result of changes in the observational network as well as decay or drift of satellites (Screen and Simmons, 2010c).

ERA-Interim initially used sea-surface temperature (SST) data and sea-ice concentration analysis from ERA-40 until 2001 which comprised of the HadISST dataset produced by the Met Office and NOAA/NCEP 2D-Var data (Uppala et al., 2005). ECMWF operational data was then used from 2001 until 2009 and after which used Operational Sea Surface Temperature and Sea Ice Analysis data (OSTIA) as the source of SST and sea-ice data. The change in sources of SST and sea-ice data has resulted in some errors in the data with SSTs found to be 0.1 K cooler from 2002 onwards and surface cooling in regions in the Arctic due to increased sea-ice concentrations (Simmons and Poli, 2014).

In spite of a few systematic errors, many studies have shown that ERA-Interim is one of the best reanalysis tools to use for studying Arctic weather and climate (Lindsay et al., 2014;

Screen and Simmonds, 2010a,b; Simmons and Poli, 2014), particularly in comparison to ERA-40 which was found to be colder than ERA-Interim due to its cold biases. Furthermore Screen and Simmonds (2011) found that in comparison to satellite data, ERA-Interim has more realistic temperature trends than ERA-40. They also highlight that the use of ERA-40 data in other studies, namely Graversen et al. (2008), who found a large warming in the mid-troposphere, are exaggerated due to warm biases in ERA-40 post 1997.

Therefore, ERAI was chosen as the main dataset to take the role as ‘observations’ in lieu of actual observations for the Arctic, which are not spatially or temporally coherent or complete, due to for example lack of observational stations in the Arctic. Reanalysis data also provides a much more spatially and temporally complete and consistent record of global atmospheric circulation (Dee et al., 2011). Furthermore it is also used to validate the model used in this study, to ascertain model skill in accurate climate simulation.

### 2.1.2 UPSCALE

The UPSCALE (UK on Prace: Weather-resolving Simulations of Climate for globAL Environmental risk) project is a 13-member ensemble run of global climate simulations based on HadGEM3 atmosphere only model (Hadley Centre Global Environmental Model 3), Global Land 3 (GL3) configurations of MetUM and Joint UK Land Environmental Simulator (JULES) (Mizielinski et al., 2014). The model was run with 85 hybrid height levels in the vertical at three different horizontal resolutions divided across the different members; with five ensemble members at N96 (130km) resolution, three at N216 (60km) resolution and five at N512 (25km) resolution. The climate runs were forced with daily SST and sea-ice forcings from OSTIA of  $1/20^\circ$  resolution covering 27 years from 1985 to 2011 (Donlon et al., 2012). Other boundary conditions such as CO<sub>2</sub>, methane, nitrous oxide, CFC and HCFC concentrations were allowed to vary through time following observations. Initial conditions for the N512 simulations were based on a five-year spin up from an N320 (40km) resolution restart file that was produced as part of the

HadGEM3 development process while initial conditions for N216 and N96 were obtained by regridding N512 restart files (Mizielinski et al., 2014).

UPSCALE is used in this study to assess circulation trends over NCG and specifically to test the robustness of these trends relative to ERAI. Since each experiment consists of multiple ensemble members, it will also highlight variability and spread of trends over NCG across the ensemble members and help detect robust signals. Finally as it uses HadGEM3-A it can also provide some comparison to model results while also further validating the model ability to accurately simulate trends over the Arctic, thus providing further confidence in results from modelled experiments.

### **2.1.3 CMIP5/AMIP**

The Coupled Model Intercomparison Project 5 (CMIP5) was designed to provide updated climate and climate change estimates in support of the IPCC Fifth Assessment Report (AR5). The Atmospheric Model Intercomparison Project (AMIP), is run as part of CMIP5 to provide a comprehensive evaluation, validation and comparison of the performance of atmospheric global climate models (AGCM). AMIP is forced with monthly mean SSTs and sea ice concentration between 1979 to 2005, run on both seasonal and interannual timescales (Gates and Gates, 1992; Taylor et al., 2012).

AMIP is specifically used as models within this are atmosphere-only and so will be more comparable to results from UPSCALE than models in the coupled CMIP5 runs. Its use in this study is similar to UPSCALE, in that it is used to assess the robustness of circulation trends over NCG relative to ERAI and to provide an inter-model comparison of circulation trends in models forced with the same observed SST, sea-ice and greenhouse gas emissions.

## 2.2 Model set-up, design and experiments

Current records of reliable, spatially and temporally coherent climate data are relatively short, which limits their use for evaluating climate variability and trends and attributing them to specific drivers. ERAI, for example only provides 37 years of data starting from 1979, which is not long enough to fully account for decadal scale climate variability and makes it challenging to attribute any changes to specific forced or unforced mechanism. Climate sensitivities and interactions also cannot be fully vetted in observations as there are many drivers and feedbacks within the system that may mask the role a specific factor has in the climate system. Climate models are therefore useful tools as they can be run for longer periods and can include or exclude individual drivers to isolate the roles of specific factors for simulated changes.

Climate models are based on a set mathematical equations whose solutions are discrete in space and time that describe as far as possible the behaviour of the climate system (Kiehl, 2006). While based on the same governing equations, all climate models will be slightly different due to differences in their dynamical core, discretizations and physical parameterisations used. Throughout this study the Unified Model (UM), which is developed and maintained by the UK Met Office, for both low and high resolution numerical weather prediction (NWP) (Davies et al., 2005), is used. Here the UM is used at version 8.4, specifically at the particular configuration of HadGEM3 for atmosphere only, at N96 resolution (130 km) at  $1.25^\circ$  latitude by  $1.875^\circ$  longitude at 38 vertical levels (Hewitt et al., 2011) is used. Below, the dynamical core of the model as well as the vertical and horizontal grids used are described and a brief overview is given of some of the parameterisations scheme that are important in the model.

### 2.2.1 The UM dynamical Core

The model core is the dynamical element of the model that resolves large scale flow on the underlying grid in a discretized manner. The UM currently employs the use of the

ENDGame dynamical core (Even Newer Dynamics for General atmospheric modelling of the environment), which is an evolution of New Dynamics (ND) core. ENDGame has inherited most of the important features of ND, such as solving a vast number of equations quickly, an important feature of all General Circulation Models (GCMs), but provides several improvements to ND such that it has obtained more detail in features such as cyclones and jet stream wind and through improved scalability has allowed an increase in resolution to global weather forecasts and thus improvements to forecast accuracy (Mayne et al., 2014).

The model is fully-compressible and non-hydrostatic, which results in a good treatment of smaller scale processes and of the non-linear behaviours of equations (Davies et al., 2005; Saito et al., 2007). It is based on a regular latitude-longitude grid, where meridians converge at the poles meaning that  $u$  is held at the poles and therefore has to be diagnosed from  $v$  at the latitude immediately surrounding it. This model is spatially discretized using Arakawa C-grid staggering (Fig 2.1) in the horizontal, which staggers the zonal and meridional wind components so that  $u$  and  $v$  velocities are centrally derived between edges of each grid cell (Collins et al., 2013; Martin et al., 2006) and mass-related variables such as pressure and temperature are derived at the centre. The vertical grid is height based and terrain-following (Hewitt et al., 2011) and is based on Charney-Phillips staggering (Fig 2.2) as it produces better balanced flows which in combination with Arakawa C results in a better representation of the dispersion properties of gravity waves.

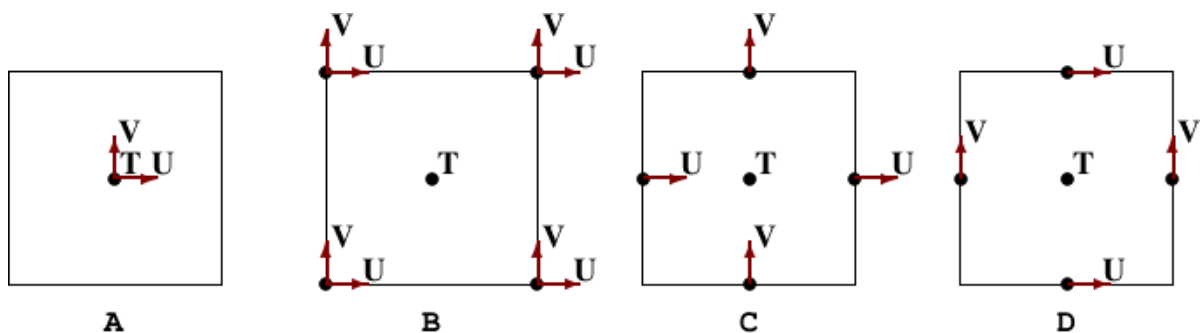


Fig. 2.1 Examples of all Arakawa staggered grids showing where difference variables are derived. Taken from <https://www.gfdl.noaa.gov/vb/gridstd/gridstdse2.html>

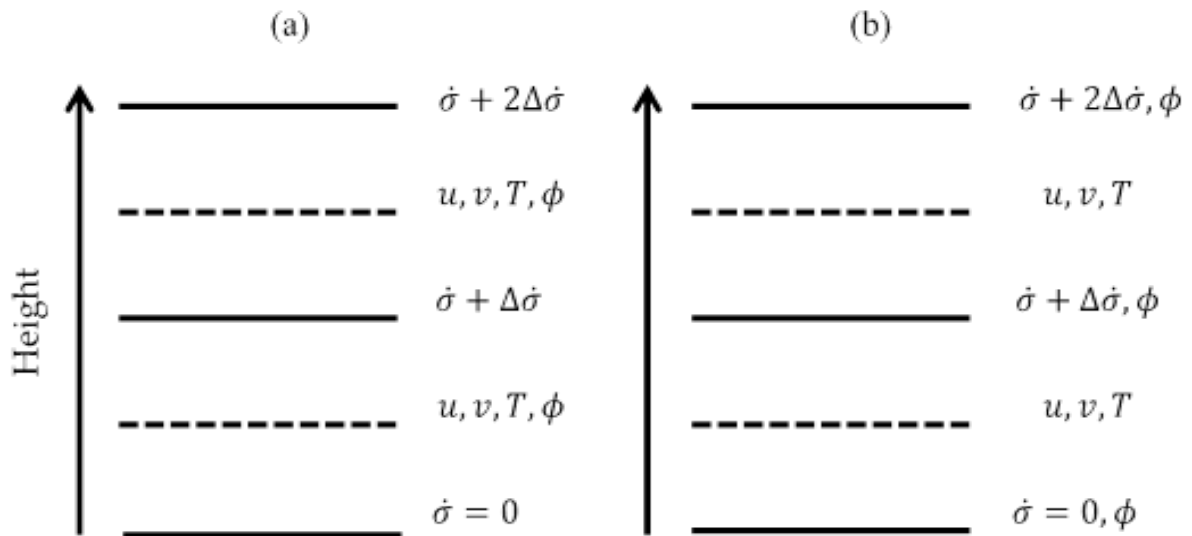


Fig. 2.2 Vertical staggered grids of [a] Lorenz and [b] Charney-Phillips (Collins et al. 2013 of *Climate Change and Regionsl/Local responses* edited by Zhang and Ray 2013)

The model core uses a semi-implicit semi-Lagrangian advection scheme. The semi-implicit scheme allows the model to take longer time steps, approximately by around a factor of six (Staniforth and Cote, 1991) with only a small increase in the number of computations needed per time step (Robert et al., 1985). It also doesn't degrade the accuracy of the solution (Staniforth and Cote, 1991) thus improving the efficiency of the model. The semi-Lagrangian component of this scheme aims to make use of both Eulerian and Lagrangian schemes whereby gaining the regular resolution of the Eulerian schemes with the enhanced stability of Lagrangian ones (Staniforth and Cote, 1991). It also offers the ability to take longer time steps without a loss of accuracy (Hewitt et al., 2011). The use of semi-implicit semi-Lagrangian together results in a time truncation error that is of the same order as the spatial truncation error (Staniforth and Cote, 1991). The continuity equation is treated in a Eulerian manner as most semi-Lagrangian schemes are generally non-conservative of mass and species in the absence of sources and sinks

## 2.2.2 Parametrisation schemes

Models are representations of a system that one is aiming to simulate however, certain elements of that system, particularly in the climate, are extremely complex, occur on very small scales and are generally still not fully understood so therefore cannot be explicitly resolved by the model. Therefore these processes need to be parametrised to ensure that their bulk effect on the system are still included to ensure an accurate representation of the climate. Some of the parameters which are most significant in this work are highlighted below.

Radiation within the model is based on Edwards and Slingo (1996) and has improved pressure and temperature scaling relative to the older version of the model, HadGEM1. This improves the performance of the ‘high-top’ model considerably, as there is a better representation of longwave fluxes travelling through the stratosphere where pressures are relatively low (Hewitt et al., 2011).

The convection scheme is similar to HadGEM1, which is based on the mass-flux scheme of Gregory and Rowntree (1990), is triggered from lifting condensation level to parameterize upward transports from the cloud base (Martin et al., 2006). HadGEM3-A has added improvements in, for example, the detrainment of the convective plume, meaning air can be detrained out during parcel ascent maintaining parcel buoyancy, so parcels can reach higher in the atmosphere. Using a two hour convective available potential energy (CAPE) closure scheme based on vertical wind speed, it specifies the time over which it will try and dissipate CAPE through adjusting the updraught mass flux in to the base of the convective column. Further improvements include representation of water content for shallow clouds as a function of precipitation and shallow convection (Hewitt et al., 2011).

The cloud scheme uses Prognostic Cloud Prognostic Condensate (PC2) scheme as described by Wilson et al. (2008) which makes it possible for clouds to slowly evolve throughout the model run as it allows variables like liquid water cloud fraction and liquid water condensate amount to be retained between timesteps. This therefore more

accurately simulates the generation, increase, decrease and destruction of clouds, allowing longer retention of cloud and improving cloud cover and precipitation (Hewitt et al., 2011).

## 2.3 HadISST

The Hadley Centre Sea Ice and Sea Surface Temperature (HadISST) is a complete monthly global SST and sea-ice concentration dataset based on a  $1^\circ$  latitude-longitude grid spanning from 1871 to present day. The SST data for 1871-1981 are based on analysis of gridded, quality-controlled in situ SST observations which include data, for example, from individual ship observations from the Met Office Marine Data Bank (MDB), which were bias corrected due to the use of bucket samples. From 1982 onwards, data came from the satellites specifically from the Advanced Very High-Resolution Radiometer (AVHRR) which are  $1^\circ$  area monthly observation estimates for day and night (Rayner et al., 2003).

HadISST uses a number of different sea ice concentration datasets, which were homogenised in time using satellite microwave-based sea ice concentrations. Both these data sets are combined through a series of statistical relationships in order to make globally complete SST fields (Rayner et al., 2003).

SST and sea-ice data from HadISST, specifically that between 1979-1988 and 2003-2012, is used to force the UM experiments in this study and its use will be further discussed in the following section.

## 2.4 Model Experiments

Addressing the aims and objectives outlined in chapter 1, regarding isolating the influence of tropical regions on climate in north Canada and Greenland, a number of time slice,

sensitivity experiments were designed. These include a control model experiment and a number of perturbation model experiments each run for a period of 59 years. In total, only the last 58 years of each experiment are actually analysed to allow for model ‘spin-up’. As seen in figure 2.3, which shows the timeseries of the annual mean of outgoing longwave radiation (OLR) for the control model experiment, it was not until year three that a model equilibrium was reached following a rapid incline in OLR in years one and two. Only sea-surface temperatures and sea-ice fields, based on HadISST, are used to force the perturbation experiments, all other forcings such as CO<sub>2</sub>, solar forcing and aerosol changes are kept fixed as in the control model experiment to allow the effect of the anomalous SSTs imposed to be separated in each of the model experiments (described in more detail below). Overall, a total of seven model experiments were designed, including the control and seven perturbation experiments. The experimental design for each case is stipulated below.

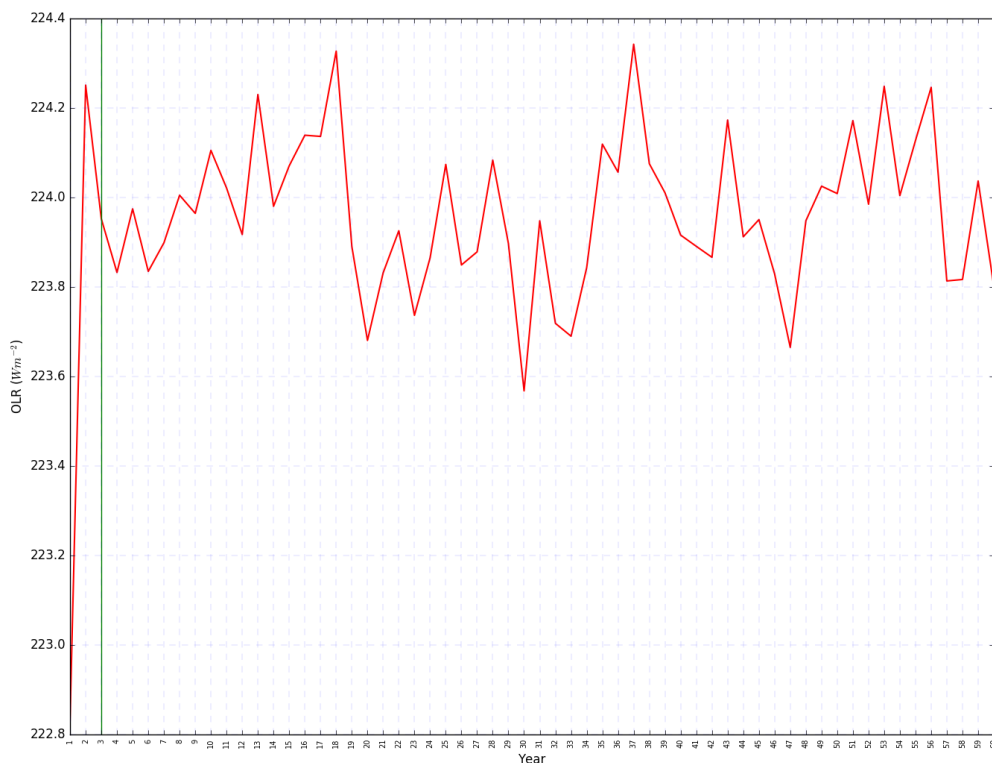


Fig. 2.3 Annual, globally meaned OLR timeseries for the control model experiment

### 2.4.1 Control model run

The first model experiment was designed as a reference state which the perturbed model experiments are compared to, to assess the impact that a tropical SST perturbation has on Arctic climate. The control run is forced with monthly averaged SST and sea ice data from a ten year climatology over the period 1979-1988 repeated every year of the model simulation.

### 2.4.2 Perturbed model runs

#### 2.4.2.1 OneSST model experiment

The first perturbed model experiment designed, OneSST, forces the model, relative to the control, with anomalous tropical SSTs (defined here as 30°N to 30°S) superimposed on climatological SSTs and sea-ice (SSTs and sea-ice from the control model experiment). These anomalous SSTs are taken as the difference between the 10 year monthly mean SSTs from 2003-2012 and 1979-1988 across the tropical band only. This region and specific time periods are used to obtain some similarity with the experiments performed by Ding et al. (2014).

A smoothing function is applied to the latitudinal edges (the outer 10°) of the forcing to minimise spurious atmospheric responses that may be caused by a sharp transition in SST across the edges of the tropics. This smoothing function increases the amplitude of the forcing between 30°N (°S) and 20°N (°S), from no forcing at 30° to full forcing at 20°. Between these two latitudes the forcing is incrementally amplified or ‘turned-up’ using a linear weighted sine function as highlighted in figure 2.4. This results in a full forcing between 20°N and 20°S and no forcing poleward of 30°N and 30°S.

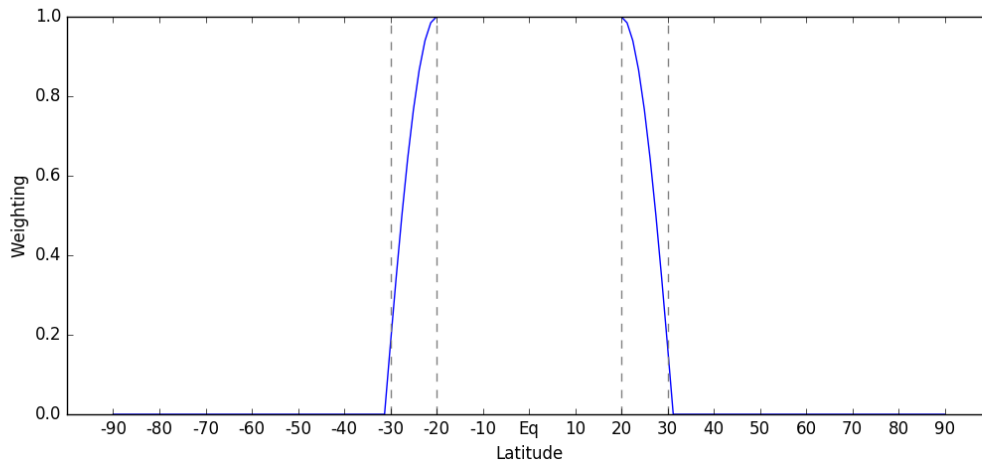


Fig. 2.4 Smoothing function applied between  $30^{\circ}\text{N}(\text{^{\circ}\text{S}})$  and  $20^{\circ}\text{N}(\text{^{\circ}\text{S}})$  between perturbed state in tropics and background state elsewhere

This weighting function is then applied to the anomalous SST field (of the difference between 2003-2012 and 1979-1988 SSTs) to smooth the anomalous SSTs on to the climatological SSTs. The annual mean of the anomalous forcing relative to the annual mean of the control model experiment SSTs is displayed in figure 2.5 and serves to spatially demonstrate the smoothing function as the SST anomaly is applied only within the tropical band. The pattern of anomalous SST forcing applied for the OneSST model experiment has anomalously warm SSTs over most of the tropical region with the tropical Indian, Atlantic and west Pacific around  $0.3\text{-}0.5^{\circ}\text{C}$  warmer than the control. East Pacific SSTs, however, are anomalously cool approximately between  $-0.2$  to  $-0.5^{\circ}\text{C}$ . This cooling in the east Pacific could be the result of either interannual or decadal variability within the Pacific ocean such as from La Niña or the PDO, of which are assessed in greater detail below.

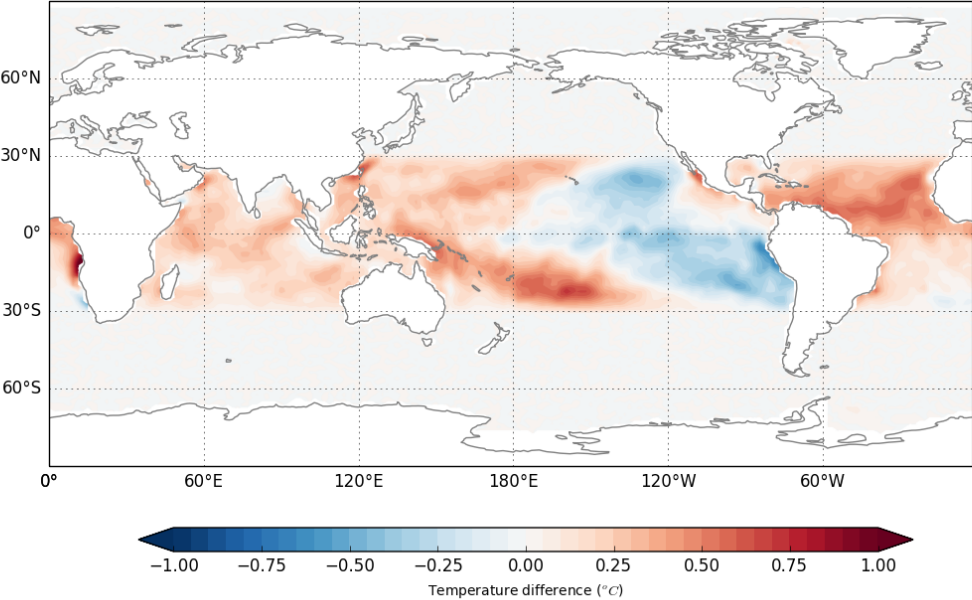


Fig. 2.5 Anomalous forcing in the OneSST model experiment relative to the background climatology SST

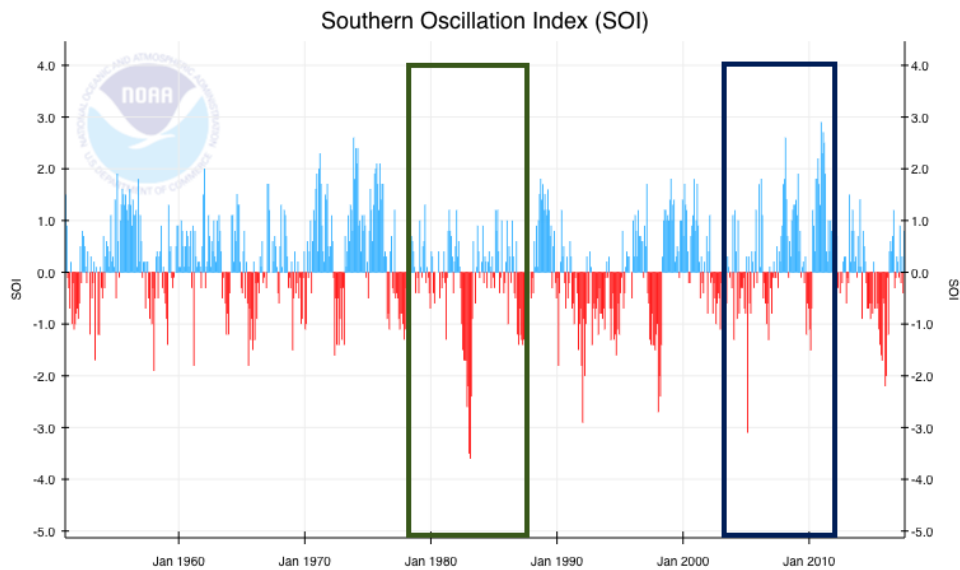


Fig. 2.6 Index of Southern Oscillation index strength from 1965 to 2017 with green rectangular box indicating the ENSO index between 1979-1988 with black rectangular box highlighting the ENSO index between 2003-2012. Taken from (<https://www.ncdc.noaa.gov/teleconnections/enso/indicators/soi/>)

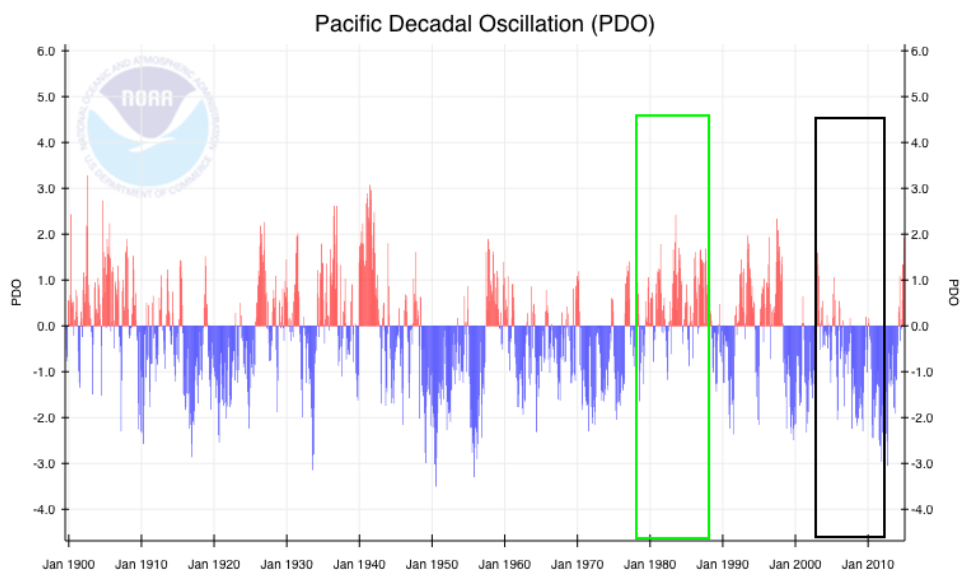


Fig. 2.7 Index of PDO strength from 1900 to 2017 with green rectangular box indicating the positive PDO index between 1979-1988 with black rectangular box highlighting the PDO index between 2003-2012 which tends to be negative in this period. Taken from National Oceanic and Atmospheric Administration (NOAA) National Centres from Environmental Information page (<https://www.ndc.noaa.gov/teleconnections/pdo/>)

Changes in ENSO phase are seen through the Southern Oscillation index from 1950-2017 in figure 2.6 with two periods of interest 1979-1988 and 2003-2012 highlighted in the green and black boxes respectively. This is a standardised index of large-scale fluctuations of mean sea level pressure between Tahiti and Darwin, Australia with positive Southern Oscillation index values correspond with cold SSTs over the eastern Pacific related to La Niña (blue in figure 2.6) and negative Southern Oscillation index values relate to warm SSTs in the eastern Pacific and thus a El Niño (red in 2.6). In this it can be seen that generally the latter period (2003-2012) tends more towards La Niña-like conditions than the earlier period, albeit with a lot of interannual variability in these two time periods. Investigating the PDO index from 1900-2017, between the two periods of interest, it is seen that the PDO between 2003 to 2012 is negative, but was positive between 1979 to 1988.

This would suggest that the latter period tends towards more La Niña/negative PDO like conditions and thus anomalously colder SSTs in the east Pacific and warmer in the west Pacific.

The OneSST model experiment, does not feature in the results chapters hereafter because initial analysis of this model experiment resulted in small and insignificant responses in eddy Z200 in DJF. Further experiments are, however, based on the experimental design.

#### **2.4.2.2 TropSST model experiment**

The second perturbed model experiment, TropSST, is identical to the OneSST model experiment, except that the magnitude of the SST forcing is doubled relative to the OneSST forcing. Anomalous tropical SST perturbations now exceed  $1^{\circ}\text{C}$  within the tropical Indian, Atlantic and west Pacific basins, with the east Pacific cooling equally as large, exceeding  $-1^{\circ}\text{C}$  (Fig.2.8). This doubling of the forcing at the tropics, aims to increase the signal to noise ratio in order to obtain a clearer signal of atmospheric response, particularly over NCG.

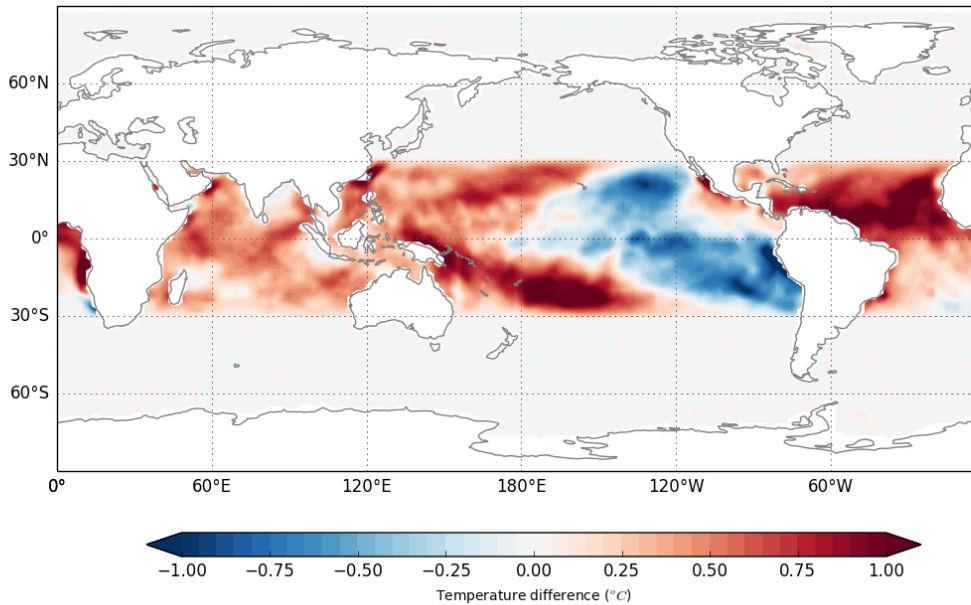


Fig. 2.8 Anomalous forcing of TropSST model relative to the background climatology SST

### 2.4.2.3 PacSST, AtlSST and IndSST model experiments

The next three perturbed model experiments were designed to separate the influence that SST changes in each tropical ocean basin; Pacific, Atlantic, Indian, has on NCG climate. SST perturbations in these model experiments are the same as in the TropSST model experiment except they are applied only for the Pacific, Atlantic and Indian ocean basins.

Alongside the smoothing function application to the outer  $10^\circ$  of the latitude bounds, the same smoothing function is applied along the coastlines of each ocean basin within  $10^\circ$  longitude from the coastlines. This function is shown in figure 2.9, which displays where the forced (red) and unforced (grey) regions are in each experiment, and where the forcing decreases in strength both latitudinally and in approaching the coastlines for

---

each ocean basin. The SST perturbations of each ocean basin, relative to the control SSTs, are as expected, the same as those for the TropSST model experiment, except forced only over the Pacific (Fig.2.10 a), Atlantic (Fig. 2.10 b) and Indian (Fig. 2.10 c).

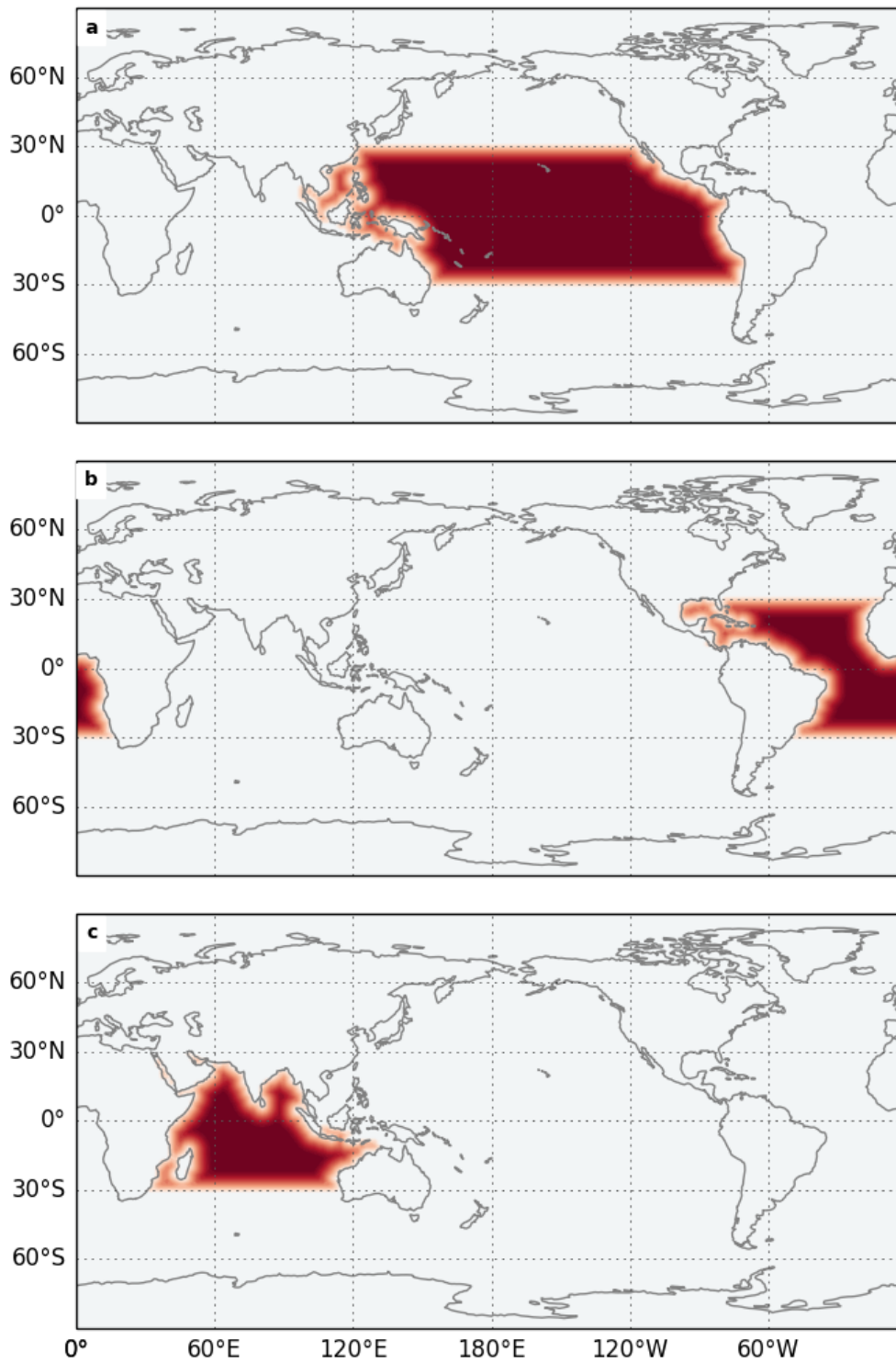


Fig. 2.9 Smoothing function applied to the SST perturbations both in latitude and longitude for the [a] PacSST, [b] AtISST and [c] IndSST model experiments.

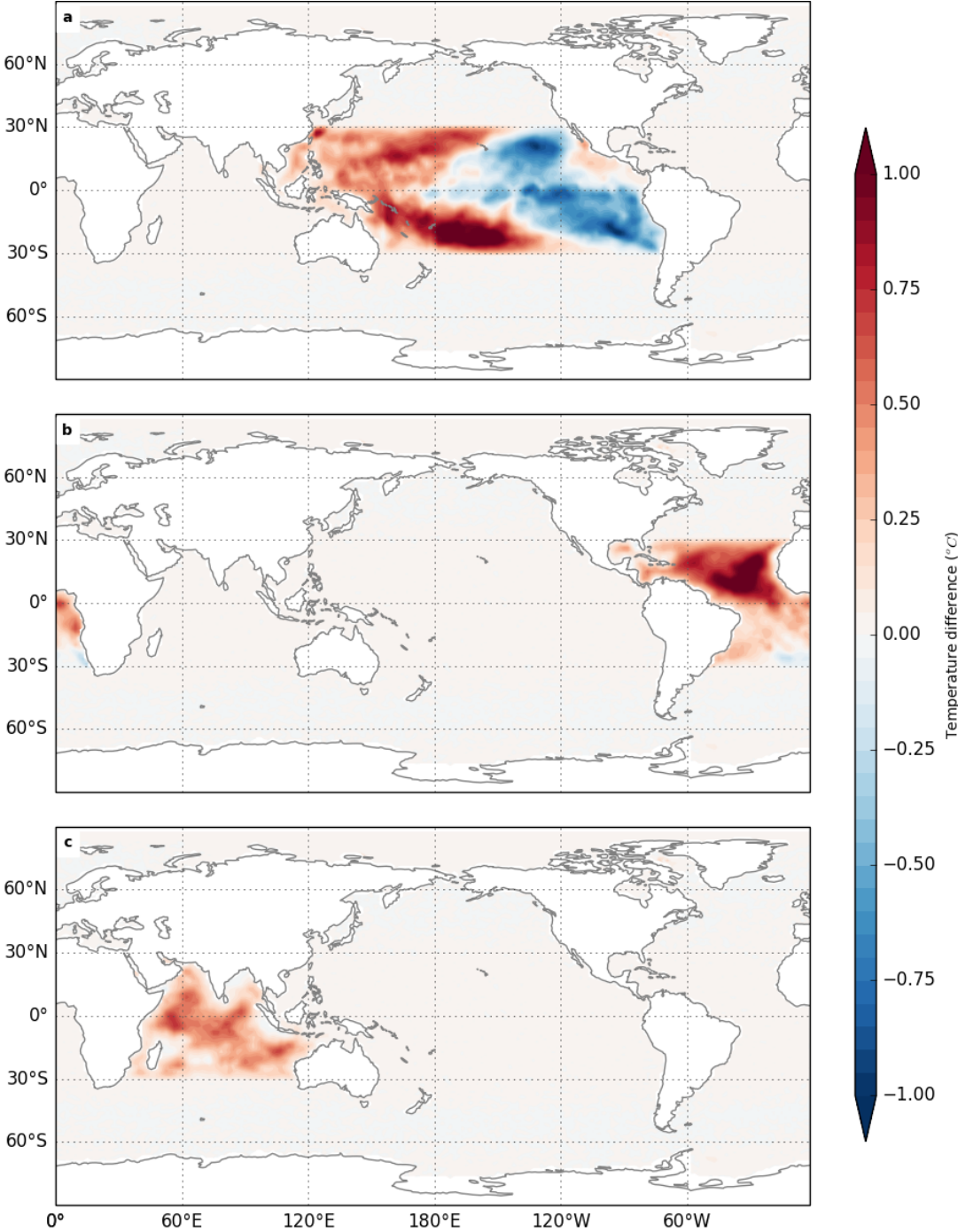


Fig. 2.10 Difference in SST forcing between the [a] PacSST model experiment, [b] AtISST model experiment, [c] IndSST model experiment and the control model experiment

#### 2.4.2.4 GloSST model experiment

The final model experiment, GloSST, was designed to ascertain how the response to globally perturbed SSTs compared to the effects of tropical forcing SSTs on Arctic climate. The SST perturbation used in this experiment is the same as in the TropSST model experiment except it is applied globally rather than within the tropical region alone. The difference of GloSST and TropSST forcing (Fig.2.11) reveals the additional SST perturbations in the extratropics imposed in GloSST. The largest SST anomalies occur in the northern hemisphere with almost all regions showing anomalously warmer SSTs exceeding 1°C except for a small region of cooler SSTs along the western coastline of North America (Fig. 2.11)

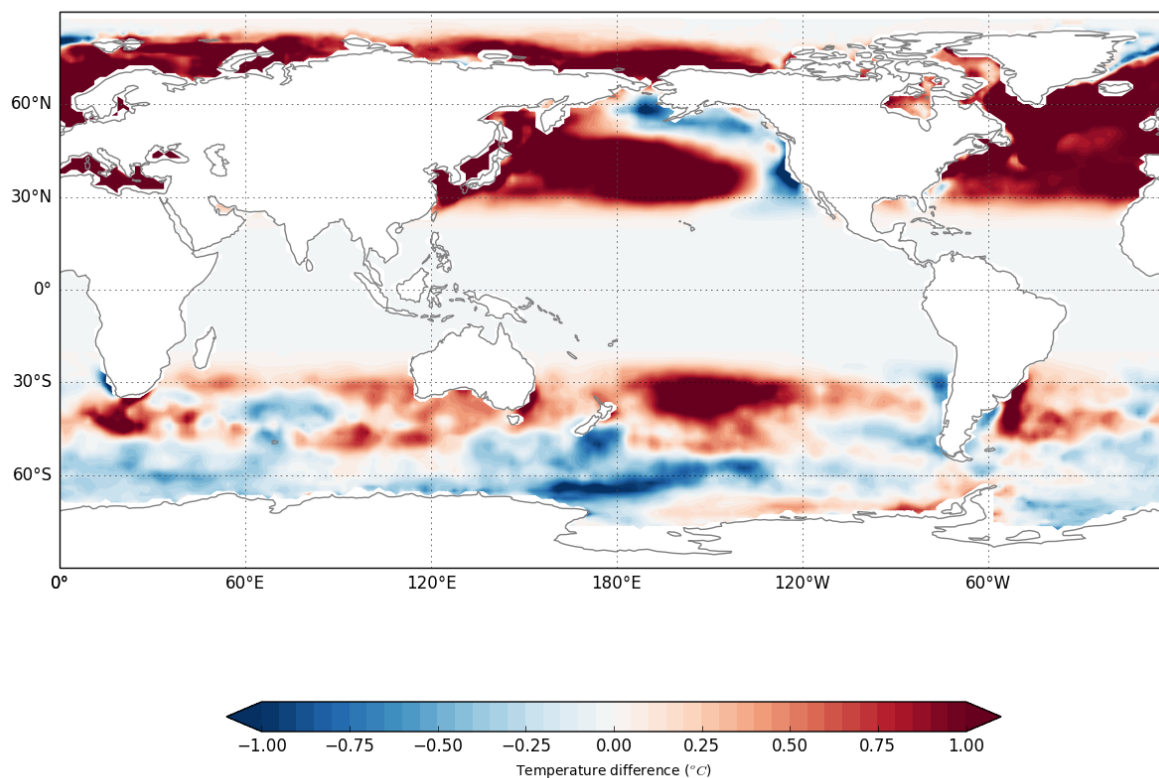


Fig. 2.11 Difference between the SST forcing of GloSST minus TropSST to show anomalous forcing in the extratropics

## 2.5 Methods used in analysis

### 2.5.1 Wave Activity Flux

Wave activity flux (WAF) as defined in Plumb (1985) and as described in chapter 1 section 1.3.3, is used in this thesis to assess the anomalous wave activity resulting from the imposed tropical SST perturbations. It is used specifically as it can calculate disturbances to a basic flow on a meridional plane. Satisfying the conservation relation:

$$\frac{DA}{Dt} + \nabla \cdot \mathbf{F}_s = C \quad (2.1)$$

where

$$A = \frac{1}{2} p q'^2 a \cos^2 \phi / \left( \frac{\partial Q}{\partial \phi} \right) \quad (2.2)$$

$$C = p s' q' a \cos^2 \phi / \left( \frac{\partial Q}{\partial \phi} \right) \quad (2.3)$$

with

$$q = f + \beta_y + \frac{\partial^2 \psi}{\partial x^2} + \frac{\partial^2 \psi}{\partial y^2} + \frac{f^2}{p} \frac{\partial}{\partial z} \left( \frac{p}{N^2} \frac{\partial \psi}{\partial z} \right) \quad (2.4)$$

where  $q$  the quasi-geostrophic potential vorticity and  $Q$  steady zonal flow for  $q$  where  $q = Q(y, z)$ , relates the rate of change of the wave density or amplitude  $A$  to the divergence of wave activity, which is equal to the sources and sinks  $C$ , which vanishes for conservative waves and  $s$  represents the sources and/or sinks of potential vorticity.

As this study focuses mainly on the horizontal component of the wave activity flux, I use  $\mathbf{F}_s$ , defined for spherical coordinates following Karoly et al. (1989):

$$\mathbf{F}_s = p \cos \phi = \begin{pmatrix} v' - \frac{1}{2\Omega a \sin 2\phi} \frac{\partial(v'\Phi')}{\partial \lambda} \\ -u'v' + \frac{1}{2\Omega a \sin 2\phi} \frac{\partial(u'\Phi')}{\partial \lambda} \end{pmatrix} \quad (2.5)$$

where  $u$  and  $v$  are the eastward and northward velocities,  $\Phi$  is the geopotential height with the prime dash denoting a perturbation from the zonal mean,  $p$  is the pressure/1000mb,  $\Omega$  is the Earth's rotation rate,  $a$  is the Earth's radius and  $\phi$  and  $\lambda$  are latitude and longitude, respectively.

## 2.6 Statistical analysis

The statistical significance of the climate responses from the perturbed model experiments, relative to the control model experiment, are found through assessing the Students t-test. The Student's t-test is generally used to assess if two datasets are statistically different from each other. It is a parametric test, which assumes that the two datasets are normally distributed and have equal variances, to determine whether the average values differs significantly between different datasets ().

The students t-test takes the actual difference between the means of two datasets and divides it by the standard error,

$$t = \frac{\bar{X}_1 - \bar{X}_2}{\sqrt{\frac{s_1^2}{n_1} + \frac{s_2^2}{n_2}}} \quad (2.6)$$

where  $\bar{X}$  is the sample mean,  $s$  is the standard deviation, and  $n$  is the number of samples taken. This highlights that the t-test is calculated through dividing the difference

of the datasets means by the sum of the standard error for each sample to determine how far away it is away from the mean thus determining how different one dataset is from another.

As well as determining whether the two distributions comes from different datasets, the Students t-test also provides a p-values which outlines the probably that the results of the t-test occurred by chance. Lower p-values are better e.g. 0.05 which states that there was a 5% chance that it occurred by chance meaning that the result is significantly different.

## 2.7 Thermal wind

The responses in zonal wind from the perturbed model experiments are assessed using the thermal wind equation.

The thermal wind is the vector difference in geostrophic wind, with height or pressure, between two pressure surfaces within a layer and highlights that vertical wind shear of the geostrophic wind is present when a horizontal temperature gradient exists (Holton and Hakim, 2013; Hoskins and James, 2014; Wallace and Hobbs, 2006b). This can be shown with respect to the expressions for the geostrophic wind in its component form,

$$u_g = -\frac{1}{\rho g} \frac{\partial p}{\partial y} \qquad v_g = \frac{1}{\rho g} \frac{\partial p}{\partial x} \qquad (2.7)$$

where  $\rho$  is density,  $g$  is gravity force and  $p$  is pressure which, based on the hydrostatic equilibrium,  $\partial p / \partial z = -\rho g$ , forms to give,

$$u_g = -\frac{g}{f} \frac{\partial z}{\partial y} \qquad v_g = \frac{g}{f} \frac{\partial z}{\partial x} \qquad (2.8)$$

where  $f$  is the Coriolis parameter. This shows that the wind depends on the tilt of a pressure surface, in other words the horizontal gradient of thickness. So where geostrophic wind increases with height, in the  $y$  direction, this states that isobaric surface in the  $x$  direction will also increase with height (Holton and Hakim, 2013).

The thickness of a layer between two isobaric surfaces is dependent upon temperature as seen from the hypsometric equation,

$$Z_T \equiv Z_2 - Z_1 = \frac{R}{g_0} \int_{p_2}^{p_1} T d \ln p \quad (2.9)$$

where  $Z$  is the geopotential height,  $g_0 = 9.80665 \text{ m s}^{-2}$  which is the global average of gravity at mean sea level,  $R$  is the gas constant of dry air ( $R = 287 \text{ J kg}^{-1} \text{ K}^{-1}$ ),  $T$  is temperature and  $p_2$  and  $p_1$  are the upper and lower pressure surfaces. This states that as the mean temperature of a layer between two pressure surfaces increases, in the  $x$  direction, this is associated with an increase in the thickness of that layer. This is because as air is less dense when it is warmer, it therefore occupies a greater vertical depth as pressure drops as the layer thickens (Holton and Hakim, 2013).

This therefore outlines that the strength of the geostrophic wind with height is dependent upon the mean temperature gradient due to its impact on the horizontal gradient of thickness. By calculating the thermal wind or vertical shear, one can find how the geostrophic wind changes in height through taking the difference of geostrophic wind between two levels, which in the form of the  $u$  component (which is of most interest in this thesis) is,

$$U_T \equiv (u_g)_{(p_2)} - (u_g)_{(p_1)} = -\frac{R}{f} \left( \frac{\partial \bar{T}}{\partial y} \right)_p \ln \left( \frac{p_2}{p_1} \right) \quad (2.10)$$

with  $\bar{T}$  denoting the average temperature of a layer between  $p_2$  and  $p_1$ .

As the thermal wind relates the change in strength of the geostrophic wind to the horizontal temperature gradient, it can also be used to estimate the geostrophic wind from a known mean temperature gradient at some reference level (Holton and Hakim, 2013; Wallace and Hobbs, 2006b). It is therefore used in this way to calculate the zonal geostrophic winds at 200 hPa in the northern hemisphere to ascertain if the responses in zonal wind are due to changes in the anomalous temperature gradients generated in response to the imposed tropical SST forcings.

## 2.8 Model Validation

Climate models are based on well-established theory for the atmosphere and while have demonstrable ability in accurately simulating weather and climate (Randall et al., 2007), still contain biases due to, for example, inaccurate representations of particular parameters such as clouds. Assessing the performance of the model is therefore important to ensure that it has adequate skill in simulating climate based on observations or reanalysis, which in the absence of accurate observations, are a good enough approximation of the real state of climate for model validation purposes (Reichler and Kim, 2008).

The control model experiment is compared to ERAI data from 1979-1988 to ensure consistency between the time periods. Data are compared for a few key climate parameters that are important for this study specifically eddy geopotential height at 200 hPa, surface air temperature and zonal winds. These are validated only within the northern hemisphere and tropical band of SST perturbations as these are the main areas of interest and analysis throughout this thesis.

Initially assessing the annual mean of eddy Z200, ERAI (Fig. 2.12 a) displays large positive anomalies in the subtropical west Pacific (around 30°N and between 120°E to 180°E), over northwestern North America (centered around 60°N and 120°W) and the North Atlantic that spans across western Europe centered around 50°N and 30°W. The

largest negative anomalies are found over east Eurasia (around  $50^{\circ}\text{N}$   $130^{\circ}\text{E}$ ) and over north Canada and Greenland ( $70^{\circ}\text{N}$ ,  $70^{\circ}\text{W}$ ). These patterns in eddy Z200 are similarly produced in the annual mean of the control model experiment (Fig. 2.12 b), albeit with varying strengths compared to ERAI. The absolute differences between the control model experiment and ERAI are shown in figure 2.12 c, purple shading highlights where the anomalies in the model are larger than in ERAI, overestimating the absolute value of the eddy Z200 and green shading indicates where the anomalies are weaker than in ERAI underestimating the absolute value of eddy Z200. The largest difference is over north Canada and Greenland where the model evidently underestimates the magnitude of the climatological trough in this region, highlighted by green shading in figure 2.12 c but is also evident by eye between figures 2.12 a and 2.12 b. Other biases show that the model overestimates eddy Z200 over the subtropical and north west Pacific with a strengthened positive anomaly over the subtropical west Pacific approximately at  $130^{\circ}\text{E}$  and  $30^{\circ}\text{N}$  and strengthened negative anomaly over the northwest Pacific. The model also shows negative bias over the subtropical east Pacific between  $175^{\circ}\text{W}$ - $115^{\circ}\text{W}$  and between  $15$ - $35^{\circ}\text{N}$  highlighting that the model simulates a much weaker negative eddy Z200 than ERAI.

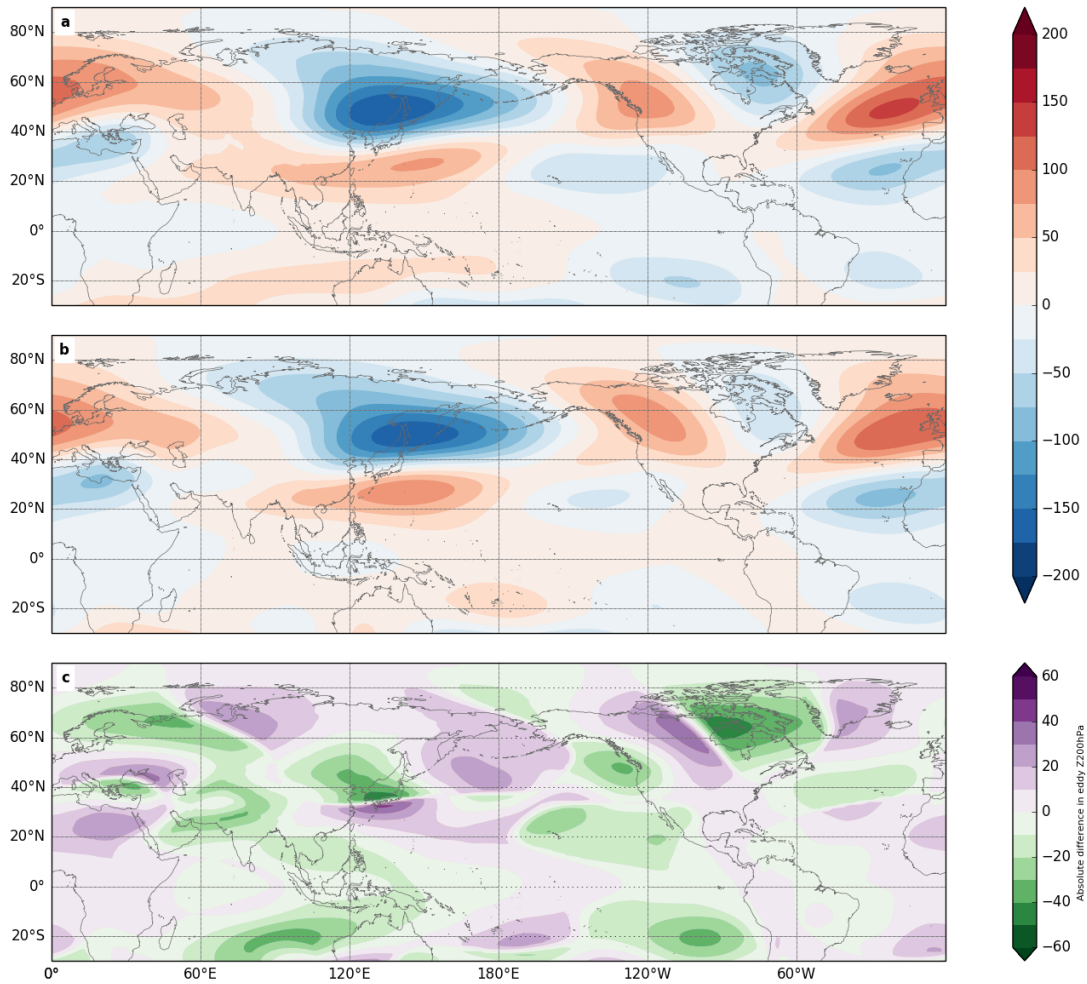


Fig. 2.12 Eddy Z200 climatology for [a] ERAI for 1979-1988 [b] Control model experiment over all model data and [c] the absolute difference between the Control model experiment and ERAI to indicate bias in model. Areas of purple in [c] highlight where model simulates larger anomalies than in ERAI and green shading indicates where the model simulates weaker anomalies than in ERAI

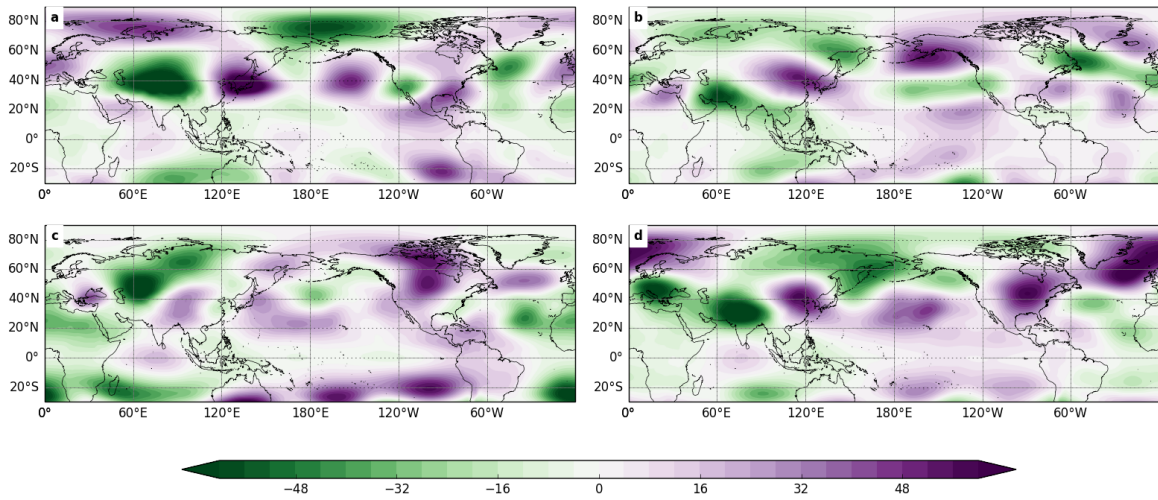


Fig. 2.13 Difference in eddy Z200 between the control model experiment and ERAI highlighting model bias, with purple showing where the model simulates larger anomalies than ERAI and green shading as weaker anomalies in model that ERAI for [a] DJF, [b] MAM, [c] JJA, [d] SON

The amplitude of the seasonal biases are similar across all seasons but the location of biases differs (Fig.2.13). Largest negative biases in boreal winter (Fig.2.13 a) are found over the Chukchi Sea and central Asia with positive biases over Japan and Kara and Barents Seas. Positive biases in eddy Z200 in spring (MAM) (Fig.2.13 b) are found over Alaska and east coast of Asia with negative biases in north east Russia, eastern Pacific ocean and the mid-North Atlantic ocean. The model tends to overestimate eddy Z200 over North America and regions of the Pacific Ocean in boreal summer (JJA) (Fig.2.13 c) and east North America and the North Atlantic in autumn (SON) (Fig.2.13 d), and underestimate it over central Eurasia and Africa in JJA and southern Eurasia and northern Russia in SON.

Surface air temperature annual means in ERAI (Fig. 2.14 a) and as simulated in the control model experiment (Fig. 2.14 b) appear very similar with warmer air temperatures across the tropical regions which become increasingly cooler towards the mid-latitudes and negative in to the Arctic. Large scale features such as the pronounced cold temperatures

over Greenland appear fairly well simulated by the control model experiment. The absolute difference between the two fields (Fig. 2.14 c), show that the largest biases are around the coastlines highlighting model inability to accurately simulate surface air temperature contrasts between land and ocean most likely due to the land-sea mask along the coastline defined in HadGEM3-A. The model also largely underestimates surface air temperatures in the Arctic region, mainly north of the Canadian Archipelago and along the coastlines within the Arctic region. This is characterised, therefore, as relatively warmer temperatures over the Arctic, compared to ERAI, which may be possibly due to the sea ice forcing.

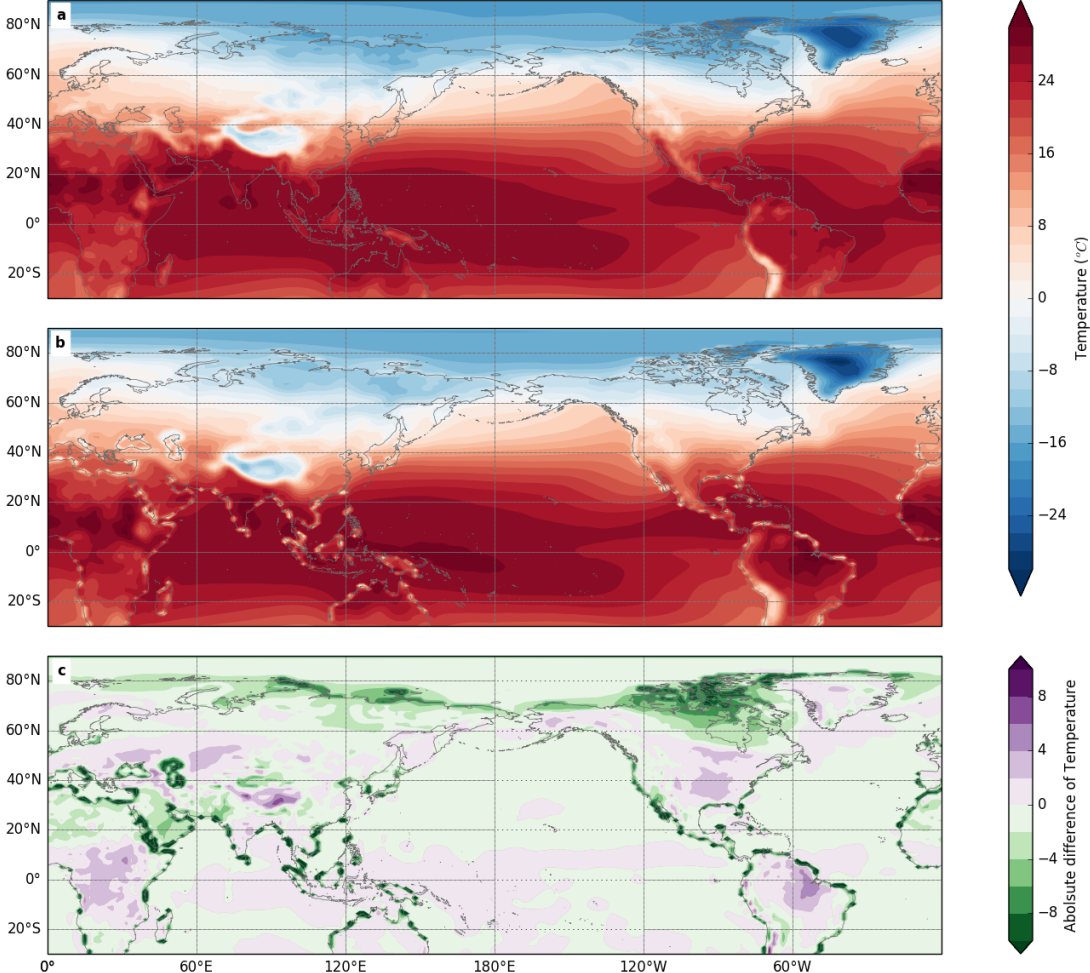


Fig. 2.14 Surface temperature climatology for [a] ERAI for 1979-1988 at 2m, [b] Control model experiment at 1.5m and [c] the difference between the control and ERAI with purple shading indicating areas of where the model temperatures are higher than in ERAI and green shading, where the model is relatively colder.

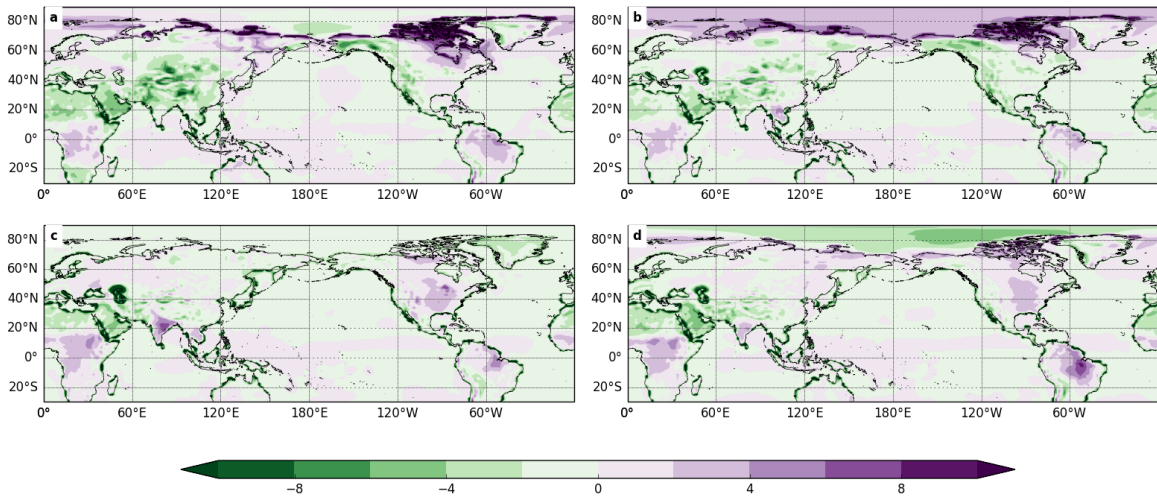


Fig. 2.15 As is figure 2.14 c, but showing the differences in surface temperature between the model and ERAI for [a] DJF, [b] MAM, [c] JJA, [d] SON

The largest seasonal biases in surface air temperature are found in spring (MAM) (Fig. 2.15 b) and autumn (SON) (Fig. 2.15 d) where the model respectively underestimates and overestimates surface air temperature across the entire Arctic region. A negative bias over is particularly pronounced over the Canadian Archipelago region and along the Arctic coastline in boreal winter (DJF) possibly due to sea ice forcing and or the models land sea mask in these regions. JJA has the weakest biases but has biases along all coastlines which may be an artefact of the land/sea mask of the model.

Annual means of zonal wind between ERAI (Fig. 2.16 a) and the control model experiment (Fig. 2.16 b) share most of the large-scale features with easterlies in the tropics straddling the equator across the tropical Indian and Pacific oceans and westerlies in the subtropics. The magnitude of these patterns are also fairly similar between the two datasets with the jets of relatively equal strength in both the Pacific and Atlantic. The absolute differences between the two (Fig. 2.16 c) are mainly pronounced in the equatorial Pacific where the model overestimates the winds in the east Pacific and over the north west coastline of South America and underestimates them in the west Pacific

therefore producing stronger easterlies in the east and north west tropical Pacific weaker equatorial westerlies around 120°E than are found in ERAI.

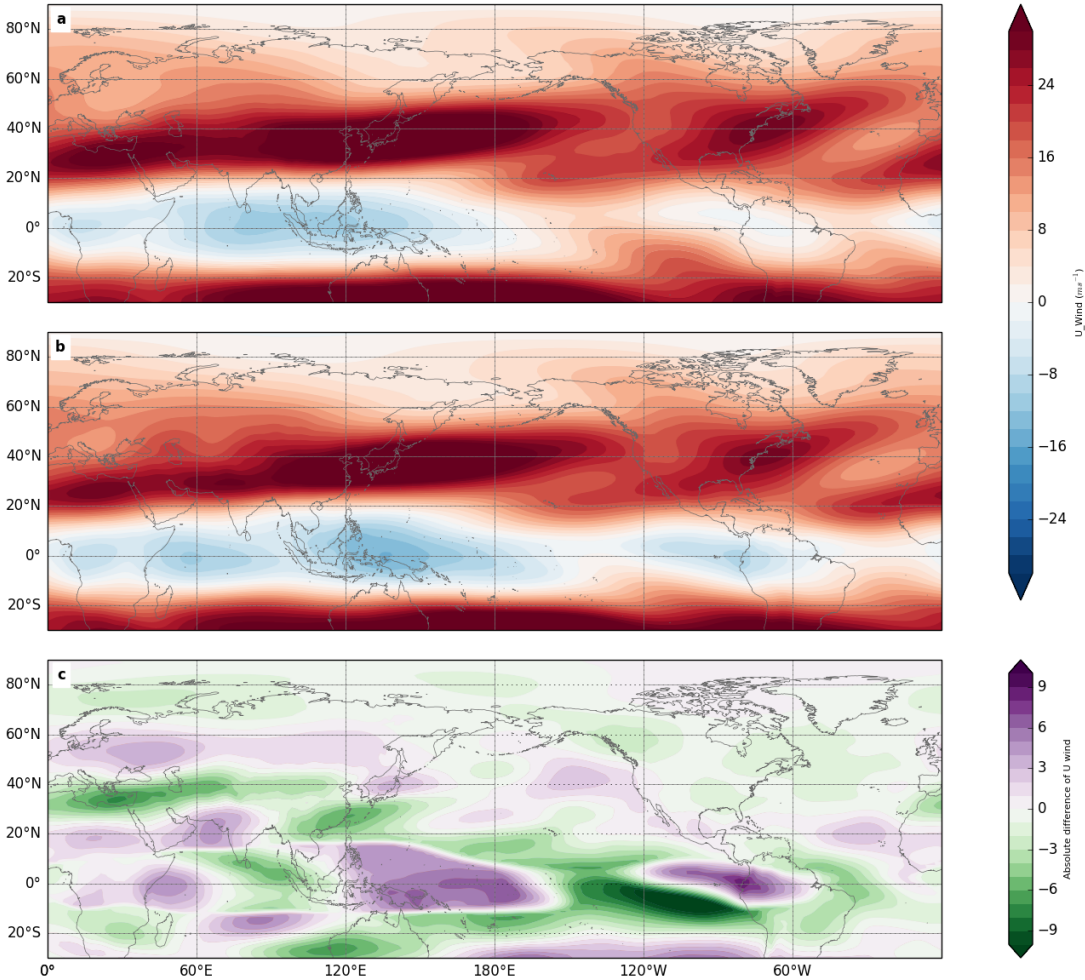


Fig. 2.16 200 hPa U wind climatology for [a] ERAI for 1979-1988, [b] Control model experiment, [c] the difference between control and ERAI with purple indicating model bias with purple representing model overestimation and green model underestimation

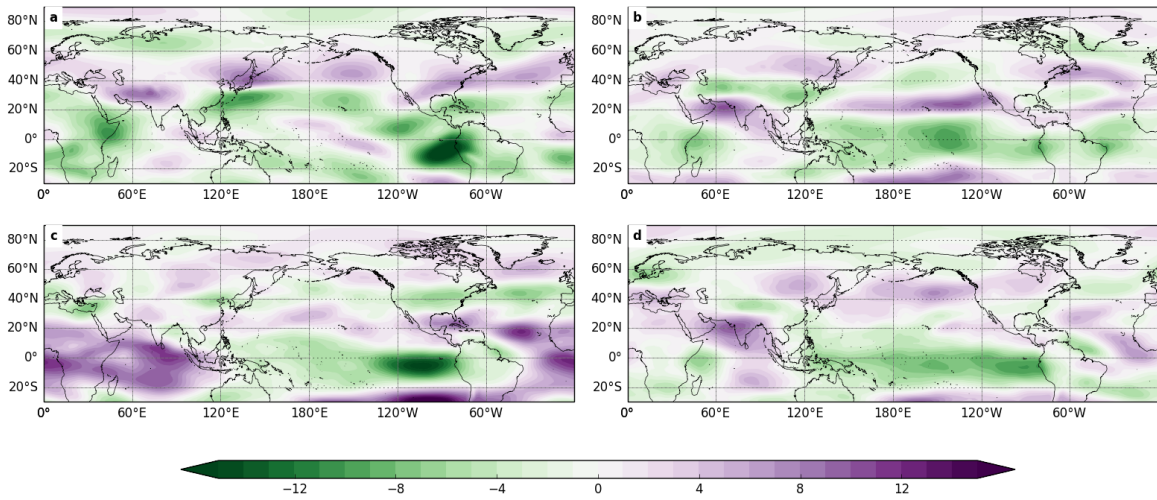


Fig. 2.17 Seasonal difference of U wind at 200 hPa between the control model experiment and ERAI to represent bias in model with purple indicating model overestimation and green indicating underestimation for [a] DJF, [b] MAM, [c] JJA, [d] SON

The largest zonal wind at 200 hPa (U200) biases in tropospheric zonal wind at 200 hPa relative to the other seasons are found in boreal summer (JJA) (Fig. 2.17 c) where positive biases are found over the tropical Atlantic Ocean, Africa and the Indian Ocean with negative biases found along the east of the equatorial Pacific. Positive biases in other seasons are found in the north Pacific and north Atlantic in winter (DJF) (Fig. 2.17 a) and spring (Fig. 2.17 b) and in the north Pacific ocean and Indian Ocean in autumn (SON) (Fig. 2.17 d). Areas of model underestimation of U200 are mainly found around the equatorial Pacific in all seasons and in to the north Pacific around 40°N for DJF.

These results from the model validation shows that the model captures the main large-scale features of the climate relative to ERAI. It does contain biases, which are expected in climate models due to different physics in the model and the use of different parameterized processes. Annual mean biases are most pronounced over NCG for eddy Z200 resulting in weaker simulation of negative eddy Z200 here, weaker surface air temperatures over the Arctic and stronger zonal easterlies around the equator in the

Pacific ocean. The seasonal biases are generally relatively small especially for DJF which is the season of interest throughout this study. In summary, as the model largely captures the same climate features of ERAI, highlights the relative skill of the model and justifies its use in this study.



# Chapter 3

## The North Canada-Greenland pattern

### 3.1 Observed changes to the north Canada and Greenland climate

Arctic climate has experienced rapid changes over the past 30 years (Screen et al., 2013). Large-scale surface temperature changes over this time have been widely documented (Cohen et al., 2014b; Francis and Vavrus, 2012; Screen et al., 2012), but changes throughout the troposphere have also been observed. Statistically significant positive annual mean trends in geopotential height at 200 hPa (Z200) of approximately  $1.5 \text{ m yr}^{-1}$  have occurred across the entire Arctic over the period of 1979 to 2012, seen in figure 3.1 and as shown similarly by Ding et al. (2014) in their decadal trends of geopotential height (Figure 1c of Ding et al. (2014)). The largest trend occurred over the north Canada and Greenland region, as outlined by the yellow dashed box in figure 3.1, where positive trends exceeded  $2 \text{ m yr}^{-1}$ . This is especially pronounced in the eddy component of Z200, found through subtracting the zonal mean from the full Z200 field, thus identifying this as a distinct localised anomaly (Fig. 3.2).

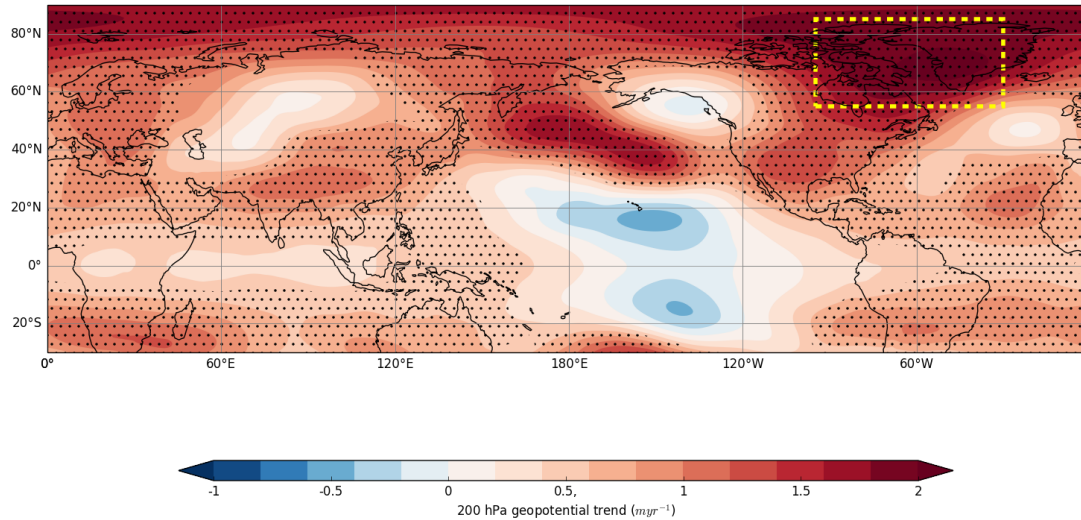


Fig. 3.1 Annual trend in geopotential height at 200hPa from 1979-2012 in ERA-Interim. Stippling denotes statistical significance at  $p < 0.05$ .

Atmospheric circulation changes over north Canada and Greenland (hereafter known as NCG) are particularly important as they can impact the stability of the Greenland ice sheet, which could result in increased future sea-level rise (Forsberg et al., 2017; Rignot et al., 2011), and also affect the growth or attenuation multi-year sea ice in the Canadian Archipelago region (Bader et al., 2011; Kwok et al., 2009; Maslanik et al., 2011). Furthermore it is imperative to understand current climate signals in order to understand how they may change in the future, particularly in a region which is already experiencing the first signs of anthropogenic climate change (Duarte et al., 2012).

A detailed analysis and thorough investigation of the eddy Z200 trends are undertaken in this chapter to gain greater insight in to their robustness. The trends derived from ERA-Interim Reanalysis data (ERA-Interim) are evaluated at both annual and DJF time scales. The ability of models to capture the observed trends over the NCG region will be evaluated using the UPSCALE and AMIP model output (see section 2.1.2 and 2.1.3), with trends across all three datasets being compared and differences between each quantified.

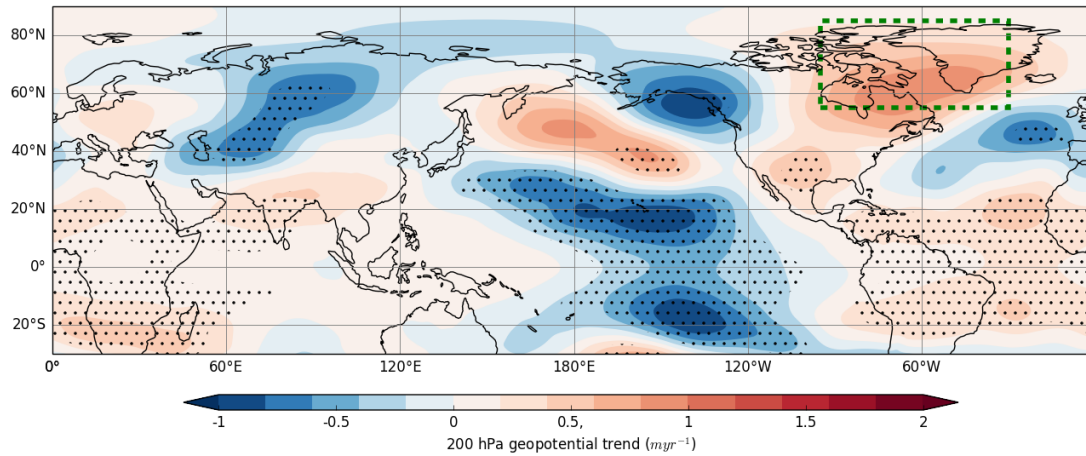


Fig. 3.2 Annual trend in eddy geopotential height at 200hPa from 1979-2012 in ERA-Interim. Stippling denotes statistical significance at  $p < 0.05$ .

Dependence on time period and variability of the magnitude and sign of recent climate trends over the NCG region will also be analysed and quantified.

## 3.2 The characteristics of the NCG pattern

In this study, a number of different datasets are used to examine the most recent climate trends over the NCG region and quantify its changes to assess how significant the positive trends are. ERA-Interim reanalysis (ERA-Interim) is used, as detailed in section 2.1.1, as the main dataset for obtaining trends of Arctic climate as observations over the Arctic are inhomogeneous (Cowtan and Way, 2014; Inoue et al., 2015) and ERA-Interim reanalysis have a proven ability in accurately simulating the Arctic climate (Lindsay et al., 2014; Screen and Simmonds, 2010a,b). Furthermore, positive temperature and geopotential height trends over NCG found by Ding et al. (2014) were found in ERA-Interim. The trends found in ERA-Interim are compared and contrasted to trends in other climate modelled datasets namely; UPSCALE (UK on Prace - weather resolving simulations of Climate for global Environmental Risk), a 13 member ensemble of HadGEM3-A model experiments, at varying resolutions; and AMIP (Atmospheric Model Intercomparison Project) from the

CMIP5 project, comprised of simulations from 30 global atmospheric models, consisting of a total of 96 model experiments. In this study, however, only the first ensemble member (r1i1p1) of each model is analysed to ensure equal weighting between models, as models had different numbers of ensembles ranging from one to approximately 11. Furthermore this study was concerned primarily with intra-model variability than the internal variability of each individual model, to understand the different realisations of the trends of geopotential over NCG.

The model simulations from both of these projects are forced with global transient sea surface temperatures (SSTs) between 1985 to 2011 for UPSCALE, and between 1979 to 2005 for AMIP. The different time periods covered by each project will mean that the characteristics of trends over different time intervals can be investigated. As well as this, analysing trends in multiple datasets is important for two main reasons;

[1] ERAI is a relatively short record covering only 38 years of climate data and provides only one realisation of climate. Using multiple datasets provides many realisations of climate and can cover different or longer time periods to provide more information about the climate system, therefore producing more robust records of climate. Global climate models (GCMs) are therefore favoured for this as they are able to produce longer climate records, in addition to running single-model or multi-model ensembles;

[2] Climate variability, specifically internal atmospheric variability can be examined both within the ensemble members and in the spread across the different models, as they are forced with the same SSTs, which can help to attribute if trends are internally driven or externally forced. Furthermore, it is important to test if these models can reproduce the response to imposed SSTs to assess their ability in simulating the real climate system.

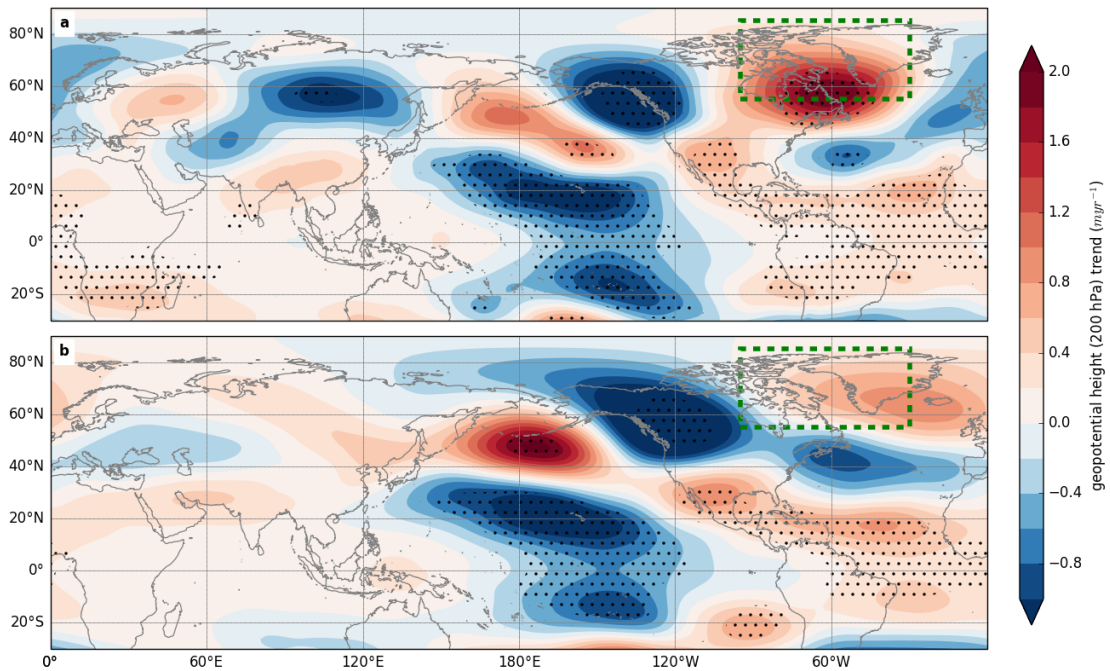


Fig. 3.3 Eddy Z200 annual mean trends for [a] ERAI from 1985 to 2011 and [b] UPSCALE ensemble mean for 1985-2011.

The annual mean eddy Z200 trends of the UPSCALE ensemble mean, AMIP multi-model mean and ERAI mean trends for the same periods of UPSCALE and AMIP are displayed in figures 3.3 and 3.4. The UPSCALE ensemble mean trend over NCG (identified in Fig. 3.3 b by green dashed box) from 1985 to 2011 displays a positive trend of approximately  $1 \text{ m yr}^{-1}$  which is not statistically significant. This is comparatively weaker to the statistically significant positive ERAI mean trend over the same period (1985 to 2011) (Fig. 3.3 a) which is around  $1.6 \text{ m yr}^{-1}$  and is more centrally located over NCG than the UPSCALE ensemble mean positive trend. The difference in statistical significance between ERAI and UPSCALE ensemble mean may emanate from the large spread and variability of ensemble members within the UPSCALE dataset, in that the trends may be of different sign in different members which may indicate why the trends in UPSCALE are weaker and not significant. Other trends of note from figure 3.3 are the large eddy Z200 trends over the northern hemisphere, namely the statistically significant tripole anomalies of alternating sign that span the North Pacific Ocean found in both

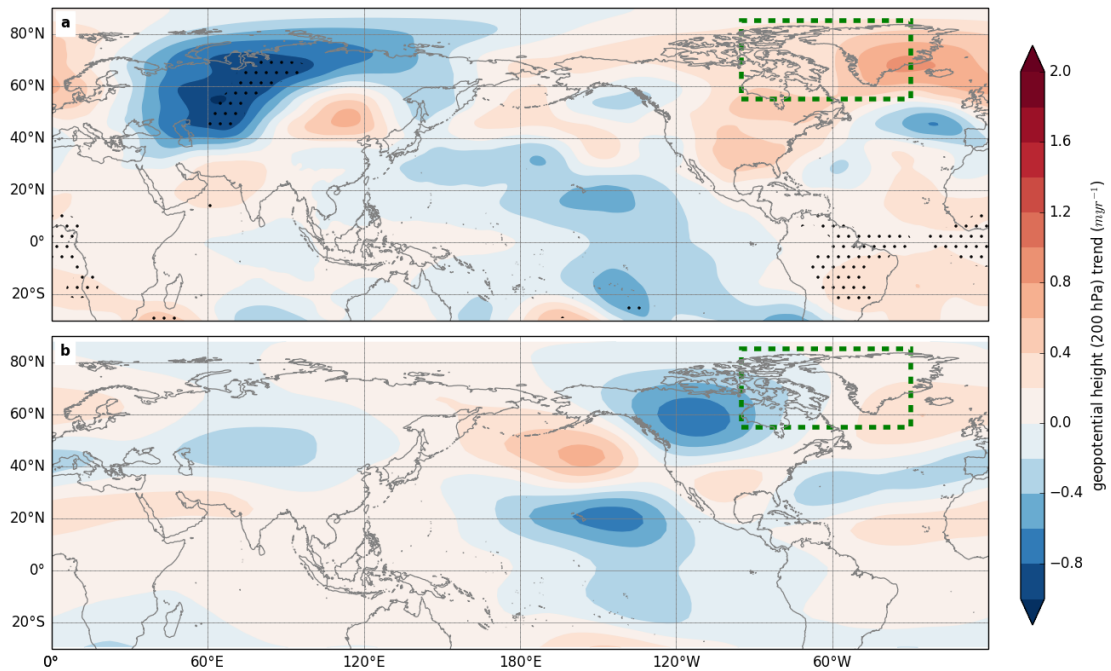


Fig. 3.4 Eddy Z200 annual mean trends in [a] ERAI for 1979-2005 (following AMIP record) [b] AMIP multi model mean for 1979 to 2005. Stippling denotes statistical significance ( $p < 0.05$ ) and green dashed box denotes area of interest north Canada and Greenland (NCG)

UPSCALE and ERAI of much greater amplitude in UPSCALE ensemble mean than in ERAI.

Annual mean eddy Z200 trends from the AMIP multi-model mean (1979 to 2005) and ERAI for the same period (Fig. 3.4) both display positive trends over NCG although these are weaker relative to the ERAI and UPSCALE means from 1985 to 2011 and show no statistical significance. The AMIP multi-model mean eddy trends are both positive and negative across NCG (Fig. 3.4 b) with positive trends across the east of the NCG region and negative across the west extending westwards over Canada. ERAI trends over the same period are positive everywhere, and similarly to the AMIP trends and at their peak are approximately  $0.8 \text{ m yr}^{-1}$  (Fig. 3.4 c) and compared to the latter period (1985-2011) have had an easterly shift in both ERAI and AMIP. These results explain some of the discrepancy between the UPSCALE and AMIP results (Figs. 3.3 b and 3.4 b), particularly the 1979 to 2005 trend which is much weaker than both the 1985-2011

and 1979 to 2012. A time dependency on the strength and statistical significance of the annual eddy Z200 trends is evident as there is a  $1.2 \text{ m yr}^{-1}$  difference in the trend over the NCG region between the UPSCALE time period and AMIP time period for ERAI and only trends from 1985-2012 in ERAI show statistical significance.

### 3.3 Quantification of temporal variability of NCG anomaly

Figure 3.5 shows the timeseries of the eddy Z200 anomalies over NCG for all three datasets. A low-pass 5-year filtering was used to smooth these anomalies to find the overall temporal trend away from the background noise. Weak negative anomalies are found in the first period, as highlighted by ERAI (in blue) and AMIP multi-model mean (in red), which spans from the start of the record to the late 1980's, early 1990s. Eddy Z200 anomalies show large fluctuations in time with annual deviations from the mean between  $\pm 1$  as highlighted by translucent lines superimposed behind their respective 5-year filtered trends for each dataset. Strong positive anomalous trends are observed in the second period, as depicted by all three data sets, which runs roughly over a 10 year period from the start of the 1990s to the end of the 1990s, beginning of the 2000s. At the end of this period, predominantly in the UPSCALE ensemble and AMIP multi-model means, there is a large peak in the actual time series (in the translucent lines in the background) around 1998 which may have been due to the strong El Nino of that year. This suggests that there is an SST dependence of these patterns, and thus indicates a potential role of remote SSTs in driving this pattern. Following this positive trend is a plateau of the trends for the latter part of the record, approximately from the start of the 2000's, where the trends remained level in ERAI mainly. This plateau of trends may be due to the global hiatus (Meehl et al., 2011; Trenberth and Fasullo, 2013), which has been widely accepted as starting in the late 1990s, early 2000s which resulted in the slow down of positive global surface temperature trends, and may also have resulted in changes in large-scale global circulation. UPSCALE, however, has a slight negative trend

in the early 2000s and then begins to rise again after this point. This decline maybe due to the sharp decline of eddy Z200 in its unfiltered timeseries (faded green line in figure 3.5) around that time relative to both ERAI and AMIP, with the rise potentially an effect of the large variability in this latter period relative to ERAI.

These temporal trends can potentially substantiate why the strength of the overall annual trends shown in figures 3.3 b and 3.4 b are variable. The AMIP multi-model mean trends, aside from the large positive trend in the late 1990s, experience generally negative overall trends. UPSCALE, comparatively, remains fairly steady or positive throughout its timeseries with only a weak negative trend in the late 1990s, early 2000s, potentially due to the global cessation of global surface air temperature (Meehl et al., 2011; Trenberth and Fasullo, 2013; Watanabe et al., 2014). The differences in temporal variation between UPSCALE ensemble means and ERAI, specifically in the early 2000s, where the UPSCALE 5-year filtered trend is less than the ERAI 5 year filtered trend, may explain why UPSCALE underestimates the ERAI trend for the same period (Fig. 3.3). AMIP, however, in most cases, overestimates the timeseries trend, and yet its overall annual trend for the entire period is weaker than ERAI trend from 1979 to 2005 (Fig. 3.4). This could be due to the smoothing of the models in the averaging processes over the spatial area there may have been a large spread across all models in AMIP.

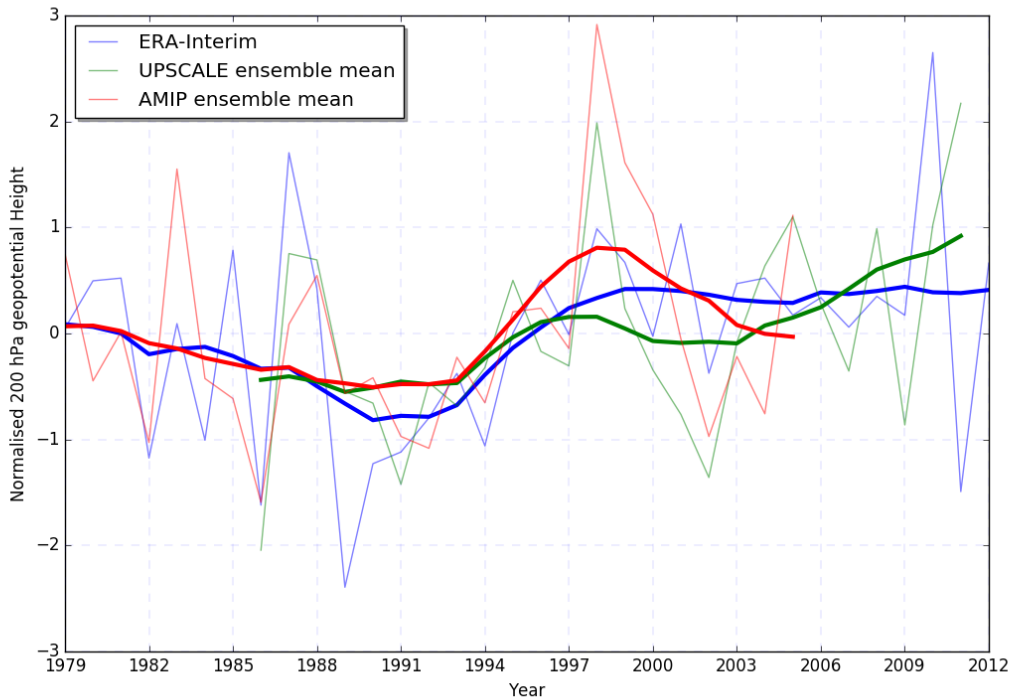


Fig. 3.5 Timeseries of eddy Z200 over NCG for ERAI from 1979-2012 (in blue), UPSCALE ensemble mean from 1985-2011 (in green) and AMIP multi-model mean from 1979-2005 (in red). Faded lines represent the actual timeseries each dataset, with bold lines represented the smoothed timeseries using lower pass five year filtering.

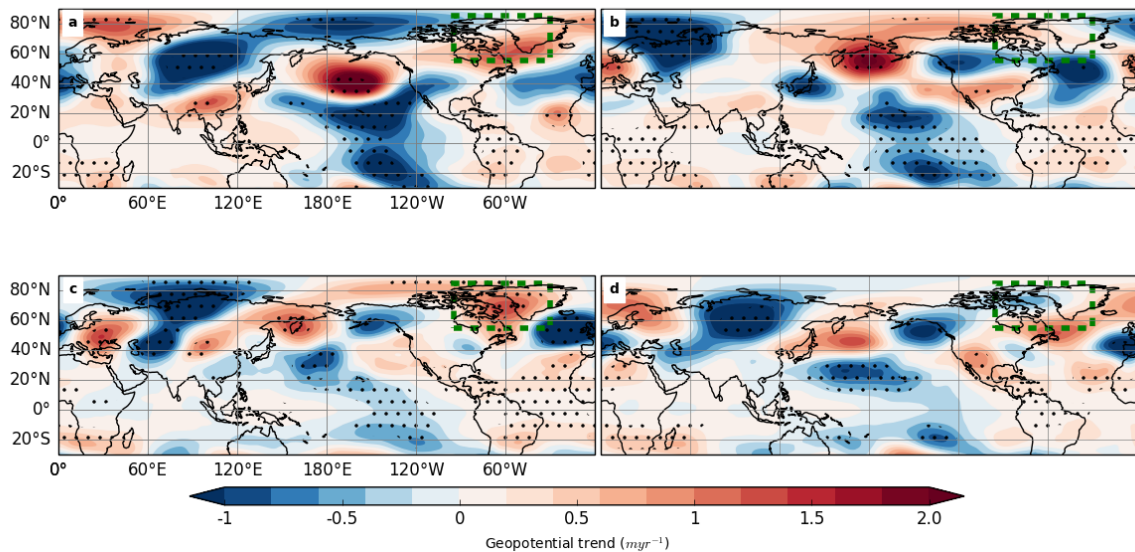


Fig. 3.6 Eddy Z200 trends for ERAI from 1979-2012 for [a] December-February, [b] March-May, [c] June-August, [d] September-November. Stippling denotes statistical significance ( $p < 0.05$ ), and green dashed box highlights the region of interest.

Quantifying the seasonality of the eddy Z200 trends, both the spatial and temporal trends are assessed to ascertain if trends are stronger in one particular season. DJF and JJA show the largest positive annual mean trends in ERAI from 1979-2012 compared to MAM and SON, which have negligible to weak negative trends (Fig. 3.6), even with large temporal variability in the anomalous timeseries (Fig. 3.7 b, d). Therefore, as they show weak to almost no trends, their role in determining the pattern of the annual mean trend appears inconsequential and so are not analysed further. The June-August (JJA) mean positive eddy Z200 trends over NCG (Fig. 3.6 c) are most probably due to the large positive interannual trend that occurs in the latter half of the time record in ERAI (solid blue line Fig. 3.7 c), from approximately the early 1990s onwards. This is also partly captured in the UPSCALE ensemble mean, but not in the AMIP multi-model mean, which is almost anomalously negative throughout. The DJF long term spatial (Fig. 3.6 a) and temporal trends (Fig. 3.7 a), however, more closely resemble the overall annual mean trend of eddy Z200 where, for example, the DJF eddy Z200 mean trends over the Pacific and Atlantic oceans are similar to those in the annual mean trend. Modelled trends (from UPSCALE and AMIP means) also largely capture these temporal trends and thus highlight how distinct and robust the positive eddy Z200 trends are in boreal winter.

This indicates that DJF plays a large role in the annual eddy Z200 trends highlighted earlier and therefore trends in this season over NCG are further analysed throughout.

### 3.4 Inter-ensemble member variability of NCG trends

As alluded to in the previous section, annual and DJF eddy Z200 trends over NCG, while positive, are subject to variability both temporally and spatially and across different datasets. The large interannual variability of the annual and DJF NCG eddy Z200 trends are evident in the unfiltered time series (Fig. 3.5 and Fig. 3.7 a) as seen by the translucent lines of similar colour to the filtered timeseries. Inter-annual anomalous vacillations of eddy Z200 between years can be as large as  $\pm 1$  standard deviation away from the

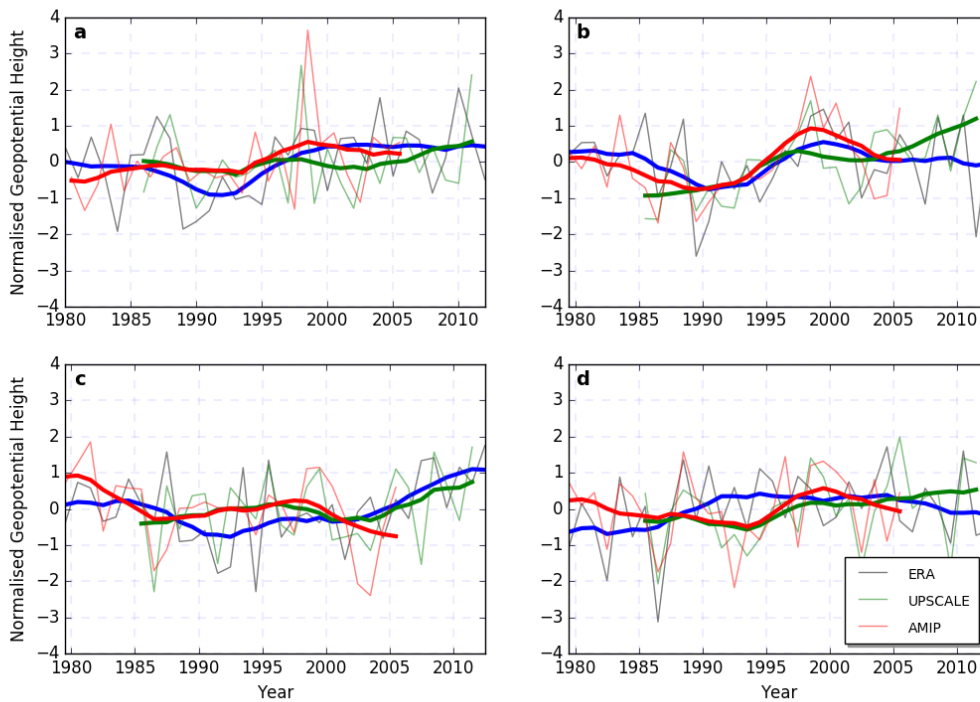


Fig. 3.7 Timeseries of eddy Z200 for ERAI from 1979-2012 (in blue), UPSCALE ensemble mean from 1985-2011 (in green) and AMIP multi-model mean from 1979-2005 (in red) for [a] DJF, [b] MAM, [c] JJA, [d] SON. The faded lines in background represent the actual timeseries whereas the bold lines in front are the smoothed timeseries, using Kernel low-pass five year filtering

mean, particularly at the start and end of the annual record when variability is largest. Variability is large in all seasons but has a larger range in boreal winter compared to other seasons as seen in the DJF timeseries (Fig. 3.7 a) with deviations away from the mean ranging between approximately -1.5 to 3.5 in AMIP compared to a difference of 3.5 between the negative and positive deviations in MAM. While a robust signal appears in MAM, which is comparable to the annual signal in figure 3.5, it did not have an annual positive trend over NCG in figure 3.6 b and so therefore was not analysed any further. The large variability of DJF in these results is similar to results from other studies that highlights that greatest variability in the Arctic occurs in the boreal winter months (Serreze and Barry, 2005). Therefore, the fact that a signal emerges amongst this variability highlights the strength of this positive trend in DJF.

Furthermore, relative to the annual mean trends in ERAI, both UPSCALE and AMIP largely underestimate the strength of the annual mean eddy Z200 trends over NCG (Figs. 3.3 and 3.4). To account for the variability within the mean model states, the individual members of both AMIP and UPSCALE are assessed.

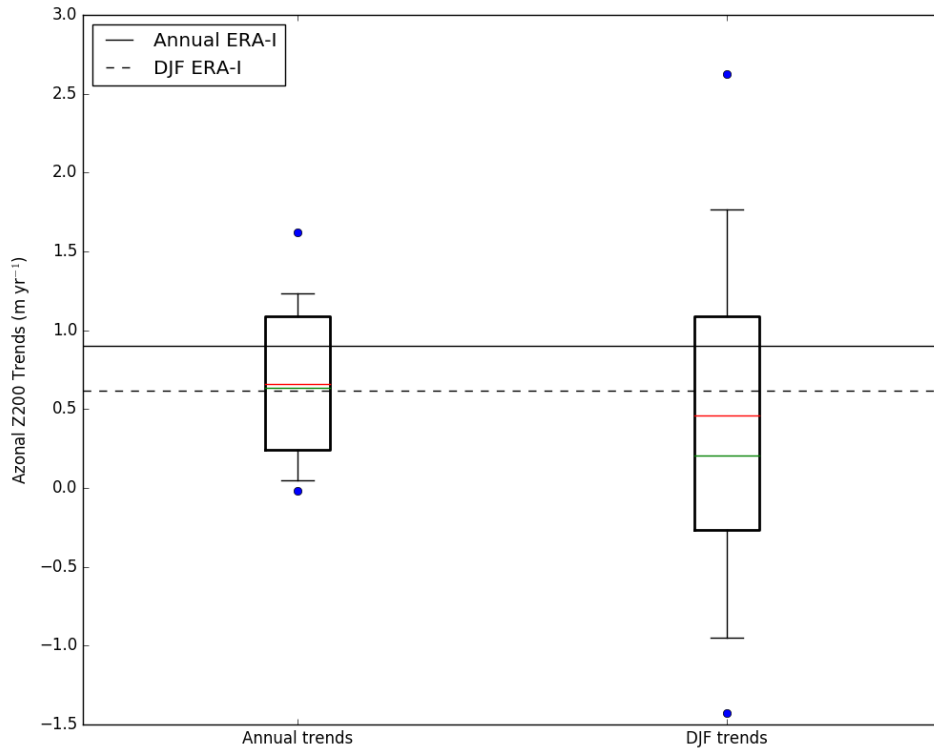


Fig. 3.8 Box and whisker plots representing the spread of all UPSCALE ensemble members for [a] annual trends in eddy Z200 over NCG and [b] DJF trends for NCG eddy Z200 from 1985-2011. Red and green solid lines in each represents the mean and median for the annual and DJF ensemble respectively. The solid and dashed lines highlight the annual and DJF ERAI trend over the same time period

Using box and whisker plots, the spread and variability of the eddy Z200 trends over NCG in the UPSCALE and AMIP ensemble and model members for both DJF and annual trends are assessed. There is a relatively large spread in the trends across all model members, particularly for DJF in both cases, where ranges in eddy Z200 DJF trends are between -1.0 to 2.0  $\text{m yr}^{-1}$  in UPSCALE ensemble members and between -1.2 to around 1.8  $\text{m yr}^{-1}$  (Fig. 3.8) in AMIP model members (Fig. 3.9) while annual trends for UPSCALE ensemble members are between 0 to 1.2  $\text{m yr}^{-1}$  (Fig. 3.8) and

between  $-0.5$  to  $0.8 \text{ m yr}^{-1}$  between the 5th and 95th percentiles (whiskers from each box) in AMIP model members (Fig. 3.9). Outliers (blue dots outside the 5th and 95th percentile whiskers) are found across all datasets; the largest in UPSCALE occurs in DJF and exceeds roughly  $2.7 \text{ m yr}^{-1}$  with similar outliers in AMIP DJF trends where two outliers exceed  $2.5 \text{ m yr}^{-1}$  and  $-1.7 \text{ m yr}^{-1}$ . This larger spread in winter, could be on account of two reasons, firstly as stated earlier, there is large variability in the Arctic over winter (Serreze and Barry, 2005) and secondly as annual trends encompass all seasons, there will be more smoothing across different seasons in the annual average which may dampen some outliers.

Most of the UPSCALE and AMIP model members in the annual and DJF trends are found to underestimate the NCG eddy Z200 trends relative to the ERAI trends for the same period. ERAI trends in all figures, highlighted by black solid and dashed lines for annual and DJF trends in boxplots in figures 3.8 and 3.9 respectively, both exceed the respective means for each dataset and each season and are around the upper quadrants (the 95th percentile) of boxplots with the majority of model members below this. This highlights that most model members have difficulty accurately simulating the eddy Z200 trends as seen in ERAI. However it must be noted, that even though, on average, the UPSCALE and AMIP models tend to underestimate the NCG eddy Z200 trends, in all cases, the ERAI trend lies well within the spread across the members of each dataset indicating that these model members are within the range of natural variability. The ERAI trends in all cases bar one, compared to the annual AMIP trends, are within the interquartile range for the spread of models, and in the case where it exceeds the interquartile range, it does not exceed the 95th percentile (the upper whisker).

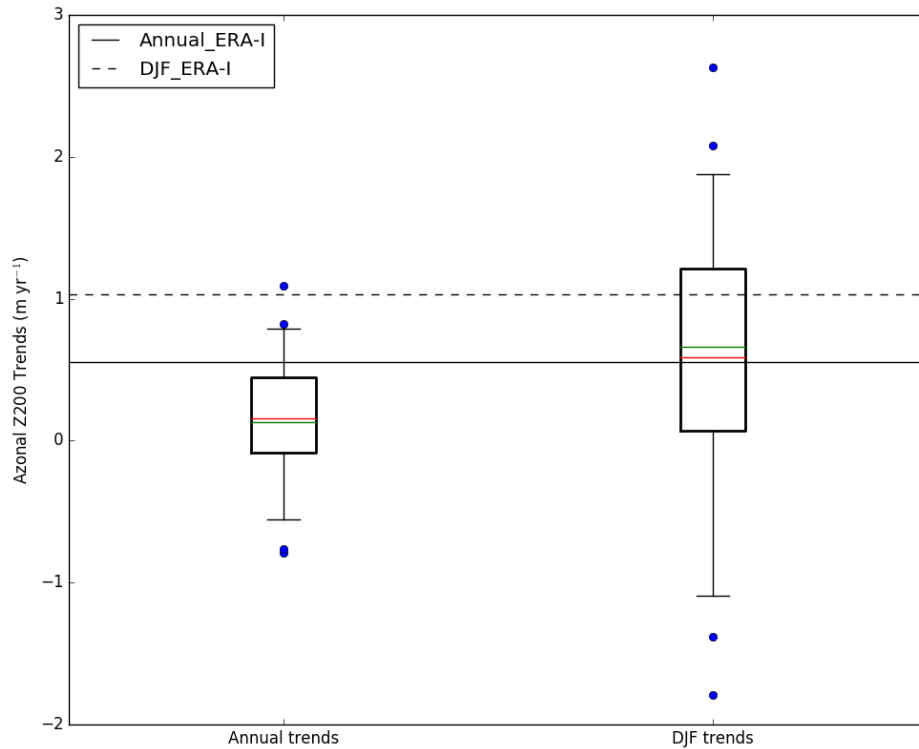


Fig. 3.9 Box and whisker plot of all AMIP model members for [a] annual and [b] DJF trends of eddy Z200 over NCG for 1979-2005. Red and green solid lines represent multi-model mean and median respectively. The solid and blue lines denote the annual and DJF trends in ERAI of eddy Z200 over NCG for 1979-2005.

The spread of the trends across UPSCALE and AMIP models are further quantified by assessing the spatial representation of annual and DJF trends across all model members. From UPSCALE, 31% and 30% of members (4 out of 13, (Fig. 3.10 c, g, h, i) and five out of thirteen in figures 3.11 a, c, f, g, h) produce a statistically significant positive annual and DJF eddy Z200 trend over the NCG region that is greater than ERAI. Only two of the thirteen members have large negative annual eddy Z200 trends (Fig. 3.10 b, e), but this increases to five in the trends for DJF. The other members in both the annual and DJF trends are either weakly negative or positive.

As UPSCALE is a resolution dependent dataset, I also assessed which resolution performed best at representing positive trends over NCG across the three different resolutions, N96, N216 and N512 for the annual eddy Z200 trends only. The UPSCALE

---

ensemble mean at N96 resolution, which contained five ensemble members, highlighted negligible to weak positive trends over NCG (as highlighted by the green dashed box), the UPSCALE ensemble mean at N216 resolution, containing three members had strong positive eddy Z200 trends over NCG and at N512 resolution, containing five members had weak positive trends over NCG. These results indicate that model resolution of N216, which is the equivalent to 60km, is the best resolution at simulating trends similar to those found in ERAI data.

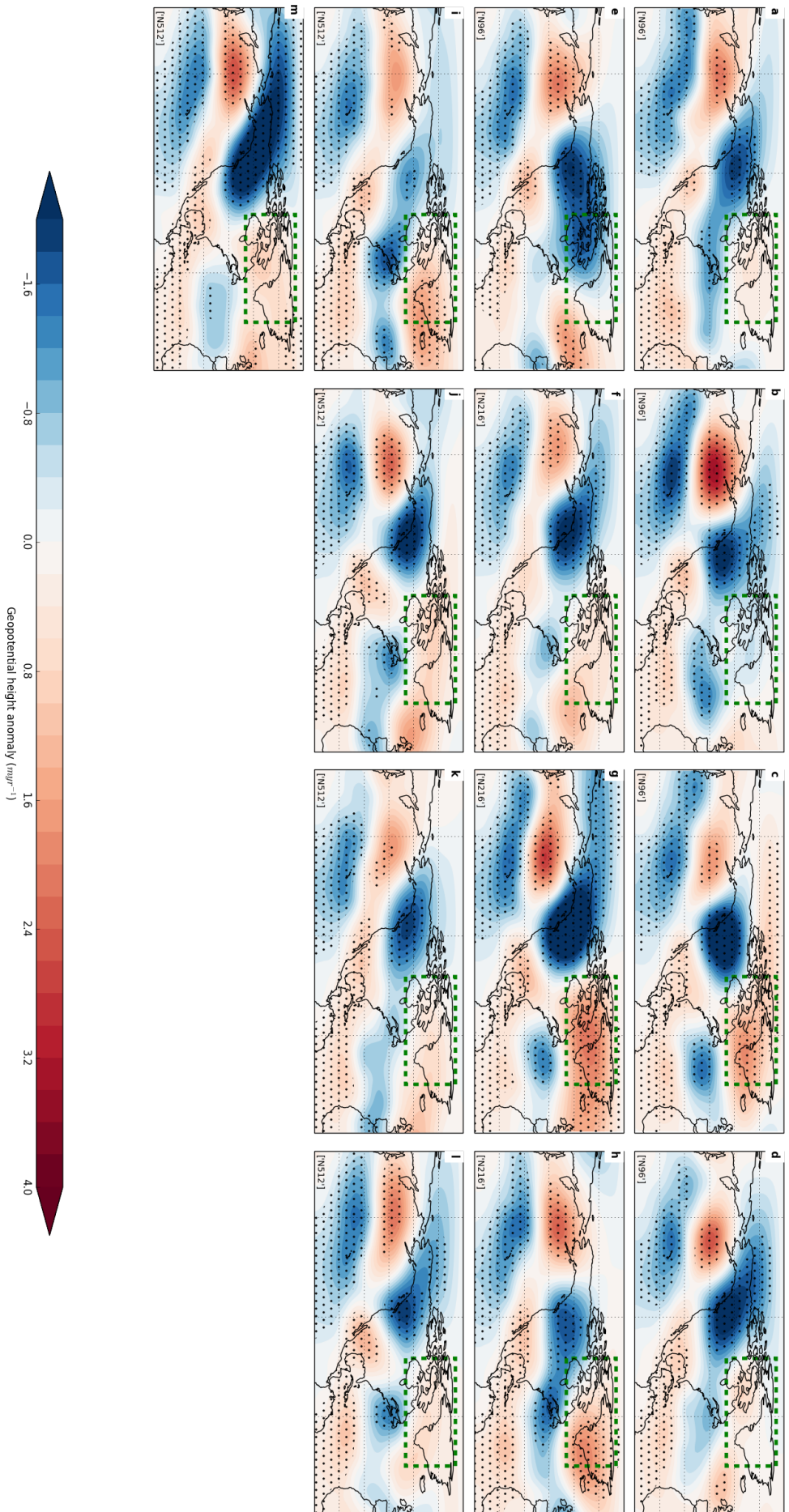


Fig. 3.10 Annual trends in eddy Z200 for all 13 UPSCALE ensemble members from 1985-2011 of [a-e] N96 resolution (130 km), [f-h] N216 resolution (60 km), [i-m] N512 resolution (25 km). The stippling denotes statistical significance ( $p < 0.05$ )

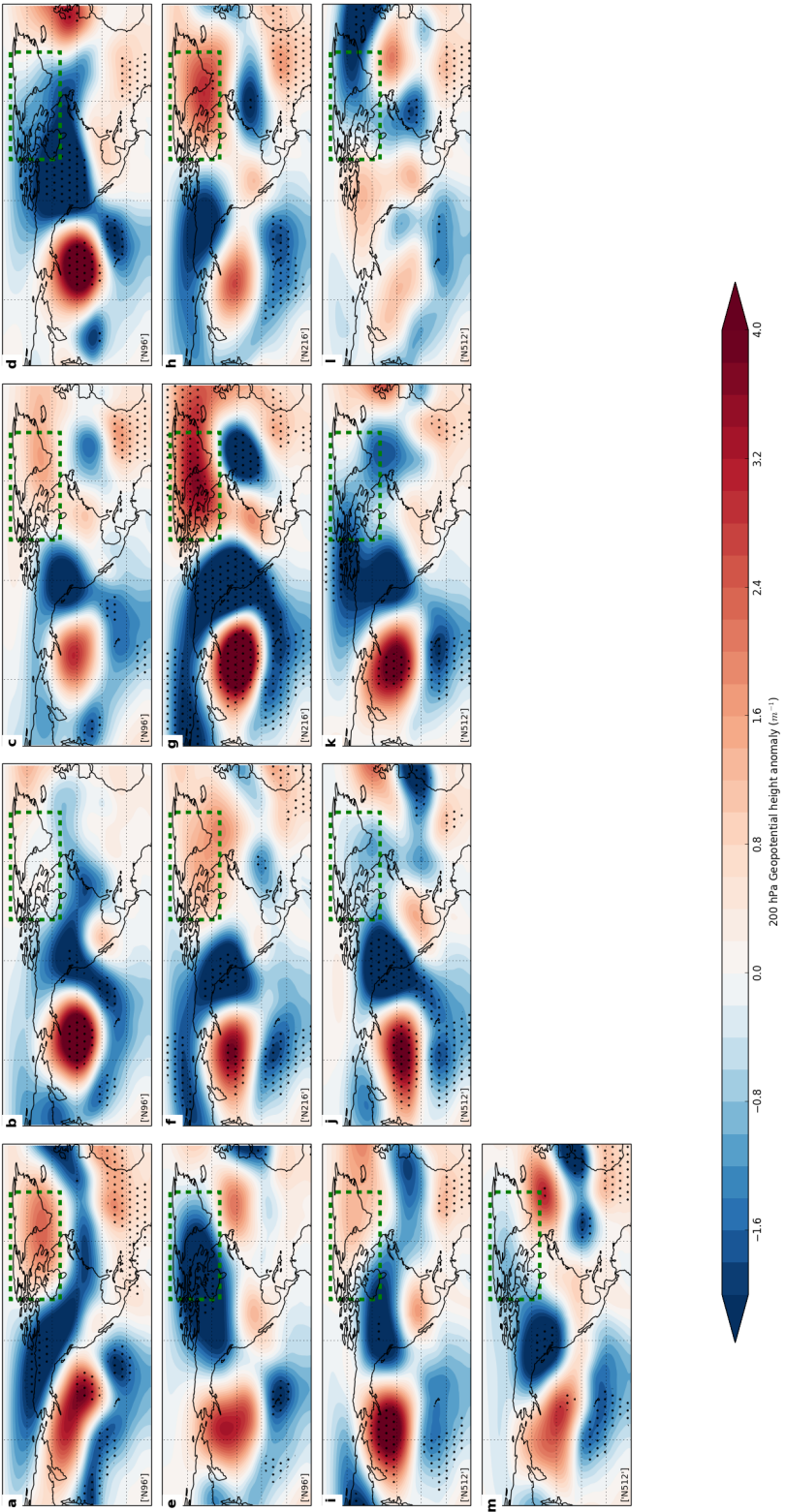


Fig. 3.11 DJF trend in eddy Z200 for all 13 UPSCALE ensemble members from 1985-2011 for [a-e] N96 resolution (130 km), [f-h] N216 resolution (60 km) and [i-m] N512 resolution (25 km). NCG is denoted by green dashed box

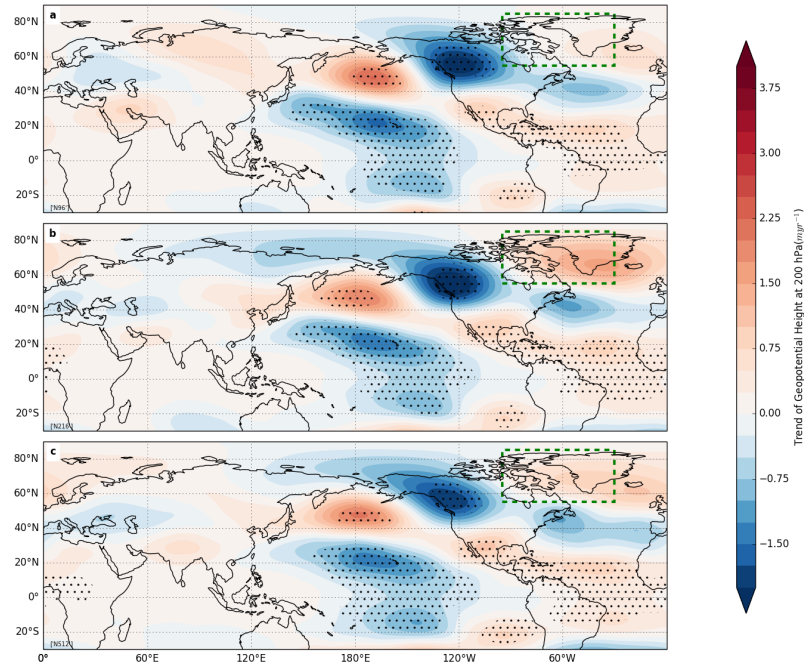


Fig. 3.12 Annual trends in eddy Z200 of UPSCALE ensemble means for [a] 5 models at N96 resolution, [b] 3 models at N216 resolution and [c] 5 models at N512 resolution. Stippling indicates statistical significance at  $p < 0.05$

AMIP model trends, due to their large number, are split between those which are greater than the ERAI mean (AMIP-GTE) and less than the ERAI mean (AMIP-LTE), as found through the annual AMIP boxplot (Fig. 3.9). A full list of all models and which of these groups they are in is listed in table 3.1. Unsurprisingly, there are more AMIP model members that are less than the ERAI mean (23 in annual trend, 20 in DJF trend), as the boxplots for annual and DJF trends indicated. The strength of the negative trends, however varies substantially between models, with only six to seven displaying large statistically significant negative annual and DJF eddy Z200 trends, six to eight with weak negative trends and the rest (38%) displaying weakly positive trends. The AMIP-GTE models had seven (ten) model members for annual (DJF) positive eddy Z200 trends that were greater than ERAI (Figs. 3.15 and 3.16). Similarly to AMIP-LTE, the strength of these trends over NCG varied across the difference model members, with differences in the annual trends ranging from approximately  $1 \text{ m yr}^{-1}$  between the strongest HadGEM2-A (Fig. 3.15 c) and weakest bcc-csm1-1-m (Fig. 3.15 a) and as much as  $2 \text{ m yr}^{-1}$  in DJF

trends between HadGEM2-A (approximately  $1.8 \text{ m yr}^{-1}$ ) (Fig. 3.16 d) and CanAM4 (approximately  $0.4 \text{ m yr}^{-1}$ ) (Fig. 3.16 b).

Variance across all the members of UPSCALE and AMIP show the potential role of atmospheric variability in driving the trends of eddy Z200 over NCG, as the annual ERA-Interim trends of eddy Z200 fell within the range of the modelled trends. However, some model members, roughly 60-70% of annual and DJF trends in AMIP-GTE and in all UPSCALE members, where the trends over NCG were positive, simultaneously occurred with a tripole of anomalous trends of alternating signs that meridionally span the Pacific ocean from the tropical Pacific to north Pacific. This highlights a potential tropical influence or some remote influence on positive trends over NCG.

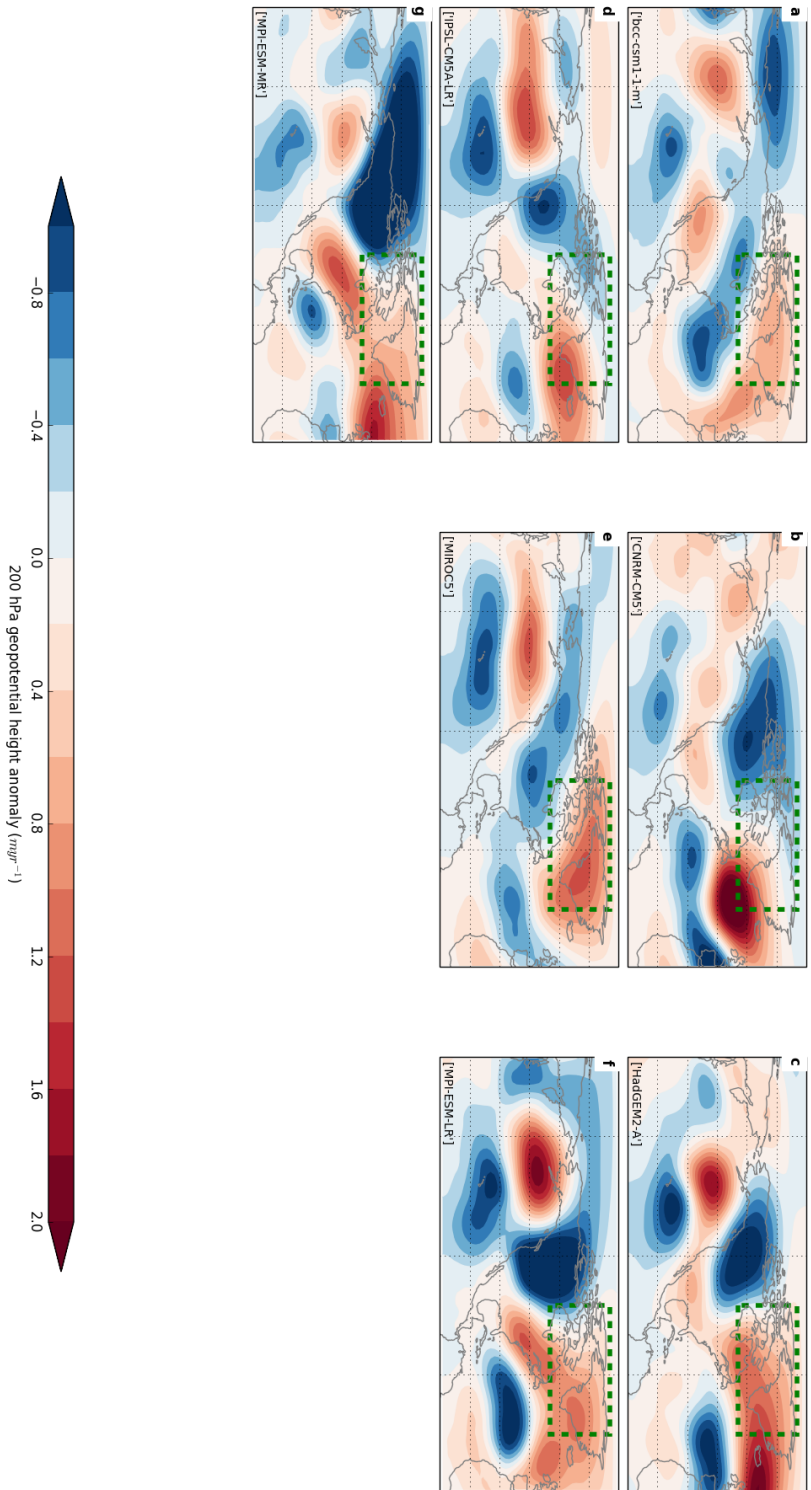


Fig. 3.13 Annual trend (1979-2005) of all AMIP models whose trend of eddy Z200 over NCG was greater than the ERAI mean over the same area (AMIP-GTE). NCG domain is outlined by green dashed box

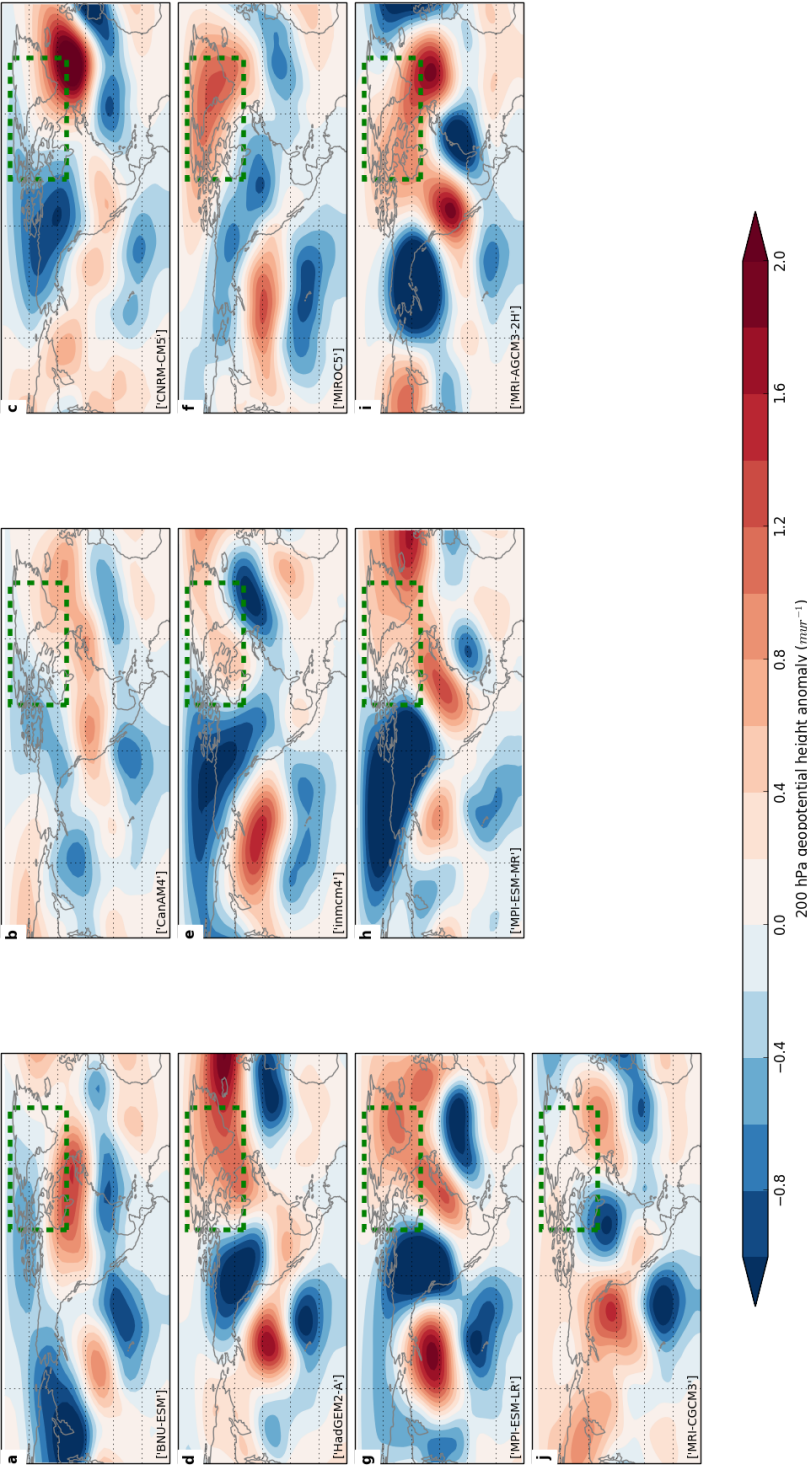


Fig. 3.14 The DJF trend in eddy Z200 of AMIP models whose model mean trend of eddy Z200 over NCG was greater than ERAI (AMIP-GTE) with NCG region highlighted by green dashed box

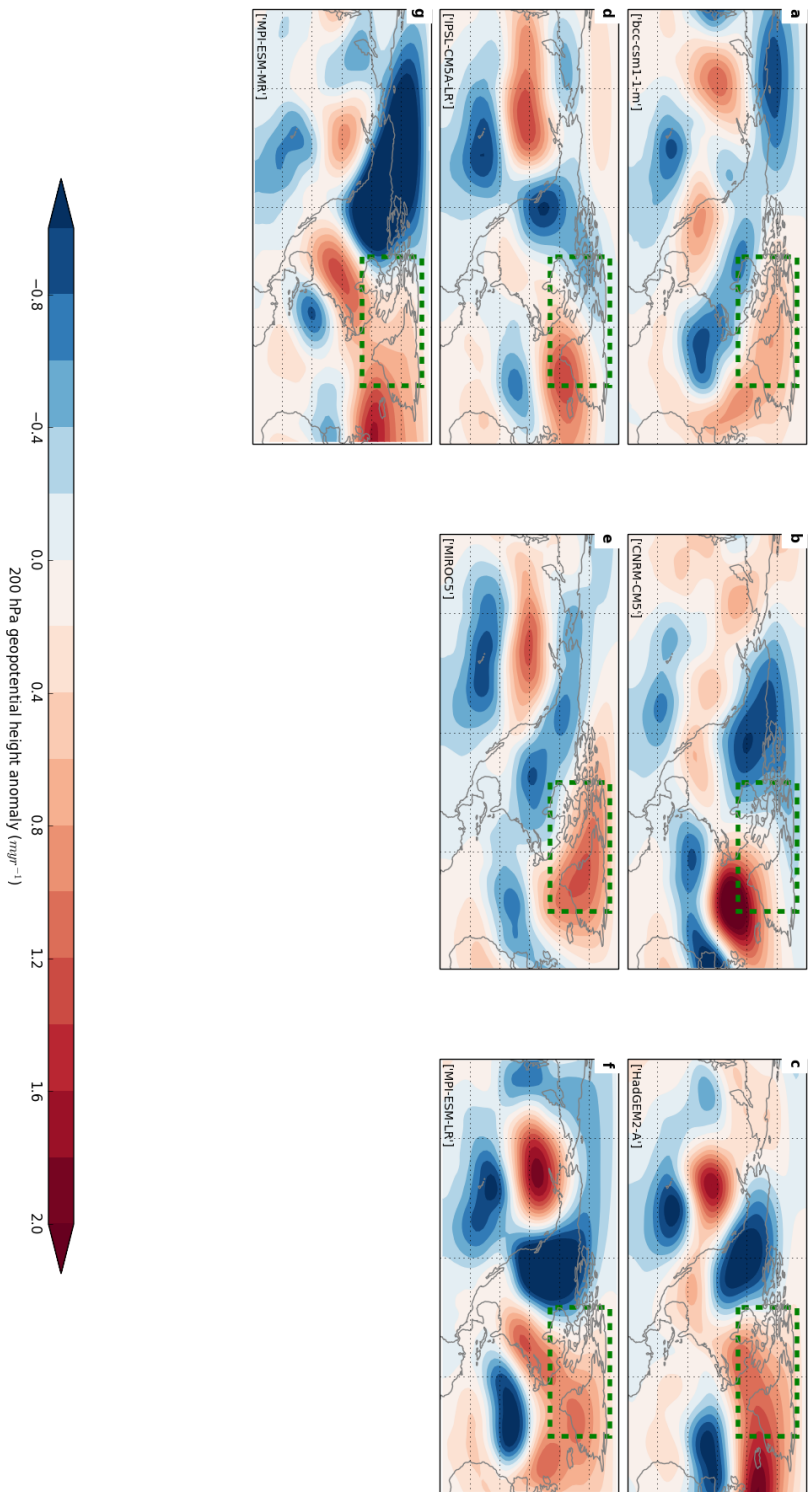


Fig. 3.15 Annual trend (1979-2005) of all AMIP models whose trend of eddy Z200 over NCG was greater than the ERAI mean over the same area (AMIP-GTE). NCG domain is outlined by green dashed box

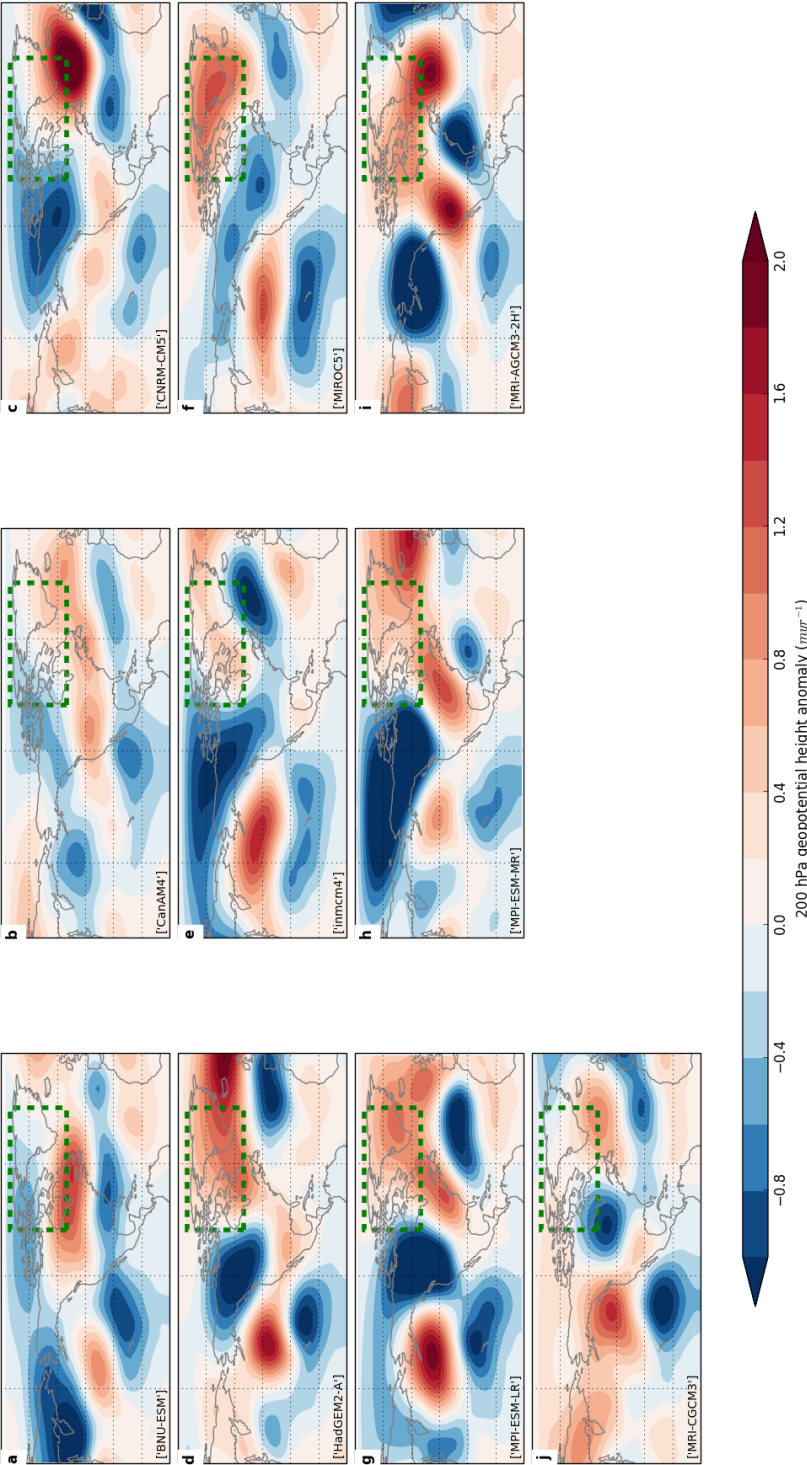


Fig. 3.16 The DJF trend in eddy Z200 of AMIP models whose model mean trend of eddy Z200 over NCG was greater than ERAI (AMIP-GTE) with NCG region highlighted by green dashed box

Overall, these results highlight that there is a large spread of intra-ensemble and inter-model variability in the strength and position of the anomaly, with both datasets tending to simulate weaker annual and DJF eddy Z200 trends relative to ERAI over the same period. This appears due to the fact that members within each dataset, and specifically for AMIP, have more models that simulate negative trends in the annual and DJF eddy Z200. The root mean squared error (RMSE) and scatterplots of annual means of eddy Z200 for UPSCALE and AMIP members and means relative to ERAI are calculated to give a more robust measure of the spread of model trends relative to observed trends. Scatterplots for AMIP (Fig. 3.19) and UPSCALE members (Fig. 3.20) shows considerable spread around their respective regression lines (in green in all figures) indicating that the predicted values, or the model results, either are subject to large variability or do not perform well at simulating ERAI eddy Z200 values over NCG. In AMIP, HadGEM2-A (Fig. 3.19 s) has the lowest RMSE score of 1.08, displaying much similar trends to ERAI as found in its annual and DJF spatial trends (Figs. 3.15 c and 3.16 d respectively) which have large positive eddy Z200 trends over NCG. The model member shown in panel W (Fig. 3.19 w), which corresponds to model IPSL-CM5B-LR, has an RMSE score of 1.55 and differs greatly to the ERAI trends as also evidenced in its annual and DJF trends in figures 3.17 s and 3.18 q, where it has a large negative eddy Z200 trend over NCG and also no distinctive trends in the Pacific similar to ERAI.

In UPSCALE, where model resolution is the most prominent difference between ensemble members, it appears that a higher resolution does not necessarily result in better, more accurate simulations, as both the best performing and worst performing member[s] are of the N96 resolution. Ensemble member shown in panel c (Fig. 3.20 c) performed the best, according to its RMSE score of 0.97 while ensemble member shown in panel b (Fig. 3.20 b) performed the worst with a RMSE score of 1.45.

The RMSE of AMIP multi-model and UPSCALE ensemble mean (Fig. 3.22) are much better than their respective members. This however is to be expected as a great deal of variability is smoothed over in the averaging process of all models therefore allowing the most important trends to prevail.

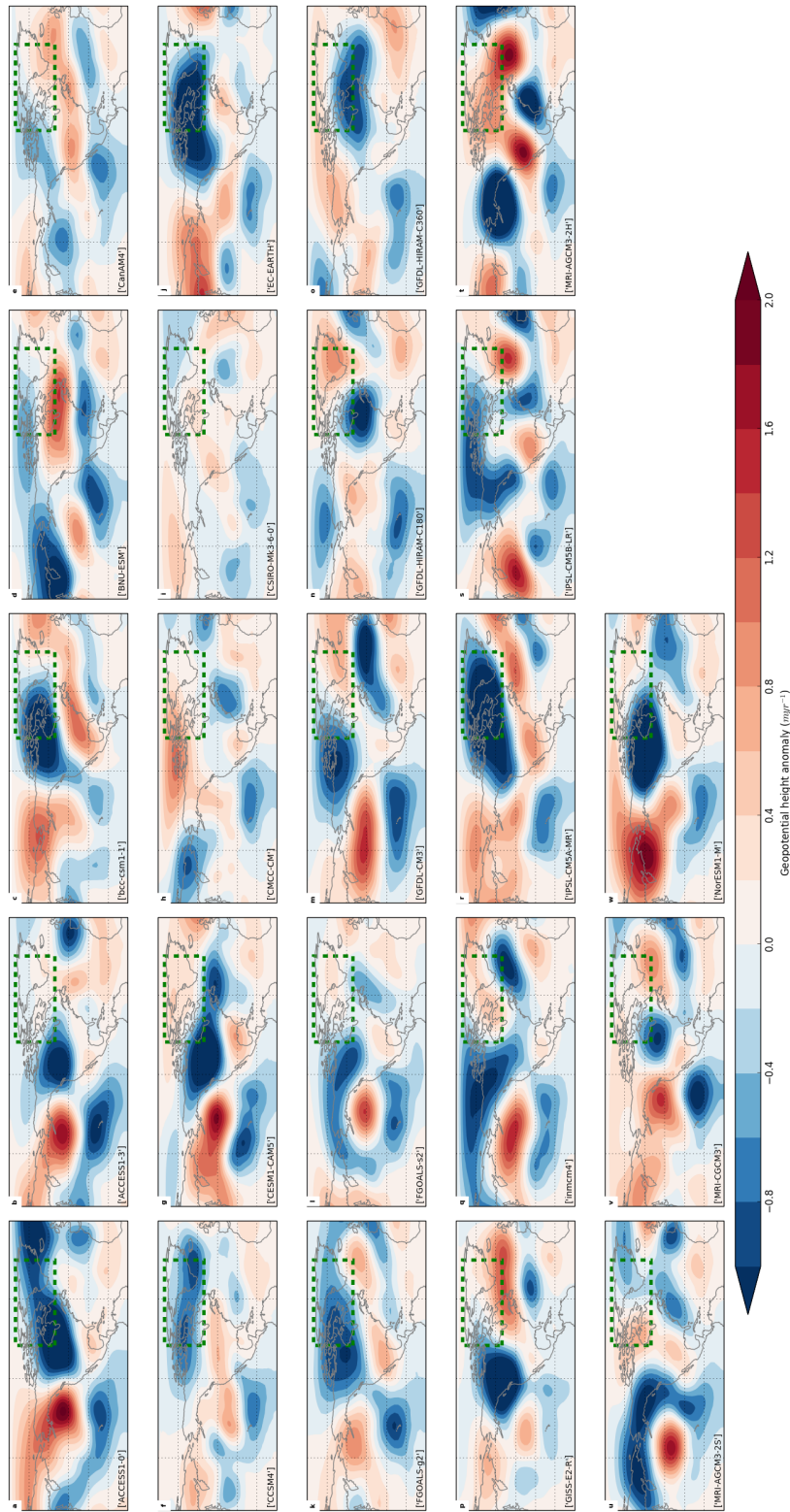


Fig. 3.17 Annual trend (1979-2005) of all AMIP models whose trend of eddy Z200 over NCG was less than the ERAI mean over the same area (AMIP-LTE). NCG region is outlined by green dashed box

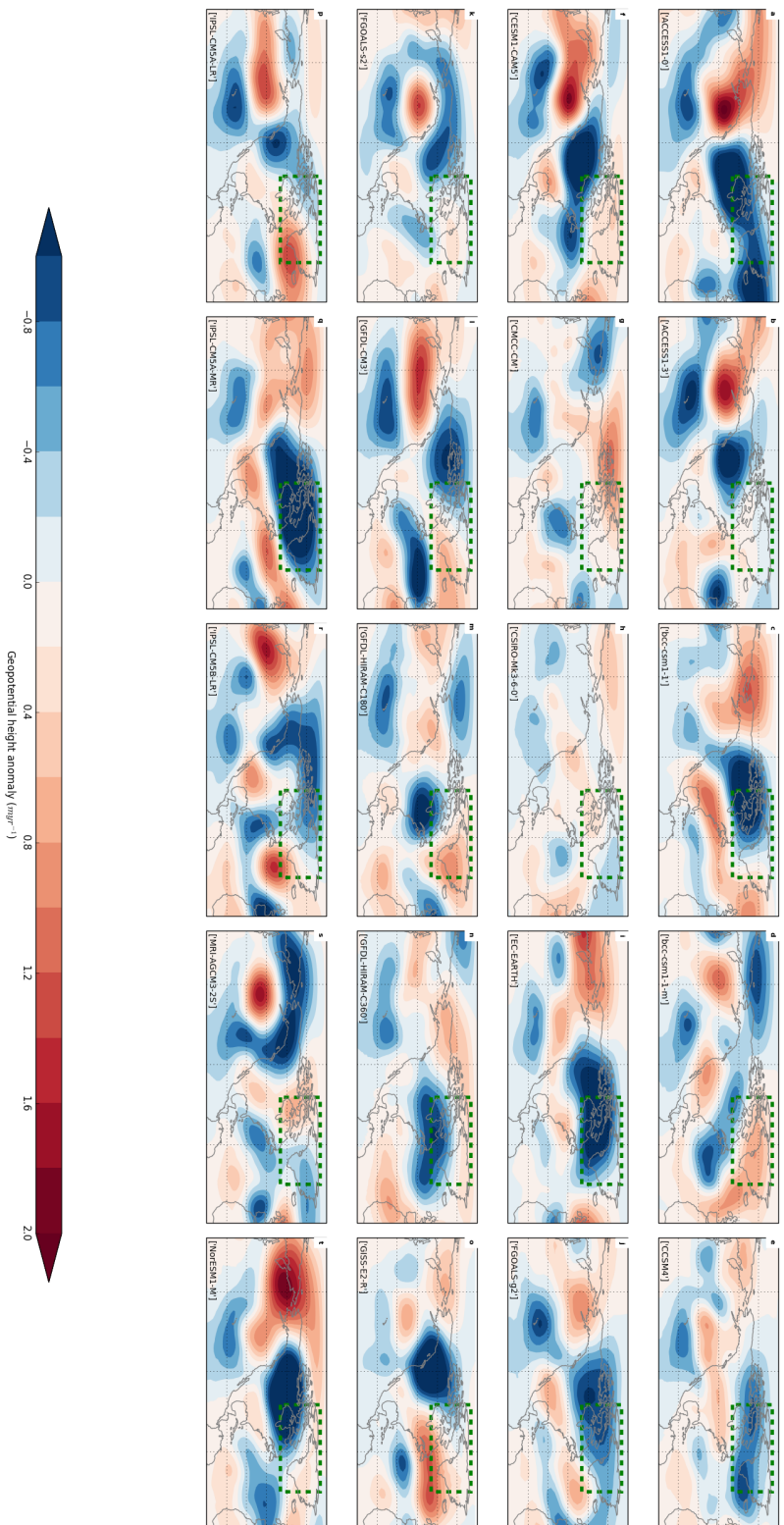


Fig. 3.18 The DJF trend in eddy Z200 of AMIP models whose model mean trend of eddy Z200 over NCG was less than ERAI (AMIP-LTE) with NCG region highlighted by green dashed box

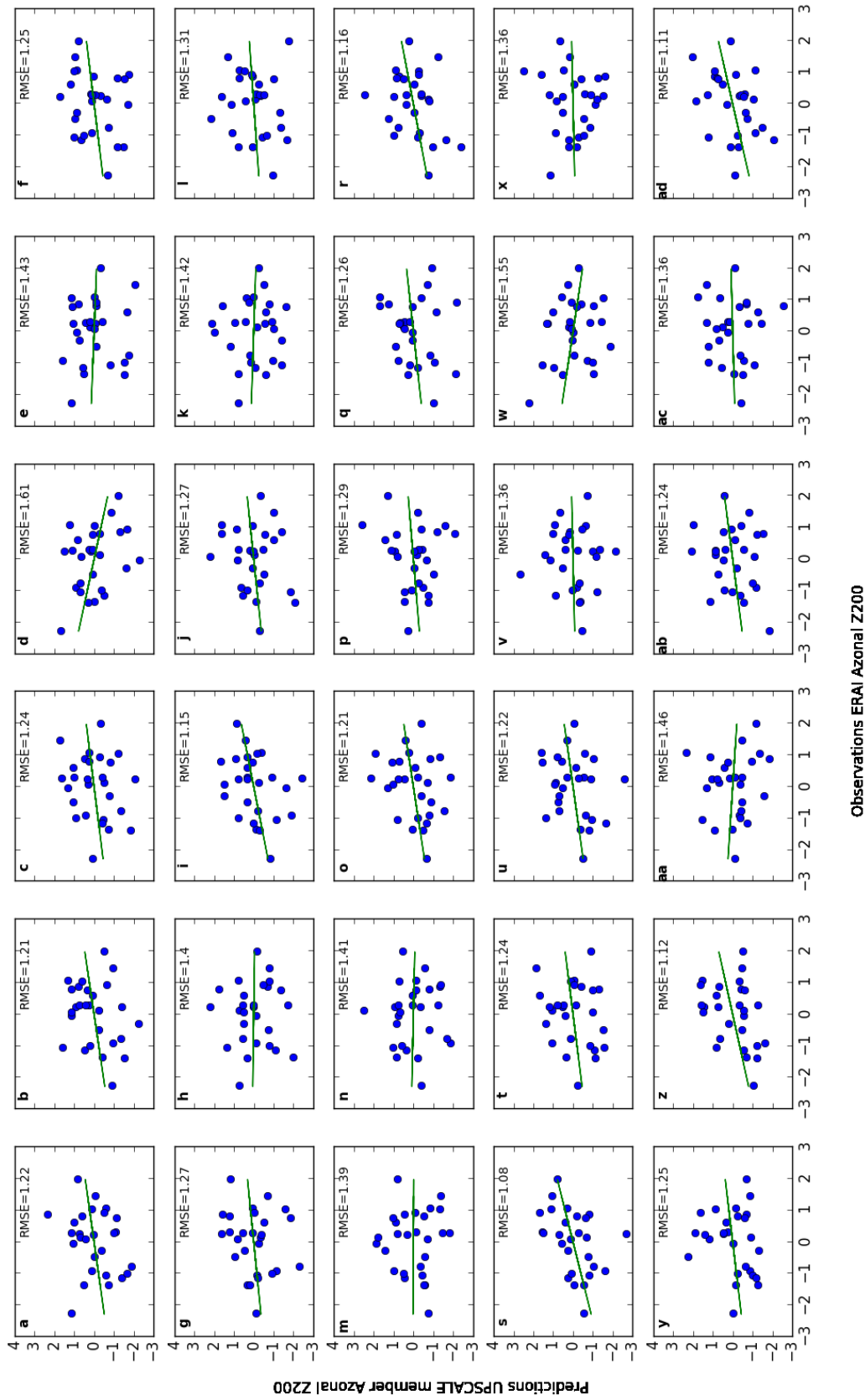


Fig. 3.19 Scatter plots of all AMIP models showing annual eddy Z200 data over NCG compared to ERAI annual eddy Z200 data from 1979-2005. Red line depicts regression line. Root mean square error of each model is highlighted in bottom right hand corner

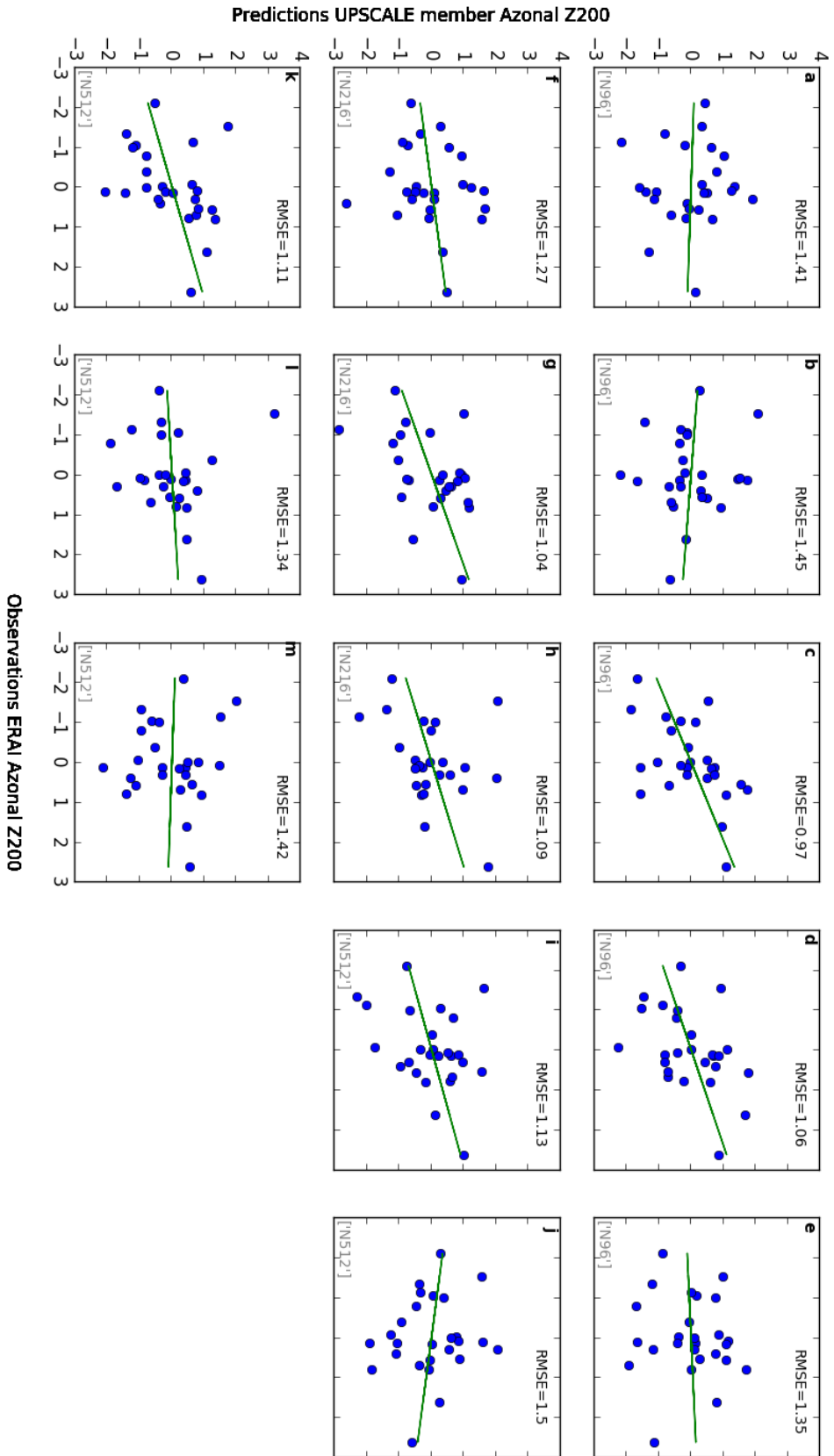


Fig. 3.20 Scatter plots of all UPSCALE members showing the annual eddy Z200 data over NCG compared to ERAI from 1985-2011 with red line depicting the linear regression line. Root mean square error of each model is highlighted in bottom right hand corner of each plot

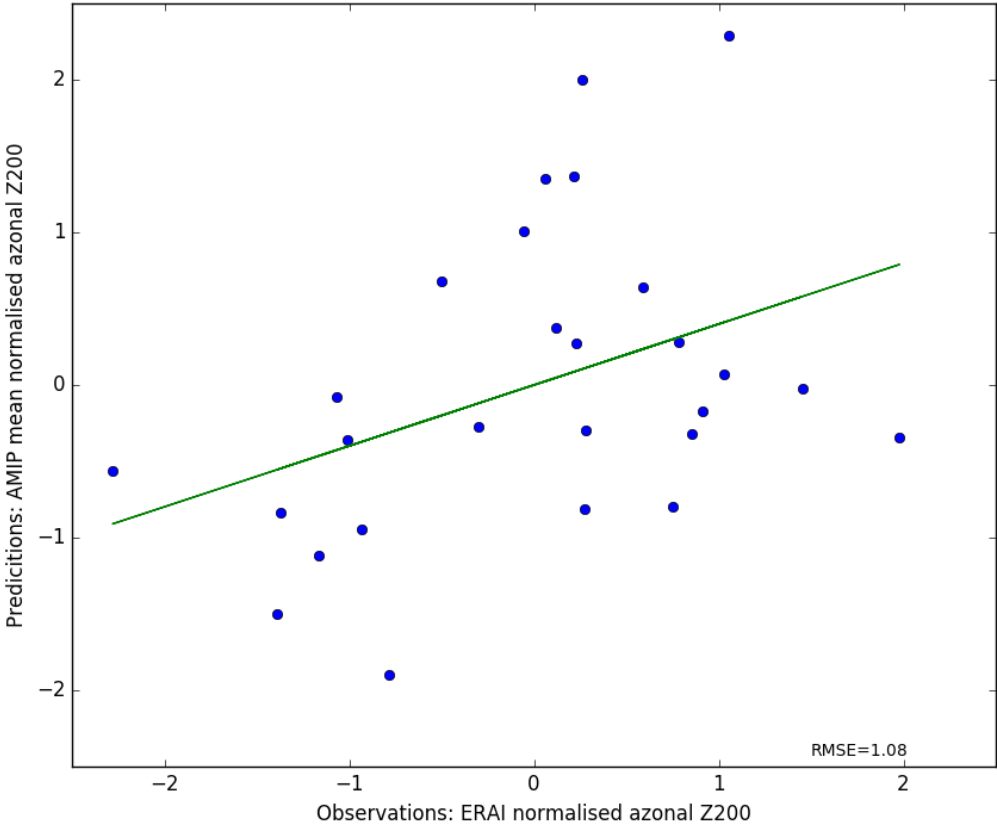


Fig. 3.21 Scatter plot of the AMIP multi-model mean annual eddy Z200 data over NCG with red line highlighting the linear regression line. Root mean square error for the multi-model mean is noted in the bottom right hand corner

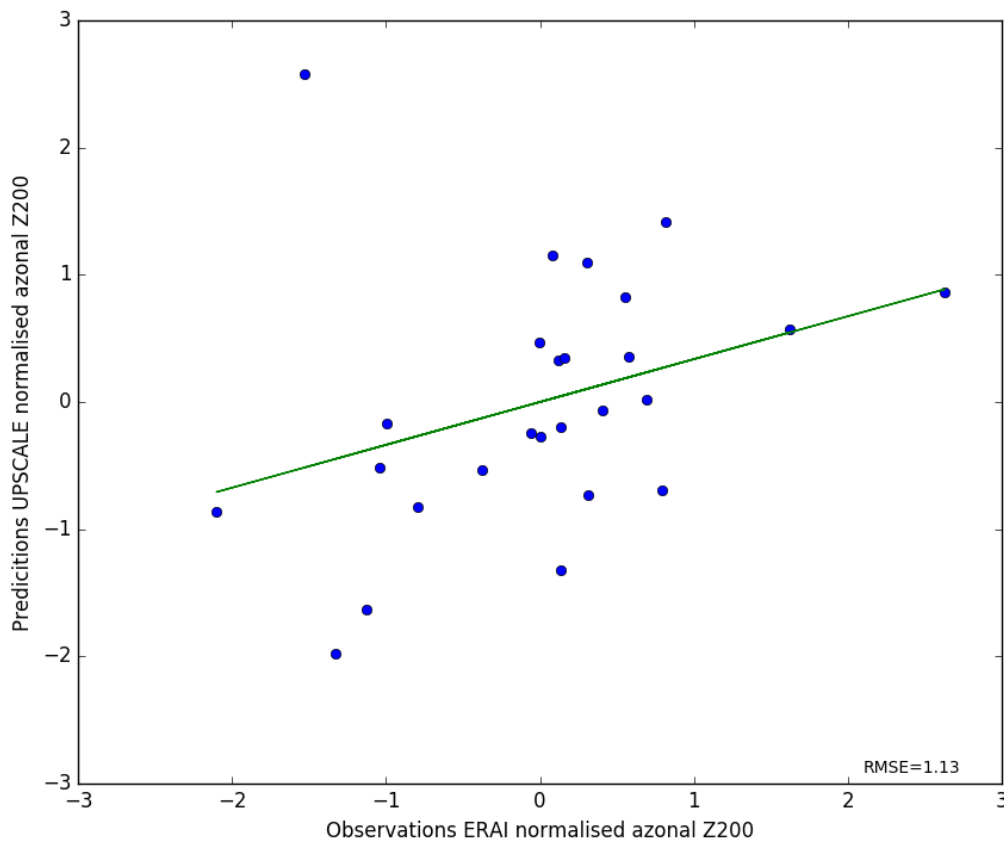


Fig. 3.22 Scatter plot of the UPSCALE ensemble mean annual eddy Z200 data over NCG with red line highlighting the linear regression line. Root mean square error for the UPSCALE ensemble mean is noted in the bottom right hand corner

These results indicate that there is a large contribution of variability in eddy Z200 trends over NCG where multi-model and ensemble means are able to fairly accurately simulate climate relative to ERAI. The accurate simulation of the eddy Z200 trends in the Pacific, a tripole pattern of eddy Z200 trends of alternating sign that propagate from the Pacific to Alaska, seem to be important in accurately simulating the eddy Z200 trends over NCG. This is because models that result in strong positive NCG eddy Z200 trends displaying very similar Pacific trends relative to ERAI. This indicates that for an accurate NCG trend, that tropical regions may play a role in this pattern. It must also be noted that the the AMIP model with the lowest RMSE and very similar eddy Z200

Index	Model Name	Annual	DJF
a	ACCESS1-0	AMIP-LTE	AMIP-LTE
b	ACCESS1-3	AMIP-LTE	AMIP-LTE
c	bcc-csm1-1	AMIP-LTE	AMIP-LTE
d	bcc-csm1-1-m	AMIP-GTE	AMIP-LTE
e	BNU-ESM	AMIP-LTE	AMIP-GTE
f	CanAM4	AMIP-LTE	AMIP-GTE
g	CCSM4	AMIP-LTE	AMIP-LTE
h	CESM1-CAM5	AMIP-LTE	AMIP-LTE
i	CMCC-CM	AMIP-LTE	AMIP-LTE
j	CNRM-CM5	AMIP-GTE	AMIP-GTE
k	CSIRO-Mk3-6-0	AMIP-LTE	AMIP-LTE
l	EC-EARTH	AMIP-LTE	AMIP-LTE
m	FGOALS-g2	AMIP-LTE	AMIP-LTE
n	FGOALS-s2	AMIP-LTE	AMIP-LTE
o	GFDL-CM3	AMIP-LTE	AMIP-LTE
p	GFDL-HIRAM-C180	AMIP-LTE	AMIP-LTE
q	GFDL-HIRAM-C360	AMIP-LTE	AMIP-LTE
r	GISS-E2-R	AMIP-LTE	AMIP-LTE
s	HadGEM2-A	AMIP-GTE	AMIP-GTE
t	inmcm4	AMIP-LTE	AMIP-GTE
u	IPSL-CM5A-LR	AMIP-GTE	AMIP-LTE
v	IPSL-CM5A-MR	AMIP-LTE	AMIP-LTE
w	IPSL-CM5B-LR	AMIP-LTE	AMIP-LTE
x	MIROC5	AMIP-GTE	AMIP-GTE
y	MPI-ESM-LR	AMIP-GTE	AMIP-GTE
z	MPI-ESM-MR	AMIP-GTE	AMIP-GTE
aa	MRI-AGCM3-2H	AMIP-LTE	AMIP-GTE
ab	MRI-AGCM3-2S	AMIP-LTE	AMIP-LTE
ac	MRI-CGCM3	AMIP-LTE	AMIP-LTE
ad	NorESM1-M	AMIP-LTE	AMIP-LTE

Table 3.1 List of all AMIP models and identification of which are in AMIP-LTE and in AMIP-GTE

trends to ERAI, HadGEM2-A is an earlier version of the model used in UPSCALE and the one to be used for further analysis on this study, thus providing further confidence in the ability of HadGEM models to accurately simulate Arctic climate, and specifically NCG patterns.

### 3.5 Concluding remarks

Analysis of the eddy Z200 trends over NCG for ERAI, UPSCALE and AMIP have shown that this signal is a robust feature as it is found across all datasets, and within ensemble and model members. There is an apparent dependency of the strength of the positive NCG trend on the time period, where it tends to be stronger within the UPSCALE record (1985 to 2012) than the AMIP record (1979 to 2005). This appears to be specifically due to a large positive anomaly in the middle of the time record, within the 1990s, which results in a stronger trend in the later period and which may have been why the trend in the AMIP models were weaker than in UPSCALE. It was also found that the trends amongst the different models and ensemble members in the AMIP and UPSCALE datasets did have a large spread around the ERAI trend. The large spread of models indicates the potential role of internal atmospheric variability in the positive eddy Z200 trends over NCG. UPSCALE, for example, had roughly the same number of models which simulated positive and negative eddy Z200 trends over NCG along with a few with no or negligible trends. While more AMIP models were within the AMIP-LTE group, while their trends over NCG were less than the ERAI mean trend for the same period, some of these models displayed positive NCG eddy Z200 trends. This indicates that while strength of the trend was not accurately simulated, AMIP model members still captured positive eddy Z200 trends over NCG. Nonetheless, as the ERAI trends, which are only one potential realisation of climate, fell amongst the models spread, this indicates that internal variability is important in these trends. As both UPSCALE and AMIP are forced with transient SSTs for each of their respective times, and are comparable to ERAI trends, it would seem that these trends are driven by changes in SSTs and with the Pacific trends so prominent in accurate NCG trend simulation, a tropical component also

---

appears to be important. The remaining chapters will further investigate the potential tropical influence on eddy Z200 over NCG.



# Chapter 4

## The tropical influence on NCG

### 4.1 The role of the tropics in high latitudes

The tropical influence on global climate is well known (Trenberth et al., 1998). Changes in tropical sea surface temperatures (SSTs) can have wide-reaching implications on weather and climate in regions thousands of kilometres away (Ciasto et al., 2014; Liu and Alexander, 2007; Sheridan and Lee, 2012), with many studies showing that these can be as far-reaching as the Antarctic and Arctic. Li et al. (2014) found that sea surface warming in the Atlantic, related to the Atlantic Meridional Oscillation, led to a reduction in surface pressure over the Amundsen Sea due to the generation and propagation of Rossby waves from the tropical Atlantic. Sea surface changes in the Pacific have also been found to affect the Antarctic and Arctic with anomalous SSTs across the central tropical Pacific resulting in warming over the West Antarctic, specifically over the the Amundsen sea due also to Rossby waves from the central tropical Pacific which advected heat in to the region (Ding et al., 2011). The positive trends in geopotential heights at 200 hPa (Z200) over north Canada and Greenland (NCG), investigated in the previous chapter, have been credited as a response to tropical SST forcing in the Pacific Ocean by Ding et al. (2014). Through analysis of observations and model simulations, they found an anomalous poleward propagating Rossby wave train that emanated from the tropics,

resulted in positive trends of surface warming and of Z200 over NCG. Their model was forced with transient observed SSTs in the tropics but had the extratropical atmosphere that was coupled to a slab ocean and a thermodynamic sea-ice component, meaning that climate trends may have been influenced by a more localised forcing and therefore may not be the direct result of the imposed tropical SST forcing.

This chapter will aim to further the understanding of tropic-NCG teleconnections by investigating the direct effect of recent tropical SST patterns on the NCG region. Initially, wave activity flux trends, derived from Plumb (1985), are calculated for each observational and model dataset discussed in the previous chapter (ERA-Interim, UPSCALE and AMIP) to ascertain if poleward propagating waves from the tropics are a prominent feature in these data. Secondly, the role of anomalous tropical forcing on NCG climate is found directly through running a series of time-slice model experiments, forced only by anomalous SSTs. As described in Chapter 2, these model experiments perturb SSTs between 30°N and 30°S with SST anomalies taken from 10 year monthly averages of 2003-2012 relative to 1979-1988. These anomalies are then doubled to increase the magnitude of forcing, with climatological SSTs (1979-1988) used elsewhere (full details of model design and experiments explained in greater detail in chapter 2). All other forcings such as sea-ice, CO<sub>2</sub> and aerosols are fixed in the model. Finally, the role of extratropical SSTs in potential amplification or dampening of tropical signals is investigated to understand whether forcings in these regions may play a role in signals that emerge over NCG. These experiments and analysis were set up with the aim to address the following questions, [1] Do observation and modelled datasets capture a poleward propagating trend emanating from the tropics? [2] How does the NCG directly respond to a tropical only forcing from HadGEM3?, [3] What role, if any do extratropical SSTs have in tropical signal over NCG?

All analysis throughout this chapter focuses specifically on response of tropical forcings in boreal winter months (DJF) as analysis in chapter 3 highlighted that the NCG anomaly was most pronounced then, and it is the season when generation and propagation of Rossby waves are strongest in the northern hemisphere (Strong and Davis, 2008; Trenberth et al., 1998).

## 4.2 Tropically induced wave trends in observational data

The sources of the largely positive eddy Z200 trends over NCG, as found from results presented in chapter 3, are now explored. The wave activity flux (WAF); a three-dimensional measure of the flux of wave activity derived for linear quasi-geostrophic (QG) disturbances to the flow by Plumb (1985), as described in chapter 2, is calculated to highlight the propagation of wave trains and thus the dynamical pathways for a potential tropical influence on climate in the northern high latitudes. This analysis is applied to all three datasets from chapter 3 (ERA-Interim, UPSCALE and AMIP) to assess whether wave trends between the tropics and northern high latitudes exist and whether these are consistent between the different datasets.

The annual mean trends of WAF for the UPSCALE ensemble mean (1985-2011), and AMIP multi-model mean (1979-2005) share many similar features to the WAF trend in ERA-Interim for 1979 to 2012 (Fig. 4.1). ERA-Interim WAF trend (Fig 4.1 a), plotted in black vectors, on top of the eddy Z200 trends as shown in chapter 3, show a strong poleward propagating wave train originating in the tropical Pacific ocean. This propagates poleward across the north Pacific Ocean, in an arc-like trajectory over North America and NCG before propagating equatorward over the north Atlantic ocean. This wave train mirrors the wave trains presented in Ding et al. (2014) and Trenberth et al. (2014) over an annual and NDJFM period, suggesting from Trenberth et al. (2014) that this is a predominantly boreal winter signal. Both the UPSCALE ensemble and AMIP multi-model means have similar WAF trends, with anomalous wave trains originating in the tropical Pacific and propagating poleward, projecting on to a negative eddy Z200 anomaly over Alaska. However the WAF trends further downstream differ from ERA-Interim. The UPSCALE ensemble mean WAF trend shows some propagation towards NCG, but not completely across it suggesting the strength and direction of propagation of the WAF trends in ERA-Interim are not fully captured in UPSCALE. Some equatorward propagation can be seen, however, this remains mainly over North America and not over the Atlantic ocean as in the aforementioned studies. The AMIP multi-model mean WAF trends, similarly to the

UPSCALE ensemble means, show some propagation in the direction of NCG, however immediately downstream of the Alaskan negative eddy Z200 anomaly, the WAF trends tend to propagate equatorwards towards the tropical Atlantic. This arc-like trajectory from the Pacific to the Atlantic ocean does bear some resemblance to the ERAI trends and those from Ding et al. (2014) and Trenberth et al. (2014). However, it is evident that the magnitude of the WAF trend is underestimated in the AMIP multi-model mean and is thus unable to propagate on to NCG. A second wave train, trapped within the tropical regions propagating only between the tropical Pacific and Atlantic oceans is found in all three datasets, demonstrating the models ability to capture tropical features, as described by Scaife et al. (2017) and Branstator (1983) however, as this feature does not propagate towards high latitudes, it is not further analysed.

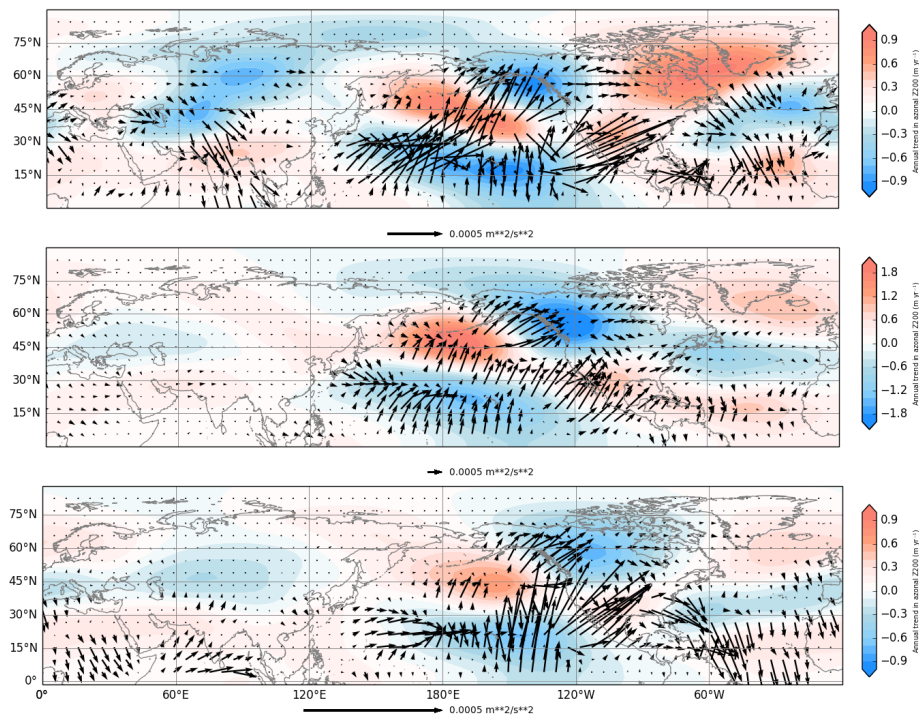


Fig. 4.1 Annual spatial trends of eddy Z200 in metres per year in coloured contours and WAF trends in black vectors for [a] ERAI from 1979-2012, [b] UPSCALE ensemble means from 1985-2011 and [c] AMIP multi-model means from 1979-2005. Vector scaling differs for each dataset and subsequent vector scaling can be found immediately below each figure.

Figure 4.1 shows there is a poleward propagating wave train, emanating from the tropical Pacific, present in the trends of all datasets suggesting a tropical influence on northern high latitude climate trends. Differences between the model simulations and ERAI reanalysis in the propagation downstream from Alaska and on to the NCG region which may be a result of model errors, as discussed in the previous chapter. Nonetheless the direct influence of tropical SSTs on the WAF trends cannot be directly concluded from these datasets, since there are a variety of factors that are changing throughout time that may also impact on the circulation. As described in chapter 2, a number of model sensitivity experiments were performed to gain a more thorough understanding of the tropical influence on NCG and the mechanisms behind this.

### **4.3 The NCG response to a modelled tropical forcing**

To briefly recap from chapter 2, the TropSST model experiment perturbs sea surface temperatures within the tropical region between 30°S to 30°N at all longitudes with anomalous SSTs from the 10 year monthly averaged period 2003-2012 relative to 1979-1988. This anomaly is then doubled to obtain a stronger signal. As seen in figure 2.8 in chapter 2, it induces a general warming across all tropical ocean basins ranging between 0.5 to 1°C, with the largest anomaly north of the equator in the tropical Atlantic Ocean and south of the equator in the west Pacific Ocean. A large cooling anomaly of approximately 0.7-1.0°C is also present over the east Pacific. Results from this model experiment are subtracted from the control run to ascertain the response of the tropical forcing on NCG and on northern hemisphere climate for DJF.

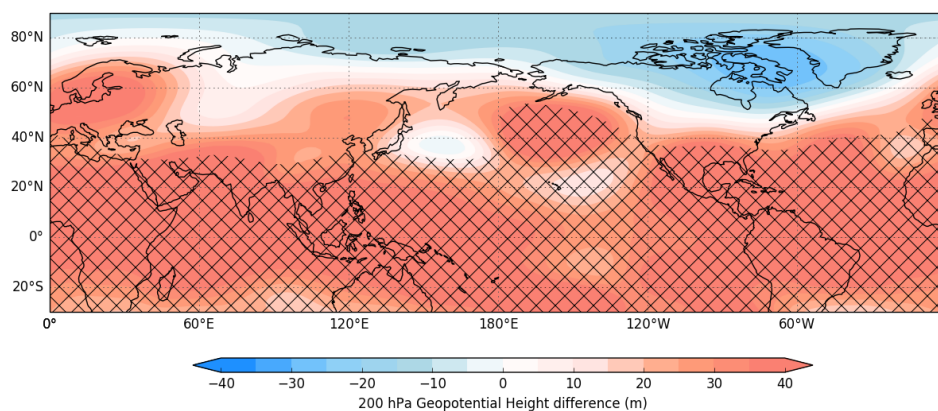


Fig. 4.2 Response of Z200 in metres of TropSST model experiment relative to control model experiment for boreal winter. Black stippling highlights statistical significance ( $p < 0.05$ ).

The response of geopotential height at 200 hPa (Z200) to the anomalous tropical forcing imposed in the TropSST model experiment is analysed first and, displayed in figure 4.2, and shows a dipole structure of Z200 anomalies in the Northern Hemisphere. The entire Arctic region has a decrease in Z200 that extends over NCG whereas the majority of the rest of the Northern Hemisphere has statistically significant increases in Z200. This is distinct from the trends in Z200 in ERAI for 1979-2012 as seen in figure 3.1 in chapter 3, which has the largest increase in Z200 over the Arctic and considerably less in the tropics, with the central tropical Pacific region showing the largest negative trends. However, this is expected since as, by design, the TropSST model experiment excludes high latitudes SST and sea ice changes that would be expected to drive warming and positive Z200 trends over the Arctic. The only perturbation, relative to the control is due to the tropical SST anomalies, which mainly cause warming in the tropical region that will result in local responses in Z200. To ascertain the anomalous response of NCG to the tropics, the zonal mean component of the Z200 is subtracted from the full Z200 field to find the eddy Z200 response.

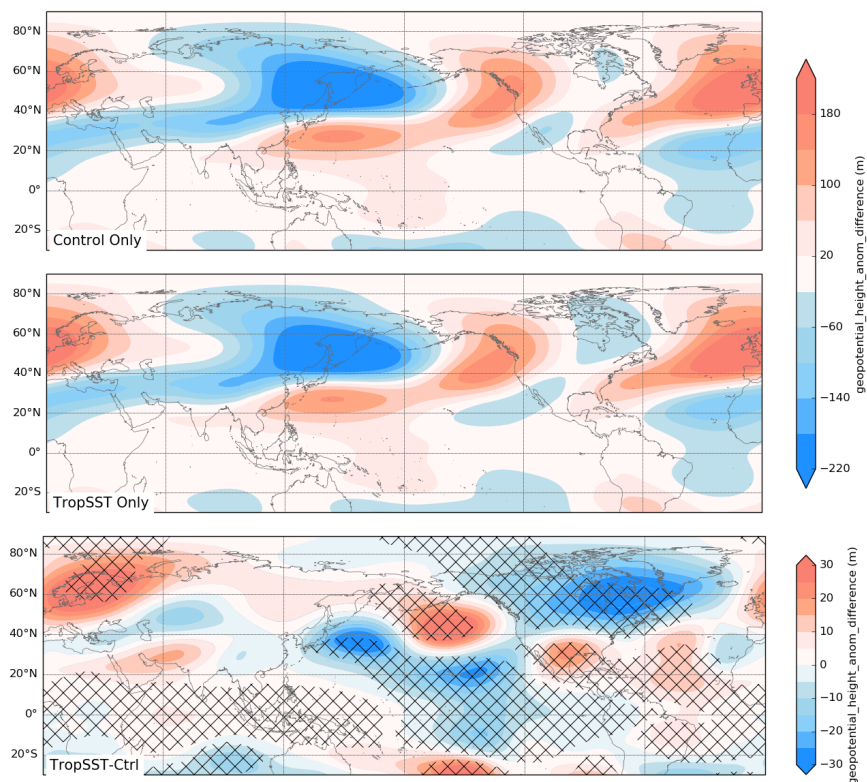


Fig. 4.3 Eddy Z200 in metres for boreal winter for [a] Control model experiment, [b] TropSST model experiment and [c] the difference between TropSST and control model experiments, relating to the response of tropical forcing. Black stipling in [c] highlights statistical significance at  $p < 0.05$

The eddy Z200, as simulated in the control and TropSST model experiments and the differences between them are shown in figure 4.3. The northern hemisphere DJF climate as simulated by both the control and TropSST model experiments (Fig 4.3 a and b) are very similar with both generating large scale stationary wave patterns across the extratropical and high-latitude regions. This figure shows a large-scale negative eddy Z200 over the northwest Pacific that extends westward across southern Asia, a positive eddy Z200 across the northeast Pacific and the north Atlantic. A smaller scale negative eddy Z200 over north east Canada and Greenland is also evident, which by eye appears larger in the TropSST model experiment. This provides confidence that the

perturbed SST model experiment is not simulating a fundamentally different climate relative to the control model experiment. The response to the tropical forcing, found through differencing the TropSST model and control model experiment is displayed in figure 4.3 c. The response over NCG to the tropical SST perturbation, is different to the trends of eddy Z200 presented in chapter 3 and to the results presented in Ding et al. (2014), specifically in that it is of opposite sign. Here the response shows a large statistically significant ( $p < 0.05$ ) negative anomaly over north eastern North America, or a deepening of the climatological trough over this region as seen from the control experiment (Fig. 4.3 a). This upper level negative anomaly has a statistically significant equivalent barotropic structure as the same signed anomalies are also found at 500 hPa and mean sea-level pressure (Fig. 4.4 a and b respectively). Further features, namely the statistically significant positive eddy Z200 anomaly over the Aleutian low region (between  $180^\circ\text{E}$  to  $130^\circ\text{E}$  and  $30^\circ\text{N}$  to  $55^\circ\text{N}$ ) in figure 4.3 also displays statistical significant equivalent barotropic structure throughout the depth of the atmosphere highlighting the barotropic nature of this model.

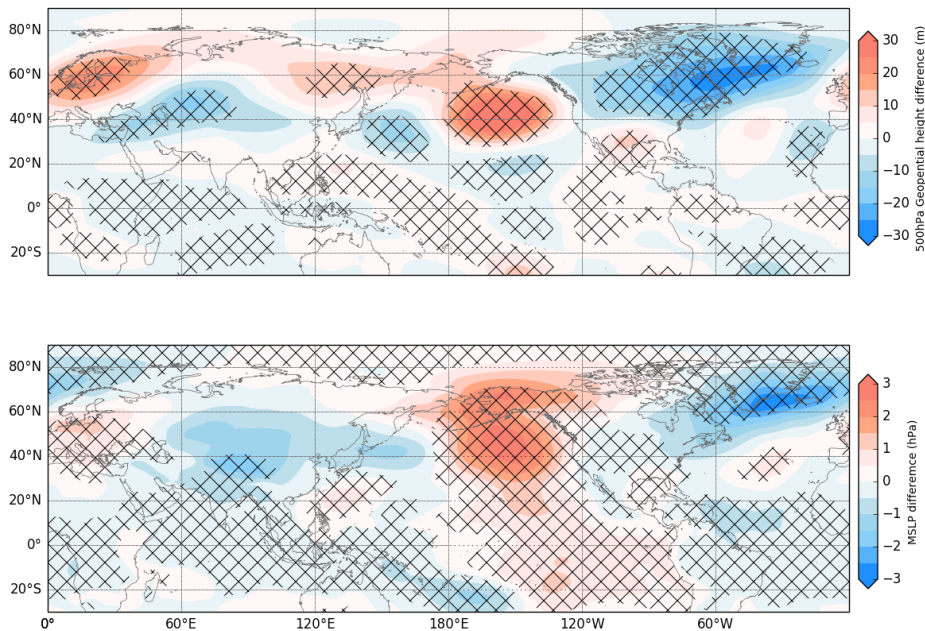


Fig. 4.4 [a] Eddy Z at 500 hPa response in the TropSST forcing and [b] The response of MSLP from TropSST forcing for boreal winter averaged over all 58 years of model simulations. Black stippling indicates statistical significance at  $p < 0.05$

The large-scale planetary waves for boreal winter at 200 hPa for the control and TropSST model experiments, found through assessing upper tropospheric WAF is shown in figure 4.5. The differences between them, which indicate their response to tropical SST perturbations, is shown in figure 4.6. Large-scale stationary waves are found to propagate across NCG in both the control and TropSST model experiments in boreal winter (Fig. 4.5). There is a strong eastward propagation of waves mainly in the extratropics, due most probably to jet streams which are strongest in these regions in boreal winter. In both model experiments there is wave propagation across NCG, albeit this is weaker than in the regions close to the jet maxima.

The response of the WAF to the anomalous tropical SST forcing, however, does not generate anomalous poleward propagating WAF between the tropics and NCG. Figure 4.6 shows the eddy Z200 response as from figure 4.3, overlaid by the WAF response. It displays a wave train emanating from the west Pacific region that propagates polewards and westwards. This appears to show some convergence poleward of a positive eddy Z200 anomaly in the north east Pacific and propagates equatorward thereafter in to the east Pacific. WAF vectors from the tropical Atlantic appear to show WAF propagating westwards, which potentially may suggest wave reflection here, however as outlined in chapter 1, waves tend to propagate in an eastward direction, so it may also indicate that the WAF has weakened within the tropical Atlantic and across the south and west of the USA. In contrast to the wave trends in the observations presented at the start of this chapter, none of these simulated anomalous wave trains directly propagate towards the NCG and are either retained within the Pacific ocean, are reflected or are weakened. A direct comparison between the model results and wave trends from ERAI, UPSCALE and AMIP, however, cannot be made due to the inherent differences in set-up and design of these model. Nonetheless this suggests that the NCG negative anomaly of eddy Z200, simulated in the model, is not obviously associated with a wave train emanating directly from the tropics.

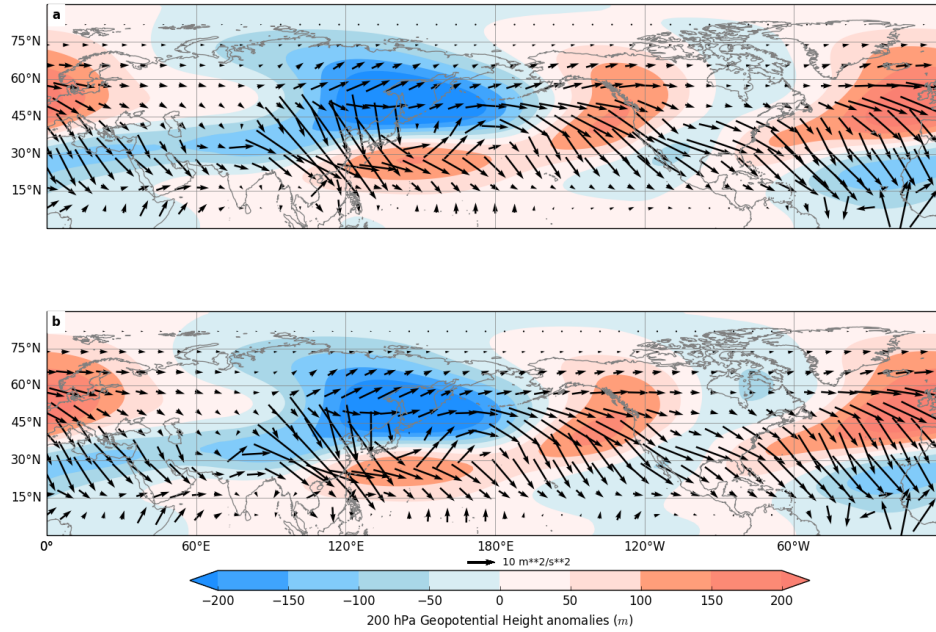


Fig. 4.5 Wave activity flux (WAF) at 200 hPa for boreal winter in black vectors superimposed over eddy Z200 climatological fields for boreal winter for [a] Control model experiment and [b] TropSST model experiment

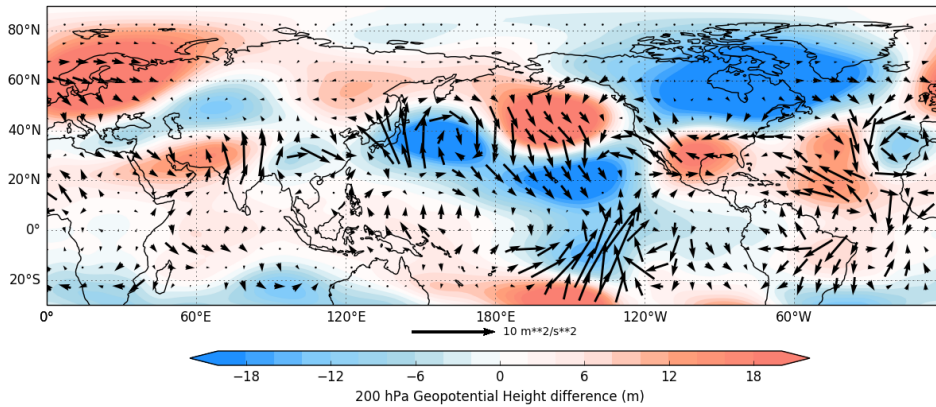


Fig. 4.6 Response in eddy Z200 (coloured contours) and WAF (black vectors) at 200 hPa from the TropSST model experiment forcing relative to the control model experiment. The statistical significance of these anomalies are shown previously in figure 4.3

To quantify the possible reasons why tropically-induced Rossby waves do not propagate to NCG, an analysis of the mechanisms which give rise to Rossby waves in the atmosphere, namely wave sources and factors which contribute to propagation are undertaken.

### 4.3.1 Rossby wave source and propagation

To begin, the source of Rossby waves in both model experiments, and its response from the imposed tropical forcing is investigated. A change in the source region of waves, induced, for example, by changes in the upper level divergence resulting from an SST perturbation, result in differences in how and where the wave can propagate, depending on background conditions (Branstator, 1983; Ding et al., 2014; Sardeshmukh and Hoskins, 1988). For example, in Ding et al. (2014), an anomalous wave train that emanated from the central tropical Pacific propagated towards NCG via the Pacific ocean in ERAI, however, a different wave train, that was sourced in the east Pacific ocean, propagated over North America into the NCG region in their ECHAM4.6 model simulations. The importance of the sources of Rossby waves and specifically the change of Rossby wave sources in response to a tropical forcing in the TropSST model experiment is analysed below.

As defined in chapter 2, Rossby wave source (RWS) as defined by Sardeshmukh and Hoskins (1988) and Shimizu and de Albuquerque Cavalcanti (2010) is dependent upon absolute vorticity, divergence and the horizontal velocity  $\mathbf{v}$  and can be calculated following:

$$S = -\mathbf{v}_\chi \cdot \nabla \zeta - \zeta D = -\nabla \cdot (\mathbf{v}_\chi \zeta), \quad (4.1)$$

where  $\zeta$  is the absolute vorticity,  $D$  is the horizontal wind divergence and  $\mathbf{v}_\chi$ , is the divergent component of the horizontal velocity. This highlights that RWSs are greater in areas of large absolute vorticity and gradient of absolute vorticity as well as divergence

and divergent wind. Shimizu and de Albuquerque Cavalcanti (2010) state that these conditions exist poleward of diabatic heating, where the divergent component of wind is greater due to convection and where there are large background gradients of vorticity.

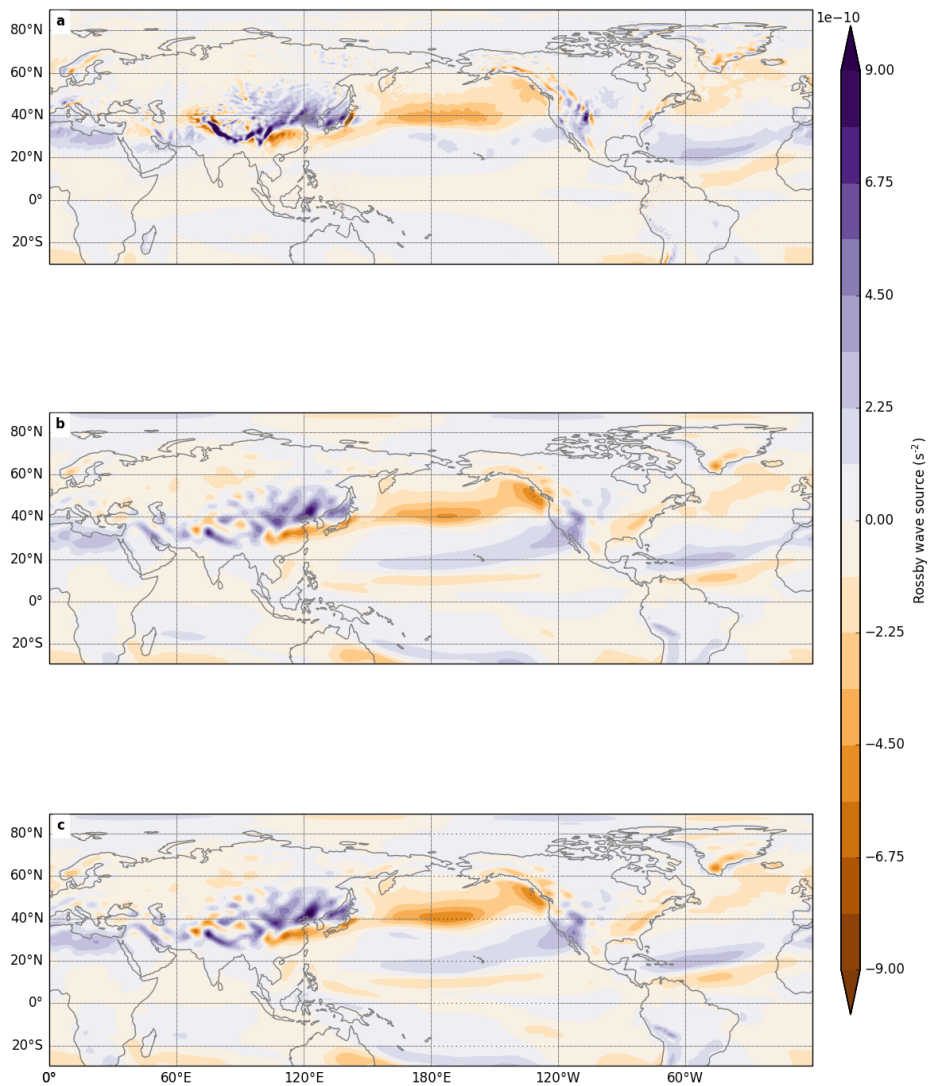


Fig. 4.7 DJF mean of Rossby wave source for [a] ERA-Interim Reanalysis, [b] Control model experiment and [c] TropSST model experiment

Before assessing the response of RWS from the TropSST model experiment, to test for model bias in Rossby wave source, a comparison of the DJF climatology from the

control and TropSST model experiment relative to ERAI is made. The main features of the RWS DJF climatology for ERAI are shown in figure 4.7 a and displays a large negative source that spans the north Pacific at around  $40^{\circ}\text{N}$  to  $60^{\circ}\text{N}$ , a large Pacific wide positive source between  $20^{\circ}\text{N}$  and  $40^{\circ}\text{N}$ , and a further positive source over the Himalayas between  $70^{\circ}\text{E}$  to  $130^{\circ}\text{E}$  at  $40^{\circ}\text{N}$ . These features are largely captured in both the control (Fig. 4.7 b) and TropSST model experiments (Fig. 4.7 c). The patterns presented here are also similar to observed RWS for DJF in NCEP/NCAR reanalysis data from Shimizu and de Albuquerque Cavalcanti (2010) as shown in figure 1.12 in chapter 1 and Moon and Ha (2003) who found that the large source over East Asia as this is the region of the downward branch of the Hadley cell circulation and therefore does not change its location. This, therefore provides confidence that the models are able to broadly capture the observed distribution of Rossby wave source.

Figure 4.8 a shows the difference in RWS between the TropSST and control model experiments. This shows that the response of RWS to the imposed tropical SST anomalies occurs mainly in the extratropics. Positive anomalies occur around  $38^{\circ}\text{N}$ ,  $140^{\circ}\text{E}$ , just off the coast of Japan and around  $41^{\circ}\text{N}$ ,  $145^{\circ}\text{W}$ , both of which represent a sign reversal relative to the climatology (Fig. 4.7 b) and a negative anomaly around  $180^{\circ}\text{E}$  in between. The changes appear to be primarily due to the positive response of absolute vorticity over  $38^{\circ}\text{N}$ ,  $140^{\circ}\text{E}$  (Fig. 4.8 b), which occurs in a region with a large background gradient of absolute vorticity rather than due to changes in divergence which are small in this region (Fig. 4.8 c). Changes in divergence are mainly confined to the tropical region, which is expected as this is the region of stronger thermal forcing and thus strongest convection.

As the response in RWS appears quite sporadic across the northern hemisphere, I investigated the response in precipitation and outgoing longwave radiation (OLR) as proxies for convection, which is a driver of Rossby waves. Figure 4.9 shows regions of statistically significant positive precipitation (fig 4.9 a) and negative OLR (fig 4.9 b) and show that most convection occurs in two bands on either side of the equator and also around  $25^{\circ}\text{N}$  and  $145^{\circ}\text{E}$  to  $160^{\circ}\text{W}$ . As noted in section 1, RWS are located poleward of regions of convection, and through comparing regions of convection and RWS (fig. 4.8 a),

the largest sources of RWS do occur poleward of convection, thus indicating that they may have been driven by tropical convection.

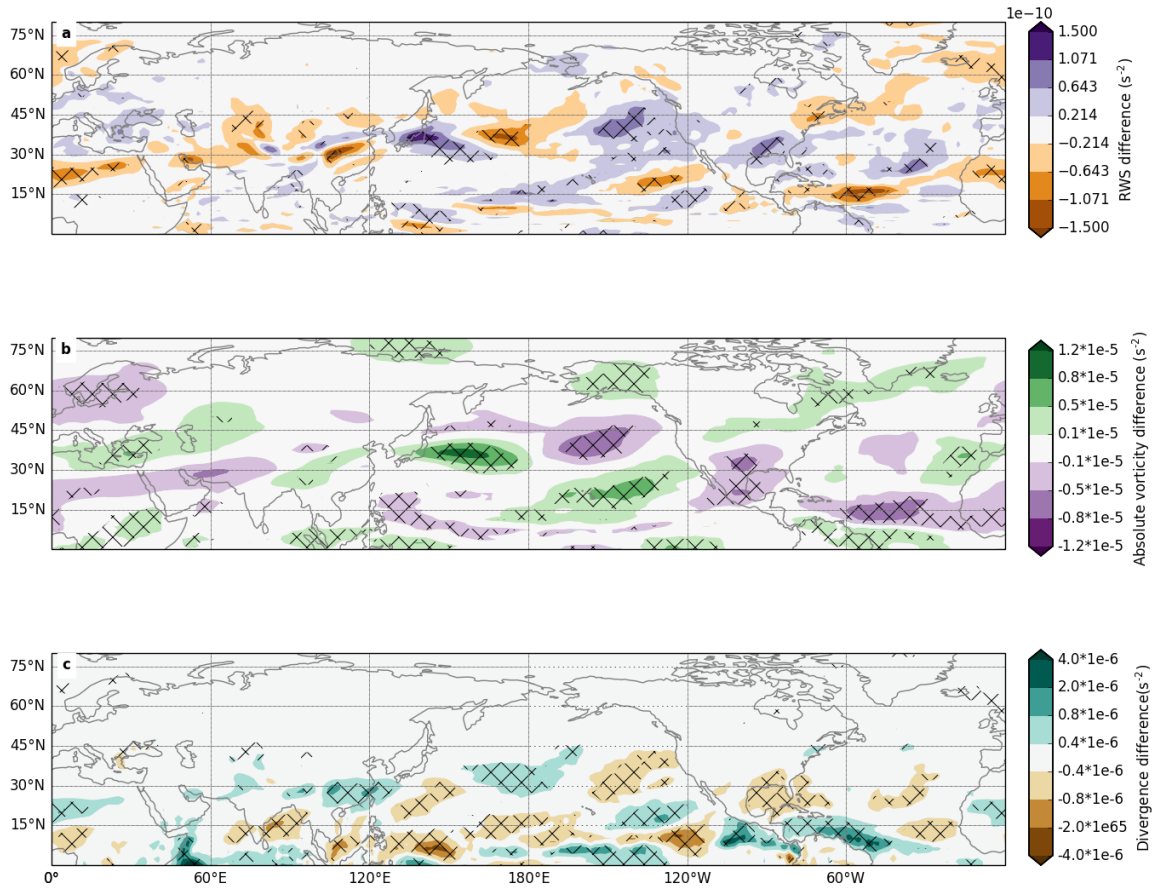


Fig. 4.8 Response of [a] Rossby wave source, [b] absolute vorticity and [c] divergence from the TropSST model experiment forcing, as an average over 58 year model simulation for DJF. Stippling indicates statistical significance at  $p < 0.05$ .

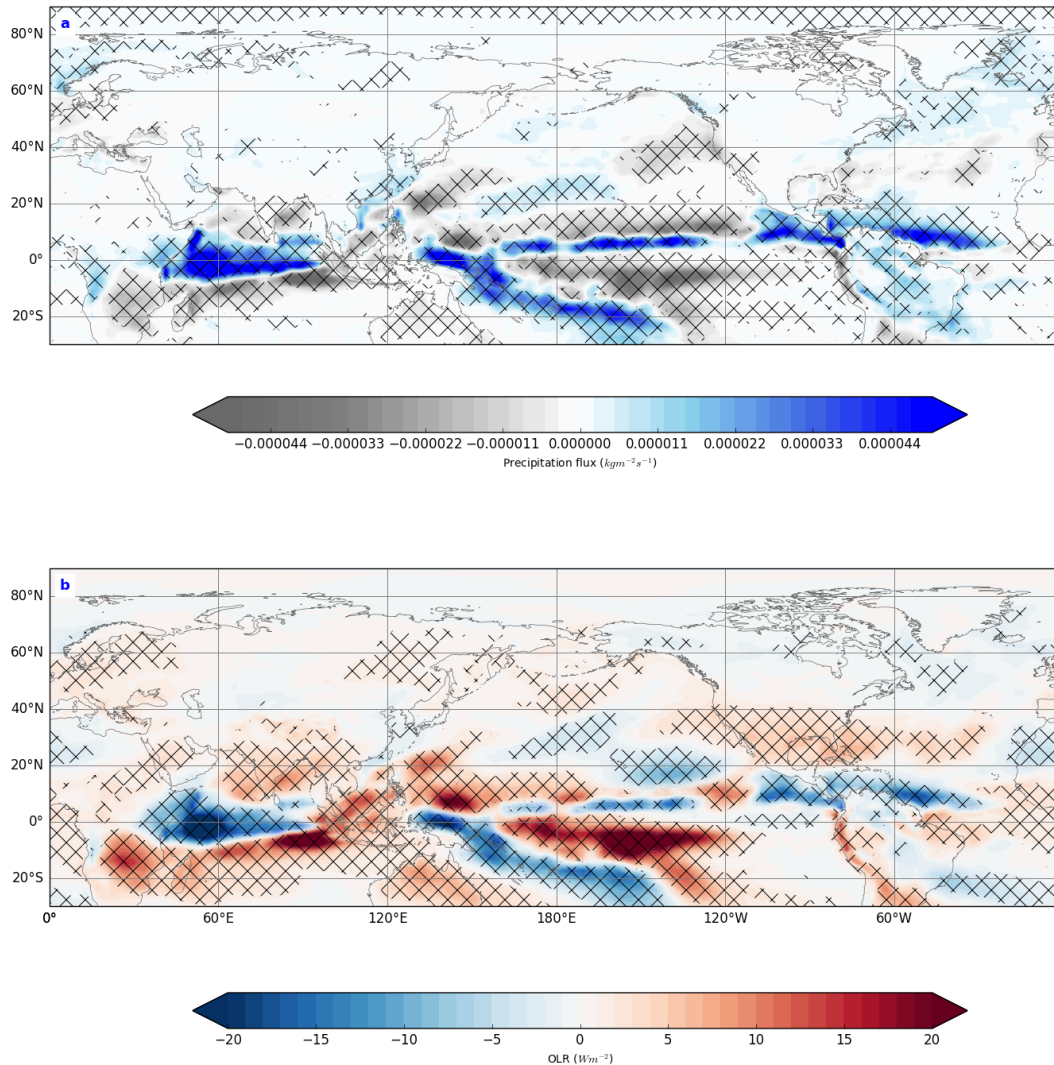


Fig. 4.9 Response of [a] Precipitation and [b] Outgoing Longwave Radiation from the TropSST model experiment forcing. Stippling indicates regions of statistical significance at  $p < 0.05$ .

The eddy Z200 and WAF anomalies that are generated from the west Pacific, are similar to those in previous studies generated from similar source regions. Simmons et al. (1983) and Hoskins and Ambrizzi (1993) found an arc-like wave that propagated across the north Pacific ocean basin but did not extend in to NCG, similar to the WAF anomalies presented here. This anomalous wave propagates within the strong zonal westerly winds

in DJF that occur in the subtropics (as seen in contours in 4.10), but do not propagate further downstream (Fig. 4.10). This may be due to the response of the zonal wind from the TropSST model experiment, for two reasons. Firstly, as shown in figure 4.10, the subtropical jet generally significantly weakens around  $40^{\circ}\text{N}$ , highlighted by green shading, in the same location as the subtropical jet exit region (contours). The weakening of this jet, relative to control model experiment, may have damped or weakened the anomalous WAF propagation across the north Pacific and potential further downstream propagation. Secondly, on the poleward flank of the climatological subtropical jet (in contours in figure 4.10) westerly winds here significantly increased in strength relative to the control, especially over the north east Pacific (brown shading in figure 4.10). The winds strengthen in order to maintain thermal wind balance as winds anomalies occur in same locations as anomalous temperature gradients in the mid-troposphere resulting in poleward shifts of the jet (Lu and Ren, 2016; Yin, 2005). The imposed tropical SST perturbation results in an anomalously strong mid tropospheric (300-800 hPa) temperature gradient in the north east Pacific (Fig. 4.11). This occurs between a statistically significant positive anomaly between  $180^{\circ}\text{W}$  and  $130^{\circ}\text{W}$  and centred around  $40^{\circ}\text{N}$  and a statistically significant negative anomaly on its northern side (Fig. 4.11) in the same region of the anomalously stronger winds. This positive wind anomaly over the north east Pacific appears to have resulted in some convergence of WAF on its poleward side and equatorward deflection of the WAF anomaly along the eastern Pacific (Fig. 4.10) as based on wave mean-flow theory which states that wave reflection occurs at either flank of the jet due to changes in absolute vorticity gradient (Fig. 4.8) (Branstator, 1983; Simmons et al., 1983). Similarly, the response of WAF in the tropical Atlantic may also have been affected by changes in the the eddy driven jet which has shifted poleward, as the anomaly (shown by shading in figure 4.10) is further poleward of the control eddy driven jet (contours). The WAF vectors, in blue, appear to be reflected westward away from the jet, however, as mentioned previously, Rossby waves propagate eastward so this may also indicate that waves in this region were weakened in response to the imposed tropical SST perturbations.

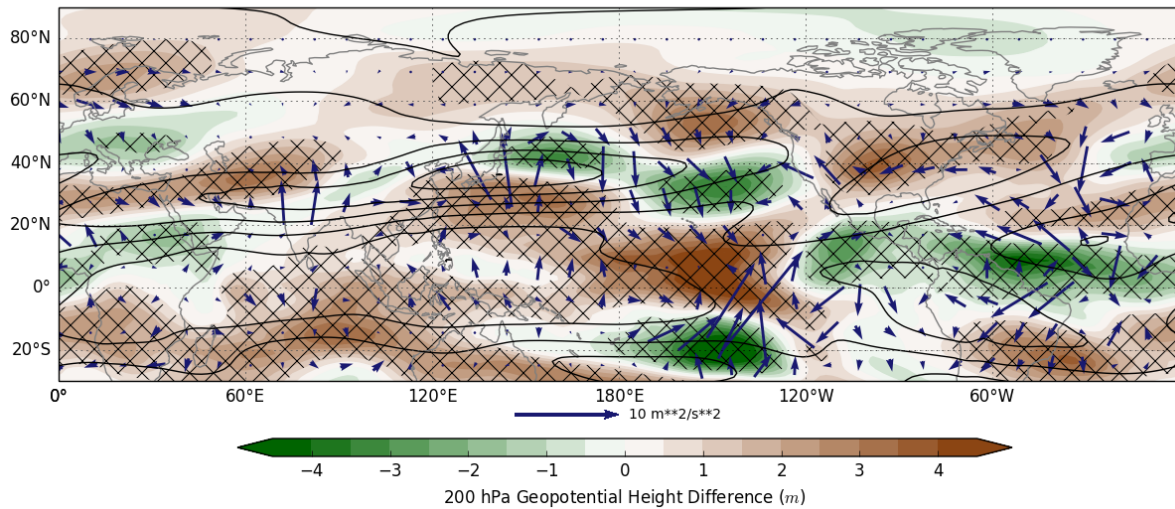


Fig. 4.10 Response in WAF from TropSST model experiment relative to control model experiment in blue vectors for boreal winter with climatological DJF winds for control model experiment in unfilled contours, at contour level of  $10 \text{ m s}^{-2}$  and for response of zonal U winds from TropSST model experiment forcing in shading. Stippling indicates regions of statistical significance ( $p < 0.05$ ).

Along with refracting waves away from the NCG region, leading to convergence in the north Pacific, the westerly anomaly in the north east Pacific generates an anomalous anticyclonic flow which appears to lead to a subsequent cyclonic flow over NCG (Fig. 4.13). This anomalous cyclonic flow will result in cold air advection from the climatologically colder DJF Arctic region (Fig. 4.12), resulting in colder mid tropospheric temperature over NCG, relative to the control model experiment (Fig. 4.11). This generates a land/sea temperature gradient, with anomalously warm temperatures over the Arctic and anomalously cold over NCG. According to (Lu and Ren, 2016; Yin, 2005), this large land/sea temperature contrast will intensify the DJF climatological trough and therefore may have contributed to the anomalous negative eddy Z200 in the TropSST model experiment.

Comparing these results to ERAI WAF trends between 1979-2012 (Fig. 4.1 a), the WAF response from the TropSST model experiment does not share many similar features namely that it does not propagate from tropical Pacific on to north Canada and

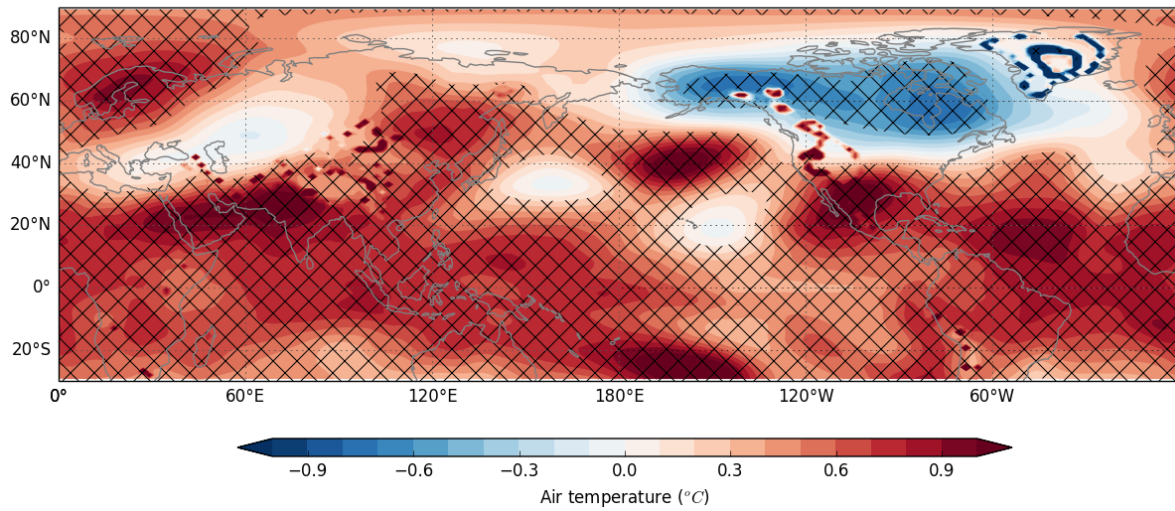


Fig. 4.11 Difference in mid tropospheric (300-800hPa) air temperature in °C between the TropSST model and control model experiments in DJF. Stippling indicates statistical significance at  $p < 0.05$

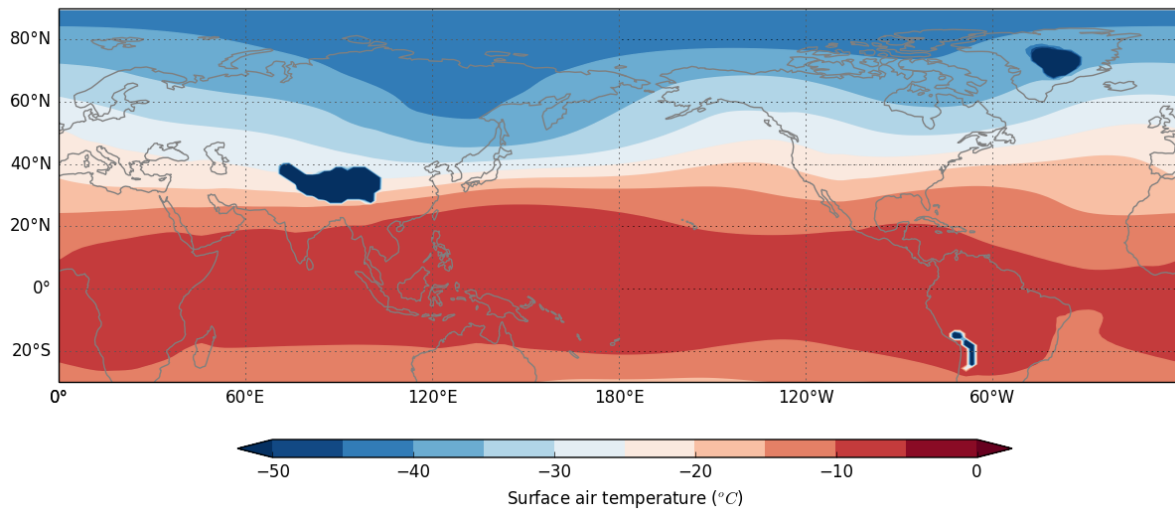


Fig. 4.12 DJF mid tropospheric (300-800hPa) air temperature in °C from control model experiment

Greenland. This appears to be due to the fact that the imposed tropical SST perturbation resulted in an anomalous RWS in the west Pacific and WAF that propagated only across

the north Pacific as far downstream as the north east Pacific due to changes in the background mean flow.

These results, so far, conclude that conversely to results presented in Ding et al. (2014) and eddy Z200 trends from ERAI, UPSCALE and AMIP as shown in figures 3.3 and 3.4 in chapter 3, that a tropical only forcing (with all other parameters fixed) results in a negative eddy Z200 over NCG.

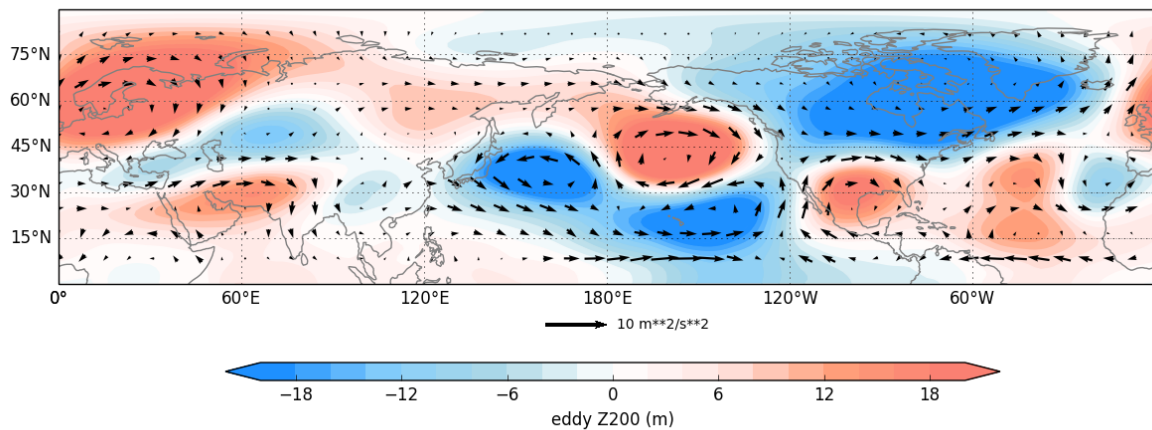


Fig. 4.13 Difference in eddy Z200 and wind vectors in DJF between the TropSST model and control model experiments

From this analysis, it appears that this response is the result of an anomalous RWS, found in the subtropical west Pacific, which generates an anomalous WAF that propagates across the north Pacific but does not propagate further downstream on to the NCG. This appears to be due to changes in the zonal wind, generated by temperature anomalies from the imposed tropical SST perturbations, specifically in the north east Pacific. This leads to a positive zonal wind anomaly, more specifically an anomalous strengthening of the westerly wind poleward of the subtropical jet, which results in some convergence and equatorial refraction of WAF, limiting WAF propagation on to NCG. This generates anomalous circulation and specifically cyclonic circulation over NCG, resulting in cold air advection from the Arctic region southwards over NCG and an anomalous temperature

gradient between the cold NCG and warm Arctic. Large land/ocean temperature gradient can intensify the climatological stationary trough (Lu and Ren, 2016; Yin, 2005) and thus may have contributed to the anomalous negative eddy Z200 over NCG.

## 4.4 Extratropical influence on NCG

The response of eddy Z200 over NCG to an imposed tropical SST perturbation is directly opposite to the trends of eddy Z200 presented in chapter 3 in ERAI, UPSCALE and AMIP data as well as from Ding et al. (2014). A key difference between the responses found from these model experiments and those specifically presented in Ding et al. (2014) is the lack of a more local forcing, such as from extratropical SSTs, which may have contributed to trends found over NCG. Therefore, the role of extratropical SSTs from the GloSST model experiment is assessed using the same SST anomaly as the TropSST model experiment except applied across global SSTs (see chapter 2). This model experiment is initially compared to the control model experiment to give an understanding of the response of eddy Z200 over NCG relative to a global forcing and is then compared to the TropSST model experiment to separate the role that extratropical SSTs have on the NCG region. Therefore, with respect to comparisons to the TropSST model experiment, responses will be as a result of extratropical SSTs and henceforth will be referred to in this manner.

The extratropical SST perturbation relative to the TropSST model experiment, as seen in figure 2.11 in chapter 2, results in mainly large positive sea surface temperature anomalies, particularly in the northern hemisphere extratropics. SSTs within this region are approximately 1°C warmer relative to the SST anomalies from the TropSST experiment, with a small limb of cooling directly along the west coast of North America extending as far north as the Bering Sea. The global and extratropical influence on NCG will be analysed in a similar manner to that for the TropSST experiment in the previous sections.

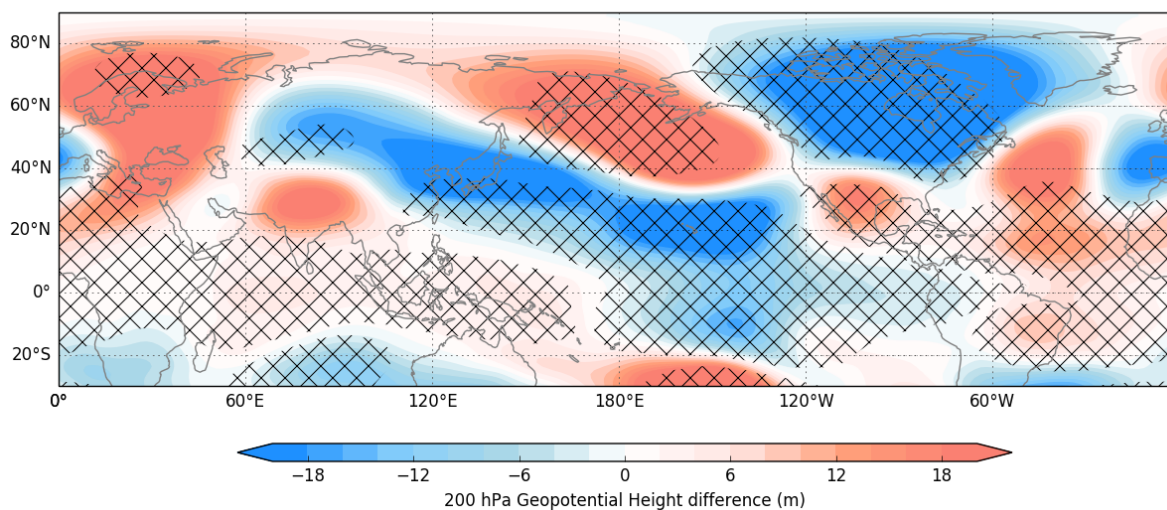


Fig. 4.14 Response of eddy Z200 anomaly from GloSST model experiment relative to control in coloured contours for DJF. Black hatching represents statistical significance at  $p < 0.05$

Figure 4.14 shows that the response in eddy Z200 in the GloSST model experiment both over NCG and the entire northern hemisphere are similar in the TropSST model experiment (Fig. 4.3). There is a large statistically significant ( $p < 0.05$ ) negative anomaly over NCG, as depicted by black hatching, that extends across much of northern North America. This response is similar to that from the TropSST model experiment, albeit larger, suggesting that the tropical regions play a dominant role in driving the overall response in eddy Z200 in the global SST forcing. This result appears consistent with previous research that states that patterns of atmospheric variability are most prominently forced by tropical SSTs over mid-latitude SSTs (Graham et al., 1994).

Relative to the TropSST model experiment, the GloSST model experiment, or the extratropical SST response (taken as the difference between the GloSST model experiment and TropSST model experiment) results in a large negative anomaly over NCG. This, however, extends further south, reaching the Gulf of Mexico and further west onto Alaska than the TropSST model experiment response (Fig. 4.15). The extratropical SST perturbation, it appears, amplifies the negative eddy response of the TropSST over

NCG, however it is not statistically significant so may be a largely tropical response more so than an extratropical response. This figure also shows a strong zonal eddy Z200 component in the anomalies implying a strong mid-latitude zonal wave is induced by extratropical SSTs more so than tropical SSTs. However, as the anomalous forcing is within this region, this is expected. The response of the NCG highlights that from both a tropical SST forcing (TropSST experiment) and extratropical SST forcing (GloSST - TropSST model experiments) that this model, HadGEM3-A, forces a negative eddy Z200 anomaly over the region thus suggesting that contrary to trends over the entire record, the tropical region induces an opposite response that from trends in observations and transiently forced models.

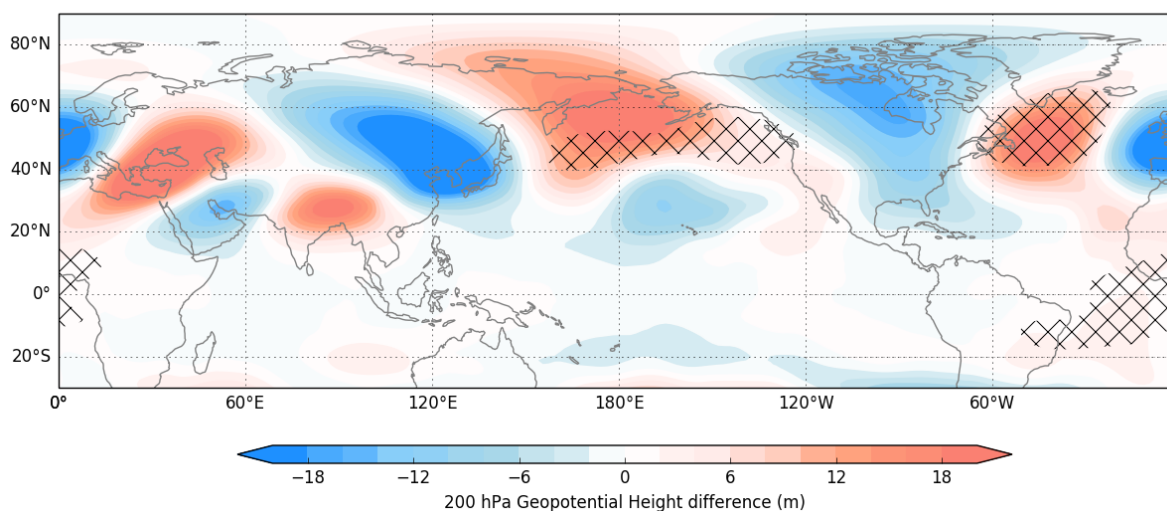


Fig. 4.15 Response of eddy Z200 anomaly from extratropical SSTs, where the GloSST model experiment is differenced with respect to the TropSST model experiment for DJF. Statistical significance where  $p < 0.05$  is depicted by black hatching

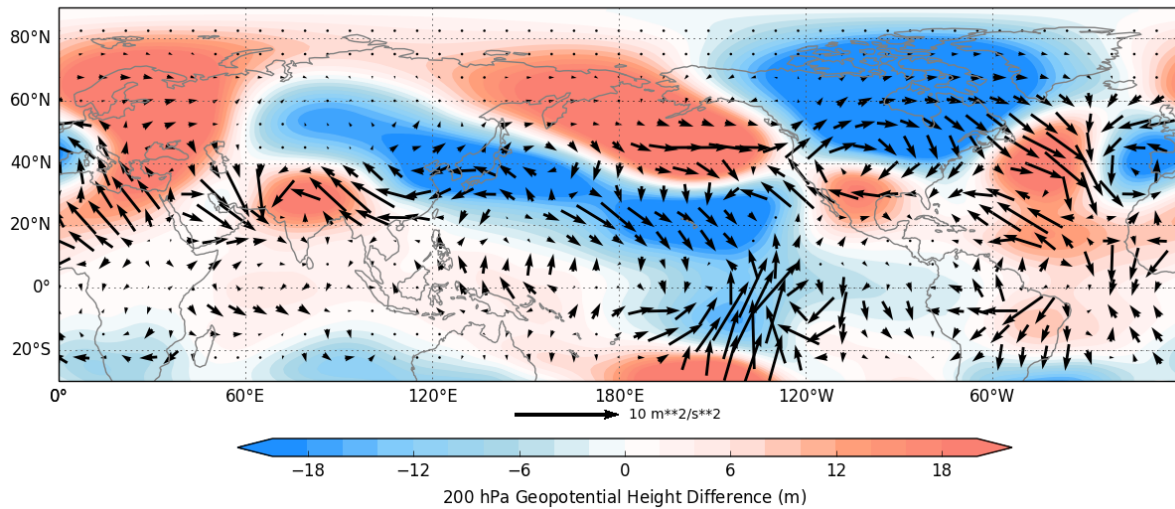


Fig. 4.16 Eddy Z200 and WAF response from GloSST model experiment relative to control model experiment in coloured contours and black vectors respectively for boreal winter

The WAF response of the GloSST model experiment shows an anomalous wave packet that does propagate towards NCG. Figure 4.16 shows that relative to the control model experiment, the WAF response in GloSST contains many similar features to the WAF response in the TropSST model experiment, except in this instance, an anomalous wave train is able to propagate over NCG. The response in WAF from the GloSST model experiment shows a wave emanating from the west Pacific, propagating poleward and eastward across the north Pacific, over NCG and into the north Atlantic ocean. This suggests that there is an extratropical influence on the wave train in the north Pacific. Differencing the WAF anomalies from GloSST model experiment with those from the TropSST model experiment, to assess the extratropical influence, seems to support this theory. Figure 4.17 highlights that an extratropical forcing results in a zonally eastward propagating anomalous WAF that propagates across NCG and in to the north Atlantic. This arc-like shape of the WAF across north America shares similar features to wave trends that appear in Trenberth et al. (2014) where a wave train, generated in the central Pacific, propagates poleward and eastward across north America, over NCG and in-to

the north Atlantic. The additional extratropical SST forcing therefore appears to play a role in the propagation of a tropical wave train in to the high-latitudes.

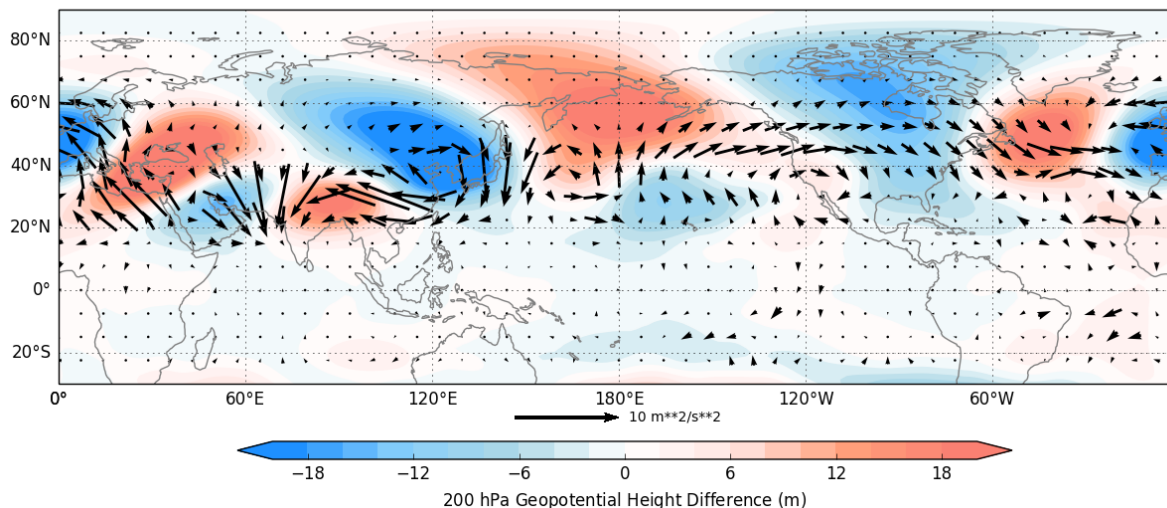


Fig. 4.17 WAF (shown by black vectors) and eddy Z200 (in coloured contours) response from extratropical SSTs through differencing of GloSST model experiment and TropSST model experiment for boreal winter

The generation of the anomalous wave train in figure 4.17 may be due to an additional source of Rossby waves within the western hemisphere over the Pacific ocean. Figure 4.18 show that an extratropical SST induced an anomalous RWS over the central north Pacific ocean (around about 45°N and 180°W, as shown in purple coloured contours). The zonal winds, however, appear to have decreased with an extratropical forcing relative to the TropSST model experiment, but slightly increased poleward which may have acted as a wave guide with anomalous WAF propagating within this across North America and north Canada and Greenland.

These results indicate that the tropics plays the greatest role in the circulation change over NCG, relative to the extratropics because the response is negative in all model experiments, in spite of an anomalous extratropically-excited wave train, that one would assume would result in an opposite response over NCG. This could be due to the fact that the GloSST model experiment includes the anomalous tropical perturbation and

so even in differencing the two model experiments, artefacts of the anomalous tropical perturbation will still be found in the extratropical response. This suggests that trends in NCG eddy Z200 from Ding et al. (2014) and from analysis in chapter 3 may be an artefact of other sources such as through changes in sea ice or it could indicate model dependency of accurate simulation of these trends.

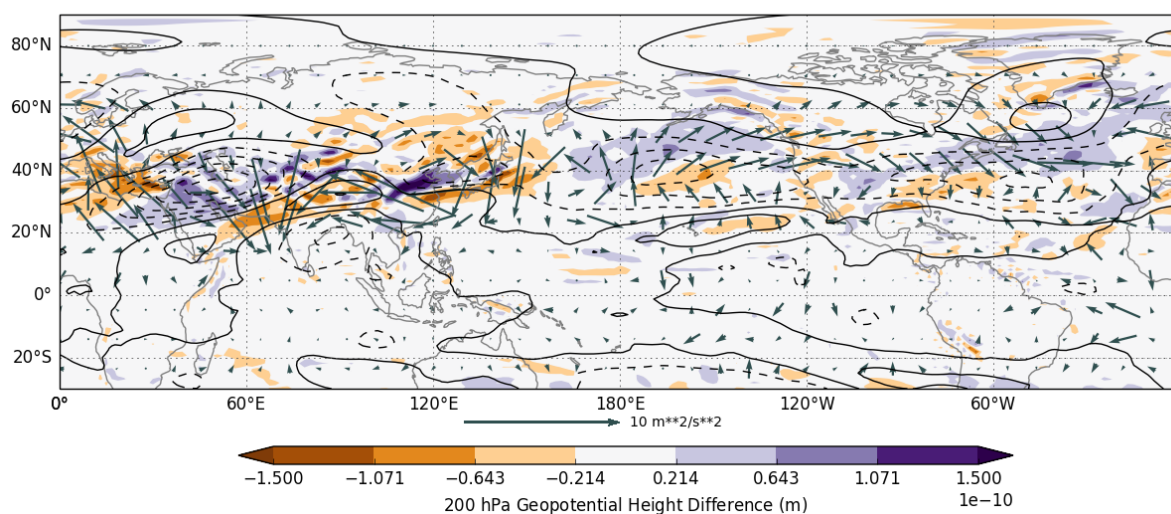


Fig. 4.18 Response of Rossby wave source, highlighted by coloured contours, zonal wind and WAF to an extratropical SST forcing (found through differencing the GloSST and TropSST model experiments) for boreal winter, averaged over 58 years of HadGEM3-A model output

## 4.5 Concluding remarks

This chapter has aimed to address the tropical influence of the tropics on the Arctic, specifically the NCG region, through the generation and propagation of waves that lead to remote teleconnections. Tropical driving of global climate is a well known phenomenon. Ding et al. (2014) attributed the positive trend in eddy Z200 over NCG in recent decades to a tropically forced Rossby wave train emanating from the tropical Pacific. Such a wave train was identified in ERAI from 1979 to 2012 and in UPSCALE and AMIP model experiments which are forced with observed historical sea surface temperatures and sea

ice from 1985 to 2011 and 1979 to 2005 respectively. The wave train propagating into the NCG region in the ensemble and AMIP were weaker than in ERAI, but the anomalies were of the same sign as those observed.

The connection between the tropics and NCG was further assessed by performing model simulations with HadGEM3-A in which perturbations in tropical SSTs (TropSST) from 2003-2012 anomalies, which were doubled to amplify the forcing, were imposed relative to a background state (control model experiment) based on the 1979-1988 global climatological SST means. The anomalous tropical forcing of warmer SSTs over the Atlantic and Indo-Western Pacific and cooler SSTs over the east Pacific, resulted in a negative Z200 and eddy Z200 anomaly over NCG, contrary to observed trends. This anomaly may not be the consequence of tropically-excited poleward propagating Rossby waves that propagated from the tropical region on to NCG. The results presented suggest that the imposed tropical SST perturbation generated an anomalous Rossby wave source in the west Pacific, around 38°N, 140°W which generated an anomalous wave activity flux (WAF). This anomalous WAF, which may act to enhance or reduce existing wave patterns, propagates across the north Pacific ocean basin but does not extend over NCG. Changes in the strength and position of the jet may have contributed to this in two ways, whereby the subtropical jet weakens in response to a tropical SST perturbation which may weaken WAF propagation. Furthermore, poleward of the climatological subtropical jet along the north eastern Pacific side, westerly winds increases, and the eddy driven jet in the Atlantic shifts polewards. This appears to have resulted in some convergence on the poleward side of the wind anomaly and some equatorward deflection of waves in the north east Pacific. An eastward deflection of waves from the Atlantic away from the NCG was also found, however this also may be showing a weakening of WAF in these regions. The lack of anomalous WAF propagation on to the NCG region may have allowed the climatological trough, seen in figure 4.2, to deepen further, due to anomalous circulation induced by wind anomalies. This results in cold air advection over the NCG region generating a large anomalous land/ocean temperature gradient. This large gradient therefore may result in intensifying the climatological trough, as

highlighted by (Lu and Ren, 2016; Yin, 2005), resulting in the negative eddy Z200 found in response to the TropSST model experiment.

To understand why these results were very different to Ding et al. and the observations, the role of the extratropics were investigated, as these other data, had some extratropical influence. The extratropical influence led to both an amplification of the negative eddy Z200 pattern over NCG similar to the response from the TropSST model experiment, but also an amplification of WAF that emanated from the tropics. This amplification resulted in waves that were then able to propagate across NCG and in to the Atlantic generated as the result of an additional anomalous RWS at 45°N and 180°W roughly, which coincided with the source of anomalous WAF in this model experiment, with climatological western winds in the region which strengthened slightly, poleward of the jet, allowed for wave propagation over NCG to occur. This therefore highlights that strong actual tropic-NCG teleconnections may be the result of both forcing from the tropical and extratropical regions.

# Chapter 5

## Influence of the three major tropical ocean basins on north Canada and Greenland

### 5.1 The importance of tropical ocean basins in generating teleconnections

The complexity in ascertaining the role of the entire tropical region on global climate means it is much more customary to focus on teleconnections generated by each individual tropical ocean basin (Li et al., 2014). Individually, the largest of these ocean basins; the Pacific, Atlantic and Indian, have been shown to generate teleconnection patterns that have far-reaching implications on climate in distant regions including high-latitudes (Hoerling et al., 2004; Kiladis, 1998; Wu et al., 2007). Anomalous sea-surface temperatures (SSTs), specifically from the Pacific and Atlantic, have resulted in surface warming and sea-ice melt in both polar regions via tropospheric and stratospheric pathways through Rossby wave propagation (Ding et al., 2012, 2011; Ineson and Scaife, 2009; Li et al., 2014; Omrani et al., 2014; Schneider et al., 2011). Following this, investigations are

undertaken into identifying the role and contribution of SST perturbations from each individual ocean basin on eddy Z200 over NCG and which is most important in driving the TropSST model experiment response.

## **5.2 Response from ocean basin forcings**

Analysis of tropical forcing on high-latitude climate is predominantly found through perturbing a particular state e.g. divergence, vorticity or SSTs over one ocean basin or within a specific region in an ocean basin (Branstator, 1983; Sardeshmukh and Hoskins, 1988). Although predominately done in idealised models, especially in the aforementioned studies, the benefit of this is that it will isolate wave trains generated from specific locations, away from noise that may be affected by a competing signal elsewhere. A number of model experiments are therefore designed for SST perturbations in each of the largest tropical ocean basins to disentangle the tropical response across the basins and isolate potential wave trains to result in a greater insight of the tropical influence on NCG.

Three model experiments are conducted for each of the three main tropical ocean basins to ascertain their forcing on NCG climate. To recall from chapter 2, each model experiment, ('PacSST', 'AtlSST' and 'IndSST'), are perturbed with anomalous SSTs between 30°N and 30°S. The perturbation is the same as that in the TropSST model experiment, whereby the observed pattern of changes in SSTs from 2003-2012 relative to 1979-1988 are outputted and then doubled to enhance the signal in the model experiment. This is applied to each ocean basin with a smoothing function applied at the latitude bounds and along the coastline and is superimposed on climatological SSTs (from 1979-1988) elsewhere (see chapter 2 for more details). These perturbations, relative to the climatological SSTs, result in warming of approximately 1°C over the entire tropical Atlantic and Indian oceans, as seen in chapter 2 in figures 2.10 b and 2.10 c, similar to the TropSST SST perturbations over the same regions (Fig 2.8 a). There is a dipole structure of anomalous SSTs across the tropical Pacific with warming of between 0.5-1°C

across the west Pacific ocean and an approximate  $1^{\circ}\text{C}$  cooling over east Pacific (Fig. 2.10). The response in climate from these model experiments is found through differencing all the perturbed (PacSST, AtlSST and IndSST) and control model experiments.

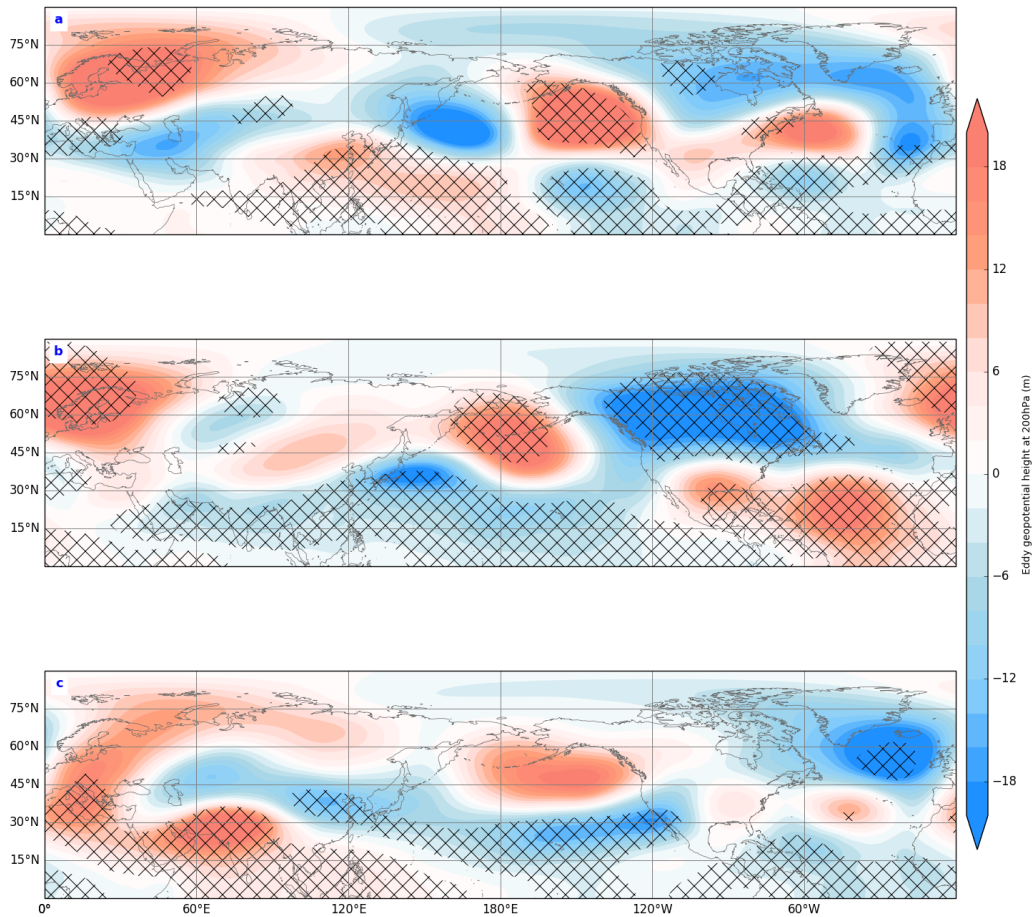


Fig. 5.1 Boreal winter response of eddy Z200 to anomalous forcing from [a] PacSST model experiment, [b] AtlSST model experiment, [c] IndSST model experiment. Hatching denotes statistical significance at  $p < 0.05$

The DJF eddy Z200 response, which is Z200 response removed from the zonal mean, over NCG is investigated in all basins and, in agreement with the eddy Z200 response from the TropSST model experiment, shows that all model experiments display negative eddy Z200 anomalies over NCG (Fig. 5.1). The most interesting feature of these model

experiments, is that the largest and most significant response is from the AtlSST model experiment (Fig. 5.1 b). This shows a large statistically significant ( $p < 0.05$ ) negative eddy Z200 anomaly that spans most of the northern North America. The response in DJF eddy Z200 over NCG from PacSST and IndSST model experiments are also negative, however much weaker than the Atlantic model experiment. The negative anomaly, in the PacSST model experiment, extends much further eastwards over the North Atlantic, than compared to eddy Z200 response in the AtlSST model experiment, with only a small area of statistical significance in central north Canada. The response from the IndSST experiment results in a statistically significant negative anomaly that is projected more over Iceland than NCG. Eddy Z200 responses in the tropics closely follow the SST perturbations. It is found that increases in eddy Z200 occur over locations of anomalously warm SSTs e.g. west Pacific in figure 5.1 a and decreases where there are anomalously cool SSTs or no additional forcing e.g. entire Pacific in figure 5.1 b under AtlSST model experiment.

Figure 5.2 shows the eddy Z200 responses from the PacSST, AtlSST and IndSST model experiments respectively with respect to the climatological eddy Z200 from the control model experiment. The response of the Z200 eddies in the PacSST model experiment (in shading), specifically over the north Pacific are similar in sign to the climatological eddies (in unfilled contours) but with increased strength over the north Pacific (Fig.5.2 a). Other anomalies in the tropical Atlantic and Pacific are also of same sign as the climatological eddies but similarly have increased in strength in response to the imposed Pacific SST perturbation. The negative eddy Z200 over NCG, however, is much larger in extent and spatial scale compared to the climatology which is comparatively a very small anomaly concentrated specifically in the NCG region. The similarity in the stationary wave pattern (in contours) to the anomalous wave pattern (shading) would suggest that this feature results in constructive wave interference and the enhancement of upward wave propagation, as the stratosphere is resolved in HadGEM3-A, which may affect the polar vortex (Garfinkel et al., 2010; Goss et al., 2016; Smith et al., 2011). However as the stratospheric response is not the purpose of this study, no further analysis is conducted.

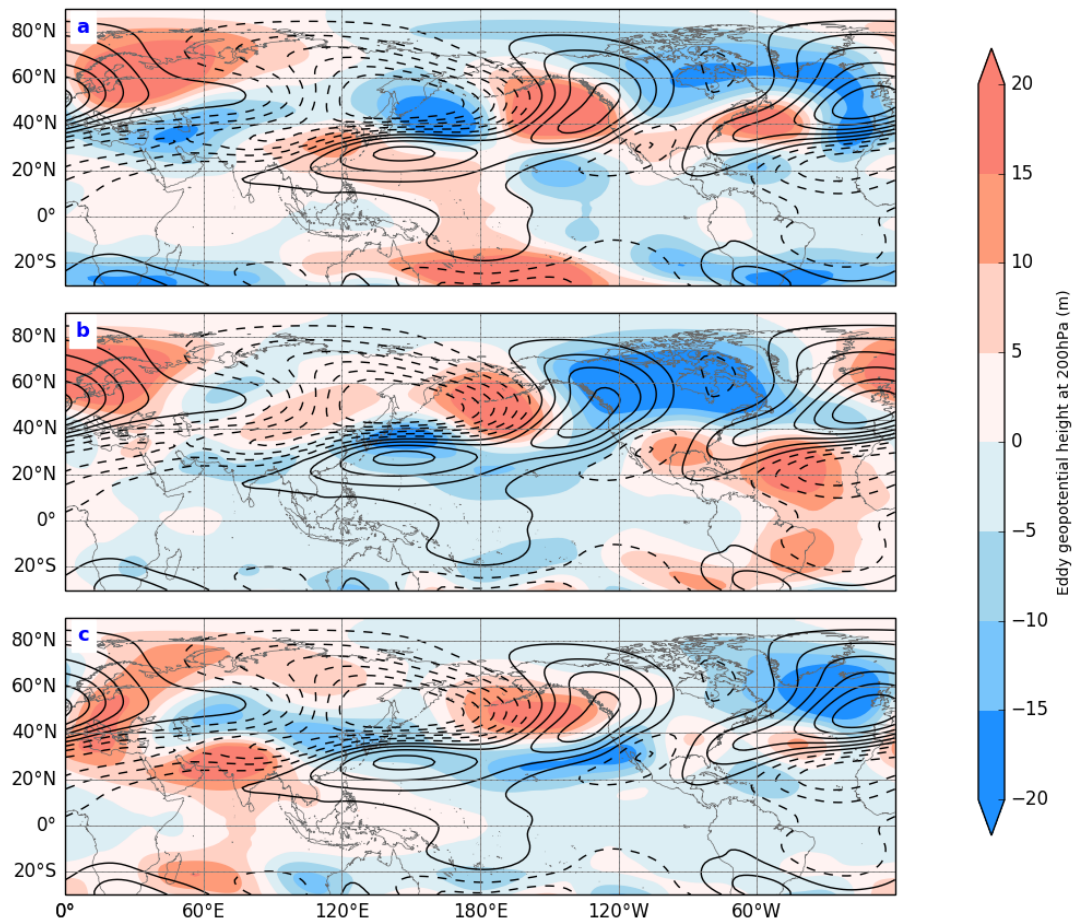


Fig. 5.2 The response of eddy Z200 from the [a] PacSST model relative, [b] AtlSST model experiment, [c] IndSST model experiment relative to the control model experiment in shading as in figure 5.1. Climatological eddy Z200 from control model experiment in contours with contour interval at 40m. Solid contours indicate positive eddies and dashed contours show negative contours.

The eddy Z200 response in the AtlSST model experiment (Fig. 5.2 b) is very different to the climatological eddies. The positive eddy Z200 anomaly over the north eastern Pacific has shifted westward with respect to the climatological Z200 eddy and the negative eddy in the north western Pacific in the climatology has shifted further equatorward. Positive anomalies are no longer present in the western tropical Pacific, but evident in the tropical Atlantic, out of phase with the climatology. However, this is because of the imposed tropical Atlantic SST perturbation. This results in an increased eddy Z200 over the tropical Atlantic and a lower Z200 in the western tropical Pacific, relative to

the climatology, due to the lack of an SST perturbation here. Similarly to the PacSST model experiment, the Z200 wave amplitude over NCG is much greater in the AtISST model experiment relative to the control experiment, with a negative anomaly that has strengthened and is of larger spatial extent.

The response of eddy Z200 in the IndSST model experiment relative to the control model experiment, similarly to the AtISST model experiment also shows a westward shift of the northeast Pacific positive eddy Z200 and an equatorward shift of the negative eddy Z200 within the northwest Pacific. Unlike the other model experiments, the negative eddy Z200 over NCG has shifted further eastward relative to the control, weakening the climatological positive eddy. These results highlight that the large-scale climatological Z200 eddies have been altered in response to imposed tropical SST perturbations particularly over the NCG region in the AtISST model experiment.

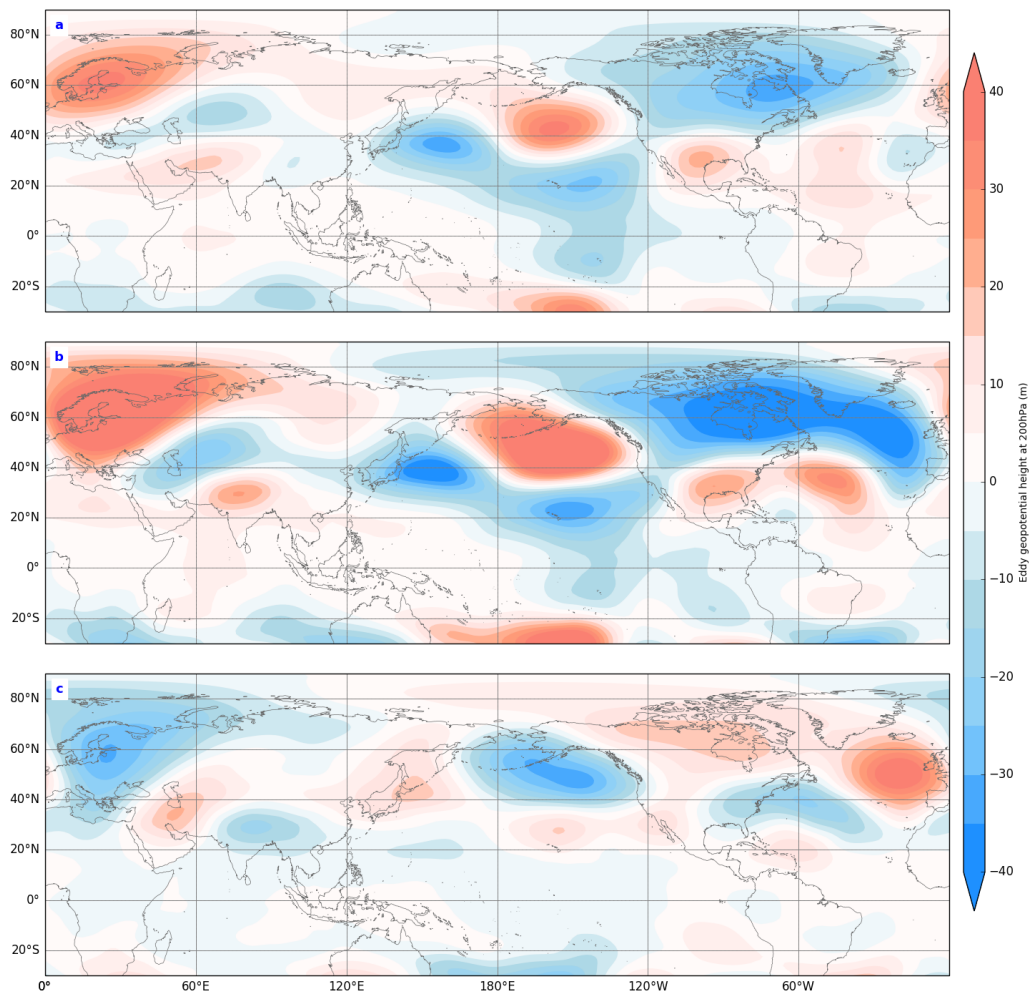


Fig. 5.3 [a] The response of eddy Z200 from the TropSST model relative to the control model experiment, [b] the sum of the response of eddy Z200 from the PacSST, AtISST and IndSST model experiments, [c] the difference between ([a]-[b]) to test linearity of model

As an aside, it is interesting to note the similarity in these results to the TropSST model experiment (Fig. 4.3) which for eddy Z200, by eye, appears to be an approximate linear summation of each ocean model experiment. To further test this, the responses of eddy Z200 from the PacSST, AtISST and IndSST model experiments are summed and compared against the TropSST model experiment response (Fig. 5.3). While the sum of the PacSST, AtISST and IndSST model experiments (Fig. 5.3 b) has fairly similar spatial

patterns of eddy Z200 to those in the TropSST model experiment, it does not exactly equate to the TropSST model experiment response. The difference between the sum of eddy Z200 from the three ocean basins and the eddy Z200 response from the TropSST model experiment is seen in figure 5.3 c and shows much stronger eddy Z200 patterns everywhere. The negative eddy Z200 over NCG as well as the positive anomaly over the Aleutian low region is much stronger in the summed ocean basin response than the TropSST model experiment result. The enhancement of the eddy Z200 from the ocean basin sum (Fig. 5.3 b) could, in part, be due to non-linearities that exist in the model. More specifically, this elucidates that different feedback processes and complex interbasin atmosphere-oceans interactions must be occurring between the three ocean basins in the TropSST model experiments relative to the forcing imposed in each basin alone (Simpkins et al., 2014). These may act to dampen or enhance the eddy Z200 patterns in the full tropical forcing in the TropSST model experiment, which may be important in the mechanistic driving of this large negative eddy Z200 anomaly over NCG.

Nonetheless, these figures show that the AtISST model experiment dominates the response over NCG relative to the other model experiments and more closely resembles the TropSST model experiment response over NCG as found in figure 4.3 in the previous chapter. This indicates that the Atlantic SST perturbation is the more important tropical SST forcing region in driving the negative eddy Z200 pattern over NCG. While Pacific SST perturbations are most widely acknowledged at exerting a large influence on extratropical and high-latitude climate (Ding et al., 2011; Ferranti et al., 1994; Karoly et al., 1989; Simpkins et al., 2012), a similar result to this was presented in a study by Simpkins et al. (2014). In this they found that trends of geopotential height at 500 hPa (Z500) over the South Pacific by Atlantic SST perturbations shared a much greater resemblance to trends associated with global SST forcing that compared to both Pacific and Indian SST perturbations and that a tropical Atlantic SST perturbations resulted in a warming over the Antarctic Peninsula due to changes in the Hadley cell and generation of anomalous Rossby waves.

### 5.3 Mechanisms of the tropical forcing on large scale climate and the effect of this on NCG

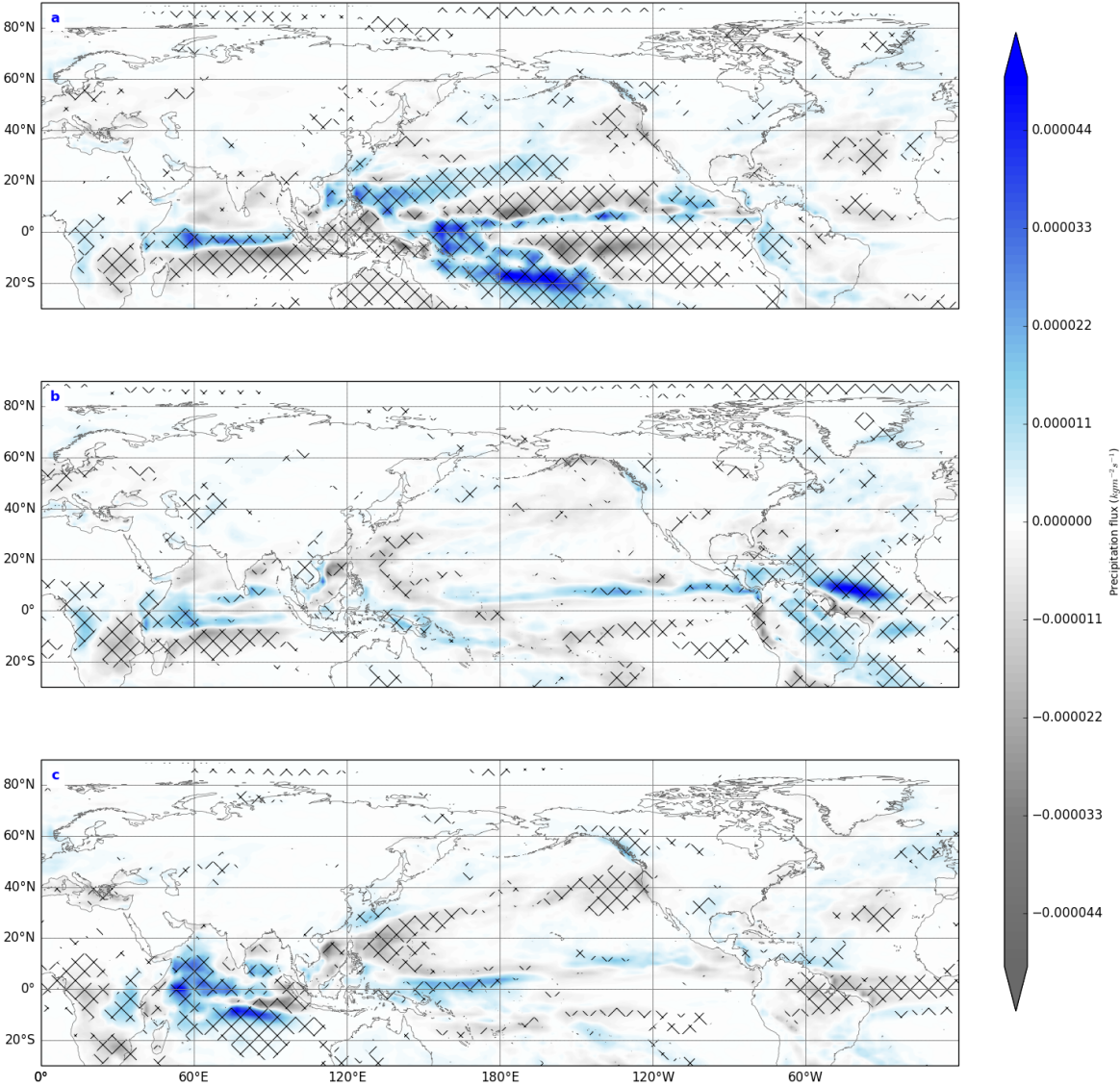


Fig. 5.4 Response of DJF precipitation rate for [a] PacSST model experiment, [b] AtlSST model experiment, [c] IndSST model experiment. Stippling indicates statistical significance at  $p < 0.05$ .

The causes of the negative eddy Z200 responses over NCG from all individual ocean basins are further investigated to diagnose the mechanisms that drive them and identify why the AtlSST model experiments contributes most to the overall TropSST model experiment response.

Convection and divergence responses in each ocean model are assessed to understand the changes in the dynamics of the atmosphere and the generation of Rossby waves. Figures 5.4 and 5.5 show the response of convection to all individual ocean model experiments using the total precipitation rate, which is the sum of the large-scale surface convective rainfall and snowfall, and outgoing longwave radiation (OLR) as indicators. Statistically significant convection in the PacSST model experiment is largely concentrated in the western tropical Pacific around 120°E to 135°W and 10°N to 20°N where the largest area of precipitation occurs (Fig. 5.4 a) and largest reduction of OLR takes place (Fig. 5.5 a) to generate upper-level of divergence at 200 hPa (Fig. 5.6 a). Statistically significant convection is also present in the Atlantic ocean in the AtlSST model experiment with increases on precipitation and decreases on OLR found around 60°W to 30°W and 5°N to 10°N (Figs. 5.4 b, 5.5 b) resulting in horizontal wind divergence at 200 hPa (Fig. 5.6). In response to the IndSST model experiment, statistically significant convection is mainly concentrated in the Indian ocean region specifically between 55°E to 75°E and 0° to 15°N with increases in precipitation (Fig. 5.4 c) and decreases of OLR (Fig. 5.5 c) found in this region.

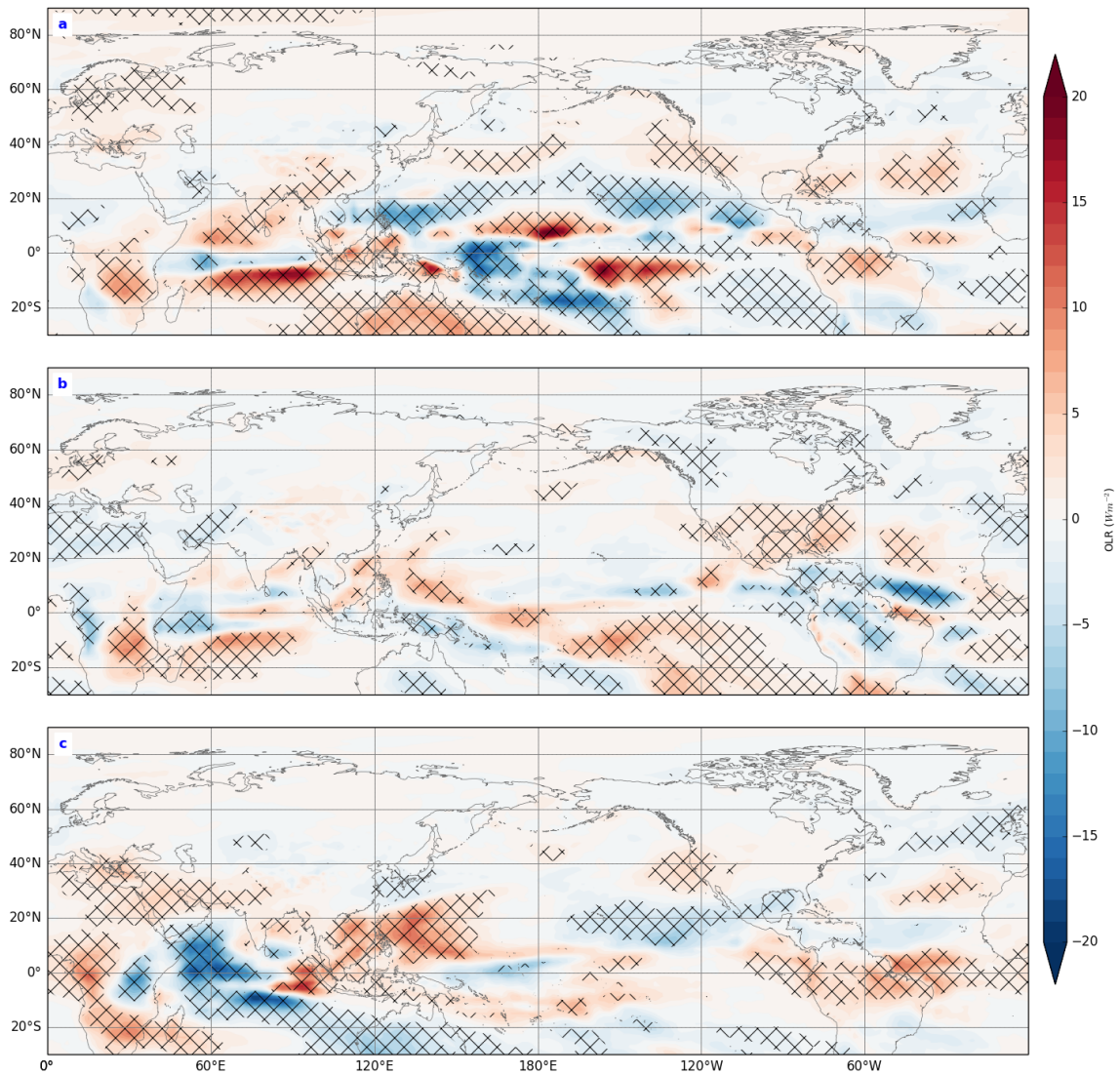


Fig. 5.5 Response of outgoing longwave radiation in DJF for [a] PacSST model experiment, [b] AtlSST model experiment, [c] IndSST model experiment. Stippling indicates statistical significance at  $p < 0.05$ .

These areas of convection results in regions of divergence (Fig. 5.6) which can then result in anomalous Rossby wave sources (RWS). As per Rossby wave source theory, as outlined in Shimizu and de Albuquerque Cavalcanti (2010), anomalous RWSs are generated away from the regions of divergence as expected based on Rossby wave source theory which can be seen here however, the anomalous RWS response is quite stochastic

in all ocean model experiments. This could be due to the fact that in each ocean model, there are statistically significant anomalous responses in precipitation and OLR in other ocean basins outside of where the forcing is. These responses therefore will have given rise to divergence and RWS anomalies which makes it difficult to interpret the response from each ocean separately. Therefore to interpret potential Rossby wave sources, greater focus is placed on precipitation (Fig. 5.4) and OLR (Fig. 5.5) and from these it can be inferred that Rossby wave sources would occur in the PacSST model experiment, northwards of  $20^{\circ}\text{N}$  in the Pacific ocean (Fig. 5.4 a). This can be seen in the RWS response in figure 5.7 a where the largest anomalous RWS in the Pacific ocean in the PacSST model experiment is found around  $30^{\circ}\text{N}$ ,  $125^{\circ}\text{E}$  to  $160^{\circ}\text{E}$  (Fig.5.7 a). In the AtlSST model experiment, where the largest region of statistically significant convection occurs around  $15^{\circ}\text{N}$ , a RWS would be expected to found poleward of this and in the RWS response (Fig.5.7 b) an anomalous source is found at approximately  $20^{\circ}\text{N}$  to  $30^{\circ}\text{N}$  and  $55^{\circ}\text{W}$  to  $20^{\circ}$  in the Atlantic ocean. The convection generated in the tropical Indian ocean, in response to the imposed tropical Indian SST perturbation (Fig. 5.6 c) infers that a RWS would occur near this region however there does not appear to be a distinct area of RWS on its poleward side (Fig. 5.7 c). This may be due to the fact that the Himalayas are north of the Indian Ocean and display both positive and negative signs of Rossby wave source, which may hid any signal from an Indian SST perturbation.

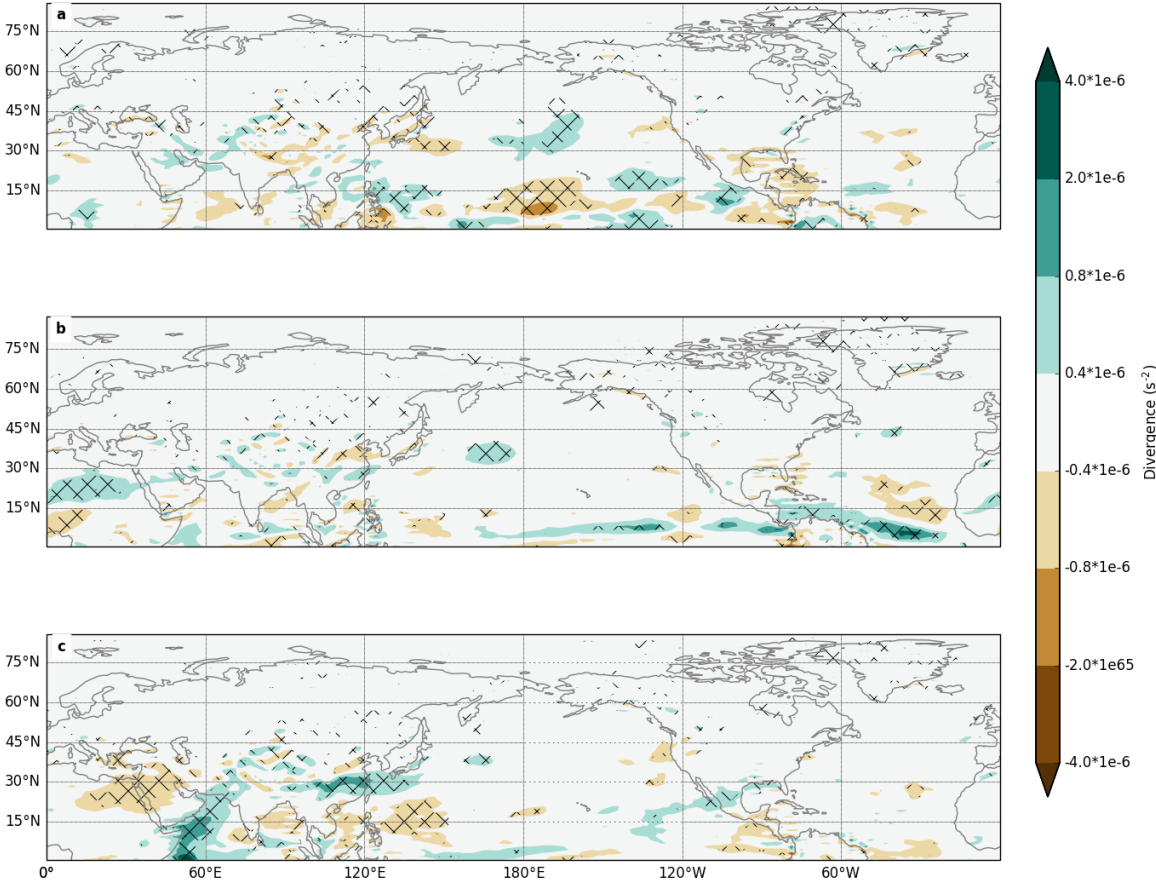


Fig. 5.6 Response of horizontal wind divergence in DJF for [a] PacSST model experiment, [b] AtlSST model experiment, [c] IndSST model experiment. Stippling indicates statistical significance at  $p < 0.05$ .

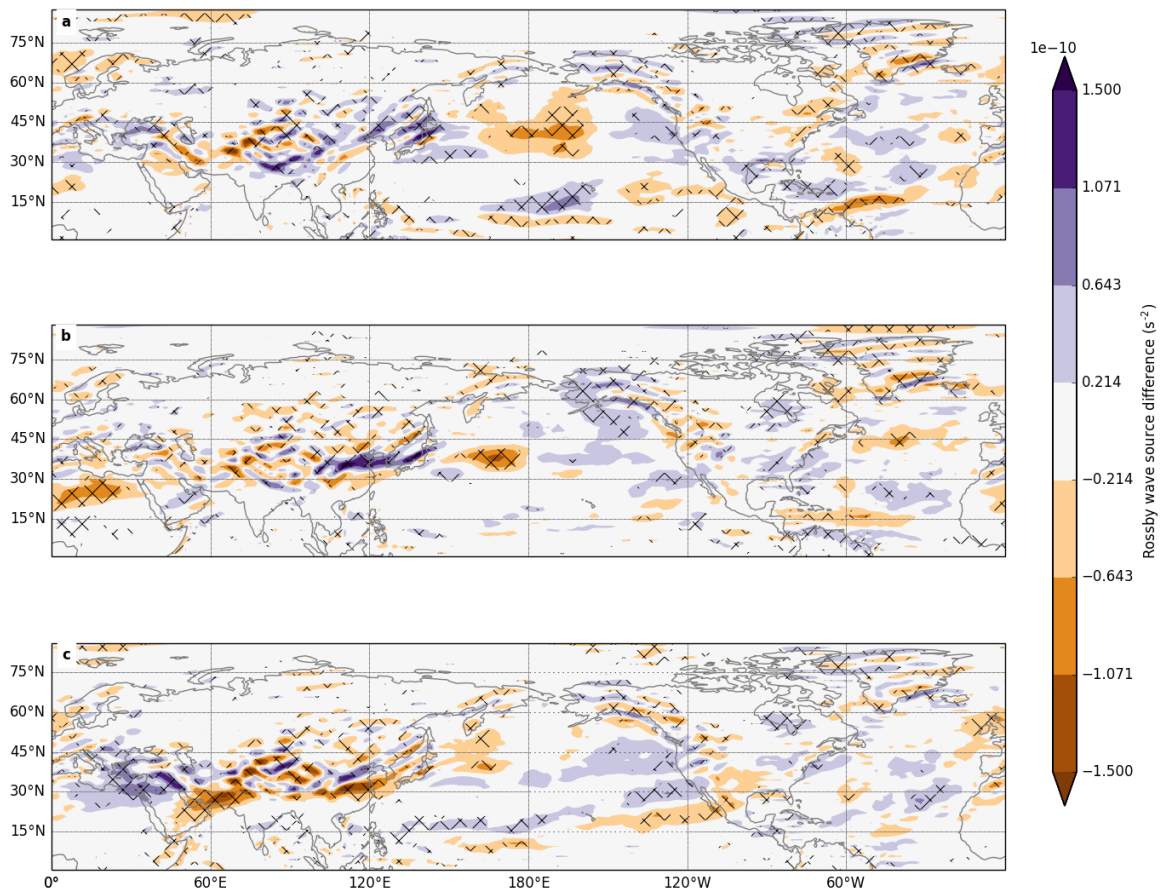


Fig. 5.7 Response of Rossby wave source in DJF from [a] PacSST model experiment, [b] AtlSST model experiment, [c] IndSST model experiment relative to control model experiment. Stippling indicates statistical significance at  $p < 0.05$ .

Wave activity flux (WAF) responses are depicted by the black vectors in figure 5.8 and superimposed on the eddy Z200 response as displayed before for [a] PacSST model experiment, [b] AtlSST model experiment and [c] IndSST model experiment. Apparent in all figures is the fact that there is no strong tropically-excited Rossby wave that appears to propagate on to NCG region similar to that from ERA Interim (Fig. 4.1). The WAF response from the PacSST model experiment (Fig. 5.8 a) highlights an anomalous WAF, generated in the west Pacific that propagates polewards and eastwards. This continues as far downstream as the western coastline of North America however, it does not extend to the NCG region. This shows some similarity to the anomalous WAF from the TropSST model experiment in figure 4.6 in chapter 4, except where it propagates over the west

---

of North America. Wave anomalies from the AtlSST model experiment show some poleward propagating vectors which appear to be deflected westward from the tropical Atlantic ocean. These appear to skirt the southern flank of the negative NCG eddy Z200 anomaly and on to the large positive eddy Z200 anomaly over the Bering Sea and north Pacific ocean. However, based on Rossby wave theory, waves generally propagate eastward with the background flow, so this WAF anomaly may signal a weakening of the climatological waves (as shown in figure 4.5 in chapter 4) or a reduction in wave activity/strength across north America e.g. due to changes in land/sea temperature contrast and not actual propagation across North America. The WAF response from the IndSST model experiment does not have large anomalous poleward propagating waves generated from its ocean basin. An anomalous wave train that extends from the Aleutian low region at approximately  $40^{\circ}\text{N}$ ,  $160^{\circ}\text{W}$  on to the west coast of North America is found instead. As this anomalous wave train is not directly driven in the Indian ocean by the Indian ocean SST perturbation it may be the result of some non-linear feedback between the tropical Indian ocean and the north Pacific ocean e.g. from the anomalous OLR and precipitation in the Pacific ocean in spite of no anomalous forcing in this ocean. As anomalous WAF between the tropics and the NCG region is not evident in these results, especially from the Atlantic ocean, which generated the largest and most significant negative eddy Z200 response suggests that this anomaly may be the cause of indirect dynamical effects or non-linear feedback processes between the different ocean basins.

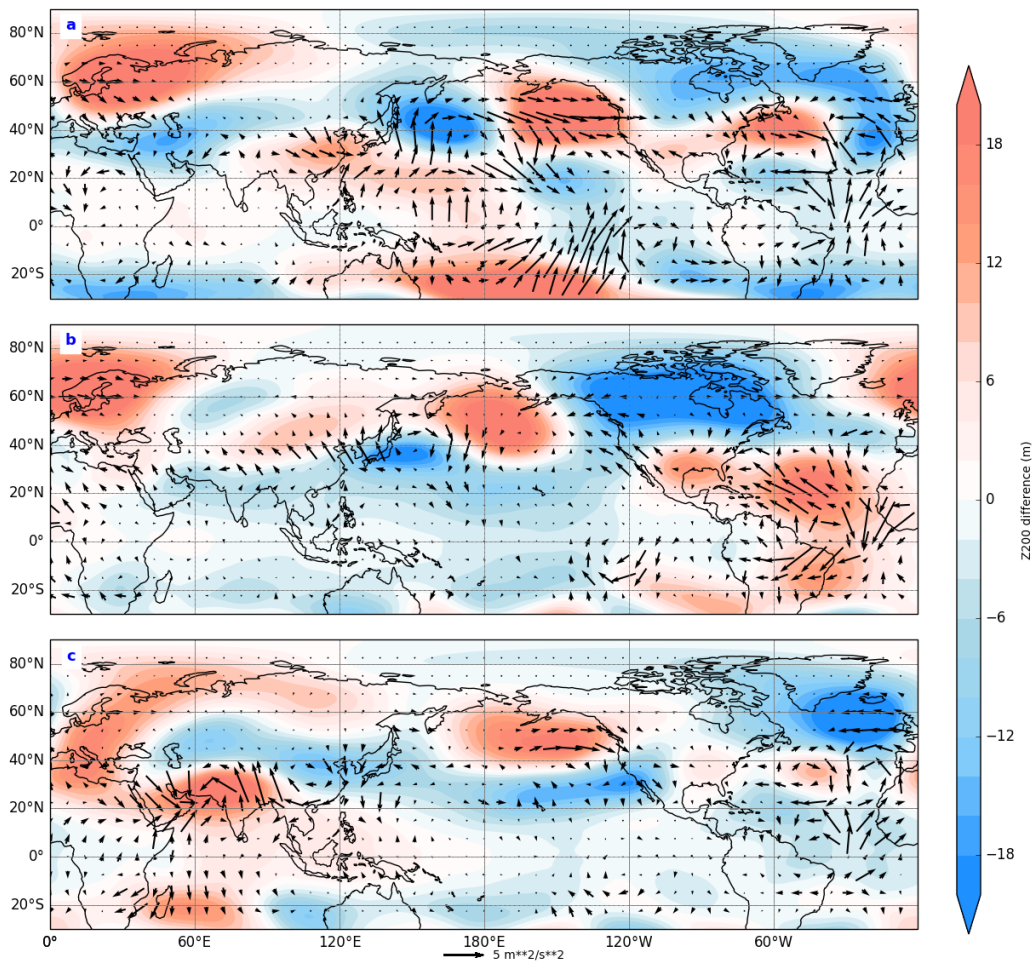


Fig. 5.8 Response of WAF (black vectors) and eddy Z200 (shading) in DJF for [a] PacSST model experiment, [b] AtISST model experiment and [c] IndSST model experiment

Previous studies demonstrate that wave propagation is due to changes in the background flow specifically in the zonal wind (Ambrizzi and Hoskins, 1997; Freitas and Ambrizzi, 2012).

Propagation of the anomalous WAF due to the zonal wind response from each of the individual ocean model experiments are investigated in further detail below. As the response over NCG in the IndSST model experiment was much weaker than the other model experiments, this suggests that it does not play an influential role on the

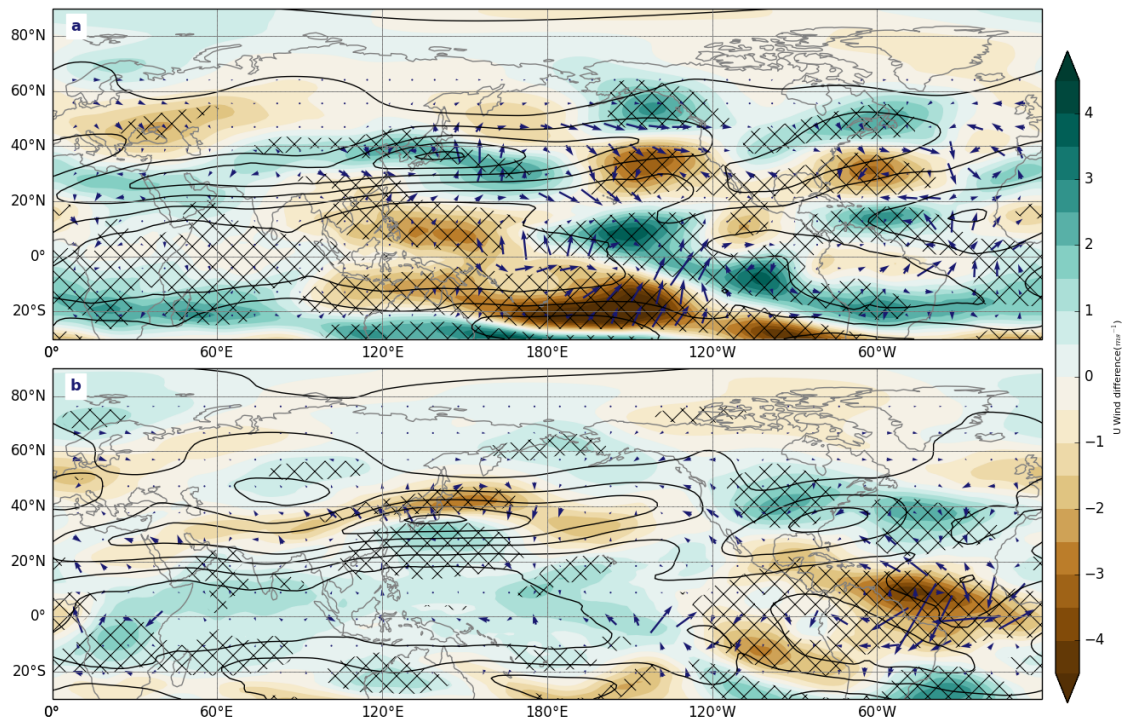


Fig. 5.9 DJF response of wave activity flux (blue vectors) and zonal wind (shading) in the [a] PacSST model experiment and [b] AtISST model experiment. Superimposed in unfilled contours in the zonal wind from the control model experiment.

negative eddy Z200 over NCG. Therefore all further analysis will only be conducted for the PacSST and AtISST model experiments.

Figure 5.9 displays the DJF WAF response (in blue vectors) and the zonal wind response (in shading) from the PacSST and AtISST model experiments, with the climatological zonal wind from the control model experiment superimposed on top in contours. The response of the zonal winds in the PacSST model experiment results in a positive zonal wind anomaly (shading) on the poleward flank of the climatological jet (contours) in the northeastern Pacific. This indicates a strengthening of the westerly winds here and suggests a potential poleward shift of the jet at this location (Fig. 5.9 a). The response of the zonal wind in the AtISST model experiment (Fig. 5.9 b) shows positive wind anomalies on both the poleward side of the eddy driven jet over North America and equatorward side of the jet in the subtropical Atlantic. This results in a strengthening of

westerly winds on both sides of the jet, which suggests a more zonal jet in response to the imposed Atlantic SST perturbation.

The changes in mid-tropospheric temperature (between 300 hPa and 800 hPa) and displayed in figure 5.10 and highlight a statistically significance warm anomaly over the north east Pacific in the PacSST experiment and in the north Pacific in the AtlSST model experiment. Both model experiments also show a cold anomaly over most of Canada, however this is strongest and statistically significance in the AtlSST model experiment. A further statistically significant warm anomaly is present within the north Atlantic around 45°N in the PacSST model experiment and 20°N in the AtlSST model experiment. The anomalies within the Pacific ocean, in the PacSST model experiment, are likely the result of warm air advection, from anomalous circulation (seen by wind vectors in figure 5.12) from the tropical west Pacific due to warmer SSTs in this region and eastward advection of warmer continental air from eastern Asia and Russia. The anomalies in the Atlantic, in the AtlSST model experiment, are due to the tropical Atlantic SST perturbation (Fig. 5.10 b) and apparent advection from the south of North America into the subtropical Atlantic in the PacSST model experiment also due to anomalous circulation generated from the model responses. The anomalous high and low spots over south Asia and Greenland are most likely due to model biases in temperature over these mountain ranges. The temperature gradient between the warm and cold anomalies in figure 5.10 for both PacSST and AtlSST model experiments, through thermal wind balance, can then generate wind anomalies. To test this, figure 5.11 shows the zonal wind response from the PacSST and AtlSST model experiments at 200 hPa calculated based on the thermal wind equation using air temperature at 200 hPa and boundary winds at 500 hPa. The zonal wind anomalies in this figure, share remarkably similar features to the actual zonal wind response at 200 hPa in figure 5.9. Figure 5.11 a shows positive wind anomalies in the north east and east tropical Pacific and subtropical Atlantic and negative zonal wind anomalies in the subtropical east Pacific in the PacSST model experiment relative to the control experiment. Zonal winds anomalies in the AtlSST model experiment between figure 5.11 b and 5.9 b also shows a similar positive wind anomaly over the north Pacific, however this is weaker in the winds calculated from

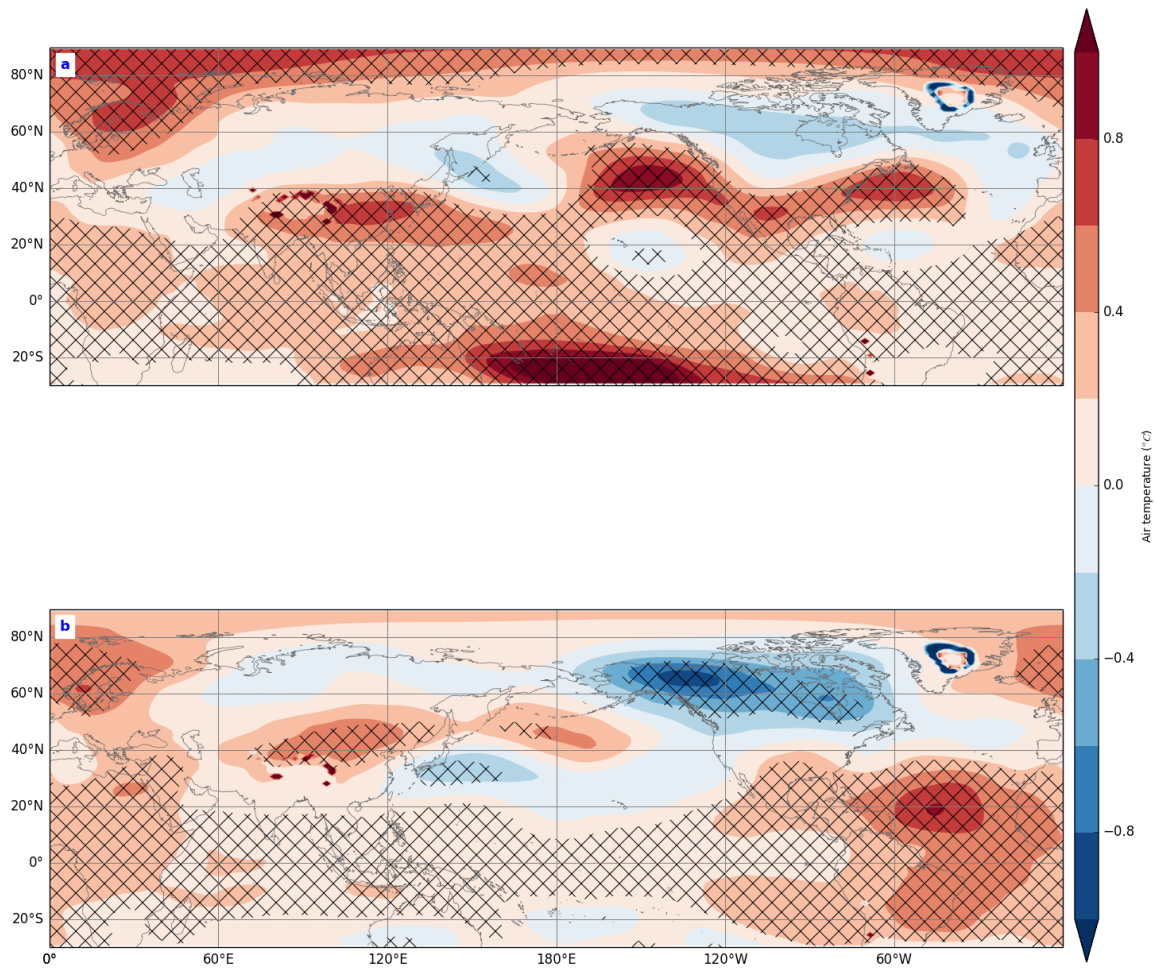


Fig. 5.10 Response of mid tropospheric air temperature taken across 350-800 hPa for [a] PacSST model experiment, [b] AtlSST model experiment. Stippling indicates statistical significance at  $p < 0.05$ .

the thermal wind relative to the actual zonal winds. This could be as a result of the integrations required when calculating thermal wind at 200 hPa which may have resulted in the slight weakening of the wind. This indicates that the zonal wind anomalies are due to the generation of temperature gradients in response to the imposed tropical SST perturbations from both the Pacific and Atlantic oceans.

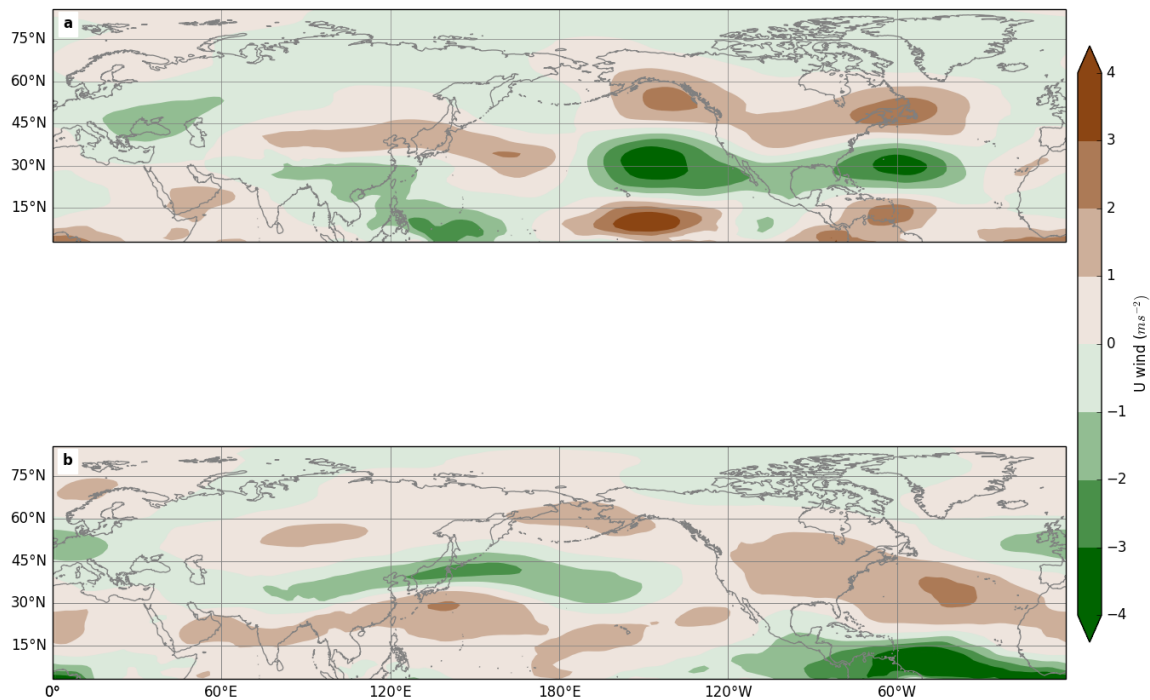


Fig. 5.11 Response of zonal wind at 200 hPa, calculating through the thermal wind equations for [a] PacSST model experiment and [b] AtlSST model experiment.

The anomalous WAF in the PacSST model experiment propagates from the west to the east Pacific due to the strong DJF climatological westerly jet in the same region (Fig. 5.9 a). Conversely to the TropSST WAF response, at the north east Pacific where the positive zonal wind anomaly is found, the wave train splits and is partially deflected southwards while a second limb is channelled along the equatorward side of the zonal wind anomaly, allowing downstream propagation of WAF. The PacSST model experiment also generates a poleward shift of the eddy driven jet in the Atlantic ocean.

The anomalous WAF, generated around 20°N and between 50°W to 20°W in the AtlSST model experiment, appears to be deflected westward by the increase in the strength of the westerly winds around the eddy driven jet. However, as stipulated previously, these anomalous vectors more likely show a weakening of the waves here and along the western coast of North America.

The response of the eddy Z200 over NCG in the PacSST and AtlSST model experiments is negative most likely due to the same mechanism detailed in chapter 4 for the TropSST model experiment. This states that the zonal wind response, which inhibits WAF propagation on to NCG, also results in anomalous cyclonic and anticyclonic flow. This results in cold air advection southward from a climatologically colder Arctic region (Fig. 4.12) as a result of the anomalous cyclonic circulation over NCG. A land/sea gradient in temperature develops between the colder NCG and warmer Arctic (Fig. 5.10) which can lead to an intensification of the stationary trough, as shown by Yin (2005) and Lu and Ren (2016), over NCG.

The negative eddy Z200 response in the PacSST model experiment is, however, not as large as the response from the AtlSST model experiment which may be because the temperature gradient between the NCG region and the Arctic is not as steep due to weaker cyclonic circulation. The propagation of the WAF anomalies from the PacSST model experiment on to the west of North America may have disturbed the flow, weakening this circulation therefore generating a less steep temperature gradient and a weaker negative eddy Z200 anomaly in comparison to the AtlSST model experiment.

The response of the negative eddy Z200 in the AtlSST model experiment is more similar to the TropSST model experiment, relative to the PacSST model experiment, due to its forcing on the westerly winds in the Pacific ocean. Westerly winds in the north Pacific, in response to the AtlSST model experiment, increases in strength specifically around the Aleutian islands. This region also experienced a strengthening of westerly winds in the PacSST model experiment. In the overall TropSST model experiment, this anomaly is strengthened even further. This suggests that the positive zonal wind anomalies from both the imposed tropical Pacific and Atlantic SST perturbations results a stronger westerly wind anomaly in the northeastern Pacific in the TropSST model experiment.

To test this hypothesis, the responses of the zonal wind and WAF from the PacSST model experiment and AtlSST model experiment were summed together and plotted with the zonal wind response from the TropSST model experiment. Figure 5.13 b highlights

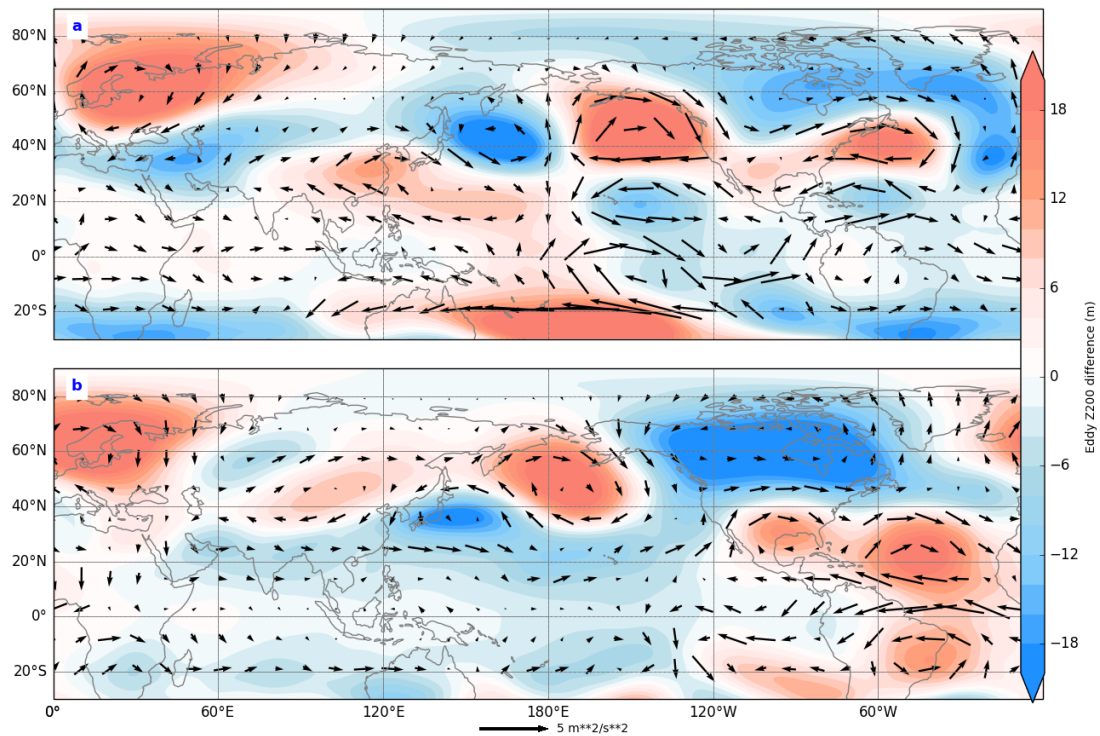


Fig. 5.12 DJF eddy Z200 response from [a] PacSST model experiment and [b] AtlSST model experiment relative to the control model experiment with wind vectors superimposed

that the summed zonal wind response from the PacSST and AtlSST model experiments (shading) is almost the same as the zonal wind response in the TropSST model experiment (contours). This indicates that the zonal wind response is a linear sum of the imposed Atlantic and Pacific SST perturbations. The sum of the WAF from the PacSST and AtlSST model experiment is also shown (blue vectors) and in comparison to the WAF response in the TropSST model experiment (Fig. 5.13 a) is also almost the same. This shows that the wave reflection in the north east Pacific in the TropSST model experiment is due to an strengthened westerly wind anomaly. The strengthening of this positive wind anomaly is due to the imposed tropical Atlantic SST perturbation as the wind anomaly from the PacSST model experiment only partially deflects the WAF but channels most of this on to the west of North America. Inhibiting the anomalous wave propagation may lead to a less disturbed circulation anomaly and therefore more cold air advection southward from the climatologically colder Arctic, therefore generating a large thermal

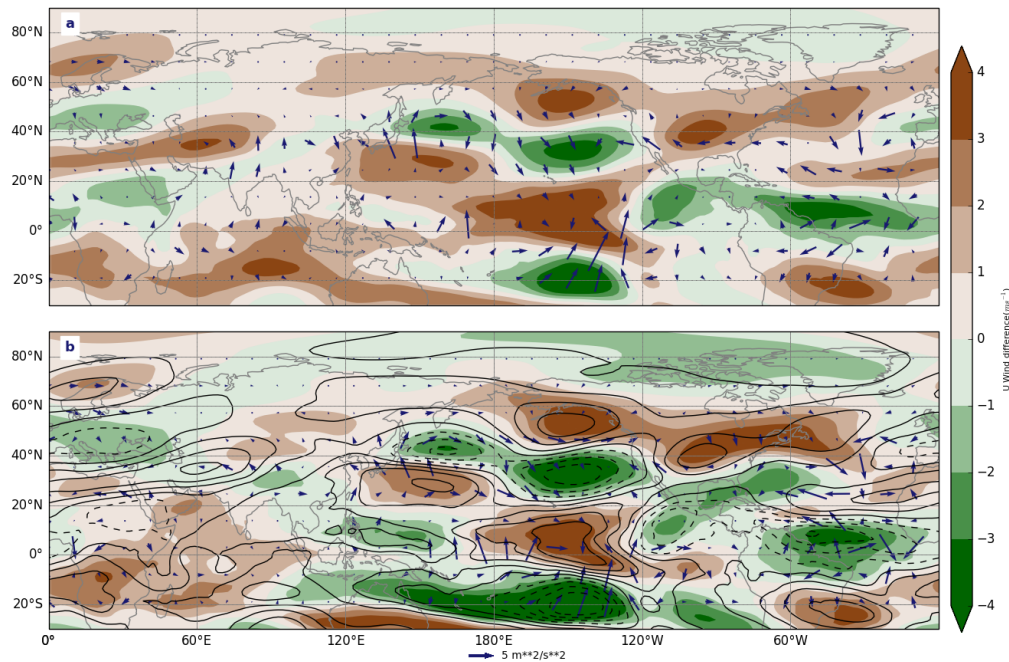


Fig. 5.13 [a] DJF WAF and U wind at Z200 response from TropSST model experiment relative to the control model experiment, [b] sum of response of DJF WAF and U wind at 200 hPa from the PacSST and AtISST model experiment

land sea contrast further intensifying the climatological trough over the NCG region (Fig. 4.3).

Therefore as the circulation anomaly over NCG in both the TropSST and AtISST model experiments is less disturbed relative to the PacSST model experiment due to lack of anomalous WAF on to the NCG, which for the TropSST model experiment, is due to the strengthened westerly wind in the north east Pacific from the positive zonal wind anomaly in the AtISST model experiment, may explain why the eddy Z200 response over NCG in the TropSST and AtISST model experiments shares is similar.

These results demonstrate that the generation of a large negative eddy Z200 anomaly over the NCG region in the PacSST and AtISST model experiments is similar to the TropSST model experiment and largely the result of a deepening of the climatological trough found over NCG in figure 4.3 a. The response of eddy Z200 over NCG from both the Pacific and Atlantic imposed tropical SST perturbations are similar in sign to the

TropSST model experiment, however the AtlSST model experiment shows more similarity. This is because, through generating a zonal wind anomaly over the north Pacific, it strengthens the westerly winds here which result in some convergence and equatorward refraction of anomalous WAF. This may result in less disruption to circulation over NCG, similar to the AtlSST model experiment, and generate stronger thermal gradients between the NCG and the Arctic and therefore a stronger negative eddy Z200 in both the TropSST and AtlSST model experiments.

## 5.4 Concluding remarks

In perturbing tropical sea surface temperatures (SSTs) for each ocean basin, one attempts to disentangle the tropical signal in patterns of eddy Z200 over NCG between each of the largest tropical ocean basins. This therefore allows for further scrutiny of the tropical influence on NCG and specifically what causes the patterns of change. Negative eddy Z200 responses over NCG were found from all ocean model experiments, relative to the control model experiment, which in comparison to the climatological eddy Z200 from the control experiment demonstrates a deepening of the climatological trough over this region. It was found that the largest and most significant negative eddy Z200 anomaly, in the NCG region, occurred in response to the AtlSST model experiment and that this bore more resemblance to the TropSST model experiment response than the other ocean model responses. This, therefore shows that the imposed tropical Atlantic SST perturbation plays a key role in the negative eddy Z200 over NCG from the all tropical forcing relative to the other individual ocean basins.

An analysis of the underlying dynamics was conducted to determine why the eddy Z200 response over NCG is negative in all models and why the tropical Atlantic SST perturbation has a larger influence on TropSST model experiment response. This finds that anomalous Rossby wave sources (RWS), shown by increases in tropical convection and upper level divergence (estimated through changes in precipitation and OLR), produces anomalous wave activity fluxes (WAF) mainly within the Pacific and Atlantic

oceans mainly. For the PacSST model experiment, this generated an anomalous wave train in the west Pacific, which propagates across the north Pacific and on to the west of North America, but does not extend further downstream and in to the NCG region while anomalous WAF from the AtlSST and IndSST model experiments, did not propagate towards the NCG region. It may be that the negative eddy Z200 over NCG is a deepening of the climatological trough caused because of the sharp land/sea temperature contrast between the Arctic and north Canada.

The strong similarity in the negative eddy Z200 over NCG between the TropSST and AtlSST model experiment, appears to be due to the zonal wind response to the imposed tropical Atlantic SST perturbation and its impact on WAF propagation. In comparing the zonal wind and WAF response from the TropSST to the PacSST and AtlSST model experiments, it is found that, relative to the PacSST experiment, that WAF anomalies in the TropSST experiment show some convergence on the poleward side of the zonal wind anomaly and equatorial deflection in the east Pacific (Fig. 5.9 a and b). This is due to a stronger westerly wind anomaly in the TropSST model experiment in the same region as found in the PacSST model experiment. This strong TropSST zonal wind response appears to be the result of the positive wind anomaly in the north Pacific generated from the AtlSST model experiment, which, when linearly summed with the PacSST model experiment's zonal wind response (Fig. 5.13) generates a very similar positive anomaly as the TropSST model experiment. The sum of the WAF responses from both the PacSST and AtlSST model experiment also shows a similar response to the TropSST model experiment WAF response. This indicates that the strengthening of the zonal wind anomaly by the AtlSST model experiment, results in some convergence, on the poleward side of the zonal wind anomaly and equatorward deflection of WAF therefore resulting in less wave propagation on the west of North America. The lack of WAF over NCG in the TropSST and AtlSST model experiments could result in less perturbed and therefore stronger cyclonic circulation over NCG relative to the PacSST model experiment resulting in stronger land/sea temperature gradients from increased cold air advection. This, therefore, would result in more similar negative eddy Z200 responses over NCG from the TropSST and AtlSST model experiments relative to the PacSST

**158** Influence of the three major tropical ocean basins on north Canada and Greenland

model experiment, and explain why the imposed tropical Atlantic SST perturbation contributed more to the TropSST model response.

# Chapter 6

## Conclusions

This study has aimed to assess and quantify the change in atmospheric circulation over north Canada and Greenland (NCG) and specify how the circulation over this region responds to perturbations in tropical sea surface temperatures (SSTs).

Previous work in this area of research indicates that a tropical forcing may play a role in circulation change over NCG, however the full nature and mechanisms that drive this are still not fully known. A study published by Ding et al. (2014), highlighted a poleward propagating wave, generated in the tropical Pacific in ERA-Interim reanalysis data (ERA-Interim) which resulted in the positive temperature and geopotential height at 200 hPa (Z200) annual trends over NCG between 1979-2012. They found similar temperature and Z200 trends in an ensemble of model integrations, using the ECHAM 4.6 climate model, forced with observed transient tropical SSTs between 30°N and 30°S, with the extratropical atmosphere coupled to a slab ocean and a thermodynamic sea ice component. A poleward propagating wave generated from the tropical Pacific was also found in these simulations, however, the trajectory of this wave differed than that from the ERA-Interim analysis. The wave generated in the ECHAM 4.6 climate model propagated over North America and on to NCG rather than in an arc-like trajectory over the Pacific ocean, across NCG and in to the north Atlantic as found in ERA-Interim and in Trenberth et al. (2014). The differences in these wave trains highlight that tropical forcing on NCG and the

mechanisms for this teleconnection are still not fully understood or properly represented in models. Therefore, this thesis aims to bridge this gap to determine how atmospheric circulation trends in NCG have changed over time, how they respond to anomalous tropical SSTs and propose a mechanism for how the imposed tropical SST perturbations have affect this region.

A number of questions were outlined in the introduction to direct the research, which generally indicate the direction of each chapter of this thesis. These are addressed below.

1. How robust are the strength of circulation trends over NCG?

Addressed in chapter 3, the strength of circulation trends over north Canada and Greenland were investigated based on the positive Z200 trends from Ding et al. (2014).

To determine the robustness of this positive trend, the annual trends of eddy Z200 from ERAI, UPSCALE, a 13 member ensemble model based on HadGEM3-A of three varying resolutions, N96, N216 and N512, and AMIP, a 30 member ensemble of different models (all models in AMIP are outlined in table 3.1), were determined. All three datasets found positive eddy Z200 trends across their respective time periods, 1979 to 2014, 1985 to 2011 and 1979 to 2005, respectively, indicating that this signal is robust and most prominent in boreal winter (DJF). It was also found that the strength of the trends across all datasets were dependent on time, where the eddy Z200 positive trend tends to be stronger in the latter part of the record (1985 - 2011)

The annual and DJF trends of the UPSCALE and AMIP model members had a relatively large spread around the ERAI annual and DJF mean; UPSCALE had roughly the same number of members which simulated positive trends and negative trends, with a few that simulated no or negligible trends. AMIP had comparatively more models whose annual and DJF trends over NCG were less than ERAI than models who had a larger trend over NCG than ERAI. The spread of these members around the ERAI mean, of which is also only one potential realisation of climate similar to the model members of UPSCALE and AMIP, indicate a potential role of atmospheric internal variability in

the generation of these trends. However, the similarity of the trends of UPSCALE and AMIP, which are forced with observed transient global SSTs, to the ERAI trends also indicates a role of SSTs in driving these trends. The tripole of eddy Z200 trends across the Pacific, similar to observations from Trenberth et al. (2014) and Ding et al. (2014) implies a potential tropical forcing of the eddy Z200 trends within these data.

The similarity of the trends from all datasets, even with the spread of trends around the ERAI mean indicate that the positive trends of eddy Z200 over NCG is a robust one and has got stronger in the later part of observational record.

2. Can the tropical regions influence atmospheric circulation over NCG and how has the circulation of NCG responded to imposed SST perturbations in the tropics?

Assessed in chapter 4, many previous studies have shown that tropically-excited planetary waves can propagate polewards (Hoskins and Ambrizzi, 1993; Hoskins and Karoly, 1981; Karoly, 1983; Simmons et al., 1983; Trenberth et al., 2014). Ding et al. (2014) specifically showed a tropically-excited Rossby wave that propagated on to NCG and resulted in positive trends of temperature and geopotential height. Analysis from ERAI, UPSCALE and AMIP also display a similar wave train to the those found in the ERAI results in figure 1 a from Ding et al. (2014) and also in figure 5 a from Trenberth et al. (2014) for DJF. The strength of these wave trains, however, vary between each of the datasets, with the wave train in both UPSCALE and AMIP not propagating on to the NCG region, but do follow the same arc-like trajectory over the north Pacific. Differences in the strength of these wave trains could be due to internal variability, as highlighted in the analysis in chapter 3, or have been smoothed due to averaging across the different ensembles and model members. The differences, however, may also indicate model inability to fully capture this large-scale wave pattern.

The connection between the tropics and NCG were further investigated to determine how the circulation of NCG responded to perturbations in tropical SSTs. For this, a model sensitivity experiment ('TropSST') was designed using HadGEM3-A, based on the observed differences of SSTs between 2003-2012 and 1979-1988, between 30°N and 30

°S. These anomalies were then doubled and imposed on to a background state poleward of 30°N and 30 °S with climatological SSTs from 1979-1988. This resulted in SSTs which were anomalously warmer over the Atlantic and Indo-west Pacific oceans and colder over the east Pacific, indicating a La-Niña like pattern of SST anomalies.

The DJF circulation response over NCG to the imposed tropical SST perturbation, resulted in a negative Z200 eddy, in direct contrast to the observed trends over the same time period as shown in chapter 3. An analysis of the boreal winter wave activity flux (WAF), based on Plumb (1985), highlighted anomalous waves within the north Pacific that propagated from the west to east Pacific, which bears some resemblance to a wave train, generated from a similar location, in Hoskins and Ambrizzi (1993). This WAF anomaly appeared to converge on to a positive eddy Z200 anomaly in the east Pacific, namely on its poleward side but was largely refracted equatorwards. Westward propagating waves were also found within the Atlantic ocean basin. Rossby wave theory, however, tells us that waves cannot propagate westward so these apparent westward propagating vectors are more likely to be a weakening of the WAF in this region.

Further investigation of the background flow found, in response to the imposed tropical SST perturbations, an anomalous Rossby wave source was generated in the west Pacific, which generated the anomalous WAF that propagated across the north Pacific. These anomalous waves, which propagated within the region of the climatological jet, may have been weakened due to a weakened jet, in response to the tropical SST perturbations, and therefore not able to continue to propagate further downstream. Furthermore, a positive zonal wind anomaly in the north east Pacific, indicating a strengthened westerly wind anomaly, formed due to the anomalous heating in the region, appeared to lead to some wave convergence and also refract anomalous WAF equatorward. This also may have inhibited further downstream propagation of the WAF anomaly and thus prevented anomalous WAF from affecting the climatological trough over NCG. Circulation over this region therefore may have been able to strengthen which may have resulted in the advection of climatologically colder air from the Arctic over NCG generating a strong land/sea contrast between NCG and the Arctic. An increase in the land/sea temperature contrast as highlighted by (Lu and Ren, 2016; Yin, 2005) can intensify stationary troughs.

---

This process therefore may have deepened the trough further resulting in the anomalous negative eddy Z200 found in these model results.

3. What are the relative contributions of each of the tropical ocean basins: the Pacific, Atlantic and Indian; on the circulation over the NCG region?

Previous studies on large-scale teleconnections generally focus on teleconnections generated from one tropical ocean basin rather than from the entire tropical region. Chapter 5 of this thesis, therefore, also disentangles this large scale tropical signal in to the three largest tropical ocean basins. This is conducted through running three different model experiments, based on the same SST perturbations as the TropSST model experiment, except imposed only for the Pacific, ('PacSST'), Atlantic, ('AtlSST'), and Indian, ('IndSST'), ocean basins.

Negative eddy Z200 responses over NCG in boreal winter were found in response to the individual ocean model experiments, similar to the TropSST model experiment. The mechanism for this appears to be similar to that found in chapter 4 the TropSST model experiment, in that the lack of anomalous WAF on to the NCG region may have resulted the negative eddy Z200. This appears to be because the cyclonic circulation is strengthened and therefore through cold air advection southward from the Arctic, can generate a larger temperature gradient between NCG and the Arctic, further intensifying the climatological trough.

The largest and most significant response was found in the AtlSST model experiment, which most closely resembles the TropSST model experiment response, compared to the PacSST and IndSST model experiments (Fig. 5.2). This indicates that the imposed tropical Atlantic SST forcing plays a more important and significant role in the large-scale eddy Z200 negative response from TropSST model experiment.

The similarity of the eddy Z200 response between the AtlSST and TropSST model experiments appears to be due to lack of anomalous WAF on to North America relative to the PacSST model experiment. This is driven in the TropSST model experiment by

the imposed tropical Atlantic SST perturbation which further strengthened westerly wind anomaly over the north east Pacific from the PacSST model experiment, which is further evidenced as both model experiment responses linearly sum to produce the TropSST zonal wind response. The stronger zonal wind anomaly results in some convergence and greater refraction of the anomalous WAF in the Pacific ocean, compared to the PacSST model experiment, where anomalous WAF propagated further downstream on to the west coast of North America. Therefore, conversely to the PacSST model experiment, there will be a strengthening of the cyclonic flow over NCG, as found in response to the AtlSST model experiment, which therefore will intensify the climatological trough through stronger NCG to Arctic temperature gradients as found in (Lu and Ren, 2016; Yin, 2005).

Therefore, this suggests that both the Pacific and Atlantic tropical forcings together contribute most of the overall all tropical forcing. However the Atlantic forcing plays a larger contribution as it strengthens the zonal wind anomalies which therefore impedes downstream propagation of the anomalous WAF from the Pacific. Therefore this resulted in a deepening of the climatological trough similar to the AtlSST model experiment.

4. Do extratropical SSTs have an important different effect on the NCG circulation pattern relative to tropical SSTs?

To determine why these results differed from the positive eddy Z200 trends over NCG from Ding et al. (2014), the role of the extratropical SST perturbation was investigated, as their model experimental design may have resulted in an extratropical influence.

The imposed extratropical SST perturbation, from the GloSST model experiment, relative to the tropical SST perturbation generates an amplification of the negative eddy Z200 response from the TropSST model experiment. This indicates that the tropics play a large role in driving the negative eddy Z200 anomalous pattern over NCG, relative to the extratropics. Analysis of the WAF response from this model shows that, in response to the GloSST model experiment, anomalous WAF was able to propagate from the Pacific over NCG. This anomalous WAF was due to the anomalous WAF imposed by the

extratropical SST perturbation indicating that the extratropics play an important role in generating anomalous tropic to high-latitude teleconnections. This may also indicate why the WAF response in the TropSST model experiment, was not similar to the observations as the role of the extratropics was excluded further suggestion the importance of this region in generating this specific wave train.

Overall, this highlights that in comparison to tropical SST perturbations, that the extratropics do not affect the NCG circulation differently, but instead amplify the tropical response.

In summary, results from this thesis indicate that positive trends of eddy geopotential height at 200 hPa are clear and robust across a number of climate data records. It was made obvious that the strength of these trends are dependent on time and highlight, along with the spread of ensemble and model members, that these trends may be the result of internal variability. External forces however cannot be ruled out as both UPSCALE and AMIP models which are forced with observed transient global SSTs, share similar features to ERAI, indicating that changes in SSTs may also be important. The potential for remote forcing are further implied as both ERAI, UPSCALE ensemble and AMIP multi-model means show poleward propagating waves from the tropical Pacific, however how far poleward they propagate varies between datasets.

The negative eddy Z200 response to an imposed tropical only SST perturbation in boreal winter, however, shows that the response to a tropical forcing on NCG circulation is opposite to what is found in observations. This may be the result of a deepening of the DJF climatological trough over the region which is most likely due to changes in zonal wind over north east Pacific that inhibited anomalous waves on to the NCG region, generating a stronger cyclonic flow here. These anomalies, it appears, were largely driven through changes from the imposed tropical Atlantic SST perturbations which increased the strength of the zonal wind in the north east Pacific in the TropSST model experiment. This inhibited anomalous wave propagation over North America, conversely to the PacSST model experiment, similar to the AtlSST model experiment which also

had no WAF forcing on North America. Therefore the cyclonic flow was strengthened in both the TropSST and AtlSST model experiments which therefore resulted in similar eddy Z200 responses in these two models.

Finally to understand why these results differed to those from Ding et al., (2014) an investigation into the role that the extratropical SSTs played on circulation over NCG found that they act to amplify the responses already imposed by the tropical SST perturbations. This, overall highlights that the remote forcing from the tropics are more important in driving changes in circulation over NCG than the extratropics.

In general, this work, therefore, shows that based on the imposed tropical forcings that used in the HadGEM3-A model experiments, that tropical regions generate a negative eddy Z200 over north Canada and Greenland, in direct contradiction to the observed trends. There are a number of reasons why these results may differ, such as through the seasonal changes in sea ice. Sea ice modulations will also result in circulation anomalies throughout the Arctic, which are considerable in early winter when sea ice begins to reform (Cassano et al., 2014). Secondly, the response of eddy Z200 found in this study is model dependent in that, the dynamical core of this model may not accurately simulate the climate of the Arctic and thus provide a different response than what other models may find. However, analysis in chapter 3 of AMIP models, highlighted that HadGEM2-A, an earlier version of the model used in this analysis, performed best in accurately simulating the trends of eddy Z200 between 1979-2005 compared to ERAI, suggesting that this may not be a model dependency problem. Thirdly the choice of observed anomalous SSTs used, from between 1979-1988 and 2003-2012, which generated a La-Niña like forcing may have contributed to this negative trend. A study by Lee et al. (2012) found that north Canada and Greenland cooled in response to La Niña and warmed due to the El Niño based on composites of strong El Niño and La Niña years from 1957-2001. Therefore, if the anomalous SST forcing between two different periods produced more El Niño like forcing, then the results may have been different, and potentially more like the observations. This therefore indicates, that more work

can be conducted in trying to ascertain the full effects of the tropical regions on north Canada and Greenland.

## 6.1 Future work

Throughout the process of conducting this research, ideas to progress this research were formed, however, these were beyond the remit of this thesis. This section aims to outline these ideas for future work and how exactly they would progress the results found in this thesis.

1. Assess the response of the stratosphere to the imposed tropical SST perturbations and whether there is a teleconnection signal between the tropics to the NCG region via the stratosphere

As highlighted in chapter 1, stratosphere-troposphere interactions are an important driver of Arctic climate variability, particularly in the polar night, due to modulations of the stratospheric polar vortex. Modulations of the polar vortex, also indicated in chapter 1, can be the result tropospheric forcing for example due to ENSO which in either phase can result in a strengthening or weakening of the polar vortex (Garfinkel and Hartmann, 2007; Garfinkel et al., 2010; Taguchi and Hartmann, 2006; van Loon and Labitzke, 1987). While the complete mechanistic understanding stratosphere-troposphere coupling is not fully understood, it is known that the changes in the stratosphere plays a role in modulating the strength of large scale modes of variability such as the Arctic Oscillation (AO) which therefore effects Arctic climate (Baldwin and Dunkerton, 1999, 2001). Therefore to get a more holistic understanding of the tropical effects on north Canada and Greenland circulation, investigation in to the stratospheric role on NCG relative to tropical SST perturbations could be undertaken.

To conduct this research, based on the same imposed tropical SST perturbations used here, the current model runs would need to be rerun, based on the same configuration

and model design. These runs, however, would need to include more output and extend current output to include more levels both in the troposphere and stratosphere, and over different vertical grids, namely theta levels, to fully diagnose if there is some downward influence between the stratosphere and troposphere that may have played a role in circulation changes over NCG.

2. Investigate the time development of the response to imposed tropical SSTs

Throughout this study, the seasonal responses to circulation over NCG from imposed tropical SST perturbations were found. This gives information predominately on a seasonally averaged response but does not provide information on the time lag of the response and the exact mechanism of how it developed in time. Therefore new transient SST model experiments could be designed based on the same 10 year periods of SST anomalies but averaged for every day and conducted only for DJF. This therefore would allow one to determine the time evolution of the mechanism that drives the wave anomalies in response to the daily SST forcing that resulted in the negative eddy Z200 response over NCG in boreal winter.

3. Assess the role of different tropical SST perturbations on circulation over north Canada and Greenland

The imposed tropical SST perturbations used throughout this study shared many similar features to La-Niña like SST perturbations. As noted previously, a study by Lee (2012) found that responses in the high latitudes to El Niño were opposite to those in La Niña cases. Therefore, to assess, the Arctic response to a different forcing, namely from El Niño like SSTs, and how it differs from the imposed SSTs in this study, new model experiments could be designed with SST perturbations across the entire tropical region, based on a composite of SSTs from strong El Niño years.

4. Assess how the remote changes of circulation affect sea ice within the north Canada and Greenland region

Over the last number of decades, sea ice in the Arctic has been rapidly declining at a rate of approximately  $13.3\%$  decade<sup>-1</sup> (Parkinson and Comiso, 2013). This has had a subsequent effect on the Arctic climate which has been warming at twice the rate as the global surface air temperature average (Cohen et al., 2014a; Screen and Simmonds, 2010b; Serreze et al., 2009; Serreze and Francis, 2006). While this rapid sea ice change has been viewed to be the direct result of increased greenhouse warming (Screen et al., 2015; Stroeve et al., 2012), changes in circulation can also impact the retention or removal of sea ice from the Arctic region (Arfeuille et al., 2000; Deser et al., 2000). As this research focuses on changes to circulation over north Canada and Greenland where multi-year sea ice, north of Canada, is found, an interesting piece of further research would be to investigate how the response of circulation to imposed tropical SST perturbations can affect sea ice retention or removal mainly in summer months, when sea ice is experiencing its most rapid decline. To do this, a new set of model experiments would need to be conducted, using HadGEM3 but coupled to a sea ice model such as CICE, the Los Alamos sea ice model (<http://oceans11.lanl.gov/trac/CICE>), to assess for changes in sea ice transport relative to circulation changes over the Arctic region in response to the same imposed tropical SST forcing.



# References

- Alexeev, V. a., Langen, P. L., and Bates, J. R. (2005). Polar amplification of surface warming on an aquaplanet in “ghost forcing” experiments without sea ice feedbacks. *Climate Dynamics*, 24(7-8):655–666.
- Ambaum, M. H. P. and Hoskins, B. J. (2002). The NAO troposphere-stratosphere connection. *Journal of Climate*, 15(14):1969–1978.
- Ambaum, M. H. P., Hoskins, B. J., and Stephenson, D. B. (2001). Arctic oscillation or North Atlantic oscillation? *Journal of Climate*, 14(16):3495–3507.
- Ambrizzi, T., Hoskins, B., and Hsu, H. (1995). Rossby wave propagation and teleconnection patterns in the austral winter. *Journal of the Atmospheric . . .*, 52(21).
- Ambrizzi, T. and Hoskins, B. J. (1997). Stationary Rossby-wave propagation in a baroclinic atmosphere. *Quarterly Journal of the Royal Meteorological Society*, 123(540):919–928.
- Andrews, D. G. (1987). On the interpretation of the Eliassen-palm flux divergence. *Quarterly Journal of the Royal Meteorological Society*, 113(475):323–338.
- Andrews, D. G. (2010). *An Introduction to Atmospheric Physics*, volume 2. Cambridge University Press.
- Andrews, D. G., Holton, J. R., and Leovy, C. B. (1987). *Middle Atmosphere Dynamics*. Academic Press.
- Arfeuille, G., Mysak, L. a., and Tremblay, L. B. (2000). Simulation of the interannual variability of the wind-driven Arctic sea-ice cover during 1958–1998. *Climate Dynamics*, 16(2-3):107–121.
- Bader, J., Mesquita, M. D. S., Hodges, K. I., Keenlyside, N., Østerhus, S., and Miles, M. (2011). A review on Northern Hemisphere sea-ice, storminess and the North Atlantic Oscillation: Observations and projected changes. *Atmospheric Research*, 101(4):809–834.
- Baldwin, M. P. and Dunkerton, T. J. (1999). Propagation of the Arctic Oscillation from the stratosphere to the troposphere. *Journal of Geophysical Research*, 104(D24):30937.

- Baldwin, M. P. and Dunkerton, T. J. (2001). Stratospheric Harbingers of Anomalous Weather Regimes. *Science*, 294(5542):581–584.
- Barnston, A. G. and Livezey, R. E. (1987). Classification, Seasonality and persistence of low-frequent atmospheric circulation patterns. *Monthly Weather Review*, 115:1083–1126.
- Blackmon, M. L., Lee, Y.-H., Wallace, J. M., and Hsu, H.-H. (1984). Time Variation of 500 mb Height Fluctuations with Long, Intermediate and Short Time Scales as Deduced from Lag-Correlation Statistics. *Journal of the Atmospheric Sciences*, 41(6):981–991.
- Branstator, G. (1983). Horizontal Energy Propagation in a Barotropic Atmosphere with Meridional and Zonal Structure. *Journal of the Atmospheric Sciences*, 40:1689–1708.
- Branstator, G. (2002). Circumglobal Teleconnections, the Jet Stream Waveguide, and the North Atlantic Oscillation. *Journal of Climate*, 15(14):1893–1910.
- Cai, M. and Huang, B. (2012). A New Look at the Physics of Rossby Waves: A Mechanical-Coriolis Oscillation. *Journal of the Atmospheric Sciences*, page 120816061703005.
- Cash, B. A. and Lee, S. (2001). Observed nonmodal growth of the Pacific-North American teleconnection pattern. *Journal of Climate*, 14(6):1017–1028.
- Cassano, E. N., Cassano, J. J., Higgins, M. E., and Serreze, M. C. (2014). Atmospheric impacts of an Arctic sea ice minimum as seen in the Community Atmosphere Model. *International Journal of Climatology*, 34(3):766–779.
- Chung, C. E. and Räisänen, P. (2011). Origin of the Arctic warming in climate models. *Geophysical Research Letters*, 38(21):n/a–n/a.
- Ciasto, L. M., Simpkins, G. R., and England, M. H. (2014). Teleconnections between Tropical Pacific SST Anomalies and Extratropical Southern Hemisphere Climate. *Journal of Climate*, page 141006071055006.
- Cohen, J., Furtado, J. C., Jones, J., Barlow, M., Whittleston, D., and Entekhabi, D. (2014a). Linking Siberian snow cover to precursors of stratospheric variability. *Journal of Climate*, 27(14):5422–5432.
- Cohen, J., Screen, J. A., Furtado, J. C., Barlow, M., Whittleston, D., Coumou, D., Francis, J., Dethloff, K., Entekhabi, D., Overland, J., and Jones, J. (2014b). Recent Arctic amplification and extreme mid-latitude weather. *Nature Geoscience*, 7(9):627–637.
- Collins, S., James, R., Ray, P., and Chen, K. (2013). Grids in numerical weather and climate models. *Grids in Numerical Weather and Climate Models*, pages 111–128.
- Comiso, J. (2012). Large decadal decline of the Arctic multiyear ice cover. *Journal of Climate*, (February):1–38.
- Comiso, J. C., Parkinson, C. L., Gersten, R., and Stock, L. (2008). Accelerated decline in the Arctic sea ice cover. *Geophysical Research Letters*, 35(1):1–6.

- Cowtan, K. and Way, R. G. (2014). Coverage bias in the HadCRUT4 temperature series and its impact on recent temperature trends. *Quarterly Journal of the Royal Meteorological Society*, 140(683):1935–1944.
- Dai, Y., Feldstein, S. B., Tan, B., and Lee, S. (2017). Formation mechanisms of the Pacific-North American teleconnection with and without its canonical tropical convection pattern. *Journal of Climate*, 30(9):3139–3155.
- Davies, T., Cullen, M. J. P., Malcolm, a. J., Mawson, M. H., Staniforth, a., White, a. a., and Wood, N. (2005). A new dynamical core for the Met Office’s global and regional modelling of the atmosphere. *Quarterly Journal of the Royal Meteorological Society*, 131(608):1759–1782.
- Dee, D. P., Uppala, S. M., Simmons, a. J., Berrisford, P., Poli, P., Kobayashi, S., Andrae, U., Balmaseda, M. a., Balsamo, G., Bauer, P., Bechtold, P., Beljaars, a. C. M., van de Berg, L., Bidlot, J., Bormann, N., Delsol, C., Dragani, R., Fuentes, M., Geer, a. J., Haimberger, L., Healy, S. B., Hersbach, H., Hólm, E. V., Isaksen, L., Kållberg, P., Köhler, M., Matricardi, M., McNally, a. P., Monge-Sanz, B. M., Morcrette, J.-J., Park, B.-K., Peubey, C., de Rosnay, P., Tavolato, C., Thépaut, J.-N., and Vitart, F. (2011). The ERA-Interim reanalysis: configuration and performance of the data assimilation system. *Quarterly Journal of the Royal Meteorological Society*, 137(656):553–597.
- Deser, C. (2000). On the teleconnectivity of the ‘Arctic Oscillation’. *Geophysical Research Letters*, 27(6):779–782.
- Deser, C., Tomas, R., Alexander, M., and Lawrence, D. (2010). The seasonal atmospheric response to projected Arctic sea ice loss in the late twenty-first century. *Journal of Climate*, 23(2):333–351.
- Deser, C., Walsh, J. E., and Timlin, M. S. (2000). Arctic Sea Ice Variability in the Context of Recent Atmospheric Circulation Trends. *Journal of Climate*, 13(3):617–633.
- Devasthale, a., Sedlar, J., Koenigk, T., and Fetzer, E. J. (2013). The thermodynamic state of the Arctic atmosphere observed by AIRS: comparisons during the record minimum sea ice extents of 2007 and 2012. *Atmospheric Chemistry and Physics*, 13(15):7441–7450.
- Ding, H., Keenlyside, Noel, S., and Latif, M. (2012). Impact of the Equatorial Atlantic on the El Nino Southern Oscillation. *Climate Dynamics*, 38:1965–1972.
- Ding, Q., Steig, E. J., Battisti, D. S., and Küttel, M. (2011). Winter warming in West Antarctica caused by central tropical Pacific warming. *Nature Geoscience*, 4(6):398–403.
- Ding, Q., Wallace, J. M., Battisti, D. S., Steig, E. J., Gallant, A. J. E., Kim, H.-J., and Geng, L. (2014). Tropical forcing of the recent rapid Arctic warming in northeastern Canada and Greenland. *Nature*, 509(7499):209–212.
- Ding, Q. and Wang, B. (2005). Circumglobal Teleconnection in the Northern Hemisphere Summer\*. *Journal of Climate*, 18(17):3483–3505.

- Donlon, C. J., Martin, M., Stark, J., Roberts-Jones, J., Fiedler, E., and Wimmer, W. (2012). The Operational Sea Surface Temperature and Sea Ice Analysis (OSTIA) system. *Remote Sensing of Environment*, 116:140–158.
- Duarte, C. M., Lenton, T. M., Wadhams, P., and Wassmann, P. (2012). Abrupt climate change in the Arctic. *Nature Climate Change*, 2(2):60–62.
- Edwards, J. M. and Slingo, A. (1996). Studies with a flexible new radiation code. I: Choosing a configuration for a large-scale model. *Quarterly Journal of the Royal Meteorological Society*, 122(531):689–719.
- Feldstein, S. B. (2000). The timescale, power spectra, and climate noise properties of teleconnection patterns. *Journal of Climate*, 13(24):4430–4440.
- Feldstein, S. B. (2002). Fundamental mechanisms of the growth and decay of the PNA teleconnection pattern. *Quarterly Journal of the Royal Meteorological Society*, 128:775–796.
- Ferranti, L., Molteni, F., and Palmer, T. N. (1994). Impact of localized tropical and extratropical SST anomalies in ensembles of seasonal GCM integrations. *Quarterly Journal of the Royal Meteorological Society*, 120(520):1613–1645.
- Forsberg, R., Sørensen, L., and Simonsen, S. (2017). Greenland and Antarctica Ice Sheet Mass Changes and Effects on Global Sea Level. *Surveys in Geophysics*, 38(1):89–104.
- Francis, J. a. and Vavrus, S. J. (2012). Evidence linking Arctic amplification to extreme weather in mid-latitudes. *Geophysical Research Letters*, 39(6).
- Franzke, C. and Feldstein, S. B. (2005). The Continuum and Dynamics of Northern Hemisphere Teleconnection Patterns. *Journal of the Atmospheric Sciences*, 62(9):3250–3267.
- Franzke, C., Feldstein, S. B., and Lee, S. (2011). Synoptic analysis of the Pacific-North American teleconnection pattern. *Quarterly Journal of the Royal Meteorological Society*, 137(655):329–346.
- Freitas, A. C. V. and Ambrizzi, T. (2012). Changes in the austral winter hadley circulation and the impact on stationary rossby waves propagation. *Advances in Meteorology*, 2012.
- Freitas, A. C. V., Frederiksen, J. S., O’Kane, T. J., and Ambrizzi, T. (2016). Simulated austral winter response of the Hadley circulation and stationary Rossby wave propagation to a warming climate. *Climate Dynamics*, pages 1–25.
- Fyfe, J. C., Boer, G. J., and Flato, G. M. (1999). The Arctic and Antarctic Oscillations and their projected changes under global warming. *Geophysical Research Letters*, 26(11):1601–1604.
- Garfinkel, C. I. and Hartmann, D. L. (2007). Effects of the El Nino-Southern Oscillation and the Quasi-Biennial Oscillation on polar temperatures in the stratosphere. *Journal of Geophysical Research Atmospheres*, 112(19):D19112.

- Garfinkel, C. I. and Hartmann, D. L. (2008). Different ENSO teleconnections and their effects on the stratospheric polar vortex. *Journal of Geophysical Research Atmospheres*, 113(18):D18114.
- Garfinkel, C. I., Hartmann, D. L., and Sassi, F. (2010). Tropospheric precursors of anomalous northern hemisphere stratospheric polar vortices. *Journal of Climate*, 23(12):3282–3299.
- Gates, W. L. and Gates, W. L. (1992). AMIP: The Atmospheric Model Intercomparison Project. *Bulletin of the American Meteorological Society*, 73(12):1962–1970.
- Gong, G., Entekhabi, D., and Cohen, J. (2003). Modeled Northern Hemisphere winter climate response to realistic Siberian snow anomalies. *Journal of Climate*, 16(23):3917–3931.
- Goss, M., Feldstein, S. B., and Lee, S. (2016). Stationary wave interference and its relation to tropical convection and Arctic warming. *Journal of Climate*, 29(4):1369–1389.
- Graham, N. E., Barnett, T.P., Wilde, R., Ponater, M., and Schubert, S. (1994). On the Roles of Tropical and Midlatitude SSTs in Forcing Interannual to Interdecadal Variability in the Winter Northern Hemisphere Circulation. *Journal of climate*, pages 1416–1441.
- Graversen, R. G. (2006). Do Changes in the Midlatitude Circulation Have Any Impact on the Arctic Surface Air Temperature Trend? *Journal of Climate*, 19(20):5422–5438.
- Graversen, R. G., Mauritsen, T., Tjernström, M., Källén, E., and Svensson, G. (2008). Vertical structure of recent Arctic warming. *Nature*, 451(January):53–56.
- Graversen, R. G. and Wang, M. (2009). Polar amplification in a coupled climate model with locked albedo. *Climate Dynamics*, 33(5):629–643.
- Haine, T. W. N. and Martin, T. (2017). The Arctic-Subarctic sea ice system is entering a seasonal regime: Implications for future Arctic amplification. *Sci. Rep.*, 7(1):1–9.
- Hewitt, H. T., Copsey, D., Culverwell, I. D., Harris, C. M., Hill, R. S. R., Keen, a. B., McLaren, a. J., and Hunke, E. C. (2011). Design and implementation of the infrastructure of HadGEM3: the next-generation Met Office climate modelling system. *Geoscientific Model Development*, 4(2):223–253.
- Higgins, M. E. and Cassano, J. J. (2009). Impacts of reduced sea ice on winter Arctic atmospheric circulation, precipitation, and temperature. *Journal of Geophysical Research Atmospheres*, 114(16).
- Hilmer, M. and Jung, T. (2000). Evidence for a recent change in the link between the North Atlantic Oscillation and Arctic Sea ice export. *Geophysical Research Letters*, 27(7):989–992.
- Hoerling, M. P., Hurrell, J. W., Xu, T., Bates, G. T., and Phillips, A. S. (2004). Twentieth century North Atlantic climate change. Part II: Understanding the effect of Indian Ocean warming. *Climate Dynamics*, 23(3-4):391–405.

- Holland, M. M. (2003). The North Atlantic Oscillation–Arctic Oscillation in the CCSM2 and Its Influence on Arctic Climate Variability. *Journal of Climate*, 16(16):2767–2781.
- Holton, J. R. and Hakim, G. J. (2013). *An Introduction to Dynamic Meteorology*. Elsevier.
- Hoskins, B. and Ambrizzi, T. (1993). Rossby wave propagation on a realistic longitudinally varying flow. *Journal of the Atmospheric Sciences*, 50(12):1661–1671.
- Hoskins, B. J. and James, I. N. (2014). *Fluid Dynamics of the Mid-Latitude Atmosphere*. John Wiley & Sons.
- Hoskins, B. J. and Karoly, D. J. (1981). The Steady Linear Response of a Spherical Atmosphere to Thermal and Orographic Forcing. *Journal of the Atmospheric Sciences*, 38:1179–1196.
- Hsieh, W. W., Wu, A., and Shabbar, A. (2006). Nonlinear atmospheric teleconnections. *Geophysical Research Letters*, 33(7):L07714.
- Huntington, H., Weller, G., and Bush, E. (2005). An introduction to the Arctic climate impact assessment. In *Arctic Climate Impact Assessment*, pages 1–20. Cambridge University Press.
- Hurrell, J. W. (1995). Decadal Trends in the North Atlantic Oscillation: Regional Temperatures and Precipitation. *Science (New York, N.Y.)*, 269(5224):676–9.
- Hurrell, J. W. (1996). Influence of variations in extratropical wintertime teleconnections on northern hemisphere temperature. *Geophysical Research Letters*, 23(6):665–668.
- Hurrell, J. W. and Deser, C. (2010). North Atlantic climate variability: The role of the North Atlantic Oscillation. *Journal of Marine Systems*, 79(3-4):231–244.
- Ineson, S. and Scaife, a. a. (2009). The role of the stratosphere in the European climate response to El Niño. *Nature Geoscience*, 2(1):32–36.
- Inoue, J., Yamazaki, A., Ono, J., Dethloff, K., Maturilli, M., Neuber, R., Edwards, P., and Yamaguchi, H. (2015). Additional Arctic observations improve weather and sea-ice forecasts for the Northern Sea Route. *Scientific Reports*, 5.
- James, I. N. (1994). *Introduction to circulating atmospheres*. Cambridge University Press, Cambridge.
- Kao, H. Y. and Yu, J. Y. (2009). Contrasting Eastern-Pacific and Central-Pacific types of ENSO. *Journal of Climate*, 22(3):615–632.
- Karoly, D. J. (1983). Rossby wave propagation in a barotropic atmosphere. *Dynamics of Atmospheres and Oceans*, 7(2):111–125.
- Karoly, D. J., Plumb, R. A., and Ting, M. (1989). Examples of the Horizontal Propagation of Quasi-stationary Waves. *Journal of the Atmospheric Sciences*, 46:2802–2811.
- Kiehl, J. T. (2006). Overview of climate modeling. In Kiehl, J. T. and Ramanathan, V., editors, *Frontiers of Climate Modeling*, pages 1–25. Cambridge University Press, Cambridge.

- Kiladis, G. N. (1998). Observations of Rossby Waves Linked to Convection over the Eastern Tropical Pacific. *Journal of the Atmospheric Sciences*, 55(3):321–339.
- Ko, K.-C. and Hsu, H.-H. (2010). Downstream Development of the Summertime Tropical Cyclone/Submonthly Wave Pattern in the Extratropical North Pacific. *Journal of Climate*, 23(8):2223–2229.
- Kug, J. S., Jin, F. F., and An, S. I. (2009). Two types of El Niño events: Cold tongue El Niño and warm pool El Niño. *Journal of Climate*, 22(6):1499–1515.
- Kwok, R., Cunningham, G. F., Wensnahan, M., Rigor, I., Zwally, H. J., and Yi, D. (2009). Thinning and volume loss of the Arctic Ocean sea ice cover: 2003–2008. *Journal of Geophysical Research: Oceans*, 114(7):C07005.
- Lau, K.-M. and Lim, H. (1984). On the Dynamics of Equatorial forcing of climate teleconnections. *Journal of the Atmospheric Sciences*, 41(2):161–176.
- Lau, N. (1979). The observed structure of tropospheric stationary waves and the local balances of vorticity and heat. *Journal of the Atmospheric Sciences*, 36(6):996–1016.
- Lee, S. (2012). Testing of the Tropically Excited Arctic Warming Mechanism (TEAM) with Traditional El Niño and La Niña. *Journal of Climate*, 25(12):4015–4022.
- Lee, S. (2014). A theory for polar amplification from a general circulation perspective. *Asia-Pacific Journal of Atmospheric Sciences*, 50(1):31–43.
- Leeson, A., Shepherd, A., Briggs, K., Howat, I., Fettweis, X., Morlighem, M., and Rignot, E. (2015). Supraglacial lakes on the Greenland ice sheet advance inland under warming climate. *Nature Climate Change*, 5(January):51–55.
- Li, X., Holland, D. M., Gerber, E. P., and Yoo, C. (2014). Impacts of the north and tropical Atlantic Ocean on the Antarctic Peninsula and sea ice. *Nature*, 505(7484):538–42.
- Lindsay, R., Wensnahan, M., Schweiger, a., and Zhang, J. (2014). Evaluation of Seven Different Atmospheric Reanalysis Products in the Arctic\*. *Journal of Climate*, 27(7):2588–2606.
- Liu, J., Curry, J. a., and Hu, Y. (2004). Recent Arctic Sea Ice Variability: Connections to the Arctic Oscillation and the ENSO. *Geophysical Research Letters*, 31(9).
- Liu, Y., Key, J. R., and Wang, X. (2009). Influence of changes in sea ice concentration and cloud cover on recent Arctic surface temperature trends. *Geophysical Research Letters*, 36(20):1–6.
- Liu, Z. and Alexander, M. (2007). Atmospheric bridge, oceanic tunnel, and global climatic teleconnections. *Reviews of Geophysics*, (2005):1–34.
- Lu, B. and Ren, H. L. (2016). SST-forced interdecadal deepening of the winter India-Burma trough since the 1950s. *Journal of Geophysical Research: Atmospheres*, 121(6):2719–2731.

- Mantua, N. and Hare, S. (2002). The Pacific Decadal Oscillation. *Journal of Oceanography*, 58:35–44.
- Martin, G. M., Ringer, M. A., Pope, V. D., Jones, A., Dearden, C., and Hinton, T. J. (2006). Properties of the Atmosphere in the New Haley Centre Global Environmental Model (HadGEM1). Part I: Model Description and Global Climatology. *Journal of Climate*, 19:1274–1301.
- Maslanik, J., Stroeve, J., Fowler, C., and Emery, W. (2011). Distribution and trends in Arctic sea ice age through spring 2011. *Geophysical Research Letters*, 38(13):1–6.
- Matsuno, T. (1970). Vertical Propagation of Stationary Planetary Waves in the Winter Northern Hemisphere. *Journal of the Atmospheric Sciences*, 27(6):871–883.
- Mayne, N. J., Baraffe, I., Acreman, D. M., Smith, C., Wood, N., Amundsen, D. S., Thuburn, J., and Jackson, D. R. (2014). Using the UM dynamical cores to reproduce idealised 3-D flows. *Geoscientific Model Development*, 7(6):3059–3087.
- McBean, G., Alekseev, G., Chen, D., and Foerland, E. (2005). Chapter 2: Arctic Climate: past and present. In *Arctic Climate Impact Assessment*, pages 21–60. Cambridge University Press, Cambridge, U.K.
- McIntosh, P. C. and Hendon, H. H. (2017). Understanding Rossby wave trains forced by the Indian Ocean Dipole. *Climate Dynamics*, 0(0):0.
- Meehl, G. a., Arblaster, J. M., Fasullo, J. T., Hu, A., and Trenberth, K. E. (2011). Model-based evidence of deep-ocean heat uptake during surface-temperature hiatus periods. *Nature Climate Change*, 1(7):360–364.
- Mizielinski, M. S., Roberts, M. J., Vidale, P. L., Schiemann, R., Demory, M.-E., Strachan, J., Edwards, T., Stephens, a., Lawrence, B. N., Pritchard, M., Chiu, P., Iwi, a., Churchill, J., del Cano Novales, C., Kettleborough, J., Roseblade, W., Selwood, P., Foster, M., Glover, M., and Malcolm, a. (2014). High-resolution global climate modelling: the UPSCALE project, a large-simulation campaign. *Geoscientific Model Development*, 7(4):1629–1640.
- Mo, R., Fyfe, J., and Derome, J. (1998). Phase-locked and asymmetric correlations of the wintertime atmospheric patterns with the ENSO. *Atmosphere-Ocean*, 36(3):213–239.
- Moore, G. W. K., Renfrew, I. A., and Pickart, R. S. (2013). Multidecadal mobility of the north atlantic oscillation. *Journal of Climate*, 26(8):2453–2466.
- National Snow and Ice Data Centre (NSIDC) (2017). Quick facts on ice sheets. <https://nsidc.org/cryosphere/quickfacts/icesheets.html>.
- Newman, M., Alexander, M. A., Ault, T. R., Cobb, K. M., Deser, C., Di Lorenzo, E., Mantua, N. J., Miller, A. J., Minobe, S., Nakamura, H., Schneider, N., Vimont, D. J., Phillips, A. S., Scott, J. D., and Smith, C. A. (2016). The Pacific decadal oscillation, revisited. *Journal of Climate*, 29(12):4399–4427.

- Omrani, N. E., Keenlyside, N. S., Bader, J., and Manzini, E. (2014). Stratosphere key for wintertime atmospheric response to warm Atlantic decadal conditions. *Climate Dynamics*, 42(3-4):649–663.
- Osborn, T. J. (2011). Winter 2009/2010 temperatures and a record-breaking North Atlantic Oscillation Index. *Weather*, 66(1):19–21.
- Palmer, T. N. (1988). Medium and extended range predictability and stability of the Pacific/North American mode. *Quarterly Journal of the Royal Meteorological Society*, 114(481):691–713.
- Parkinson, C. L. and Comiso, J. C. (2013). On the 2012 record low Arctic sea ice cover: Combined impact of preconditioning and an August storm. *Geophysical Research Letters*, 40(7):1356–1361.
- Philander, S. (1985). El Niño and La Niña. *Journal of Atmospheric Sciences*, 42(23):2652–2662.
- Picaut, J., Masia, F., and du Penhoat, Y. (1997). An Advective-Reflective Conceptual Model for the Oscillatory Nature of the ENSO. *Science*, 277:663–666.
- Plumb, R. A. (1985). On the Three-Dimensional Propagation of Stationary Waves. *Journal of the Atmospheric Sciences*, 42(3):217–229.
- Qin, J. and Robinson, W. A. (1993). On the Rossby Wave Source and the Steady Linear Response to Tropical Forcing. *Journal of the Atmospheric Sciences*, 50(12):1819–1823.
- Randall, D. A., Wood, R. A., Bony, S., Colman, R., Fichefet, T., Fyfe, J., Kattsov, V., Pitman, A., Shukla, J., Srinivasan, J., Stouffer, R. J., Sumi, A., and Taylor, K. E. (2007). Climate Models and Their Evaluation. *Climate Change 2007 The Physical Science Basis..Contribution of Working Group I to Fourth Assessment Report of the Intergovernmental Panel on Climate Change*, pages 591–662.
- Rasmusson, E. M. and Wallace, J. M. (1983). Meteorological Aspects of the El Niño/Southern Oscillation. *Science*, 222:1195–1202.
- Rayner, N. A., Parker, D. E., Horton, E. B., Folland, C., Alexander, L., Rowell, D., Kent, E., and Kaplan, A. (2003). Global analyses of sea surface temperature, sea ice, and night marine air temperature since the late nineteenth century. *Journal of Geophysical Research*, 108(D14):4407.
- Reichler, T. and Kim, J. (2008). How well do coupled models simulate today’s climate? *Bulletin of the American Meteorological Society*, 89(3):303–311.
- Rignot, E., Velicogna, I., Van Den Broeke, M. R., Monaghan, A., and Lenaerts, J. (2011). Acceleration of the contribution of the Greenland and Antarctic ice sheets to sea level rise. *Geophysical Research Letters*, 38(5).
- Robert, A., Yee, T. L., and Ritchie, H. (1985). A Semi-Lagrangian and Semi-Implicit Numerical Integration Scheme for Multilevel Atmospheric Models. *Monthly Weather Review*, 113(3):388–394.

- Saito, K., Ishida, J.-i., Aranami, K., Hara, T., Segawa, T., Narita, M., and Honda, Y. (2007). Nonhydrostatic Atmospheric Models and Operational Development at JMA. *Journal of the Meteorological Society of Japan*, 85B:271–304.
- Salby, M. L. (2012). *Physics of the Atmosphere and Climate*. Cambridge University Press.
- Salby, M. L. and Garcia, R. R. (1987). Transient response to localized episodic heating in the tropics. Part I: Excitation and Short-Time Near-Field Behavior. *Journal of the Atmospheric Sciences*, 44:458–498.
- Sardeshmukh, P. and Hoskins, B. (1988). The generation of global rotational flow by steady idealized tropical divergence. *Journal of the Atmospheric Sciences*, 45(7):1228–1251.
- Sardeshmukh, P. D. and Hoskins, B. J. (1985). Vorticity balances in the tropics during the 1982-83 El Niño-Southern Oscillation event. *Quarterly Journal of the Royal Meteorological Society*, 111:261–278.
- Scaife, A. A., Comer, R. E., Dunstone, N. J., Knight, J. R., Smith, D. M., MacLachlan, C., Martin, N., Peterson, K. A., Rowlands, D., Carroll, E. B., Belcher, S., and Slingo, J. (2017). Tropical rainfall, Rossby waves and regional winter climate predictions. *Quarterly Journal of the Royal Meteorological Society*, 143(702):1–11.
- Schneider, D. P., Deser, C., and Okumura, Y. (2011). An assessment and interpretation of the observed warming of West Antarctica in the austral spring. *Climate Dynamics*, 38(1-2):323–347.
- Schneider, N. and Cornuelle, B. D. (2005). The forcing of the Pacific Decadal Oscillation. *Journal of Climate*, 18(21):4355–4373.
- Screen, J. A. (2014). Arctic amplification decreases temperature variance in northern mid- to high-latitudes. *Nat. Clim. Chang.*, 4(7):577–582.
- Screen, J. A., Deser, C., and Simmonds, I. (2012). Local and remote controls on observed Arctic warming. *Geophysical Research Letters*, 39(10).
- Screen, J. A., Deser, C., and Sun, L. (2015). Projected changes in regional climate extremes arising from Arctic sea ice loss. *Environmental Research Letters*, 10.
- Screen, J. A. and Francis, J. A. (2016). Contribution of sea-ice loss to Arctic amplification is regulated by Pacific Ocean decadal variability. *Nature Climate Change*, 6:856–861.
- Screen, J. a. and Simmonds, I. (2010a). Increasing fall-winter energy loss from the Arctic Ocean and its role in Arctic temperature amplification. *Geophysical Research Letters*, 37(May):1–5.
- Screen, J. a. and Simmonds, I. (2010b). The central role of diminishing sea ice in recent Arctic temperature amplification. *Nature*, 464(7293):1334–7.
- Screen, J. A. and Simmonds, I. (2010c). The central role of diminishing sea ice in recent Arctic temperature amplification. Supplementary Information. *Nature*, 464(7293):1334–1337.

- Screen, J. a. and Simmonds, I. (2011). Erroneous Arctic Temperature Trends in the ERA-40 Reanalysis: A Closer Look. *Journal of Climate*, 24(10):2620–2627.
- Screen, J. a., Simmonds, I., Deser, C., and Tomas, R. (2013). The Atmospheric Response to Three Decades of Observed Arctic Sea Ice Loss. *Journal of Climate*, 26(4):1230–1248.
- Serreze, M., Barrett, A., and Stroeve, J. (2009). The emergence of surface-based Arctic amplification. *The Cryosphere*, pages 11–19.
- Serreze, M. C. and Barry, R. G. (2005). Physical characteristics and basic climatic features. In Serreze, M. C. and Barry, R. G., editors, *The Arctic Climate System*, pages 17–54. Cambridge University Press.
- Serreze, M. C. and Francis, J. A. (2006). The Arctic Amplification Debate. *Climatic Change*, 76(3-4):241–264.
- Serreze, M. C., Holland, M. M., and Stroeve, J. (2007). Perspectives on the Arctic’s shrinking sea-ice cover. *Science (80-. )*, 315(June):1533–1536.
- Serreze, M. C. and Stroeve, J. C. (2015). Arctic sea ice trends, variability and implications for seasonal ice forecasting. *Philos. Trans. R. Soc. A Math. Phys. Eng. Sci.*, 373(2045):20140159.
- Sheridan, S. and Lee, C. C. (2012). Synoptic climatology and the analysis of atmospheric teleconnections. *Progress in Physical Geography*, 36(4):548–557.
- Shimizu, M. H. and de Albuquerque Cavalcanti, I. F. (2010). Variability patterns of Rossby wave source. *Climate Dynamics*, 37(3-4):441–454.
- Simmons, A. (1982). The forcing of stationary wave motion by tropical diabatic heating. *Quarterly Journal of the Royal Meteorological Society*, 108:503–534.
- Simmons, A. J. and Poli, P. (2014). Arctic warming in ERA-Interim and other analyses. *Quarterly Journal of the Royal Meteorological Society*, 141(689):1147–1162.
- Simmons, A. J., Poli, P., Dee, D. P., Berrisford, P., Hersbach, H., Kobayashi, S., and Peubey, C. (2014). Estimating low-frequency variability and trends in atmospheric temperature using ERA-Interim. *Quarterly Journal of the Royal Meteorological Society*, 140(679):329–353.
- Simmons, a. J., Wallace, J. M., and Branstator, G. W. (1983). Barotropic Wave Propagation and Instability, and Atmospheric Teleconnection Patterns. *Journal of the Atmospheric Sciences*, 40(6):1363–1392.
- Simmons, A. J., Willett, K. M., Jones, P. D., Thorne, P. W., and Dee, D. P. (2010). Low-frequency variations in surface atmospheric humidity, temperature, and precipitation: Inferences from reanalyses and monthly gridded observational data sets. *Journal of Geophysical Research Atmospheres*, 115(1):1–21.
- Simpkins, G. R., Ciasto, L. M., Thompson, D. W. J., and England, M. H. (2012). Seasonal relationships between large-scale climate variability and antarctic sea ice concentration. *Journal of Climate*, 25(16):5451–5469.

- Simpkins, G. R., McGregor, S., Taschetto, A. S., Ciasto, L. M., and England, M. H. (2014). Tropical connections to climatic change in the extratropical Southern Hemisphere: The role of atlantic SST trends. *Journal of Climate*, 27(13):4923–4936.
- Smith, K. L., Kushner, P. J., and Cohen, J. (2011). The role of linear interference in northern annular mode variability associated with Eurasian snow cover extent. *Journal of Climate*, 24(23):6185–6202.
- Staniforth, A. and Cote, J. (1991). Semi-Lagrangian Integration Schemes for Atmospheric Models; A Review. *Monthly Weather Review*, 119(9):2206–2223.
- Straus, D. M. and Shukla, J. (2002). Does ENSO force the PNA? *Journal of Climate*, 15(17):2340–2358.
- Stroeve, J., Markus, T., Boisvert, L., Miller, J., and Barrett, A. (2014). Changes in Arctic melt season and implications for sea ice loss. *Geophysical Research Letters*, pages 1–10.
- Stroeve, J. C., Kattsov, V., Barrett, A., Serreze, M., Pavlova, T., Holland, M., and Meier, W. N. (2012). Trends in Arctic sea ice extent from CMIP5, CMIP3 and observations. *Geophysical Research Letters*, 39(16):1–7.
- Strong, C. and Davis, R. E. (2008). Variability in the Position and Strength of Winter Jet Stream Cores Related to Northern Hemisphere Teleconnections. *Journal of Climate*, 21(3):584–592.
- Suarez, M. J. and Schopf, P. S. (1988). A Delayed Action Oscillator for ENSO. *Journal of the Atmospheric Sciences*, 45(21):3283–3287.
- Taguchi, M. and Hartmann, D. L. (2006). Increased occurrence of stratospheric sudden warmings during El Niño as simulated by WACCM. *Journal of Climate*, 19(3):324–332.
- Taylor, K. E., Stouffer, R. J., and Meehl, G. A. (2012). An Overview of CMIP5 and the experiment design. *Bulletin of the American Meteorological Society*, 3(april):485–498.
- Thompson, D. W. J. and Wallace, J. M. (1998). The Arctic oscillation signature in the wintertime geopotential height and temperature fields. *Geophysical Research Letters*, 25(9):1297.
- Thompson, D. W. J. and Wallace, J. M. (2000a). Annular Modes in the Extratropical Circulation. Part 1: Month-to-Month Variability. *Journal of Climate*, 13(5):1000–1016.
- Thompson, D. W. J. and Wallace, J. M. (2000b). Annular Modes in the Extratropical Circulation. Part II: Trends. *Journal of Climate*, 13(5):1018–1036.
- Thompson, D. W. J. and Wallace, J. M. (2001). Regional Climate Impacts of the Northern Hemisphere Annular Mode. *Science*, 293:85–89.
- Trenberth, K. E., Branstator, G. W., Karoly, D., Kumar, A., Lau, N.-C., and Ropelewski, C. (1998). Progress during TOGA in understanding and modeling global teleconnections associated with tropical sea surface temperatures. *Journal of Geophysical Research*, 103(C7):14291.

- Trenberth, K. E. and Fasullo, J. T. (2013). An apparent hiatus in global warming? *Earth's Future*, 1(1):19–32.
- Trenberth, K. E., Fasullo, J. T., Branstator, G., and Phillips, A. S. (2014). Seasonal aspects of the recent pause in surface warming. *Nature Climate Change*, 4(October):911–916.
- Uppala, S. M., Kallberg, P. W., Simmons, A. J., Andrae, U., Bechtold, V. D. C., Fiorino, M., Gibson, J. K., Haseler, J., Hernandez, A., Kelly, G. A., Li, X., Onogi, K., Saarinen, S., Sokka, N., Allan, R. P., Andersson, E., Arpe, K., Balmaseda, M. A., Beljaars, A. C. M., Berg, L. V. D., Bidlot, J., Bormann, N., Caires, S., Chevallier, F., Dethof, A., Dragosavac, M., Fisher, M., Fuentes, M., Hagemann, S., Hólm, E., Hoskins, B. J., Isaksen, I., Janssen, P. A. E. M., Jenne, R., McNally, A. P., Mahfouf, J.-F., Morcrette, J.-J., Rayner, N. A., Saunders, R. W., Simon, P., Sterl, A., Trenberth, K. E., Untch, A., Vasiljevic, D., Viterbo, P., and Woollen, J. (2005). The ERA-40 re-analysis. *Quarterly Journal of the Royal Meteorological Society*, 131(612):2961–3012.
- van Angelen, J. H., van den Broeke, M. R., Wouters, B., and Lenaerts, J. T. M. (2014). Contemporary (1960–2012) Evolution of the Climate and Surface Mass Balance of the Greenland Ice Sheet. *Surveys in Geophysics*, 35(5):1155–1174.
- van Loon, H. and Labitzke, K. (1987). The Southern Oscillation. Part V: The Anomalies in the Lower Stratosphere of the Northern Hemisphere in Winter and a Comparison with the Quasi-Biennial Oscillation. *Monthly Weather Review*, 115(2):357–369.
- Venegas, S. A. and Mysak, L. A. (2000). Is there a dominant timescale of natural climate variability in the Arctic? *Journal of Climate*, 13(19):3412–3434.
- Wallace, J. and Gutzler, D. (1981). Teleconnections in the geopotential height field during the Northern Hemisphere winter. *Monthly Weather Review*, 109:784–812.
- Wallace, J. M. and Hobbs, P. V. (2006a). *Atmospheric Science, An Introductory Survey*. Elsevier.
- Wallace, J. M. and Hobbs, P. V. (2006b). Cloud Microphysics. *Atmospheric Science*, i(2006):209–269.
- Wang, C., Deser, C., and Yu, J. (2012a). El Niño and Southern Oscillation (ENSO): A review.
- Wang, H., Kumar, A., Wang, W., and Xue, Y. (2012b). Seasonality of the Pacific decadal oscillation. *Journal of Climate*, 25(1):25–38.
- Watanabe, M., Shiogama, H., Tatebe, H., Hayashi, M., Ishii, M., and Kimoto, M. (2014). Contribution of natural decadal variability to global warming acceleration and hiatus. *Nature Climate Change*, 4(10):893–897.
- Wu, L., He, F., Liu, Z., and Li, C. (2007). Atmospheric Teleconnections of Tropical Atlantic Variability: Interhemispheric, Tropical–Extratropical, and Cross-Basin Interactions. *Journal of Climate*, 20(5):856–870.

- 
- Wyrski, K. (1975). El Niño—The Dynamic Response of the Equatorial Pacific Ocean to Atmospheric Forcing. *Journal of Physical Oceanography*, 5(4):572–584.
- Yang, D. (1999). An improved precipitation climatology for the Arctic Ocean. *Geophysical Research Letters*, 26(11):1625–1628.
- Yin, J. H. (2005). A consistent poleward shift of the storm tracks in simulations of 21st century climate. *Geophysical Research Letters*, 32(18):1–4.
- Zebiak, S. E. and Cane, M. A. (1987). A model El Niño-Southern Oscillation. *Monthly Weather Review*, 115(10):2262–2278.